UILU-ENG 91-3602

Report No. 156

# A MODEL FOR THE LONG-LIFE FATIGUE BEHAVIOR OF SMALL NOTCHES

**by**
**Chih-Hsien Ting**
**and**
**F. V. Lawrence**
**Metallurgical Engineering**

A Report of the

MATERIALS ENGINEERING—MECHANICAL BEHAVIOR

College of Engineering, University of Illinois at Urbana-Champaign

November 1991

# A Model for the Long-Life Fatigue Behavior of Small Notches

Chih-Hsien Ting, Ph.D.
Department of Materials Science and Engineering
University of Illinois at Urbana-Champaign, 1991
Frederick V. Lawrence, Jr., Advisor

## Abstract

The effect of notches and intrinsic defects on the long-life regime fatigue properties was studied. A crack-closure-at-a-notch (termed CCN) model for predicting the fatigue life and fatigue threshold stress was developed based on the assumption that the da/dN vs. $\Delta K_{eff}$ relation is a unique material property independent of crack length. The variation of crack closure level with crack length for a crack emanating from a notch was found to depend on the material properties, the notch size, the notch acuity, and the applied load conditions.

The stress-life (S-N) properties of a cast aluminum alloy 319 were studied at room temperature under the R = -1 condition for both as-cast and polished cylindrical bar specimens. The test results showed that the fatigue strength of cast aluminum alloy 319 was not significantly affected by the surface conditions but strongly influenced by the size of defects which initiate fatigue cracks. Crack growth rate tests (da/dN vs. $\Delta K$) for R = -1 were also carried out on single-edge-notch plate (SENP) specimens. The fatigue threshold stresses and fatigue lives for both cylindrical bar specimens and SENP specimens were successfully predicted by the CCN model. The validity of this model was further confirmed through comparison of predictions with the experimental results reported in the literature.

The CCN model considered intrinsic defects to be small notches. The limits of the CCN model applicability were studied. The maximum non-damaging notch depth for a material was quantitatively determined. A general description of the effect of a notch on the fatigue threshold stress was proposed.

## ACKNOWLEDGEMENTS

I would like to express my sincere gratitude to Professor F. V. Lawrence, Jr. for his guidance, encouragement and many generous contributions to my personal and professional development. I also would like to express my gratitude to professor J. K. Shang for his stimulating discussions and guidance. I also wish to express my appreciation to my colleagues: Dr. Gregory Banas, for his help with the experimental parts of this study, Mr. Gary Fry, and Ms. Jill Oderio for their help in the preparation of this thesis.

Thanks are also extended to Dr. Peter Kurath for his assistance in conducting the laboratory experiments. This research was supported by the General Motors Technical Center, General Motors Corporation. Special thanks are extended to Mr. Richard J. Osborne, Dr. Dale A. Gerard, and Dr. Paul N. Crepeau for their valuable suggestions and donation of the test specimens.

I wish to express my appreciation to my parents and my family for their spiritual support and abundant encouragement. In addition, I wish to express my deepest appreciation to my wife, Chin-Shih for her boundless love and patience.

## TABLE OF CONTENTS

# LIST OF SYMBOLS AND ABBREVIATIONS

## SYMBOLS

| | |
|---|---|
| a | Crack length including the notch depth |
| b | Fatigue strength coefficient for smooth specimen |
| c | The half length of an elliptical crack on the specimen surface (mm) |
| $C_1$,$m_1$ | Paris' constant for da/dN versus $\Delta K$ data in Stage I (near-threshold), $C_1$ has a unit of m/cycle |
| $C_2$,$m_2$ | Paris' constant for da/dN vs. $\Delta K$ data in Stage II (mid-growth rate regime) |
| $C'_1$,$m_1$ | Paris' constant for da/dN vs. $\Delta K_{eff}$ data in Stage I (near-threshold regime) |
| $C'_2$,$m_2$ | Paris' constant for da/dN vs. $\Delta K_{eff}$ data in Stage II (mid-growth rate regime) |
| d | Grain size |
| D | Notch depth; for edge notch, D is the full notch length, and for centered notch D is half of notch length (mm) |
| $D_{eff}$ | Effective notch depth in determination of threshold stress |
| $D_{max}$ | The maximum notch depth above which $K_{fn}$ always equals $K_{tn}$ |
| da/dN | General description of fatigue crack growth rate (m/cycle) |
| E | Elastic modulus |
| $F_P$ | Fraction of plasticity-induced crack closure |
| H | Plastic modulus |
| K | Stress intensity factor (MPa$\sqrt{m}$) |
| $K_f$,$K_{fn}$ | Gross and net-section fatigue notch factor |
| $K_{IC}$,$K_{IQ}$ | Fracture toughness |
| $K_t$, $K_{tn}$ | Gross and net-section elastic stress concentration factor |
| $l_t$ | Transition crack length from Dowling [4]; used as initial crack length for life prediction, (mm) |
| $L_o$ | Intrinsic crack length (mm) |
| N | General description of fatigue cycle (cycles) |
| $N_f$ | Total propagation life |
| $N_I$ | Fatigue initiation life (sum of the nucleation and early crack propagation life) |
| $N_n$ | Fatigue crack nucleation life |

| | |
|---|---|
| $N_T$ | Total fatigue life |
| R | Load ratio |
| $S_e$ | Maximum stress of $\Delta S_e$, termed fatigue limit |
| $S_{max}$ | Maximum applied stress (gross section) (MPa) |
| $S_{opo}$ | Stabilized opening stress for a long crack |
| $S_{op}(x)$ | Opening stress for a crack emanating from a notch |
| $S_{th}$,$S_{thn}$ | Gross and net-section maximum stress under threshold condition |
| $S_u$ | Tensile strength |
| $S_y$ | Yield strength |
| T | Fatigue initiating defect size ($= \sqrt{Area}$, mm) |
| $U_o$ | Effective stress intensity ratio (dimensionless) |
| $U_{tho}$ | Effective threshold stress intensity ratio for a long crack |
| $U^*_{th}$ | Effective threshold stress intensity ratio for a short crack at $x = x^*$ |
| U(x) | Effective stress intensity ratio for a crack emanating from a notch |
| $U^{O/R}(x)$ | The function of U(x) calculated based on the roughness and oxide induced crack closure mechanisms |
| $U^S(x)$ | Sun and Sehitoglu's model for effective stress intensity ratio for a crack in a notched specimen |
| $U^T(x)$ | Tanaka's model for effective stress intensity ratio for a crack originating from a smooth specimen |
| $U_{th}(x)$ | Effective threshold stress intensity ratio for a crack emanating from a notch |
| x | Crack length (mm) |
| $x_f$ | Final crack length at failure |
| $x_i$ | Initial crack length for predicting the fatigue life |
| $x_{th}$ | Greatest possible length of a non-propagating crack (mm) |
| x' | Equivalent crack length in an un-notched specimen which has the same value of $U^*_{th}$ at $x^*$ as the crack in the notched specimen |
| $x^*$ | Spatial extent of notch stress field boundary (mm) |
| $X_{BC}$ | The maximum non-damaging notch depth |
| $(UK)_{eff}$ | Combined effect of crack closure and stress concentration factor in determination of threshold stress |
| Y(x) | Geometrical factor for stress intensity factor |
| $\alpha$ | Peterson's constant |
| $\alpha_I$ | Type I Peterson's constant (Eq. 2.4) |
| $\alpha_{II}$ | Type II Peterson's constant (Eq. 2.5) |

| | |
|---|---|
| $\Delta h$ | The depth of polish from original surface (mm) |
| $\Delta K$ | Stress intensity range |
| $\Delta K_{eff}$ | Effective stress intensity range |
| $\Delta K_{eff.tho}$ | Long crack effective threshold stress intensity range (material property) |
| $\Delta K_{eff}(x)$ | Short crack effective stress intensity range as a function of crack length |
| $\Delta K_S$ | Stress intensity range for crack within the notch stress field boundary |
| $\Delta K_{tho}$ | Long crack threshold stress intensity range (material property) |
| $\Delta K_{th}(x)$ | Short crack threshold stress intensity range which is a function of crack length |
| $\Delta K_x$ | Point of intersection of $\Delta K$ in a bi-linear model of da/dN versus $\Delta K$ relation |
| $\Delta S$ | Applied stress range (gross section) |
| $\Delta S_e$ | Range of fatigue limit for a smooth specimen |
| $\Delta S_{th}$, $\Delta S_{thn}$ | Gross and net-section threshold stress range of notched specimen |
| $\Delta x$ | $= x' - x^*$ |
| $\rho$ | Notch root radius |
| $\sigma'_f$ | Fatigue strength coefficient for a smooth specimen |

## ABBREVIATIONS

| | |
|---|---|
| AAE% | Average Absolute Error% |
| AR | Aspect Ratio (= a/c) |
| CCN | Crack-Closure-at-a-Notch |
| CDF | Cumulative Distribution Function |
| CNB | Circumferential Notch in a cylindrical Bar |
| CNP | Center Notch in a Plate |
| DAS | Dendrite Arm Spacing (mm) |
| DCS | Dendrite Cell Size (mm) |
| DENP | Double Edge Notches in a Plate |
| EPFM | Elastic-Plastic Fracture Mechanics |
| Error% | Percentage of the difference between predicted value and experimental value divided by the experimental value |
| FEM | Finite Element Method |
| LCMA | Limit of CCN Model Applicability |
| LEFM | Linear Elastic Fracture Mechanics |

| | |
|---|---|
| MDR | Microstructure Dominated Region |
| NSFB | Notch-Stress-Field Boundary |
| NPC | Non-propagating Crack |
| OICC | Oxide-Induced Crack Closure |
| PICC | Plasticity-Induced Crack Closure |
| PTS(I) | Peterson's model using Type I Peterson's constant ($\alpha_I$) |
| PTS(II) | Peterson's model using Type II Peterson's constant ($\alpha_{II}$) |
| RICC | Roughness-Induced Crack Closure |
| SENP | Single Edge Notch in a Plate |
| SIF | Stress Intensity Factor |
| Sun(O) | The original model proposed by Sun and Sehitoglu |
| Sun(M) | Modified Sun and Sehitoglu model proposed in this study |

# 1. INTRODUCTION

## 1.1 Background

In most engineering applications, fatigue resistance is controlled by the presence of notches which are either intentional notches or intrinsic defects. From the mechanics point of view, notches cause high stress concentrations; and hence, fatigue cracks always initiate at these notches and begin propagating as short cracks. Once a fatigue crack initiates at a notch and when the crack length is longer than a certain critical length, the notch depth elevates the crack tip stress intensity factor and causes more rapid fatigue crack growth rate.

The anomalous growth of short cracks emanating from notches is a perplexing phenomenon. Short cracks grow below the long-crack threshold stress intensity range ($\Delta K_{tho}$) and grow faster than a long crack at the same stress intensity range ($\Delta K$). This anomalous behavior leads to difficulty in applying the conventional LEFM analyses.

The long-life regime fatigue behavior of notched components is the subject of this study. Predicting the growth rate of short cracks emanating from notches is important because, in the long-life regime, the period devoted to the growth of the short cracks is the major part of the total fatigue life. In addition, the threshold condition is controlled by the equilibrium of non-propagating (short) cracks.

## 1.2 Objective and Scope of this Research

A major objective of this study was to develop a model which predicts the long-life regime fatigue properties for notched components. An analytical model for Crack Closure at a Notch(termed the CCN model) was developed to predict the behavior of fatigue cracks at a notch. The effects of R ratio, notch depth, notch acuity, notch and specimen type, crack closure mechanisms, and material properties on the long-life regime fatigue life and fatigue threshold stress were considered.

This study was limited to constant amplitude loading. Environmental effects such as elevated temperature, humidity and corrosion were not considered. The accuracy of the CCN model was confirmed by comparing predictions with experimental results of a cast aluminum alloy and with test results of other materials reported in the literature. Steel and aluminum alloys were considered.

The long-life fatigue behavior of a cast aluminum alloy 319 was studied. The influence of the fatigue initiating casting defects on the long-life regime was treated as a

small notch problem. Uniaxial stress-life (S-N) tests for R = -1 were performed on cylindrical cast specimens having as-cast and polished (30μm) surface conditions. To aid in the modelling of the fatigue behavior of this cast material, supplemental R = -1 crack growth rate tests (da/dN-ΔK) on machined-notched specimens were performed. The statistical characteristics of the fatigue strength for this cast alloy was studied. The reliability-based fatigue strength for this cast alloy was estimated based on the statistical distribution of fatigue-initiating-defect size and the CCN model.

## 1.3 Organization

The main body of the text deals with the concept of the CCN model and its predictions. Chapter 2 presents the background for the CCN model and introduces other models for the behavior of short cracks. Chapter 3 is an overview of the CCN model. Chapter 4 compares the the experimental data with the predictions of the CCN model for various specimen geometries and materials. Chapter 5 provides a discussion of the CCN model, a summary of the effect of notches, and suggestions for further study.

Nine appendices give background information relating to the development of the CCN model and the experimental procedures and results for a cast aluminum alloy 319:

Appendix A - Stress Intensity Factor Solutions lists all the formula for calculating stress intensity factors for the specimen geometries used in this study.

Appendix B - The Notch-Stress-Field Boundary (NSFB) details the development of notch stress field boundary (x*) used for the CCN model.

Appendix C - CCN Model for Predicting the Threshold stress details the development of the model for predicting the threshold stress. This model can be used for notches or intrinsic defects in steel and aluminum alloys having various specimen geometries and load ratios.

Appendix D - Model for Fatigue Life based on Short and Long Crack Propagation details the development of the model for predicting the fatigue crack propagation life.

Appendix E - The Relationship between da/dN and $\Delta K_{eff}$ proposes a concept to derive the relationship of da/dN versus $\Delta K_{eff}$ which is unique for each material.

Appendix F - The Limit of the CCN Model Applicability proposes a concept to quantitatively determine the range where the CCN model is applicable.

Appendix G - Experimental Procedures and Results for a Cast Aluminum Alloy 319 presents the experimental procedures and results for cast aluminum alloy 319. The statistical size distributions of casting pores and fatigue-initiating defects were measured. Fatigue properties of this alloy are described.

Appendix H - S-N Data Test Statistics applies the theory of test statistic to test the equality of two S-N curves under different experimental conditions.

Appendix I - Observation of Crack Nucleation and Early Growth presents the direct observations of the sources of crack nucleation and early growth by replicating the surface cracks with acetate films.

# 2. LITERATURE REVIEW

## 2.1 Life Prediction using the Initiation-Propagation Concept

Lawrence et al. [1,2,3] proposed a model (the Total Life Model) to assess the fatigue life of notches. The fatigue life of notched components was divided into three parts: the fraction of life devoted to the development of active fatigue cracks (nucleation), the fraction of life devoted to the early growth and linking of short cracks (early crack propagation), and the fraction of life devoted to dominant crack enlargement until fracture occurs (propagation). The fatigue life spent in the nucleation and early growth stages was termed initiation life ($N_I$) and the life spent in the final stage was termed propagation life ($N_P$). The total fatigue life ($N_T$) is given by:

$$N_T = N_I + N_P \tag{2.1}$$

The fatigue crack initiation life ($N_I$) can be predicted based on the strain-life relationship [1-6]. In the long-life regime, Lawrence et al. [5] used the Basquin-Morrow equation with the concept of fatigue notch factor ($K_{fn}$) to predict $N_I$:

$$S_{an} = \frac{\sigma'_f}{K_{fn}} \left(1 - \frac{\sigma_m}{\sigma'_f}\right) (2N_I)^b \tag{2.2}$$

where:
- $S_{an}$ = Remote applied stress amplitude (net section)
- $\sigma'_f$ = Fatigue strength coefficient for smooth specimen
- $b$ = Fatigue strength exponent for smooth specimen
- $\sigma_m$ = Local mean stress
- $K_{fn}$ = Fatigue notch factor (net section) at threshold condition

$$= 1 + \frac{K_{tn} - 1}{1 + \frac{\alpha}{\rho}} \qquad \text{(Peterson equation )} \tag{2.3}$$

- $\alpha$ = Peterson's constant
- $\rho$ = Notch root radius
- $K_{tn}$ = Theoretical stress concentration factor (net section)

In Eq. 2.2, the use of $K_{fn}$ factor (instead of $K_{tn}$) for predicting initiation life implicitly considered the effect of short crack behavior. The values of Peterson's constant ($\alpha$) for different materials were experimentally determined and can be estimated by [7]:

$$\alpha_I = 140 \left(\frac{\Delta K_{tho}}{S_e}\right)^2 \qquad \text{(Type I Peterson's constant)} \tag{2.4}$$

where $\alpha_I$ = unit of mm

$\Delta K_{tho}$ = Long-crack threshold stress intensity range, unit in MPa$\sqrt{m}$

$S_e$ = Fatigue limit of smooth specimen, unit in MPa

Another expression for estimating Peterson's constants is [5]:

$$\alpha_{II} = 0.025 \left(\frac{2070}{S_u}\right)^{1.8} \qquad \text{(Type II Peterson's constant)} \tag{2.5}$$

where $\alpha_{II}$ = unit of mm

$S_u$ = Tensile strength, unit in MPa

Knowing the value of $\alpha$, the long-life regime fatigue strength or fatigue initiation life ($N_I$) can be estimated using Eq. 2.2 and Eq. 2.3.

The total life model (I-P concept) also takes the propagation life ($N_P$) into consideration. The propagation life can be estimated by integrating the Paris law [8] (which will be discussed later) from a specified initial crack length ($x_i$) to the final crack length ($x_f$) at which the final fracture occurs:

$$N_P = \int_{x_i}^{x_f} \frac{da}{C\,(\Delta K)^m} \tag{2.6}$$

Where: $x_i$ = Initial crack length

$C$ = Paris' constant

$m$ = Paris' exponent

$x_f$ = Final defect depth at fracture; calculated by:

$$K_{IC} = S_{max}\, Y(D+x_f) \sqrt{\pi(D+x_f)}$$

$K_{IC}$ = Fracture toughness

$\Delta K$ = Stress intensity range = $Y(a)\,(1-R)\,S_{max}\sqrt{\pi a}$

$Y(a)$ = Geometrical factor where 'a' ranged from $D + x_i$ to $D + x_f$

$D$ = Notch depth

$S_{max}$ = Maximum applied stress in a cyclic stress range

A difficulty encountered with the I-P concept is the determination of the value of initial crack length ($x_i$). Several researchers [1,4,6,7] have made progress in this area. It seems that these studies have been successful in estimating the fatigue life of notched components. However, the use of the $K_{fn}$ concept in estimating $N_I$ to overcome the short crack problem for the early crack propagation life is empirical, and the physical meaning of the Peterson equation is unknown. Furthermore, Socie [6] has questioned the applicability of the I-P concept in dealing with very shallow notches (e.g. $D \leq 2.5$ mm). These problems with the I-P concept may be overcome by directly predicting the crack growth rate of short cracks emanating from a notch (or a defect) using the concept of crack closure.

## 2.2 Crack Closure Mechanisms and the Nature of Fatigue Crack Propagation

Crack closure controls the nature of fatigue crack propagation. The known crack closure mechanisms were reviewed by Suresh and Ritchie [9]. The most important crack closure mechanisms are: plasticity-induced, oxide-induced, and roughness-induced crack closure. Plasticity-induced crack closure (PICC) results from the constraint of plastically deformed material at and in the wake of the fatigue crack tip by the surrounding elastically deformed material. The applied stress or stress intensity factor is the main factor which affects plasticity-induced crack closure. Oxide-induced crack closure (OICC) results from oxide deposits within the crack, and roughness-induced crack closure (RICC) results from contact at discrete points between fatigue fracture surface asperities when Mode II crack displacements are present. The latter two crack closure mechanisms are strongly dependent on the material properties (i.e., grain size and yield strength) and environmental conditions, and these mechanisms play a dominant role at near-threshold conditions [9-13]. The extent of OICC and RICC generally becomes greater as fatigue crack growth rates approach the threshold levels.

For a long crack, Allison [10] schematically described the importance of each closure mechanism as a function of the maximum stress intensity factor ($K_{max}$) shown in Fig. 1. When $K_{max}$ is high, PICC plays a dominant role, and when $K_{max}$ is low (at near threshold conditions) RICC and OICC are believed to dominate. At this time, the relative

importance of each closure mechanism and the value of $K_{max}$ at which the dominant crack closure mechanisms change have not been identified.

The variation of fatigue crack propagation rate (da/dN) with $\Delta K$ is usually represented by the sigmoidal curve shown in Fig. 2. Three regimes of fatigue crack propagation behavior and their corresponding mechanisms were discussed by Ritchie and Suresh [13]. Since the present study is concerned with long-life fatigue properties, the crack growth mechanisms in the mid-growth rate and the near-threshold regimes are of primary importance and are discussed below.

2.2.1 Behavior of Long Cracks in the Mid-Growth Rate Regime

When the applied $\Delta K$ is in the mid-growth rate regime, Mode I crack-tip displacement is dominant and a planar fracture surface morphology is observed. In this regime, the fatigue crack growth rate (da/dN) for long-cracks can be represented by the Paris law [8]:

$$\frac{da}{dN} = C\,(\Delta K)^m \tag{2.7}$$

where $C$ = Paris' constant = f(R)
$\Delta K$ = Long-crack stress intensity range
$m$ = Paris' exponent

Different values of Paris' constant C must be used for different load ratios (R).

In the early 1970's, Elber [14] proposed a concept of crack closure which provided better correlations for long-crack growth rate by using the effective stress intensity range ($\Delta K_{eff}$):

$$\frac{da}{dN} = C\,(\Delta K_{eff})^m \tag{2.8}$$

where: $\Delta K_{eff} = U_o\,\Delta K$

$U_o = \dfrac{S_{max} - S_{opo}}{S_{max} - S_{min}} = \dfrac{K_{max} - K_{opo}}{K_{max} - K_{min}}$ ; suffix 'o' means stabilized value for long-crack

$S_{max}$ = Maximum stress in a cyclic loading condition
$S_{min}$ = Minimum stress in a cyclic loading condition
$S_{opo}$ = Stabilized opening stress for long crack in a cyclic loading condition
$K_{max}$ = Maximum stress intensity factor in a cyclic loading condition

$K_{min}$ = Minimum stress intensity factor in a cyclic loading condition

$K_{opo}$ = Stabilized opening stress intensity factor for long crack in a cyclic loading condition

In Eq. 2.8, the Elber's constant C is independent of the load ratio (R). The value of $U_o$ is termed long-crack effective stress intensity ratio, and is dependent upon the R value. For $-0.1 < R < 0.7$, Elber first proposed an empirical relationship between $U_o$ and R for 2024-T3 aluminum alloy:

$$U_o = 0.5 + 0.4\,R \tag{2.9}$$

It is evident that the relation between $U_o$ and R is material dependent. Other relations between $U_o$ and R for other materials were reviewed by Schijve [8]. Some researchers reported that $U_o$ could also depend on maximum applied stress intensity factor ($K_{max}$) and R [9]. Elber's concept is an oversimplification which may only be valid over a limited range of $K_{max}$. Because the measurement of crack closure level has not been standardized, different measuring methods result in different values of $U_o$. Thus, whether $U_o$ is only an R-dependent variable or a both R and $K_{max}$ dependent variable is still unclear at this date. Nevertheless, the influence of R and $K_{max}$ on the crack growth rate in this regime was explained by using the plasticity-induced crack closure mechanism [14-17]. The ratio of opening stress ($S_{opo}$) to maximum applied stress ($S_{max}$) (i.e. $S_{opo}/S_{max}$), and the value of $U_o$ increase with increasing maximum applied stress and R ratio.

### 2.2.2 Behavior of Long Cracks in the Near-Threshold Regime

In the near-threshold regime, the Stage I mechanism controls fatigue crack propagation which is a combination of Mode I and Mode II displacements. Fatigue crack growth in this regime results in a serrated or faceted fracture surface morphology coupled with crack tip Mode II displacements. Consequently, fatigue crack growth in this regime would be expected to have a higher closure stress than that in the mid-growth rate regime due to the operation of RICC and OICC mechanisms. The $S_{opo}/S_{max}$ in this regime would be expected to be larger than those in the mid-growth rate regime, thus, $U_o$ would be less than that in the mid-growth rate regime. To distinguish the values of $U_o$ for near-threshold regime and mid-growth rate regime, the long-crack effective stress intensity ratio in the near-threshold regime is denoted as $U_{tho}$ and that in the mid-growth rate regime is denoted as $U_o$. Generally, $U_{tho}$ must be smaller than or equal to $U_o$.

The fatigue crack growth rate (da/dN) and the value of long-crack threshold stress intensity range ($\Delta K_{tho}$) are dependent on the grain size (d), load-ratio (R), yield strength ($S_y$) and environmental conditions. Generally, for the same material system at the same $\Delta K$ level, higher load ratio, smaller grain size or higher yield strength would exhibit higher crack growth rates and lower values of $\Delta K_{tho}$. Additionally, increasing load ratio generally decreases the influences of grain size and yield strength on the $\Delta K_{tho}$ [12,13,18-24]. These characteristics are inherent in the RICC and OICC mechanisms.

The effects of grain size (d) on the long-crack growth behavior in the near-threshold regime can be explained mainly by the RICC mechanism. Coarse-grained materials have a more serrated (rougher) fracture surface which enhances the RICC mechanism, this leads to a higher $\Delta K_{tho}$. The influence of R ratio and yield strength on $\Delta K_{tho}$ is generally interpreted by the combination of PICC, RICC and OICC mechanisms. Oxide deposits were observed on the fracture surface which affect the closure stress for a fatigue crack; the thicker the oxide layer, the higher the closure stress. The development of fretting-oxidation layers are associated with the amount of RICC and PICC mechanisms. Under high R ratio conditions, the crack remains open during a larger portion of the cycle (thus very little crack closure), which results in a smaller amount of fretting-oxidation between the fracture surfaces. The thinner oxide layer, in turn, would reduce the amount of OICC and consequently decrease $\Delta K_{tho}$. Materials with higher yield strength would have lower values of $\Delta K_{tho}$ due to the smaller amount of oxide fretting (OICC). Some researchers [18] believe that the effect of the R-ratio on the $\Delta K_{tho}$ is mainly due to the effect of OICC; because the lack of the R-dependence on the $\Delta K_{tho}$ was found in vacuum. A strong R-dependence was observed in air. However, the lack of R-ratio dependence on $\Delta K_{tho}$ was also found in a very fine grain-size P/M IN9021-T4 (grain size 0.1-1.0 μm) [19]. For this very fine grain material, there is almost no RICC effect. Assuming RICC is the dominant closure mechanism for this material in the near-threshold regime, the lack of RICC results in the lack of R-dependence on $\Delta K_{tho}$.

Without considering the aggressive (or corrosive) influence of environment on the fatigue crack growth behavior, many researchers believe that the growth rate of a fatigue crack [4,10,12] for a given material system can be correlated uniquely with the effective stress intensity range ($\Delta K_{eff}$). In addition, the effective long-crack threshold stress intensity range ($\Delta K_{eff.tho}$) is also an unique material property. Liaw [12] found a linear relationship between $\Delta K_{eff.tho}$ and the value of Young's modulus (E):

$$\Delta K_{eff.tho} = \eta E \qquad (2.10)$$

where $\eta = 1.5 \times 10^{-5}$ for steel

$\eta = 2.0 \times 10^{-5}$ for aluminum alloys

$E$ = Young's modulus (MPa)

$\Delta K_{eff.tho}$ = Effective long-crack threshold stress intensity range (MPa$\sqrt{m}$)

In contrast to $\Delta K_{tho}$, the value of $\Delta K_{eff.tho}$ is insensitive to grain size (d), yield strength ($S_y$) and load ratio (R). Figure 3 schematically shows the relation between da/dN and $\Delta K_{eff}$ and the variations of the relationship between da/dN and $\Delta K$ with grain size, applied stress, load ratio and short crack behavior. As shown in Fig. 3, short cracks exhibit higher crack growth rates than long cracks and grow at lower $\Delta K$ values than the long-crack $\Delta K_{tho}$ value. This anomalous crack growth behavior of short cracks, under some circumstances, can be explained by crack closure and rationalized by the $\Delta K_{eff}$ concept as discussed below.

## 2.3 Behavior of Short Cracks

The distinction between "small" and "short" cracks and the classification of short cracks was clearly defined by Ritchie and Lankford [25]. Short cracks are generally two dimensional through-thickness flaws, and small cracks are generally three dimensional surface cracks. Both small and short cracks can be classified into *microstructurally*, *mechanically* and *physically* small or short cracks. The anomalous crack growth rate of mechanically short cracks can be rationalized by delayed crack closure development; whereas, the crack growth rate of a microstructurally short crack is partly controlled by the microstructural features (e.g. grain boundary) and partly controlled by crack closure. Short cracks emanating from a notch can be categorized as mechanically short cracks unless the notch size is so small that the notch size is comparable to the microstructural features. For a crack emanating from a notch, the initial faster growth rate of the mechanically short crack is attributed to the higher $\Delta K_{eff}$ values relative to the long crack at the same $\Delta K$. This distinction of the rates can be rationalized by the relationship between da/dN and $\Delta K_{eff}$ [9,11,12,15,19,26-31].

Mechanically short cracks are less affected by closure than long cracks because of their shorter crack wakes and thus a smaller incidence of crack closure. As shown in Fig. 4, the opening stress starts from $S_{min}$ at zero crack length ($x = 0$) and gradually increases with increasing crack length and finally approaches the stabilized opening stress, $S_{opo}$. In other words, the value of effective stress intensity ratio starts from 1 at $x = 0$ and gradually

decreases with increasing crack length and finally approaches the stabilized value $U_o$ (or $U_{tho}$) as the crack becomes a long crack.

As discussed above, the stabilized $U_o$ (or $U_{tho}$) may be influenced by grain size, yield strength, R-ratio and $K_{max}$ (or $S_{max}$). In studying a specified material with specified yield strength and grain size, R-ratio and $K_{max}$ (or $S_{max}$) are the most important parameters affecting the value of $U_o$ (or $U_{tho}$). In the short crack regime where crack closure level has not reached a stable value, crack length (x) is also a parameter affecting the effective stress intensity ratio. Thus, to explain the peculiar behavior of cracks emanating from notches, the effective stress intensity ratio should consider the effect of R, x and $K_{max}$. For simplicity, the variation of effective stress intensity ratio for a short crack emanating from a notch is denoted as U(x), which implicitly includes the effects of R, $K_{max}$ (or $S_{max}$).

Several parameters may affect the function of U(x) for a crack emanating from a notch. These parameters are:

- the applied stress and its corresponding crack closure mechanisms,
- the notch acuity and notch depth, and
- the material properties.

Mechanics researchers [26-29,32-34] used finite element methods (FEM) to analitically model U(x) and assumed that crack closure resulted only from plasticity-induced crack closure (PICC). However, in estimating the near-threshold fatigue properties, analyses based on the finite element method and the PICC dominant mechanism should be questioned. When fatigue cracks propagate in the near-threshold regime, other closure mechanisms such as roughness and oxide closure mechanisms (RICC and OICC) may become more important than PICC. Thus, models based solely on the PICC mechanism are valid only when:

- the applied stress is high, or,
- the applied stress is low but the crack length is within the the notch stress field where notch plasticity dominates the crack closure behavior.

The intent of this study is to develop a comprehensive model for crack closure at a notch, that is, to determine quantitatively the function of U(x) for cracks emanating from a notch. Thus the work of Tanaka et al. which models all the possible crack closure mechanisms at the threshold condition and the work of Sun et al. which models the PICC mechanism will be discussed below.

2.3.1 Short Cracks in Smooth Specimens at Near-Threshold Conditions (Tanaka)

Without reference to any particular mechanism of crack closure, Tanaka et al. [35] found empirically that the change of threshold stress intensity range ($\Delta K_{th}(x)$) with crack length for cracks in a smooth specimen was:

$$\Delta K_{th}(x) = \Delta K_{tho} \sqrt{\frac{x}{x+L_o}} \tag{2.11}$$

where:

$\Delta K_{th}(x)$ = Short crack threshold stress intensity range
$\Delta K_{tho}$ = Long crack threshold stress intensity factor (material property)
$x$ = Crack length (mm)
$L_o$ = Intrinsic crack length (mm)

Equation 2.11 indicates that the threshold stress intensity range for a material is not a constant value but a crack length and a material property (i.e. $L_o$) dependent variable. The threshold stress intensity range ($\Delta K_{th}(x)$) increases with increasing crack length, and the rate of increase is dependent on the intrinsic crack length ($L_o$), see Fig. 5. When the crack becomes very long (e.g. $x >> L_o$), $\Delta K_{th}(x)$ approaches $\Delta K_{tho}$. The intrinsic crack length ($L_o$) is given by:

$$L_o = \frac{1}{\pi}\left(\frac{\Delta K_{tho}}{\Delta S_e}\right)^2 \tag{2.12}$$

where:

$\Delta S_e$ = Stress range at the fatigue limit of a smooth specimen

The fact that a shorter crack has a smaller $\Delta K_{th}(x)$ value may be attributed to the smaller crack closure effect which causes $\Delta K_{th}(x)$ to be closer to $\Delta K_{eff.tho}$, assuming that there exists a long-crack material property $\Delta K_{eff.tho}$ which is independent of crack length. Tanaka derived an expression which correlates the effective threshold stress intensity ratio for a crack in a smooth specimen (denoted as $U^T(x)$) with the crack length ($x$), material properties ($L_o$) and the stabilized long-crack effective threshold stress intensity ratio ($U_{tho}$):

$$U^T(x) = U_{tho} \sqrt{\frac{x+L_o}{x}} \tag{2.13}$$

where: $U^T(x)$ = Tanaka's model for the effective threshold stress intensity ratio for a crack in a smooth specimen

$U_{tho}$ = Effective long-crack threshold stress intensity ratio = $\frac{\Delta K_{eff.tho}}{\Delta K_{tho}}$

$\Delta K_{eff.tho}$ = Effective long-crack threshold stress intensity ratio, a material property

Note that when x decreases to a very small value, $U^T(x)$ in Eq. 2.13 becomes greater than 1. Under this condition ($U^T(x) > 1$), the crack is a microstructurally short crack; and thus, models based on crack closure behavior in this region are probably meaningless.

El Haddad et al. [36] suggested that models for short crack behavior may converge with models for long crack behavior if the stress intensity range is modified by adding $L_o$ to the crack length. This idea also leads to an expression similar to the Tanaka model (Eq. 2.13). The expression of $U^T(x)$ combined all the possible crack closure mechanisms at near-threshold conditions for a crack in a smooth specimen in which the RICC and OICC mechanisms are believed to play more important roles than the PICC mechanism.

2.3.2 Short Cracks in Notched Specimens

Finite element analyses [32-34] can predict the variation of crack closure with crack length by assuming that the closure of a crack emanating from a notch is fully controlled by the PICC mechanism. Sun and Sehitoglu [34] developed empirical equations from the results of finite element calculations. The variation of crack closure with crack length for a crack emanating from a notch was expressed in terms of opening stress ($S_{op}(x)$). The function of $S_{op}(x)$ under plane stress condition was expressed as :

$$\frac{S_{op}(x)}{S_{max}} = \left[\frac{S_{opo}}{S_{max}} - \left(A_1 \frac{S_{max}}{S_y} + A_2\right) \exp\left(\frac{-\frac{x}{D}}{\left(\frac{S_{max}}{S_y}\right)^{A_3}}\right)\right] \left(1 - \exp\left(-10^6 \frac{x}{D}\right)\right)$$

$$+ R \exp\left(-10^6 \frac{x}{D}\right) \qquad (2.14)$$

Where:

$S_{opo}$ = Stabilized opening stress for long crack

$S_y$ = Yield Strength

D = Half length for centered notch and full length for edged notch

x = Crack length from notch root

$S_{max}$ = Maximum stress value of applied stress range

For a ratio of plastic modulus to elastic modulus H/E = 0.07 :

$$\frac{S_{opo}}{S_{max}} = 0.49 + 0.01R - (0.10 - 0.30R) \frac{S_{max}}{S_y} \qquad (2.15a)$$

$$A_1 = -0.255 - 1.375R + (0.085 - 0.075\,R)K_t$$

$$A_2 = 0.298 + 0.563R - (0.043 + 0.198\ R)K_t$$
$$A_3 = 1.700 + 1.475R + (0.100 - 0.225\ R)K_t$$

For a ratio of plastic modulus to elastic modulus H/E = 0.01:

$$\frac{S_{opo}}{S_{max}} = 0.95 + 0.13R - (0.70 - 0.30R)\frac{S_{max}}{S_y} \qquad (2.15b)$$
$$A_1 = -1.138 - 1.138R + (0.163+0.163R)\ K_t$$
$$A_2 = 0.902 + 0.507R - (0.089+0.164R)\ K_t$$
$$A_3 = 3.400 + 2.575R - 0.125RK_t$$

Equations 2.14 and 2.15 are valid within the range when $S_{max} = (0.4 \sim 0.8)\ S_y$ and $K_t$ is between 3 and 7. The variation of the effective stress intensity ratio of a notched component with crack length predicted by Sun and Sehitoglu can be expressed as:

$$U^S(x) = \frac{1 - \frac{S_{op}(x)}{S_{max}}}{1 - R} \qquad (2.16)$$

where:

$U^S(x)$ = The Sun and Sehitoglu model for the variation of effective stress intensity ratio with crack length for a crack emanating from a notch

The variation of stress intensity ratio with crack length for the Sun and Sehitoglu model is different from that of Tanaka's; the former deals mainly with the notch problem at higher than the near-threshold conditions, while the latter deals mainly with the near-threshold and smooth conditions. Neither model covers the complete range for analyzing the threshold stress and life estimation for a notched component. For example, $U^S(x)$ is not a suitable function for determining the threshold condition; and Tanaka's model is not valid for use in the notched components, since the effect of a notch stress field on crack closure was not considered. A hybrid model which combines these two models will be proposed in Chapter 3.

## 2.4 Threshold Stress Range for Notched Components

The fatigue threshold stress range ($\Delta S_{th}$ or $\Delta S_{thn}$ - the suffix 'n' denotes a net-section basis) of a notched component is the greatest stress range which can be applied to the component without causing fatigue failure, that is, the largest applied stress range for infinite life (under constant amplitude loading and in the absence of corrosion). For a smooth specimen, the value of $\Delta S_{th}$ equals the fatigue limit ($\Delta S_e$). It is known that the material properties, the notch acuity, the notch depth, and the load ratio are important parameters in determining the value of $\Delta S_{th}$. The threshold stress ($S_{th}$) is the maximum stress under the threshold condition which is given by:

$$S_{th} = \frac{\Delta S_{th}}{1-R} \tag{2.17}$$

where: R = Load ratio (i.e., the minimum applied stress divided by maximum applied stress)

Experimental work of Frost [37] and Tanaka [38] on the relationship between the notch acuity and the applied stress range is schematically represented in Fig. 6 in which the net-section threshold stress range ($\Delta S_{thn}$) is plotted as a function of the net-section elastic stress concentration factor ($K_{tn}$). Notches can be categorized as blunt or sharp, and the boundary between blunt and sharp notches occurs when $K_{tn} = K_{tc}$, that is, at the least value of $K_{tn}$ at which non-propagating fatigue cracks (NPC) are observed. In the case of blunt notches ($K_{tn} \leq K_{tc}$), $\Delta S_{thn}$ is approximately equal to the fatigue limit of smooth specimen divided by the theoretical stress concentration factor ($\Delta S_e/K_{tn}$). For sharp notches ($K_{tn} \geq K_{tc}$), the values of $\Delta S_{thn}$ (according to the Frost relation) remain constant. Furthermore, the ranges of net-section threshold stress ($\Delta S_{thn}$) for sharp notches are always larger than $\Delta S_e/K_{tn}$. Thus, when the applied stress range equals $\Delta S_{thn}$ in a sharp notch, the crack grows a short distance from the notch root, arrests, and becomes a non-propagating crack.

Experiments of Lukas [39], Topper [40], and DuQuesnay [41] showed that the notch depth (D) or the notch root radius ($\rho$) is also a very important parameter in determining $\Delta S_{thn}$. The relation between $\Delta S_{thn}$ and D (or $\rho$) is schematically shown in Fig. 7. Experiments were carried out with geometrically similar circular notches ($D = \rho$). When D is very small, the values of $\Delta S_{thn}$ equal $\Delta S_e$; this fact can not be appreciated using the Frost relation (Fig. 6). Figure 7 (denoted as Lukas relation) also indicates that for small

notches, $\Delta S_{thn}$ varys with notch depth in a manner apparently inconsistent with the behavior shown in Fig. 6. The discrepancy between the Frost relation (Fig. 6) and the Lukas relation (Fig. 7) suggests that $K_{tn}$ is not a complete description of the severity of a notch and that the description of notch severity requires two variables. However, there must be some interrelationship between Fig. 6 and Fig. 7 and this interrelationship will be investigated subsequently. Several models predicting the threshold stress are reviewed below:

2.4.1 Simple LEFM Approach

The first approximate relationship for $\Delta S_{th}$ was derived from a simple Linear Elastic Fracture Mechanics (LEFM) concept in which the notch size was considered to be the crack size and the threshold condition was obtained when the applied stress intensity range equals the long-crack threshold stress intensity range of the material [4,42,43]:

$$\Delta S_{th} = \frac{\Delta K_{tho}}{Y\sqrt{\pi D}} \tag{2.18}$$

Equation 2.18 is applicable for sharp notches and is valid only for certain range of notch depths. In many cases, the threshold stress of a notched component was controlled by the presence of non-propagating crack (NPC) which was basically a phenomenon resulting from the short crack behavior. Thus, equation 2.18 (based on long crack behavior) is not valid for general cases. The works of Peterson, Lukas et al. and Topper et al. suggested alternative ways to predict $\Delta S_{th}$ which roughly considered the effects of crack closure for short cracks emanating from a notch.

2.4.2 Peterson Model

The fatigue notch factor ($K_{fn}$) used in the Peterson model implicitly included the effect of the short crack behavior. As seen in Eq. 2.3, when the notch root radius is small (sharp notch), $K_{fn}$ is smaller than $K_{tn}$; and when the notch root radius is large (blunt notch), $K_{fn}$ approaches to $K_{tn}$. The relationship between $K_{fn}$ and $K_{tn}$ for a given notch is determined by Peterson's constant ($\alpha$) which implicitly represents the effect of material properties on the short crack behavior. Knowing the value of $\alpha$ for a given material from Eqs. 2.4 and 2.5, the value of $K_{fn}$ for a given notch geometry ($K_{tn}$) can be predicted using Eq. 2.3. The fatigue threshold stress range ($\Delta S_{thn}$) or the fatigue life in the long-life regime (Eqs. 2.1 and 2.6) may be estimated. The threshold stress is given by:

$$\Delta S_{thn} = \frac{\Delta S_e}{K_{fn}} \tag{2.19}$$

Lawrence et al. [5,7] developed a worst-case-notch concept based on the Peterson equation (Eq. 2.3). For notches with constant notch depth but various root radii, there is a worst-case-notch condition. The maximum $K_{fn}$ (termed $K_{fmax}$) value occurred when the notch root radius equals Peterson's constant ($\rho = \alpha$) which is given by:

$$K_{fmax} = 1 + \sqrt{\frac{D}{\alpha}} \tag{2.20}$$

The concept of $K_{fmax}$ is useful in determining the threshold stresses for components with variable or undefined notch root radii such as weldments or "natural" notches (defects) in a material. However, the validity of the Peterson equation and the intrinsic material properties which affect the value of $\alpha$ (i.e., Eq. 2.4 and Eq. 2.5) need to be investigated. This consideration will be described in Chapter 4.

2.4.3 Lukas Model

Systematic studies of the effects of notch size and notch acuity on the fatigue threshold stress were reported by Lukas et al. [39,44,45]. They proposed an expression to calculate the stress intensity range for a short crack emanating from a notch ($\Delta K_S$):

$$\Delta K_S = \frac{1.122 K_t \Delta S \sqrt{\pi x}}{\sqrt{1 + 4.5(x/\rho)}} \tag{2.21}$$

where:

$K_t$ = Stress concentration factor (gross section)
$\Delta S$ = Applied stress range (gross section)
$\rho$ = Notch root radius
$x$ = Crack length

The suffix 'S' in the term of $\Delta K_S$ denotes that the crack is in the short crack regime. The condition for a notch to be non-damaging with respect to fatigue threshold is:

$$\Delta K_S \leq f \Delta K_{tho} \tag{2.22}$$

where $f$ = A constant between 0 and 1
$\Delta K_{tho}$ = Long-crack threshold stress intensity range

The physical meaning of $f$ implies that there exists a short crack threshold stress intensity range which is less than the long-crack threshold stress intensity range. Lukas et al. assumed that the depth of microcracks on the surface of smooth specimens and the depth of microcracks at the notch root are the same at the fatigue threshold condition. This threshold crack length was denoted as $l_o$. Thus, the border between propagation and non-propagation is given by:

$$f\Delta K_{tho} = 1.122\Delta S_e\sqrt{\pi l_o} \qquad \text{for a smooth specimen} \qquad (2.23)$$

$$f\Delta K_{tho} = \frac{1.122K_{tn}\Delta S_{thn}\sqrt{\pi l_o}}{\sqrt{1 + 4.5(l_o/\rho)}} \qquad \text{for a notched specimen} \qquad (2.24)$$

Equating Eq. 2.23 with Eq. 2.24, the threshold stress for notched specimens can be given by:

$$\Delta S_{thn} = \Delta S_e \qquad (\text{for } \rho \le \rho_o)$$
$$\Delta S_{thn} = \Delta S_e \frac{\sqrt{1+4.5(l_o/\rho)}}{K_{tn}} \qquad (\text{for } \rho > \rho_o) \qquad (2.25)$$

where: $l_o$ = Maximum non-propagating crack length
$\rho$ = Notch root radius
$\rho_o = \frac{4.5}{K_{tn}^2 - 1} l_o$ ; critical notch root radius

Since the value of $f$ is an unknown value, $l_o$ can not be derived directly. The value of $l_o$ was then determined from the best fit of Eq. 2.25 to experimental data. It is questionable whether $l_o$ would remain the same if the tests were carried out using different notch and specimen geometries. Furthermore, long-term tests are required to obtain a best fit result of $l_o$ to the experimental threshold stress data. The value of $f$ was determined after the value of $l_o$ was obtained. The value of $f$ was determined to be approximately 0.73 for a 2.25Cr-1Mo steel and 0.55 for a copper. Basically, the Lukas model considered the effects of a short crack on the value of $\Delta K_{tho}$, and this effect is reflected in the values of $f$ and $l_o$. Lukas et al. assumed that the short crack effect is the same for both notched and smooth conditions, and they also assumed that the variations of crack closure level with

crack length are same for all notches (i.e., the notch acuity effect on crack closure was not considered).

2.4.4 Topper Model

El Haddad and Topper [40,41] suggested a stress intensity formulation for a crack emanating from a notch :

$$\Delta K = K'\Delta S \sqrt{\pi(x + L_o)} \tag{2.26}$$

where: $K'$ = A stress concentration function (decreases as crack length increases)

$= \sqrt{\frac{(x+D+L_o)}{(x+L_o)}}$ as crack passes outside the notch stress field

$L_o$ = Intrinsic crack length as define in Eq. 2.12

$D$ = Notch depth

The physical meaning of adding $L_o$ to the crack length is the same as the Tanaka model. Assuming the effective stress intensity range for a short crack emanating from a notch is:

$$\begin{aligned}\Delta K_{eff} &= U^T(x)\,\Delta K \\ &= \left(U_{tho}\sqrt{\frac{x+L_o}{x}}\right)\left(K'\Delta S\sqrt{\pi x}\right) \\ &= U_{tho}K'\Delta S\sqrt{\pi(x+L_o)}\end{aligned} \tag{2.27}$$

and,

$$\Delta K = \frac{\Delta K_{eff}}{U_{tho}} \tag{2.28}$$

Equation 2.26 can be derived by combining Eq. 2.27 with Eq. 2.28. Topper et al. further proposed that the threshold stress range can be derived from the condition that the stress intensity range of a growing crack equals the long-crack threshold stress intensity range of the material. The maximum non-propagating crack length ($x_{th}$) and the threshold stress range are given by:

$$x_{th} = \sqrt{DL_o} \tag{2.29}$$

$$\Delta S_{thn} = \frac{Y\,\Delta S_e}{1+\sqrt{\frac{D}{L_o}}} \tag{2.30}$$

where $Y$ = Geometrical factor for stress intensity factor ($\approx 1.12$)

$D$ = Notch depth

$\Delta S_e$ = Range of fatigue limit for smooth specimen

The effect of crack closure for short cracks emanating from notches in the Topper model was the same as in Tanaka's which represented the crack closure behavior in smooth specimens. In other words, the effect of notch acuity on the crack closure behavior was not considered.

It has been observed that the crack growth rate for a crack emanating from a sharp notch is lower than that from blunt notches when both cases are compared at the same $\Delta K$ at certain range of crack length [21,29,46]. This notch acuity effect on crack closure was not considered in the Topper model.

## 2.5 Short Summary

The Initiation-Propagation (I-P) concept for fatigue life prediction of notches uses the fatigue notch factor ($K_{fn}$) combined with the Basquin-Morrow equation to predict the initiation life (the sum of nucleation life and early crack propagation life). The use of $K_{fn}$ (based on Peterson's equation) implicitly considers the short-crack behavior in the early crack propagation regime.

A better alternative for predicting short-crack behavior which results in a single model to deal with both short and long crack growth is the concept of crack closure and $\Delta K_{eff}$. Three crack-closure mechanisms and the parameters affecting these crack closure mechanisms were discussed. The anomalous growth rate of short cracks was explained by the crack closure concept and rationalized by the $\Delta K_{eff}$ concept. Based on these ideas, a crack-closure-at-a-notch (CCN) model was developed and will be discussed in the next Chapter.

Finally, four models for predicting threshold stress proposed by other researchers were reviewed and, in chapter 4, will be compared with the CCN model.

# 3. Overview of the Crack-Closure-at-a-Notch (CCN) Model

## 3.1 Fundamental Concepts of the CCN Model

The fundamental concepts of the CCN model are that the relationship between da/dN and $\Delta K_{eff}$ is a unique material property and that $\Delta K_{eff.tho}$ is a material constant independent of crack length as shown in Fig. 8 and discussed in Appendix E. The anomalous crack growth rate of a (mechanically) short crack emanating from a notch is mainly attributed to the higher $\Delta K_{eff}(x)$ value in the short crack region. The $\Delta K_{eff}(x)$ for a crack emanating from a notch can be obtained from the product of the stress intensity range ($\Delta K(x)$) and the effective stress intensity ratio ($U(x)$):

$$\Delta K_{eff}(x) = U(x)\,\Delta K(x) \tag{3.1}$$

The major objective in the development of the CCN model is to model the function of $U(x)$ which depends upon the applied stress ratio, the notch parameters (i.e., $K_t$, D, and Y) and the material properties (i.e., $S_e$, $S_y$, $U_{tho}$, $L_o$, and $\Delta K_{tho}$). In developing the model for $U(x)$, different stress intensity factors and crack closure mechanisms must be invoked for cracks within or beyond the notch-root stress field. Therefore, the concept of notch-stress-field boundary (NSFB, also denoted as x*) was introduced (see Appendix B) which permitted the development of a hybrid model for $U(x)$. The function of $U(x)$ developed for the CCN model combines the work of Tanaka for short cracks and the work of Sun and Sehitoglu for short cracks at notches. The basic concept of this hybrid model for $U(x)$ is represented by Fig. 9 and the details are described in Appendices C and D. The limit of the applicability of the CCN model is discussed in Appendix F.

## 3.2 Estimating the Stress for Infinite Life using the CCN Model

The threshold stress ($\Delta S_{th}$) can be determined from the condition that the minimum value of $\Delta K_{eff}(x)$ just equals the experimentally determined effective threshold stress intensity range for a long-crack ($\Delta K_{eff.tho}$) as shown in Fig. 10. There is a minimum value of $\Delta K_{eff}(x)$ for a crack growing from a notch. The curve of $\Delta K_{eff}(x)$ having a minimum value equal to $\Delta K_{eff.tho}$ is $\Delta K_{eff.th}(x)$, and the applied stress range is the threshold stress range of the notched component. Figure 10 shows three different cases of effective stress intensity range ($\Delta K_{eff}(x)$) resulting from three different applied stress ranges for a crack

emanating from a notch. In the case that the applied stress range equals $\Delta S_{th}$, the effective stress intensity range for the crack emanating from this notch has a minimum value of $\Delta K_{eff.tho}$, and the greatest possible length of the non-propagating crack is located at x = $x_{th}$.

Appendix C details the model for predicting the threshold stress range ($\Delta S_{th}$). The value of $\Delta S_{th}$ for the relatively small notches can be given by:

$$\Delta S_{th} = \frac{\Delta S_e}{Y(D+x_{th})} \left(\frac{\sqrt{L_o}}{\sqrt{L_o}+\sqrt{D_{eff}}}\right) \tag{3.2}$$

where: $\Delta S_e$ = Range of fatigue limit of smooth specimen

$Y(D+x_{th})$ = Geometrical factor; see details in Appendix A

$x_{th}$ = The maximum non-propagating crack length

$L_o$ = The intrinsic crack length; see Eq. 2.12

$D_{eff}$ = Effective notch depth = D - $\Delta x$

D = Notch depth

$\Delta x$ = A modifier for the Tanaka model for crack closure due to the presence of notch stress concentration

and the value of $\Delta S_{th}$ for the relatively large notches can be given by:

$$\Delta S_{th} = \frac{\Delta S_e \, U_{tho}}{U_{th}^{*} \, Y(x^*)} \sqrt{\frac{L_o}{(D + x^*)}} \tag{3.3}$$

where: $x^*$ = Notch stress field boundary (NSFB)

$U_{th}^{*}$ = The value of $U_{th}(x^*)$ calculated based on the Sun and Sehitoglu model

The derivation of the effective notch depth ($D_{eff}$) and $U_{th}^{*}$ is described in Appendix C.2. An iterative calculation must be carried out to obtain the exact value of $\Delta S_{th}$ and $\Delta S_{thn}$ (calculated from the $\Delta S_{th}$ and area of gross and net-section). When the calculated value of $\Delta S_{thn}$ is smaller than $\Delta S_e/K_{tn}$, no fatigue crack should form at the notch root, and Eqs. 3.2 and 3.3 are not applicable; therefore, under this condition, the largest applied stress range ($\Delta S_{thn}$) for infinite life would be $\Delta S_e/K_{tn}$. In this case, the threshold stress is controlled by the crack nucleation process.

The effect of R ratio on the threshold stress range is mainly determined by $\Delta S_e$ and $L_o$, which are both R-dependent variables. The effect of notch geometry ($K_t$ and D) on $\Delta S_{th}$ is mainly reflected in the values of $D_{eff}$ or $U^*_{th}$.

## 3.3 Fatigue Life Prediction using the CCN Model

Figure 11 schematically shows the concept for estimating the total propagation life ($N_f$) of short and long cracks in a notched component using the CCN model. Once the function $\Delta K_{eff}(x)$ is derived, the variation of crack propagation rate (da/dN) with crack length (x) can be obtained using the experimentally determined relationship between da/dN and $\Delta K_{eff}$ (see Appendix E). The detailed procedures for modeling U(x) are discussed in Appendix D.1.

The CCN model details the behavior of short cracks or early crack growth by modeling U(x) for short cracks emanating from a notch. This total propagation life is estimated by integrating the relation of da/dN vs. $\Delta K_{eff}(x)$ in which the crack length starts from a defined initial crack length ($l_t$ concept of Dowling [4]) to the crack length at final fracture. The total propagation life ($N_f$) for a notch is given by:

$$N_f = \int_{x_i}^{x_f} \frac{dx}{C'_i \, (U(x) \, \Delta K)^{m_i}} \tag{3.4}$$

where:
- $x$ = crack length from notch
- $C'_i$, $m_i$ = Constants; see Appendix E
- $U(x)$ = The variation of stress intensity ratio with crack length; see Appendix D
- $x_i$ = Initial crack length for integration = $l_t$
- $l_t$ = Transition crack length from Dowling [4]
- $x_f$ = Final crack length at failure

The formulations for stress intensity factor (SIF) for a crack near the notch root and far from the notch are different. The transition point for the formulation of SIF was set at the notch stress field boundary (x*). Appendix D.2 details the development of the model for predicting the total fatigue propagation life ($N_f$).

The crack nucleation life for a crack nucleated from a notch can be estimated by using the local strain approach based on the strain-life relationship. Because the CCN model considers the details of the "early" crack propagation life, the value of $K_{tn}$ can be directly used to predict the crack nucleation life based on the Basquin-Morrow equation in the long-life regime. The total fatigue life ($N_T$) is considered to be the summation of crack nucleation life ($N_n$) and the total propagation life ($N_f$):

$$N_T = N_n + N_f \tag{3.5}$$

where $N_n$ = Crack nucleation life; in long-life regime, $N_n$ can be derived from the Basquin-Morrow equation (Eq.2.2) and $K_{tn}$:

$$N_n = \frac{1}{2}\left(\frac{S_{an}\, K_{tn}}{\sigma'_f \left[1 - \frac{\sigma_m}{\sigma'_f}\right]}\right)^{1/b} \tag{3.6}$$

For a large, blunt notch, $N_n$ may dominate the total fatigue life; but for a small or sharp notch, $N_f$ may dominate the total fatigue life.

# 4. CONFIRMATION OF THE CCN MODEL

## 4.1 Cast Materials with Intrinsic Defects

### 4.1.1 Previous Studies of Cast Aluminum Alloy 319

A cast aluminum alloy 319 was studied. This material is intended for use in automobile engine blocks which are required to resist fatigue failure for over $10^8$ cycles. Thus, the long-life regime fatigue properties of this material are of great interest. The fatigue resistance of a cast component is largely determined by its casting porosity [45-47,64-68]. Casting pores cause high stress concentrations and hence reduce the fatigue crack nucleation life. Moreover, once a fatigue crack nucleates at a casting pore, the large size of the casting pore elevates the stress intensity factor and leads to more rapid fatigue crack growth.

Uniaxial fatigue data for this cast alloy was first developed by Tyler [50] and later by Siljander et al. [47] at a load ratio R of 0.1. The study of Siljander et al. showed that the influence of casting pores on the fatigue properties could be estimated using a model for fatigue crack growth based on the Paris law (i.e., using Eq. 2.6).

The General Motors Corporation carried out a field test of the engine blocks, which showed that the stress history of an engine block had almost no net mean stress; and thus the engine block service load history was similar to the R equals -1 condition.

While Siljander's crack growth model gave good agreement with test data for the R equals 0.1 condition, there was concern that it would not predict experimental data for the R equals -1 condition due to crack closure behavior under compressive loads. Long life ($N_T$ for run-out specimen is defined by $1.25 \times 10^8$ cycles) stress-life (S-N), R equals -1 tests were performed on cylindrical bar specimens having both as-cast and polished (30 μm) surface conditions. To aid in the modelling of the fatigue behavior of this cast material, supplemental R = -1 crack growth rate tests (da/dN-ΔK) on single-edge-notch plate specimens (SENP) were performed. All the experimental procedures and results are described in Appendix G. The stress - life (S-N) data for both as-cast surface and polished surface conditions, fatigue crack growth rate data (da/dN vs. ΔK) tested using constant-load and load-shedding methods, the statistical distribution of casting pores sizes and the statistical distribution of fatigue initiating defect sizes were experimentally determined. The basic mechanical properties and fatigue properties of this material are listed in Tables 1 and 2. The test results of S-N data and the corresponding fatigue-initiating-defect sizes are listed in Tables 3 - 5.

One of the objectives of this study was to model the statistical characteristics of the fatigue properties for this cast aluminum alloy 319 in the long-life regime. The CCN model was used to predict the fatigue life and threshold stress (i.e., maximum stress for infinite fatigue life) as a function of defect size distribution. Thus, the reliability of this material under a given applied stress range can be estimated.

4.1.2. Fatigue Properties of Cast Aluminum Alloy 319

Fatigue cracks were observed to initiate from near-surface casting pores in the polished specimens and from cast-surface texture discontinuities in the as-cast specimens. The initiating defect size was quantified by the square root of its area projected onto the plane normal to the applied stress direction, i.e., T or $\sqrt{\text{Area}}$. Statistical analysis showed that T (or $\sqrt{\text{Area}}$) is a normal distribution function with a mean of 0.5 mm and a standard deviation of 0.16 mm for both as-cast and polished specimens.

In the calculation of the stress intensity factor for a surface crack or a crack emanating from the near-surface casting defects in a cylindrical specimen, a parameter termed aspect ratio (AR) must be introduced. The aspect ratio is the crack depth divided by half of the crack length on the surface (see Appendix A.1). When the fatigue initiating defect is considered to be a 'natural' notch and when the crack closure of a crack emanating from this 'notch' is considered, the fatigue properties of this cast alloy are dependent on:

- Load ratio,
- Defect size,
- Defect shape (aspect ratio and acuity of the defect),
- Specimen geometry.

From a practical point of view, the defect shape is hard to determine. In general, the shape of a crack emanating from the near-surface casting defect is considered to be similar to the shape of a thumbnail (including the casting defect itself). The aspect ratio of this crack shape falls approximately within $0.8 \pm 0.1$[51,52]. The details of this parameter (aspect ratio, AR) are discussed in Appendix A. Fatigue cracks observed in this study initiated from the most acute locations on the outer perimeter of near-surface casting pores (see Appendix I). Thus, the casting defects were considered to be very sharp notches, and the notch root radii ($\rho$) for all the fatigue initiating defects were assumed to be 0.02 mm. In fact, the notch root radii ($\rho$) of the fatigue initiating defects were non-determinable. The assumption of the value of 0.02 mm for $\rho$ was based on the fact that the smallest radius of the casting defect is approximately equal to or less than the size of the dendrite arm spacing (~ 0.03 mm; see Appendix G).

Siljander's LEFM model and the CCN model were used to predict the fatigue life for the R equals 0.1 data and the R equals -1 data.

4.1.3 Predictions Based on the Siljander Model

Siljander [47] found that the role of fatigue defects can be quantified using a linear-elastic fracture mechanics (LEFM) model. Based on this simple LEFM model, the fatigue life and threshold stress can be estimated for an R ratio of 0.1. The relation between threshold stress ($S_{th}$) and the defect depth (D) is:

$$S_{th} = \frac{\Delta K_{tho}}{(1 - R)Y(D)\sqrt{\pi D}} \tag{4.1}$$

where: $\Delta K_{tho}$ = The long-crack threshold stress intensity range; see data in Table 2.
$R$ = Load ratio
$Y(D)$ = Geometrical factor for stress intensity calculation
$D$ = Initial defect depth

The fatigue life can be calculated using the Paris law:

$$N_T = N_P = \int_D^{D_f} \frac{da}{C\,(\Delta K)^m} \tag{4.2}$$

Where: $D$ = Initial defect depth
$C$ = Paris' constant in stage II; see data in Table 2
$m$ = Paris' exponent in stage II; see data in Table 2
$D_f$ = Final defect depth at fracture; calculated by:

$$K_{IQ} = S_{max}\, Y(D_f) \sqrt{\pi(D_f)}$$

$K_{IQ}$ = Fracture toughness = 9.0 MPa$\sqrt{m}$
$\Delta K$ = Stress intensity range = $Y(a)\,(1 - R)\,S_{max}\sqrt{\pi a}$
$Y(a)$ = Geometrical factor where 'a' ranged from D to $D_f$

The total fatigue life ($N_T$) was assumed equal to the propagation life because the casting defects were considered to be "crack-like" defects (the initiation life can be neglected). The test results from Siljander's study [47] were compared with the predictions based on a simple LEFM model (Eqs. 4.1 and 4.2) as shown in Fig. 12. The

experiments were carried out using cylindrical specimens with 7.62 mm diameter for the R equals 0.1 condition. Experimental results were separated into three groups by defect depth: $0.2 \leq D \leq 0.5$ mm, $0.5 < D \leq 0.9$ mm, and $D > 0.9$ mm. In the predictions, three values of defect depth were selected: 0.4, 0.7, and 1.2 mm. The aspect ratios (AR) of the fatigue initiating defects were assumed to be 0.8. It is apparent that the LEFM model gives satisfactory predictions for the R equals 0.1 condition as shown in Fig. 12.

Using the LEFM model to predict the S-N curve for the R equals -1 condition, the predictions and experimental data for the cylindrical specimens of this study are compared in Fig. 13. The fact that the experimental data are always lower than the predictions indicates the LEFM model (Siljander's approach) can not be used for the R equals -1 condition. The reason that the LEFM model can be used at R equals 0.1 but cannot be used at R equals -1 is mainly due to crack closure behavior: the effect of crack closure increases with decreasing R-ratio and the influence of anomalous crack growth rate for short cracks increases with decreasing R-ratio (see Chapter 2). Thus, the CCN model, which considers the effects of crack closure and the behavior of short cracks, was used as an alternative to the simple LEFM model.

4.1.4 Predictions Based on the CCN Model for Cylindrical Specimens

Comparisons between predictions made using the CCN model and the experimental data for the R equals 0.1 condition are shown in Fig. 14. Comparing Fig. 14 with Fig. 12 ($R = 0.1$), the predictions made using the CCN model give better results than predictions from the Siljander model. Figure 15 compares the experimental data with predictions from the CCN model for the R equals -1 condition. The predictions agree very well with the experimental data.

Comparisons between predicted and experimental lives for cylindrical specimens are given in Figs. 16a - 16d. The fatigue life is plotted against defect size for various levels of applied stresses. Fairly good results can be seen in all cases, although the CCN model provides conservative estimates of the fatigue life. A trend observed in Fig. 16 shows that the effect of defect size on fatigue life was more severe in the low stress range than in the high stress range. The as-cast surface condition seems to have a lower fatigue life than the polished condition under the low stress conditions as shown in Fig. 16a and 16b. The cause may be attributed to the different aspect ratios of the two surface conditions. The cast-surface texture discontinuities in as-cast specimens facilitate the crack growth on the surface, which consequently leads to lower aspect ratios. However, the S-N behaviors of these two surface conditions are not significantly different from a statistical point of view (see Appendix H).

Because the size distribution of the fatigue initiating defects can be represented by a normal distribution with a mean of 0.5 mm and a standard deviation 0.16 mm, the S-N curve for a certain probability of survival can be obtained by assuming that the defect size is the dominant parameter which affects the scatter of fatigue life at a given stress. From the normal distribution of defect sizes, 99.99% of the defects have sizes less than 1.09 mm, 99% of the defects have sizes less than 0.87 mm, and 50% of the defects have sizes less than 0.5 mm. Using 1.09, 0.87 and 0.5 mm as the criteria for the 99.99%, 99% and 50% survival levels and assuming an aspect ratio of 0.8, the fatigue lives corresponding to these levels of reliability were calculated. The predicted results were compared with the experimental data as shown in Fig. 17.

The predicted and experimental data of the threshold stress (gross-section $S_{th}$) are compared in Fig. 18 in which the threshold stress is plotted against fatigue initiating defect size. The solid symbols represent the failed-specimen data, and open symbols represent the run-out data ($N_T > 1.25 \times 10^8$ cycles). The predictions are shown by lines with aspect ratio values of 0.7, 0.8 and 0.9. Applied stresses in the region below a given line would lead to infinite fatigue life. Using 1.09 mm as the criterion for the 99.99% survival limit and assuming a conservative value of the aspect ratio (AR = 0.7), a threshold stress of 33.3 MPa (4.83 ksi) would ensure a 99.99% survival level.

Further confirmation of the accuracy of the CCN model was made by analyzing the test data obtained from the Central Foundry Division of the General Motor Corporation [74]. The material used in these tests was from a similar casting process and the same heat treatment as the material used in this study, but contained more Si and Mg. Tests were carried out using as-cast surface specimens with an R of -1. The test results are listed in Table 5. The predictions based on an aspect ratio of 0.8 are compared with the test results in Fig. 19. Defect sizes of 0.5, 0.87 and 1.09 mm are used to define the survival levels of 50.00%, 99.00% and 99.99%, respectively. Four experimental data points at $S_{max} < 60$ MPa are seen to exhibit shorter than average fatigue lives. Three of these four broken specimens were observed using an SEM to measure the fatigue initiating defect sizes. All three specimens have fatigue-initiating defect sizes ($T = \sqrt{Area}$) larger than 0.7 mm; see the data in Table 5 and the photograghs in Fig. 20. Although the fatigue crack growth behavior and the defect size distributions might be slightly different than those used in this study -- due to different compositions -- the CCN model still gives satisfactory predictions. These results may imply that slight changes of chemical compositions do not affect the fatigue properties.

4.1.5 Life Predictions Based on the CCN Model for SENP Specimens

Comparisons of predictions with experimental fatigue properties for single-edge-notch plate specimens (SENP) were made. Using the equation described in Appendix A to calculate $\Delta K$ for the SENP specimen and the CCN model detailed in Appendix D to predict the function of U(x) for a crack emanating from a notch, the variations of crack growth rate (da/dN) with crack length (x) were estimated for various notch and stress conditions. The predicted da/dN and the measured da/dN as a function of crack length are compared in Fig. 21a ($K_{tn} = 4.85$) and Fig. 21b ($K_{tn} = 11$). The solid lines are the predicted results, and the data points are the experimental results. For both notched conditions, the predictions are fairly good in the higher stress ranges but not very good in the low stress range ($\Delta S = 73$ MPa) for which the cracks are shorter than about 1 mm.

The CCN model was used to predict the fatigue lives of SENP specimens with a constant notch depth (D = 1.6 mm) and various root radii ($\rho = 0.06$, 0.4, and 0.8 mm). The predictions are compared with experimental data in Fig. 22. In addition to yielding good predictions for the lives of the cast specimens, the CCN model is also capable of predicting the lives of machine-notched specimens for cast aluminum alloy 319.

## 4.2 Components with Machined Notches

To further confirm the validity of the CCN model, ten sets of fatigue data found in the literature were compared with the predicted values of the threshold stress range ($\Delta S_{thn}$). The materials included two aluminum alloys, three carbon steels, and three special alloy steels. The specimens and notch types included circumferentially notched cylindrical bars (CNB), center notched flat plates (CNP), and double-edge notched flat plates (DENP). The geometrical factors (Y(a)) used in the stress intensity factor solutions of the assorted notched specimen geometries are summarized in Appendix A.

Table 6 lists the material properties required for all of the predictions: (1) yield strength ($S_y$), (2) fatigue limit of smooth specimens ($\Delta S_e$), (3) long-crack threshold-stress-intensity range ($\Delta K_{tho}$), (4) the effective-threshold-stress-intensity ratio for a long crack ($U_{tho}$), and (5) tensile strength ($S_u$). The values of $U_{tho}$ were derived as described in Eq. 2.13 (i.e. $U_{tho} = \Delta K_{eff.tho}/\Delta K_{tho}$). For the cases when the values of $\Delta K_{eff.tho}$ could not be assessed, equation 2.10 ($\Delta K_{eff.tho} = \eta E$) was used. The values of H/E were assumed to be 0.01 for aluminum alloys and 0.07 for steel.

The experimental results and predictions of the CCN model are compared in Table 7. It is apparent that the predictions based on the CCN model agree well with most of the experimental data except in the case of the BS L65 aluminum alloy (Case 6 in Table 7f).

As discussed in Section 2.4, the relationship between $\Delta S_{thn}$ and $K_{tn}$ for a constant-depth notch (D = constant) can be described by the Frost relation (Fig. 6), and the relationship for a geometrically similar notch ($K_t$ = constant) can be described by the Lukas relation (Fig. 7). These trends were also predicted by the CCN model. Figure 23 plots the normalized threshold stress ($\Delta S_{thn}/\Delta S_e$) as a function of $K_{tn}$ for the constant-depth notches (Cases 1-3 in Table 7). Figure 24 (Cases 4,5,7,and 8 in Table 7) shows the relations between normalized threshold stress and notch depth (radius) for the geometrically similar notches in which all the values of $K_t$ are about 3. However, the values of $K_{tn}$ decrease with increasing notch depth. As seen in Fig. 24, $\Delta S_{thn}$ approaches $\Delta S_e$ for very shallow notches, but decreases rapidly to a minimum value with increasing notch depth. Thus, the threshold stress of a notched component ($\Delta S_{thn}$) is a function of both stress concentration ($K_{tn}$) and notch depth (D).

## 4.3 Comparison of CCN Predictions with Those of Other Models

Six other models were used to predict $\Delta S_{thn}$, and these predictions were compared with the experimental results and the CCN model predictions. The six models are: Peterson (Type I and Type II), Lukas, Topper, Sun (M) and Sun (O). Two different equations (Eqs. 2.4 and 2.5) were used to derive the values of Peterson's constant ($\alpha_I$ and $\alpha_{II}$). The first one, termed PTS(I), uses Eq. 2.4 to calculate Peterson's constant ($\alpha_I$) and the second one, termed PTS(II), uses Eq. 2.5 to calculate Peterson's constant ($\alpha_{II}$). The predicted results from these models are listed in Table 7. The value of $f$ (see Section 2.4.3) used in the Lukas model was assumed to be 0.73 for all cases. The definitions of the Sun(M) and Sun(O) model will be discussed later.

As seen from Table 7, the Topper, Lukas and Sun (M) models agree well with most of the experimental data except for the case of the BS L65 aluminum alloy (case 6 in Table 7f); whereas, the Peterson models (both PTS(I) and PTS(II)) and Sun (O) model overestimate the threshold stresses in many cases. Statistical analyses were performed to compare the validity of the seven models and are presented below:

### 4.3.1 Quantities used to Compare the Validity of Models

The "Error%" is defined as the difference between the predicted value and the experimental value divided by the experimental value:

$$\text{Error\%} = \frac{\Delta S_{thn(pred)} - \Delta S_{thn(exp)}}{\Delta S_{thn(exp)}} \times 100\% \qquad (4.3)$$

where:

$\Delta S_{thn(pred)}$ = Predicted value of threshold stress range ($\Delta S_{thn}$)

$\Delta S_{thn(exp)}$ = Experimental value of threshold stress range ($\Delta S_{thn}$)

The "Error%" calculated from each model was considered to be a normal distribution. The cumulative distribution function (CDF) of the "Error%" was plotted using normal distribution paper. The CDF versus the "Error%" calculated from each model was used to verify the validity of the model. A good model should have its "Error%" distributed around 0% and have a steep slope in the CDF versus the "Error%" plot.

The average absolute "Error%" (AAE%) is another quantity used to compare the validity of models. A good model should have low value for the "AAE%". The "AAE%" is defined as the sum of the total absolute error divided by the total number of observations:

$$\text{AAE\%} = \frac{\sum_{i=1}^{N} \left| (\text{Error\%})_i \right|}{\text{No}} \qquad (4.4)$$

where: No = Total number of observations

4.3.2 Comparison of the CCN Model with the Peterson Model

Figure 25 compares the cumulative distribution functions of the "Error%" for the results predicted from the CCN model and from the two of Peterson equations. Of the data predicted by the CCN model, 95% fall within ± 20% (Error). Only about 60% of the predictions made by the Peterson models fall within ± 20% (Error). These results indicate that either $\alpha_I$ and $\alpha_{II}$ are not good models for predicting Peterson's constants or the Peterson model itself is not a good model for predicting the threshold stress.

4.3.3 Comparison of the CCN Model with the Topper Model and the Lukas Model

Comparisons of the validity of the CCN, Lukas and Topper models using the normal distribution plot of the CDF of the "Error%" are shown Fig. 26. The fact that the CDF of the "Error%" calculated using the CCN model has the highest slope indicates that the CCN model gives the best predictions of the three models. It is noted that the

predictions of the Topper model have a trend of under-prediction, and the predictions of the Lukas model are almost as good as the CCN model, but the scatter band of the "Error%" resulting from the Lukas model is larger than that of the CCN model.

4.3.4 Comparison of the CCN Model with the Sun(O) Model and the Sun(M) Model

As discussed in Section 2.3.2, the $U^S(x)$ function proposed by Sun and Sehitoglu described the variation of stress intensity ratio with crack length for a crack emanating from a notch. The CCN model used Sun and Sehitoglu model to describe $U_{th}(x)$ for a crack within the notch stress field boundary but a modification of the stabilized opening stress ($S_{opo}$) was made as discussed in Appendix C.1. This modification was based on the concept that at the threshold condition the calculated $U_o$ value based on the plasticity-induced crack closure (PICC) mechanism should not be lower than the experimentally determined long-crack threshold stress intensity ratio ($U_{tho}$). Thus, there are two possible $U^S(x)$ functions: the first is the Original $U^S(x)$ function, which does not consider the threshold limitation (i.e., $U_o$ may be smaller than $U_{tho}$), and the second is the Modified $U^S(x)$ function, which considered the minimum $U_o$ to be limited by $U_{tho}$. The CCN model combined the Modified $U^S(x)$ function with the Tanaka model.

The threshold stress range can be predicted based on the combination of $\Delta K$ with the $U^S(x)$ function. Utilizing the $U^S(x)$ function, the threshold stress is obtained by the condition that the minimum $\Delta K_{eff,th}(x)$ just equals $\Delta K_{eff,tho}$ (the same procedures as described in Chapter 3). The threshold stress derived by the Sun(M) model was based on the Modified $U^S(x)$ function, and that derived by the Sun(O) model was based on the Original $U^S(x)$ function.

Figure 27 compares the "Error%" of the predictions based on the CCN, the Sun(M) and the Sun(O) models. It is apparent that the Modified model (Sun(M)) gives a better prediction than the Original one (Sun(O)). As seen in Table 7, the different predicted results of the Sun(O) and Sun(M) models occurred in the aluminum alloys in which the (experimentally determined) $U_{tho}$ values were higher than the calculated $U_o$ values. The improved results from the Sun(M) model imply that the concept to force a minimum $U_o$ value at $U_{tho}$ may be justified. Figure 27 also shows that the predictions from the CCN model are better than the Sun(M) model, especially for the small notches (see cases 4, 5,7, and 8 in Table 7).

Figure 28 compares the "AAE%" resulting from all the models and also shows that the CCN model has the least average absolute error in predicting the threshold stress range for notched specimens.

## 4.4 Short Summary

The roles of casting defects and machined notches on the fatigue behavior of cast aluminum alloy 319 were successfully predicted by the CCN model. Good agreement was also found between estimated values of the threshold stress and the experimental data reported in the literature. The CCN model appears to provide better predictions of the fatigue behavior at near-threshold conditions than other models.

# 5. DISCUSSION

## 5.1 The Long-Life Regime Fatigue Behavior of Cast Aluminum Alloy 319

### 5.1.1 Comparison of Experimental Results with Predictions of the CCN Model

Fatigue cracks were observed to initiate from near-surface casting pores in the polished specimens and from cast-surface texture discontinuities in the as-cast specimens (see Figs. G.8 and G.9). The initiating defect size was quantified by the square root of its area projected onto the plane of observation, i.e., T or $\sqrt{\text{Area}}$ (Fig. G.9). The quantity (T) proved to be a useful measure for representing the severity of a defect. This study also showed that there was a difference between the size distribution of casting pores and the size distribution of fatigue initiating defects (see Fig. G.12). However, using the size of (apparently isolated) casting pores as a quality control parameter ignores the fact that the pores are often three-dimensional aggregates. Simple metallographic techniques may not expose the plane which contains the maximum projected area of a defect, and thus may yield a very poor indication of the true quality of a casting.

Statistical analysis showed that the fatigue-initiating defect sizes for both polished specimens and as-cast specimens were the same (Fig. G.10). The size distribution of the fatigue initiating defects in the cast aluminum alloy 319 is a normal distribution with a mean of 0.5 mm and a standard deviation of 0.16 mm.

As described in Appendix I, it was observed that the fatigue cracks originated from the most acute locations on the outer perimeter of an initiating defect, and that the crack nucleation life ($N_n$) was almost negligible. These observations indirectly suggest that the notch root radius ($\rho$) of the initiating defect must be very small. The notch root radii of all the fatigue initiating defects were assumed to be 0.02 mm for the CCN model. The fatigue life predictions based on this assumption agree with the experimental results (see Figs. 14-16).

The CCN model was employed to predict the fatigue lives of the SENP specimens which had a constant notch depth (D = 1.6 mm) and variable notch root radii ($K_{tn}$ = 11, 4.85 and 3.6). Experimental results showed that the blunt notches have lower fatigue lives than the sharp notches; this phenomenon was successfully demonstrated by the CCN model (see Fig. 22).

### 5.1.2 Difficulties with the LEFM and EPFM Models

Siljander [47] used a simple LEFM model (da/dN versus $\Delta K$ relationship) to predict S-N data ($N_T > 10^5$ cycles) for R = 0.1 and found that his predictions agreed with his

experimental data satisfactorily. Starkey [66] used the theory of Elastic Plastic Fracture Mechanics (EPFM) (da/dN versus $\Delta J$ relationship) to predict S-N data ($N_T < 10^5$) for $R \geq 0.1$ and found that the calculated lives agreed with the experimental lives within a factor of four. Both of these studies neglected the effect of crack closure.

However, for any R ratio $\leq -1.0$, the effect of crack closure becomes significant. The LEFM model failed to predict the fatigue life of cast aluminum alloy 319 for the R = -1 condition, as discussed in Chapter 4. In developing the life prediction model for cast aluminum alloy CP 601, Couper et al. [49] used the relationship of da/dN versus $\Delta K_{eff}$ to predict the fatigue life (as a function of defect size). Couper assumed that $\Delta K_{eff} = U\Delta K$ (where U is a constant independent of crack length), and found that the best predictions were obtained when U was assumed to be 0.5. However, the selection of U = 0.5 was empirical and may not be generally applicable.

In contrast to Couper's model, the CCN model predicts U(x) as a function of crack length (x), applied stress conditions (R, $S_{max}$), material properties ($S_y$, $L_o$, E, and $U_{tho}$), and notch conditions ($K_t$ and D). Therefore, the CCN model has the ability to predict the fatigue lives and the threshold stresses for both natural defects and machined notches in the long-life regime.

## 5.2 The Role of Notches in Fatigue Suggested by the CCN Model

Notches cause stress concentrations which enhance the crack nucleation processes in the plastic zone ahead of the notch root. Sharper notches are believed to have shorter crack nucleation lives ($N_n$). The crack nucleation life can be predicted using $K_t$ and strain-life approaches in the long-life regime. Once a crack has nucleated at a notch, the effective stress intensity range ($\Delta K_{eff}(x)$) controls the crack growth rates; and hence dominates the total propagation life ($N_f$).

The main parameters which influence the nucleation life ($N_n$) and the total propagation life ($N_f$) for notched components are:

1. Model parameters:
    - The value of initial crack length for integrating the fatigue life ($x_i$)
    - The value of notch stress field boundary (NSFB)
2. Material properties:
    - Yield strength ($S_y$)
    - Fatigue strength coefficient of smooth specimen ($\sigma'_f$)

- Fatigue strength exponent of smooth specimen (b)
- Elastic modulus (E)
- Range of fatigue limit ($\Delta S_c$) for smooth specimens
- The value of H/E ( = 0.01 for Aluminum alloys and 0.07 for steel)
- Long-crack threshold stress intensity factor ($\Delta K_{tho}$)
- da/dN vs. $\Delta K_{eff}$ (or da/dN vs. $\Delta K$) data obtained by load-shedding

3. Notch parameters:
   - Notch acuity ($K_t$)
   - Notch depth (D)

The influence of the above parameters on predicted values of $\Delta S_{th}$ and $N_T$ under constant stress amplitude conditions was investigated. Ten hypothetical materials were assumed and their properties are shown in Fig. 29. These materials (AL-1 to AL-5 and ST-1 to ST-5) were used to study the role of material properties on the fatigue notch effect in the following sections. The AL-1 and ST-1 are the highest strength materials and the AL-5 and ST-5 are the softest materials used in these CCN model simulations. Both the AL and ST series have the same material properties except for the value of H/E (H/E = 0.01 for AL and H/E = 0.07 for ST). Note that all the materials have the same da/dN versus $\Delta K_{eff}$ relationship. The simulations were based on a centered notch in a plate (CNP) specimen with semi-infinite width (W = 10,000 mm). The plane-stress condition was assumed.

5.2.1 Influence of Model Parameters

The total propagation life ($N_f$) predicted using the CCN model is calculated by integrating the crack length from $x_i$ to $x_f$: see Eq. 3.4. The value of $x_i$ was assumed to be $l_t$ : see Eq. B.3. The CCN model uses Dowling's concept [4] of $l_t$ as an initial crack length for life prediction. As asserted by Dowling, for cracks shorter than $l_t$, the plasticity effect near notch generally causes large errors in $\Delta K$ calculation due to plasticity effects [35]. Thus, the CCN model estimates the total propagation life ($N_f$) for $x \geq l_t$.

The influence of the initial crack length on the CCN model was investigated by varying the $x_i$ values from $0.5l_t$ to $1.5l_t$. Material AL-1 ($L_o$ = 0.0052 mm) was selected as the basis of the simulation. According to the CCN model, changing the value of $x_i$ does not affect the predicted value of threshold stress ($\Delta S_{th}$) because the minimum in $\Delta K_{eff.th}(x)$ occurs at crack lengths larger than the notch stress field boundary (x*) which is larger than $l_t$ (see Fig. B.1).

However, as shown in Fig. 30, changing the value of $x_i$ does affect the predicted total propagation life ($N_f$) especially for small notches. Figure 30 compares the predicted $N_f$ by changing $x_i$ values for AL-1 with four notch depths. The predicted values of $N_f$ are strongly affected by the value of $x_i$ for D = 0.1 and 0.5 mm, but they are not significantly affected for $D \geq 1.0$ mm.

The effect of the values of notch stress field boundary (NSFB) on the CCN model was also investigated. The sensitivity of the NSFB on the CCN model was studied by varying NSFB values from $l_t$ (about $0.05\sqrt{D\rho}$) to $0.24\sqrt{D\rho}$ for notches of $K_{tn} = 7$. The predicted fatigue life is little affected by varying the value of NSFB; the larger the NSFB, the longer the fatigue life. Figure 31 shows the influence of selected values of NSFB on the predicted threshold stress. The smaller notch is more sensitive to the selected values of NSFB. However, in the range between $0.13\sqrt{D\rho}$ and $0.21\sqrt{D\rho}$ (the possible NSFB suggested by Smith et al.; see Appendix B), the dependence of the selected values of NSFB on threshold stress is almost negligible.

5.2.2 Effect of Material Properties and Notch Parameters on the Fatigue Life

The difference in fatigue life between sharp and blunt notches is determined by two competing processes: $K_t$ for crack nucleation life and $\Delta K_{eff}(x)$ for subsequent crack propagation life. Figures 32a (based on material AL-3) and Fig. 32b (based on material AL-5) show the changes of S-N relationship with notch depths and with two $K_t$ values ($K_t$ = 3 and 7). For sharp notches ($K_t = 7$), the total fatigue lives ($N_T$) are always dominated by the total propagation lives ($N_f$) no matter how deep the notches are. For large-blunt notches ($K_t = 3$) of higher strength material (AL-3), $N_n$ dominates the total fatigue life in the long-life regime; but this result is not seen in the softer material (AL-5) for which the total fatigue life is still dominated by the total propagation life ($N_f$). These results indicate that the change of the S-N relationship for a notched component is dependent on notch depth, notch acuity and the material properties. Generally, high strength materials are more likely to be dominated by the crack nucleation process (for blunt and large notches); whereas, low strength materials are more apt to be dominated by the crack propagation process.

From an engineering point of view, the total propagation life ($N_f$) can be separated into two parts: the early crack propagation life ($N_{p1}$) and the propagation life ($N_{p2}$). While the transition from early crack propagation to propagation is not sharply defined, there is a general concept of early crack propagation which is assumed to be that portion of life spent

in developing an engineering size crack (0.25 mm). Thus, the total fatigue life ($N_T$) can be given by:

$$N_T = N_n + N_f = N_n + N_{p1} + N_{p2} \tag{5.1}$$

where: $N_T$ = Total fatigue life
$N_n$ = Crack nucleation life
$N_{p1}$ = The early crack propagation life for crack growing to an engineering crack size (0.25 mm)
$N_{p2}$ = The propagation life for crack growing from 0.25 mm to failure

Figures 33a and 33b illustrate the effect of material properties (AL-1, AL-3 and AL-5) and notch depths (D = 0.5 mm and 5.0 mm) on the importance of each fatigue-life portion for the geometrically similar blunt notches ($K_t$ = 3) and sharp notches ($K_t$ = 7). For high strength material (AL-1), most of the fatigue life was controlled by the crack nucleation life ($N_n$). For soft material (AL-5), fatigue life is more likely to be dominated by the propagation life ($N_{p2}$), especially for the sharp notches or the large-blunt notches. Figure 33 proposes a concept for in-service inspection and repair on the notched structure reliability. For example, if an engineering size crack (0.25 mm) was found in a structure made from AL-1, this component should be repaired immediately, but, if this structure is made from AL-3 or AL-5, the need for repairing this structure depends on the depth and acuity of the notch from which the crack emanated. Generally, for an engineering structure made from a soft material, the total fatigue life is controlled by the propagation life ($N_{p2}$), thus, the structure would sustain a long fatigue life even an engineering-size crack develops.

5.2.3 Effect of Material Properties and Notch Parameters on the Threshold Stress

In the long-life regime, the most important fatigue property is the threshold stress which depends upon the value of $K_{fn}$:

$$\Delta S_{thn} = \frac{\Delta S_e}{K_{fn}} \tag{2.19}$$

Figure 34 shows the variation of $K_{fn}$ with notch depth as a function of $L_o$ and H/E for a blunt notch ($K_{tn}$ = 3 in Fig. 34a) and for a sharp notch ($K_{tn}$ = 7 in Fig. 34b). For low $L_o$ materials, there is no significant difference between the two different H/E values

(aluminum and steel); however, for high $L_o$ materials, the difference is significant. For both aluminum and steel, the values of $K_{fn}$ increase with increasing notch depth until $K_{fn} = K_{tn}$. Neglecting the effect of H/E values, the maximum notch depth ($D_{max}$) above which $K_{fn}$ always equals $K_{tn}$ and the fatigue notch size effect vanishes can be estimated by:

$$D_{max} = L_o K_{tn}^2 \tag{5.2}$$

Equation 5.2 indicates that a high strength material (low $L_o$ material) has a higher notch sensitivity because it has a smaller $D_{max}$. As shown in Fig. 34b, for notches with $K_{tn} = 7$ and D = 1 mm, the highest strength material (AL-1; $L_o = 0.0052$ mm) has $K_{fn} = K_{tn} = 7$, the medium strength material (AL-3; $L_o = 0.177$ mm) has $K_{fn} \approx 2.7$, and the lowest strength material (AL-5; $L_o = 0.934$ mm) just has $K_{fn} \approx 1.7$. The above example indicates that the value of intrinsic crack length ($L_o$) is the most important material property in describing the effect of material properties (compared at the same H/E value and the same $\Delta K_{eff.tho}$) on the fatigue of notches at the threshold condition.

## 5.3. Geometrically Similar and Constant Depth Notches

### 5.3.1 The Apparent Discrepancy Between the Work of Frost and Lukas

The effects of notch depth (D) and notch acuity ($K_{tn}$) on threshold stress range ($\Delta S_{thn}$) are schematically illustrated by the Frost relation (Fig. 35a and 35b) which completely describes the effect of notches in fatigue. Figure 35a shows the variation of threshold stress with notch acuity for constant depth notches with three different depths. For a small *constant depth notch* (e.g., $D_1$), $\Delta S_{thn}$ equals the fatigue limit of a smooth specimen ($\Delta S_e$) up to a certain $K_{tn}$ value, and then decreases with increasing $K_{tn}$; finally, $\Delta S_{thn}$ approaches a stable value. The threshold stresses varying with $K_{tn}$ for this constant depth notch ($D = D_1$) are all controlled by the existence of non-propagating cracks (NPC). When notch size is large and greater than $D_{max}$ (e.g., $D_3$), the values of $\Delta S_{thn}$ always equal $\Delta S_e/K_{tn}$ and no non-propagating cracks should be observed. The Frost relation ($K_{fn}$ is almost a constant for $K_{tn} \geq K_{tc}$; see Fig. 6) only occurs in the middle range of notch size (e.g. the $D_2$ constant depth notch in Fig. 35a) in which the threshold conditions are controlled either by the non-propagating cracks (NPC), for sharp notches, or by the nucleation of cracks for blunt notches.

For *geometrically similar notches* ($D/\rho$ = constant ; see Fig. 35b), $\Delta S_{thn}$ equals $\Delta S_e$ when D is smaller than a critical notch size (the maximum non-damaging notch size). When D is larger than the maximum non-damaging notch size, $\Delta S_{thn}$ sharply decreases

with increasing notch size to a minimum value and then increases with increasing notch depth.

The apparent discrepancy between the Frost and Lukas relations as discussed in section 2.4 is reconciled in Fig. 35b. The dashed lines in the left-hand side of Fig. 35b (Frost relation) represent the relation between $\Delta S_{thn}$ and D for two *geometrically similar notches* ($K_t$ = 3 and 7). The corresponding Lukas relation was also shown in the right-hand side of Fig. 35b. As seen in the case of notch with $K_t$ = 3, when $D \leq D_1$, $\Delta S_{thn}$ equals $\Delta S_e$; when $D \geq D_1$, $\Delta S_{thn}$ decreases with increasing D; and when D increases to $D_3$, $\Delta S_{thn}$ reaches a minimum value. All the threshold stresses were determined by the non-propagating crack behavior for $D \leq D_3$. When $D \geq D_3$, $\Delta S_{thn}$ increases with increasing D, because in this range, $\Delta S_{thn}$ is controlled by the value of $\Delta S_e/K_{tn}$ (i.e., "no cracks" range). The value of $D_3$ shown in Fig. 35b is the $D_{max}$ of this geometrically similar notch ($K_t$ = 3). Equation 5.2 shows that $D_{max}$ is proportional to the square of $K_{tn}$ (higher $K_{tn}$ notches have higher $D_{max}$ values). This trend is also represented in Fig. 35b; the sharp geometrically similar notches ($K_t$ = 7) have a larger value of $D_{max}$ ($D_{max} = D_4$) than the blunt ones ($D_{max} = D_3$). Figure 35b also shows that a sharp notch has a smaller value of maximum non-damaging notch depth than a blunt notch (i.e., $D_0 < D_1$).

5.3.2 The Worst Case, Constant Depth Notch

The effect of notch acuity and notch depth on the threshold stress for the *constant depth notches* can be represented using the relationship between $K_{fn}$ and $K_{tn}$ shown in Fig. 36. For a constant depth notch, $K_{fn}$ generally achieves a maximum value as one increases the notch acuity. For a deep notch, the value of $K_{fn}$ equals $K_{tn}$ up to a maximum value ($K_{fmax}$) and then slightly decreases with increasing $K_{tn}$; whereas, for a shallow notch, $K_{fn}$ slightly increases with increasing $K_{tn}$ and approaches a stable $K_{fmax}$. However, as pointed out in Eq. 5.2, the existence of a worst case notch must be limited for $D < D_{max}$; when $D > D_{max}$, $K_{fn}$ always equals $K_{tn}$.

Lawrence et al. first proposed the concept of the existence of worst-case notch ($K_{fmax}$ ; see Eq. 2.20) which implies that the damaging effect of a notch on the fatigue strength does not directly correlate with the sharpness of the notch and that the sharpest notches may not be the most damaging. This $K_{fmax}$ concept was also verified by the CCN model as shown in Fig. 36. As seen in Fig. 36a and 36b, for a given material, the values $K_{fmax}$ increase with increasing notch depth. By comparing the effect of material properties on the variation of $K_{fn}$ with $K_{tn}$ based on the same notch depth (Figs. 36a and 36b), one sees that the relatively high strength material (AL-3) always has a higher $K_{fmax}$ than the relatively low strength material (AL-5).

The values of $K_{fmax}$ between the previous work of Lawrence and the CCN model would be different. Lawrence $K_{fmax}$ model was derived based on the Peterson model, thus, the accuracy of this model must be dependent on the assumption that the Peterson model is accurate. As seen in Fig. 25, the Peterson model has a trend of over-predicting threshold stress (i.e., under-predicting the $K_{fn}$ value). The Lawrence $K_{fn}$ model takes the maximum $K_{fn}$ value from the Peterson model, thus, the Lawrence $K_{fmax}$ model might give good predictions of $K_{fmax}$ values [7], but the $K_{tn}$ value where $K_{fmax}$ is located would be questioned, because the trend of $K_{fn}$ versus $K_{tn}$ proposed by the Peterson model did not agree well with the experimental results (see Table 7 and Fig. 25).

### 5.3.3 The Worst Case, Geometrically Similar Notch

The work of Lukas suggested that geometrically similar notches had a minimum value of $\Delta S_{thn}$ for some value of notch depth, that is, for some maximum value of $K_{fn}$. From inspection of Fig. 35b, it is clear that the worst case for geometrically similar notches occurs when the notch size equals $D_{max}$. Above the $D_{max}$ value, the notch size becomes large enough that the existence of a non-propagating crack is impossible at the threshold condition. The values of $K_{fmax}$ for geometrically similar notches are different from the $K_{fmax}$ values for constant depth notches.

## 5.4 The Maximum Non-Damaging Notch Depth ($X_{BC}$)

It is well known that the fatigue life or the threshold stress of a low strength material is not affected by small defects or slight surface roughness. The question is what is the maximum defect size a material can tolerate and have the same fatigue resistance as a smooth specimen. This topic has been studied for several years by Lukas et al. [39,45], and they proposed that a notch is non-damaging when:

$$\rho \leq \frac{4.5\, l_o}{K_{tn}^2 - 1} \tag{5.3}$$

where: $l_o$ = Maximum non-propagating crack size for smooth specimen (Also see Eqs. 2.23 - 2.25)

However, Eq. 5.3 is only valid for the condition that $K_{tn} \leq 4$ [45]. Thus, a general quantitative determination of the maximum non-damaging notch depth has not been established yet; but qualitatively, it is well known that a higher strength material has a

smaller maximum non-damaging notch depth than a lower strength material. As discussed in Appendix F, the maximum non-damaging notch depth (denoted as $X_{BC}$) can be considered to be the limit of the CCN model applicability at the fatigue limit; when the notch depth is smaller than the $X_{BC}$, $K_{fn} = 1$ and when notch depth is larger than the $X_{BC}$, $K_{fn} > 1$. Thus, a specimen with a notch depth smaller than the $X_{BC}$ value may be treated as a smooth specimen.

The influence of the material property $L_o$ on $X_{BC}$ for aluminum alloys is shown in Fig. 37a. The values of $X_{BC}$ increase with increasing $L_o$. The variations of $X_{BC}$ with $K_t$ at the same $L_o$ indicate that the value of $K_t$ is also an important parameter affecting $X_{BC}$. When the data points in Fig. 36a are represented by the relation between $X_{BC}$ and $L_o/\sqrt{K_t}$, all the data points fall into a nearly straight line (Fig. 37b), and, $X_{BC}$ is given by:

For aluminum alloys with $3 \le K_t \le 7$ and $R = -1$,

$$X_{BC} = \frac{1}{Y_o}(2.5\ (\mu m) + 0.52\ \frac{L_o}{\sqrt{K_t}}) \tag{5.4a}$$

where:
- $Y_o$ = Geometrical factor for crack length approaching zero
- $Y_o$ = About 0.76 for a semi-circular surface crack in a cylindrical bar assuming that the aspect ratio equals 0.8, and $X_{BC}$ is the length in the radial direction.
- $Y_o$ = 1.0 for a center notch in a plate (CNP)
- $Y_o$ = 1.12 for a single edge notch in a plate (SENP) and for a circumferential notch in a cylindrical bar (CNB).

Separate studies for steel were performed as shown in Fig. 38. It was found that for steel with $3 \le K_t \le 7$ and $R = -1$, $X_{BC}$ is:

$$X_{BC} = \frac{1}{Y_o}(2.5\ (\mu m) + 0.79\ \frac{L_o}{K_t}) \tag{5.4b}$$

For the cast aluminum alloy 319 ($L_o = 934\ \mu m$) as shown in Fig. 18, the maximum non-damaging defect depth falls within the range of 200 to 300 μm (see run-out data for $N_T = 1.25 \times 10^8$ at $S_{max} = 62$ MPa). Using Eq. 5.4a and assuming that $K_t = 7$, the predicted value of $X_{BC}$ is about 240 μm which is close to the test results.

Another experimental result for steel 15313 ($L_o$ = 237 μm) was obtained by Lukas et al. [39,45] who found that the maximum non-damaging notch depth is about 60 μm in CNB specimens with $K_t$ = 3 (see data in Table 7g). Using Eq. 5.4b, the predicted $X_{BC}$ value for the CNB specimen is 58 μm ($K_t$ = 3.0) which agrees with experimental observations quite well. Unfortunately, no further data can be found to support the validity of Eqs. 5.4.

High strength materials have lower $L_o$ values, and hence, smaller values of maximum non-damaging notch depth. A small defect which may not affect the fatigue resistance of low strength materials may severely damage the fatigue resistance of a high strength material. In the material design, if one ignores the damage of the small notch (scratch, surface defect) on the fatigue resistance of a high strength material, it may cause costly disaster. For example, as seen in Fig. 34a, a 0.01mm (10 μm) defect could reduce the fatigue strength of AL-1 by 33% ($K_{fn}$ = 1.5), and a 20 μm defect could reduce the fatigue resistance by 50% ($K_{fn}$ = 2). Thus, $X_{BC}$ is an important parameter which can be used as an index for the quality control of a material. Further work in this area is strongly recommended.

## 5.5 Areas for Applying CCN Model and Future Study

The major contribution of the CCN model is the prediction of the influence of small defects (or notches) on the long-life regime fatigue properties of a material. The CCN model may be used as a basis for fatigue damage-tolerant analysis of components which contain either intentional notches or intrinsic defects.

Because the proposed CCN model considers the effect of applied and mean stresses, it has the ability to deal with variable amplitude loadings. The deterministic CCN model could also be used as the basis for stochastic modelling of the fatigue properties using the Monte Carlo methods.

In Chapter 4, the CCN model proved accurate for the notches with $K_t \geq 3$, but its accuracy has not been proven for notches with $K_t < 3$. Whether the CCN model is applicable for $K_t < 3$ conditions remains to be seen.

Another problem with the CCN model is that it utilizes the function $U^S(x)$ adapted from the Sun and Sehitoglu model which is based on the plane-stress condition for a crack emanating from a notch. The reason for selecting the plane-stress condition is that the specimens dealt with in this study are mostly thin, and the short cracks are mainly near the free surfaces of the notch roots which further imply the plane stress condition. In engineering components, there are few instances of purely plane strain or purely plane

stress conditions. Thus, the selection of the plane stress condition for predicting the threshold stress and fatigue life in this study may result in an ineluctable error.

Many changes are still required to improve the CCN model. The effect of residual stresses on the crack closure behavior has not yet been considered. The roles of Mode II and Mode III loading conditions on the crack closure are recommended for future study. The influence of over-loading (or under-loading) conditions on the crack growth rate of short cracks should be investigated in order to estimate the fatigue life in variable amplitude loading conditions. Environmental effects such as high temperature and corrosion are also important in real-world applications.

# 6. CONCLUSIONS

1. A crack closure at a notch (CCN) model was developed which was based on the behavior of short cracks at notches and which predicts the fatigue threshold stress and fatigue life for general notched specimens under various R ratios.

2. The fatigue properties of cast aluminum alloy 319 were studied. The role of casting defects and machined notches on the fatigue behaviors was successfully predicted by the CCN model

3. This study proposed a general theory of the role of notches in fatigue particularly at or near threshold conditions. This study reconciles the apparent discrepancy between the work of Frost and Lukas by showing that neither $K_{tn}$ nor notch depth alone is a complete description of notch severity in fatigue.

4. This study verified the existence of a worst-case notch for which the fatigue notch factor ($K_{fn}$) is a maximum ($K_{fmax}$). The value of $K_{fmax}$ and hence the minimum value of the threshold stresses ($\Delta S_{thn}$) for constant depth notches and geometrically similar notches are radically different.

5. The maximum non-damaging notch depth ($X_{BC}$) and the maximum notch depth ($D_{max}$) above which $K_{fn}$ always equals $K_{tn}$ were investigated. Both values are dependent on the intrinsic crack length ($L_o$) and the notch acuity ($K_{tn}$).

6. The results of this study indicate that the intrinsic crack length ($L_o = 1/\pi\,[\Delta K_{tho}/\Delta S_e]^2$) is the most important material parameter in describing the effect of material properties on fatigue of notches at the threshold condition.

# TABLES

## TABLE 1

MECHANICAL PROPERTIES OF THE CAST ALUMINUM ALLOY 319

| | | | |
|---|---|---|---|
| Elastic Modulus | E | 75000 | MPa |
| Hardness | HRB | 45 | |
| Yield Strength | $S_y$ | 190 | MPa |
| Ultimate Tensile Strength | $S_u$ | 206 | MPa |
| Fracture Strength | | 204 | MPa |
| Reduction in Area | %RA | 1.815 | |
| Total Elongation | $\%e_f$ | 0.708 | |
| True Fracture Strain | $\varepsilon_f$ | 0.0165 | |
| True Fracture Strength | $\sigma_f$ | 208 | MPa |
| Strain Hardening Exponent | n | 0.1253 | |
| Strain Hardening Coefficient | K | 419 | MPa |

TABLE 2

FATIGUE PROPERTIES OF THE CAST ALUMINUM ALLOY 319

| | | | |
|---|---|---|---|
| *Uniaxial Constant Stress Amplitude Data* | | | |
| Estimated Fatigue Limit (R = -1) | $S_e$ | 60 | MPa |
| Estimated Fatigue Limit (R = 0.1) | $S_e$ | 93 | MPa |
| *Uniaxial Constant Strain Amplitude Data for R = -1 only** | | | |
| Cyclic Strain Coefficient | $K'$ | 367 | MPa |
| Cyclic Strain Hardening exponent | $n'$ | 0.084 | |
| Fatigue Strength Coefficient | $\sigma'_f$ | 315 | MPa |
| Fatigue Strength Coefficient** | $\sigma'_f$ | 170 | MPa |
| Fatigue Ductility Coefficient | $\varepsilon'_f$ | 0.005 | |
| Fatigue Strength Exponent | b | -0.098 | |
| Fatigue Strength Exponent** | b | -0.051 | |
| Fatigue Ductility Exponent | c | -0.43 | |
| *Long-Crack Fatigue Crack Growth Data* | | | |
| Effective Threshold Stress Intensity Range | $\Delta K_{eff,tho}$ | 1.4 | $MPa\sqrt{m}$ |
| Threshold Stress Intensity Range | $\Delta K_{tho}$ | | |
| (R = -1) | | 6.5 | $MPa\sqrt{m}$ |
| (R = 0.1) | | 2.78 | $MPa\sqrt{m}$ |
| Crack Growth Constant for $da/dN \sim \Delta K_{eff}$ | $C'_i$ (i = 1,2) | | |
| (Stage I) | $C'_1$ | $1.747 \times 10^{-14}$ | m/cycle |
| (Stage II) | $C'_2$ | $1.320 \times 10^{-10}$ | m/cycle |
| Crack Growth Exponent for $da/dN \sim \Delta K_{eff}$ | $m_i$ (i = 1,2) | | |
| (Stage I) | $m_1$ | 16.7 | |
| (Stage II) | $m_2$ | 4.7 | |

* The strain-life data can be separated into elastic and plastic portion, and the strain-life relation is given by:

$$\varepsilon_a = \frac{\sigma'_f}{E}(2N)^b + \varepsilon'_f (2N)^c$$

where $\varepsilon_a$ is the strain amplitude and N is the fatigue cycles.

** Obtained by assuming that the fatigue-initiating-defect size equals zero. Data were analyzed in the long-life-regime S-2N diagram based on the Basquin-Morrow equation; see Appendix F.

TABLE 3

EXPERIMENTAL RESULTS AND PREDICTIONS BASED ON THE CCN MODEL FOR THE CAST ALUMINUM ALLOY 319

30 μm POLISHED SURFACE CONDITION (R = -1)

| Specimen | Smax (MPa) | $\sqrt{Area}$ (mm) | $N_T$ (Exp.) (Cycles) | Pred. $N_T$ (AR = 0.8) (Cycles) |
|---|---|---|---|---|
| B71 | 48.28 | 0.56 | >125,000,000 | 83,160,000 |
| B15 | 55.17 | 0.57 | >125,000,000 | 8,040,000 |
| B15 | 62.07 | 0.57 | 4,780,000 | 1,470,000 |
| B16 | 62.07 | 0.80 | 1,260,000 | 641,000 |
| B17 | 62.07 | * | 864,500 | ** |
| B18 | 62.07 | 0.97 | 920,000 | 542,000 |
| B91 | 62.07 | 0.23 | 64,000,000 | 54,790,000 |
| B92 | 62.07 | 0.52 | 9,380,000 | 2,042,000 |
| B93 | 62.07 | 0.34 | >125,000,000 | 10,940,000 |
| B71 | 68.97 | 0.57 | 752,700 | 632,000 |
| BA1 | 68.97 | 0.62 | 1,400,400 | 591,000 |
| BA2 | 68.97 | 0.30 | 2,470,000 | 3,240,000 |
| BA3 | 68.97 | 0.43 | 1,110,000 | 1,063,000 |
| BA4 | 68.97 | 0.36 | 1,570,000 | 1,760,000 |
| BA5 | 68.97 | 0.37 | 6,260,000 | 1,617,000 |
| BA6 | 68.97 | 0.46 | 1,510,000 | 905,600 |
| BA7 | 68.97 | * | 899,500 | ** |
| BA8 | 68.97 | 0.44 | 1,675,000 | 1,000,100 |
| BA9 | 68.97 | 0.60 | 1,675,000 | 604,500 |
| BB1 | 75.86 | 0.33 | 1,230,000 | 792,600 |
| BB2 | 75.86 | 0.48 | 640,000 | 542,300 |
| BB3 | 75.86 | 0.37 | 927,000 | 663,600 |
| BB4 | 75.86 | 0.51 | 445,800 | 523,000 |
| BB5 | 75.86 | 0.57 | 434,500 | 491,100 |
| BC1 | 82.76 | 0.50 | 431,300 | 429,800 |
| BC2 | 82.76 | 0.40 | 345,700 | 477,600 |
| BC3 | 82.76 | 0.63 | 152,900 | 385,200 |

* Not measured
** Life prediction is not available

TABLE 4

EXPERIMENTAL RESULTS AND PREDICTIONS BASED ON THE CCN MODEL FOR THE CAST ALUMINUM ALLOY 319

AS-CAST SURFACE CONDITION (R = -1)

| Specimen | Smax (MPa) | $\sqrt{Area}$ (mm) | Exp. $N_T$ (Cycles) | Pred. NT (AR = 0.8) (Cycles) |
|---|---|---|---|---|
| AC2 | 82.76 | 0.54 | 172,800 | 414,400 |
| AC3 | 75.86 | 0.78 | 375,100 | 410,600 |
| AC4 | 75.86 | 0.39 | 692,000 | 623,000 |
| AC5 | 68.97 | * | 787,700 | ** |
| AC6 | 68.97 | 0.29 | 5,825,700 | 3,657,000 |
| AC7 | 68.97 | 0.75 | 444,700 | 517,000 |
| AC8 | 62.07 | 0.60 | 1,240,000 | 1,252,000 |
| AC9 | 62.07 | 0.43 | 4,105,000 | 4,250,000 |
| AC10 | 62.07 | * | 2,393,000 | ** |
| AC11 | 62.07 | 0.36 | 7,710,000 | 8,670,000 |
| AC12 | 55.17 | 0.62 | 5,556,000 | 5,823,000 |
| AC13 | 55.17 | 0.60 | 6,801,000 | 6,296,000 |
| AC14 | 55.17 | 0.32 | >125,000,000 | 10,820,000 |

* Not measured
** Life prediction is not available

TABLE 5

EXPERIMENTAL RESULTS AND PREDICTIONS BASED ON THE CCN MODEL FOR THE CAST ALUMINUM ALLOY 319 (DATA SUPPLIED BY THE GENERAL MOTORS CORPORATION [74])

CYLINDRICAL SPECIMENS WITH AS-CAST SURFACE CONDITION (R = -1)

| Specimen (GM- ) | Smax (MPa) | $\sqrt{\text{Area}}$ (mm) | Exp. $N_T$ (Cycles) | Pred. $N_T$ (AR = 0.8) (Cycles) |
|---|---|---|---|---|
| GM-27 | 92.57 | * | 282,721 | ** |
| 49 | 93.17 | * | 256,037 | ** |
| 25 | 88.50 | * | 234,355 | ** |
| 4 | 90.21 | * | 222,298 | ** |
| 43 | 82.59 | * | 507,164 | ** |
| 21 | 80.99 | * | 859,379 | ** |
| 44 | 82.59 | * | 773,143 | ** |
| 2 | 79.95 | * | 622,582 | ** |
| 18 | 78.93 | * | 365,617 | ** |
| 41 | 71.26 | * | 1,379,416 | ** |
| 11 | 68.97 | * | 2,014,352 | ** |
| 17 | 67.66 | * | 1,559,544 | ** |
| 22 | 70.73 | * | 2,432,977 | ** |
| 5 | 67.66 | * | 2,451,080 | ** |
| 14 | 67.99 | * | 1,563,366 | ** |
| 1 | 68.43 | * | 2,318,836 | ** |
| 3 | 68.43 | * | 1,122,449 | ** |
| 24 | 68.43 | * | 820,052 | ** |
| 8 | 68.43 | * | 2,158,127 | ** |
| 35 | 66.51 | * | 2,091,827 | ** |
| 15 | 63.30 | * | 3,143,026 | ** |
| 46 | 63.72 | * | 2,238,296 | ** |
| 39 | 64.14 | * | 4,790,089 | ** |
| 19 | 63.72 | * | 4,444,017 | ** |
| 26 | 63.72 | * | 1,646,480 | ** |
| 42 | 63.72 | * | 2,548,092 | ** |
| 30 | 58.99 | * | 2,714,300 | ** |
| 6 | 51.32 | 1.28 | 1,897,830 | 654,100 |
| 32 | 57.86 | 0.73 | 1,661,064 | 1,371,000 |
| 31 | 56.63 | 0.89 | 4,827,898 | 868,000 |

* Not measured
** Life prediction is not available

TABLE 6

MATERIAL PROPERTIES USED IN THRESHOLD STRESS PREDICTIONS

| Material | R | $S_y$ (MPa) | $\Delta S_e$ (MPa) | $\Delta K_{tho}$ (MPa$\sqrt{m}$) | $U_{tho}$ | $S_u$ (MPa) |
|---|---|---|---|---|---|---|
| Steel SM41B [27,38] | -1.0 | 194 | 326 | 12.36 | 0.25 | 423 |
| | 0.0 | 194 | 274 | 8.36 | 0.366 | 423 |
| | 0.4 | 194 | 244 | 6.38 | 0.48 | 423 |
| Mild Steel [37,70] (0.15% C) | -1.0 | 340 | 420 | 12.8 | 0.24* | 448 |
| Al-2024-T351 [41,63] | -1.0 | 357 | 248 | 5.0 | 0.34 | 466 |
| Steel SAE 1045 [41,63] | -1.0 | 472 | 608 | 13.9 | 0.28 | 745 |
| Steel 15313 [39] | -1.0 | 380 | 440 | 12.0 | 0.32 | 530 |
| Steel G40.11 [64] | -1.0 | 376 | 570 | 15.9 | 0.20* | 504 |
| NiCr Steel [70,71] (EN 26) | -1.0 | 834 | 1000 | 12.8 | 0.24* | 973 |
| 18/8 Stainless [70,71] | -1.0 | 222 | 720 | 12.0 | 0.26* | 685 |
| AL-B.S. L 65 [7,71] | -1.0 | 433 | 300 | 4.2 | 0.34* | 494 |
| Cast Al-319 Alloy | -1.0 | 190 | 120 | 6.5 | 0.215* | 206 |
| [see Appendix G] | 0.1 | 190 | 84 | 2.78 | 0.504 | 206 |

* Assumed value based on the $\Delta K_{eff.tho} = \eta E$ (Eq. 2.10)

TABLE 7

COMPARISON OF EXPERIMENTAL RESULTS WITH PREDICTIONS FROM MODELS

(a) Case 1: Steel JIS SM41B [27,38]

CNP Specimens: W = 45 mm, D = 3.0 mm, R = -1 except marked data

Unit in 'MPa' for $\Delta S_{thn}$

| | ρ (mm) | $K_{tn}$ | Exp $\Delta S_{thn}$ | Predicted $\Delta S_{thn}$ from Models | | | | | | |
|---|---|---|---|---|---|---|---|---|---|---|
| | | | | CCN | PTS(I) | PTS(II) | Topper | Lukas | Sun(M) | Sun(O) |
| | 0.16 | 8.48 | 110 | 112 | 145 | 108 | 103 | 98 | 112 | 112 |
| | 0.39 | 5.72 | 120 | 105 | 128 | 101 | 103 | 103 | 105 | 105 |
| | 0.83 | 4.23 | 110 | 103 | 124 | 105 | 103 | 110 | 103 | 103 |
| | 3.00 | 2.60 | 148 | 125 | 144 | 136 | 125 | 142 | 125 | 125 |
| * | 0.16 | 8.48 | 73 | 75 | 99 | 91 | 73 | 69 | 75 | 75 |
| ** | 0.16 | 8.48 | 73 | 60 | 76 | 81 | 60 | 55 | - | - |

* R = 0
** R = 0.4
- Not available

(b) Case 2: Mild Steel (0.15% C) [37,70]

CNB Specimens: W = 43 mm, D = 5.08 mm, R = -1 for all data

Unit in 'MPa' for $\Delta S_{thn}$

| ρ (mm) | $K_{tn}$ | Exp $\Delta S_{thn}$ | Predicted $\Delta S_{thn}$ from Models | | | | | | |
|---|---|---|---|---|---|---|---|---|---|
| | | | CCN | PTS(I) | PTS(II) | Topper | Lukas | Sun(M) | Sun(O) |
| 0.05 | 14.0 | 118 | 114 | 196 | 170 | 91 | 105 | 131 | 131 |
| 0.10 | 10.0 | 104 | 114 | 171 | 149 | 91 | 108 | 131 | 131 |
| 0.13 | 9.0 | 116 | 114 | 161 | 141 | 91 | 107 | 131 | 131 |
| 0.25 | 6.6 | 118 | 113 | 149 | 132 | 91 | 115 | 130 | 130 |
| 0.64 | 4.4 | 118 | 112 | 146 | 135 | 91 | 131 | 130 | 130 |
| 1.27 | 3.3 | 132 | 127 | 160 | 152 | 127 | 153 | 127 | 127 |
| 5.08 | 1.9 | 208 | 220 | 231 | 229 | 220 | 233 | 220 | 220 |

(Table 7 Cont'd)

(c) Case 3: Mild Steel (0.15% C) [37,70]

DENP Specimens: W = 64 mm, D = 5.08 mm, R = -1 for all data

Unit in 'MPa' for $\Delta S_{thn}$

| ρ | $K_{tn}$ | Exp | Predicted $\Delta S_{thn}$ from Models | | | | | | |
|---|---|---|---|---|---|---|---|---|---|
| (mm) | | $\Delta S_{thn}$ | CCN | PTS(I) | PTS(II) | Topper | Lukas | Sun(M) | Sun(O) |
| 0.10 | 12.5 | 100 | 92 | 147 | 126 | 91 | 87 | 107 | 107 |
| 0.25 | 8.2 | 108 | 92 | 125 | 110 | 91 | 93 | 108 | 108 |
| 0.50 | 6.1 | 100 | 91 | 120 | 109 | 91 | 100 | 108 | 108 |
| 1.27 | 4.0 | 124 | 105 | 134 | 127 | 91 | 126 | 105 | 105 |
| 7.62 | 2.1 | 186 | 200 | 207 | 205 | 91 | 207 | 200 | 200 |

(d) Case 4: Al-2024-T351 [41]

CNP Specimens: W = 45 mm, D = ρ, R = -1 for all data

Unit in 'MPa' for $\Delta S_{thn}$

| ρ | $K_{tn}$ | Exp | Predicted $\Delta S_{thn}$ from Models | | | | | | |
|---|---|---|---|---|---|---|---|---|---|
| (mm) | | $\Delta S_{thn}$ | CCN | PTS(I) | PTS(II) | Topper | Lukas | Sun(M) | Sun(O) |
| 0.12 | 3.00 | 160 | 180 | 147 | 166 | 142 | 144 | 196 | 241 |
| 0.25 | 2.96 | 124 | 138 | 122 | 138 | 116 | 118 | 145 | 198 |
| 0.50 | 2.94 | 124 | 106 | 106 | 117 | 94 | 103 | 108 | 165 |
| 1.50 | 2.82 | 90 | 89 | 96 | 101 | 89 | 95 | 89 | 124 |

(e) Case 5: Steel SAE 1045 [41]

CNP Specimens: W = 45 mm, D = ρ, R = -1 for all data

Unit in 'MPa' for $\Delta S_{thn}$

| ρ | $K_{tn}$ | Exp | Predicted $\Delta S_{thn}$ from Models | | | | | | |
|---|---|---|---|---|---|---|---|---|---|
| (mm) | | $\Delta S_{thn}$ | CCN | PTS(I) | PTS(II) | Topper | Lukas | Sun(M) | Sun(O) |
| 0.12 | 3.00 | 360 | 357 | 384 | 326 | 368 | 387 | 392 | 392 |
| 0.25 | 2.96 | 310 | 290 | 320 | 276 | 305 | 309 | 309 | 309 |
| 0.50 | 2.94 | 276 | 235 | 273 | 245 | 249 | 264 | 247 | 247 |
| 1.50 | 2.82 | 248 | 217 | 241 | 229 | 217 | 237 | 217 | 217 |

(Table 7 Cont'd)

(f) Case 6: Al-Alloy BS L65 [7,71]

CNB Specimens: W = 43 mm, D = 5.08 mm, R = -1 for all data

Unit in 'MPa' for $\Delta S_{thn}$

| ρ (mm) | $K_{tn}$ | Exp $\Delta S_{thn}$ | Predicted $\Delta S_{thn}$ from Models | | | | | | |
|---|---|---|---|---|---|---|---|---|---|
| | | | CCN | PTS(I) | PTS(II) | Topper | Lukas | Sun(M) | Sun(O) |
| 0.013 | 27.00 | 80 | 50 | 80 | 151 | 34 | 35 | 50 | 128 |
| 0.051 | 14.00 | 77 | 50 | 58 | 109 | 34 | 39 | 50 | 128 |
| 0.102 | 10.00 | 46 | 50 | 56 | 96 | 34 | 44 | 50 | 128 |
| 0.203 | 7.30 | 46 | 50 | 59 | 88 | 34 | 52 | 50 | 128 |
| 0.508 | 4.85 | 62 | 50 | 72 | 90 | 62 | 69 | 50 | 128 |
| 1.270 | 3.30 | 93 | 91 | 160 | 163 | 91 | 95 | 91 | 122 |

(g) Case 7: Steel 15313 (2.25 Cr-1 Mo) [39]

CNB Specimens: W = 5 mm, D = ρ, R = -1 for all data

Unit in 'MPa' for $\Delta S_{thn}$

| ρ (mm) | $K_{tn}$ | Exp $\Delta S_{thn}$ | Predicted $\Delta S_{thn}$ from Models | | | | | | |
|---|---|---|---|---|---|---|---|---|---|
| | | | CCN | PTS(I) | PTS(II) | Topper | Lukas | Sun(M) | Sun(O) |
| 0.03 | 2.99 | 440 | 440 | 388 | 371 | 363 | 440 | 440 | 440 |
| 0.05 | 2.95 | 420 | 440 | 364 | 342 | 338 | 440 | 440 | 440 |
| 0.07 | 2.92 | 340 | 344 | 345 | 320 | 320 | 411 | 412 | 412 |
| 0.20 | 2.68 | 280 | 275 | 285 | 261 | 257 | 296 | 329 | 329 |
| 0.40 | 2.34 | 296 | 254 | 265 | 247 | 214 | 274 | 310 | 310 |
| 0.76 | 1.87 | 320 | 275 | 281 | 270 | 235 | 297 | 354 | 354 |

(h) Case 8: Steel G40.11 [40]

CNP Specimens: W = 70 mm, D = ρ, R = -1 for all data

Unit in 'MPa' for $\Delta S_{thn}$

| ρ (mm) | $K_{tn}$ | Exp $\Delta S_{thn}$ | Predicted $\Delta S_{thn}$ from Models | | | | | | |
|---|---|---|---|---|---|---|---|---|---|
| | | | CCN | PTS(I) | PTS(II) | Topper | Lukas | Sun(M) | Sun(O) |
| 0.20 | 2.98 | 338 | 303 | 351 | 323 | 336 | 351 | 269 | 269 |
| 0.48 | 2.96 | 242 | 241 | 281 | 262 | 267 | 271 | 201 | 201 |
| 4.80 | 2.59 | 238 | 220 | 232 | 229 | 220 | 231 | 220 | 220 |

(Table 7 Cont'd)

(i) Case 9: Stainless Steel AISI 304 [70]

CNB Specimens: W = 43 mm, D = 5.08 mm, R = -1 for all data

Unit in 'MPa' for $\Delta S_{thn}$

| ρ (mm) | $K_{tn}$ | Exp $\Delta S_{thn}$ | Predicted $\Delta S_{thn}$ from Models | | | | | | |
|---|---|---|---|---|---|---|---|---|---|
| | | | CCN | PTS(I) | PTS(II) | Topper | Lukas | Sun(M) | Sun(O) |
| 0.05 | 14.0 | 124 | 113 | 173 | 190 | 94 | 108 | 128 | 128 |

(j) Case 10: NiCr Steel (EN 26) [70,71]

CNP Specimens: R = -1 for all data, Unit in 'MPa' for $\Delta S_{thn}$

| W (mm) | D (mm) | ρ (mm) | $K_{tn}$ | Exp. $\Delta S_{thn}$ | Predicted $\Delta S_{thn}$ from Models | | | | | | |
|---|---|---|---|---|---|---|---|---|---|---|---|
| | | | | | CCN | PTS(I) | PTS(II) | Topper | Lukas | Sun(M) | Sun(O) |
| 43.0 | 5.08 | 0.05 | 14.0 | 116 | 122 | 179 | 185 | 103 | 123 | 117 | 117 |
| 31.8 | 5.08 | 0.13 | 8.0 | 142 | 139 | 197 | 201 | 103 | 167 | 132 | 132 |
| 22.6 | 0.508 | 0.13 | 4.6 | 247 | 238 | 323 | 329 | 271 | 290 | 257 | 257 |

## FIGURES

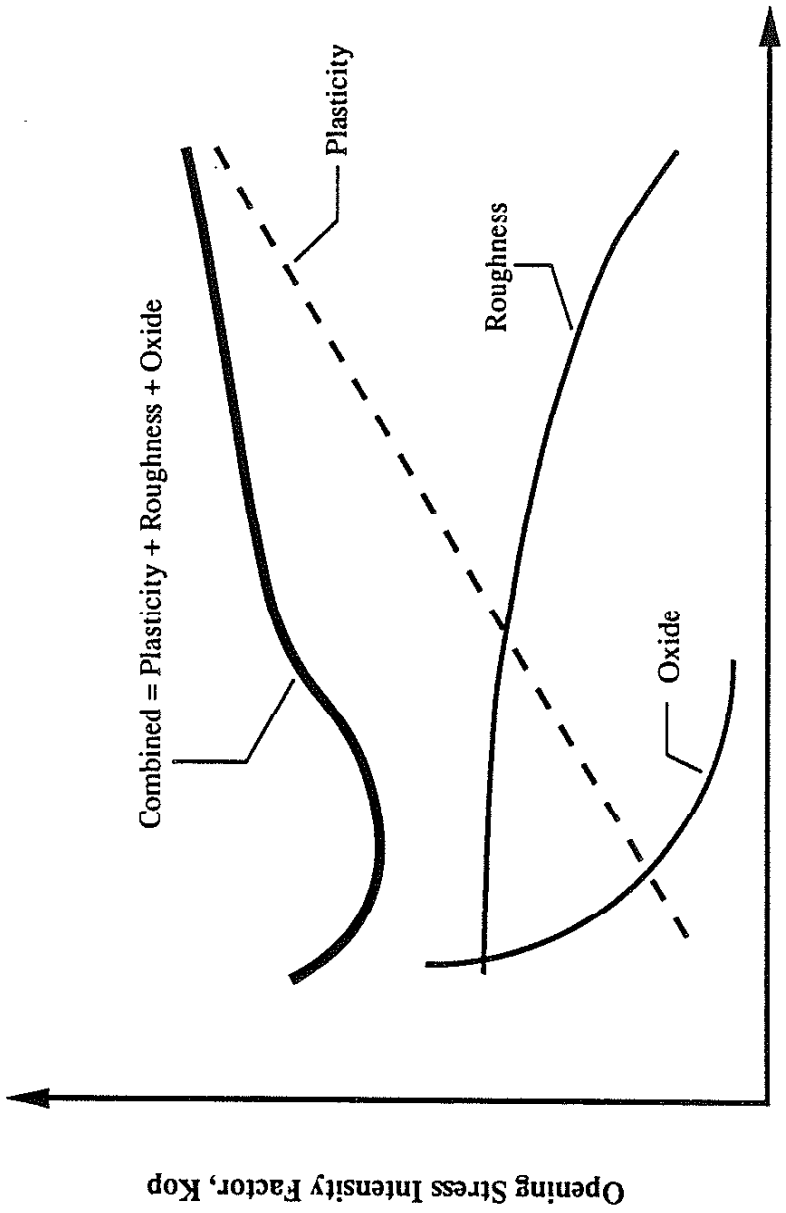


Figure 1 The influence of $K_{max}$ on the crack closure for the three crack closure mechanisms and their combined influence (after Ref. 10)

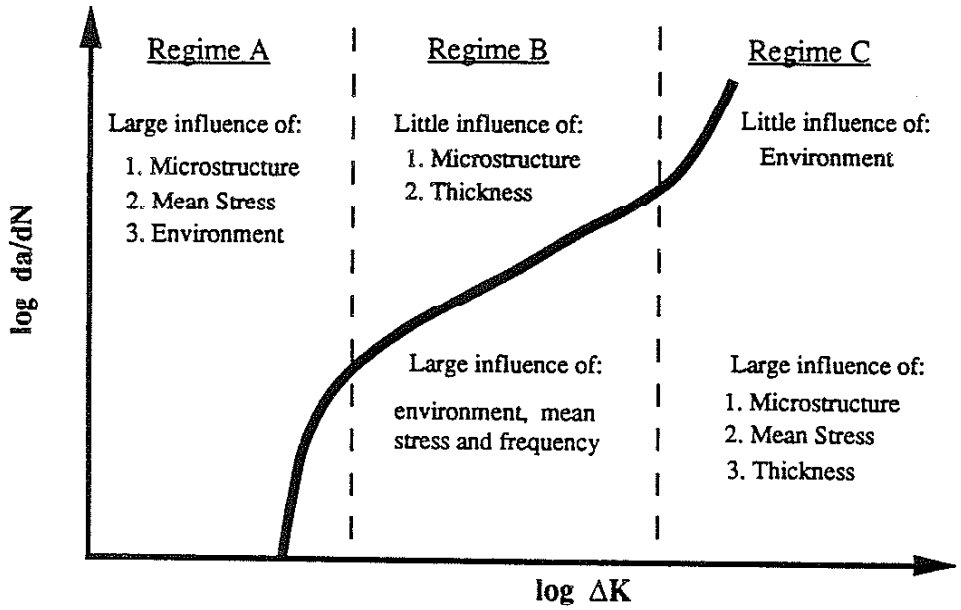


| Regime | Near-Threshold | Mid-Growth Rate | High-Growth rate |
|---|---|---|---|
| Terminology | Stage I | Stage II | — |
| Mechanism | Single Shear | Alternating or Simultaneous Shear on Two Slip Systems (Striation Growth) | Additional Static Modes |
| Crack Tip Displacement | Mode II + I | Mode I | Mode I |
| Nature of Fracture Surfaces | Serrated or Faceted | Planar (Striations) | Additional Cleavage, Intergranular or, Microvoid Coalescence |
| Closure Level | High $(\frac{Kcl}{Kmax} \geq 0.5)$ | Low $(\frac{Kcl}{Kmax} \leq 0.2)$ | — |
| Occurrence | Plastic Zone Size ≤ Grain Size | Plastic Zone Size ≥ Grain Size | Plastic Zone Size >> Grain Size |

Figure 2 Schematic illustration of the three regimes of fatigue crack propagation behavior and their corresponding mechanisms and characteristics (after Ref. 13).

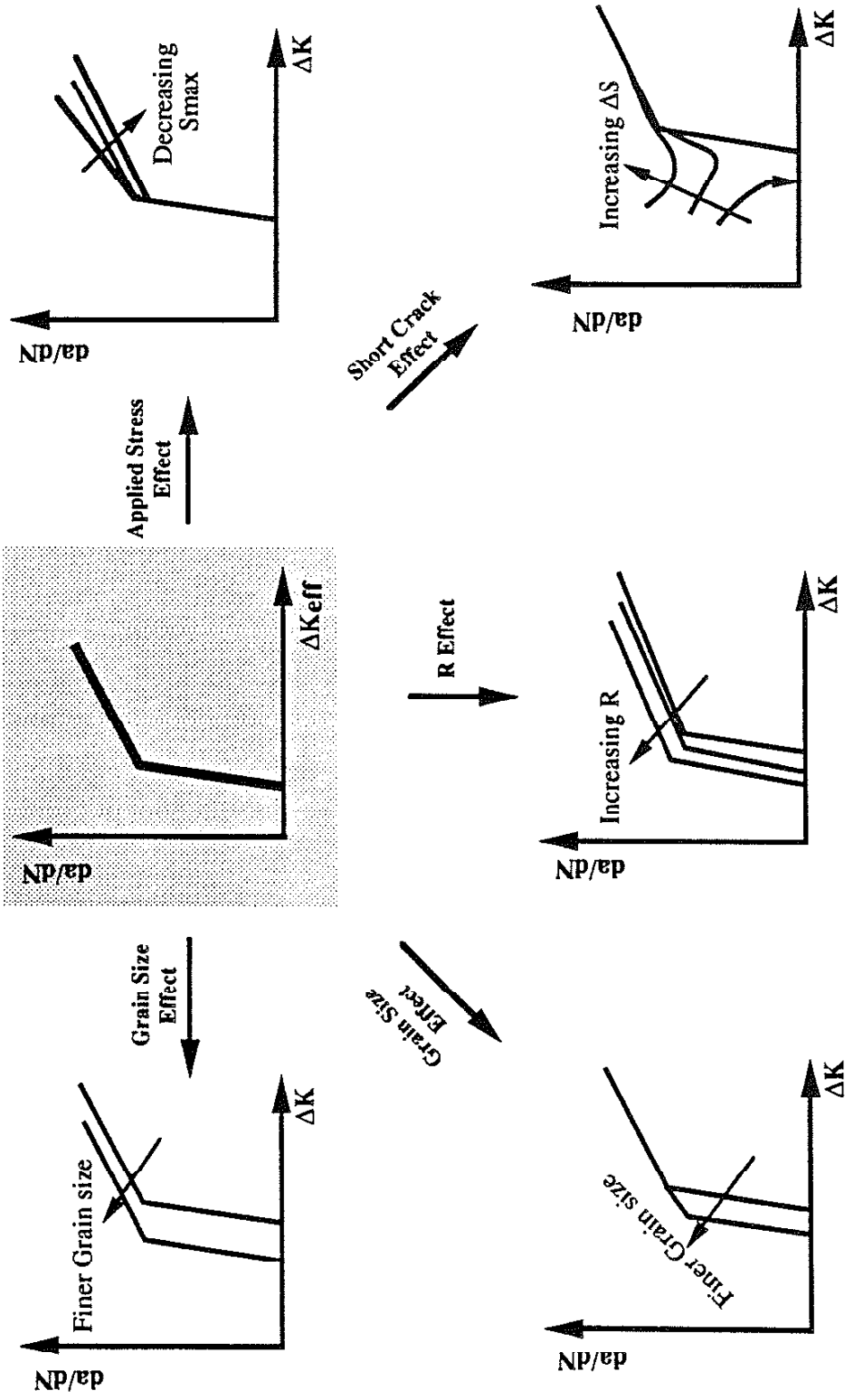


Figure 3 Schematic illustration of the relation between da/dN and $\Delta K_{eff}$ and the variations of the relationship between da/dN and ΔK with grain size, applied stress, load ratio and short crack behavior.

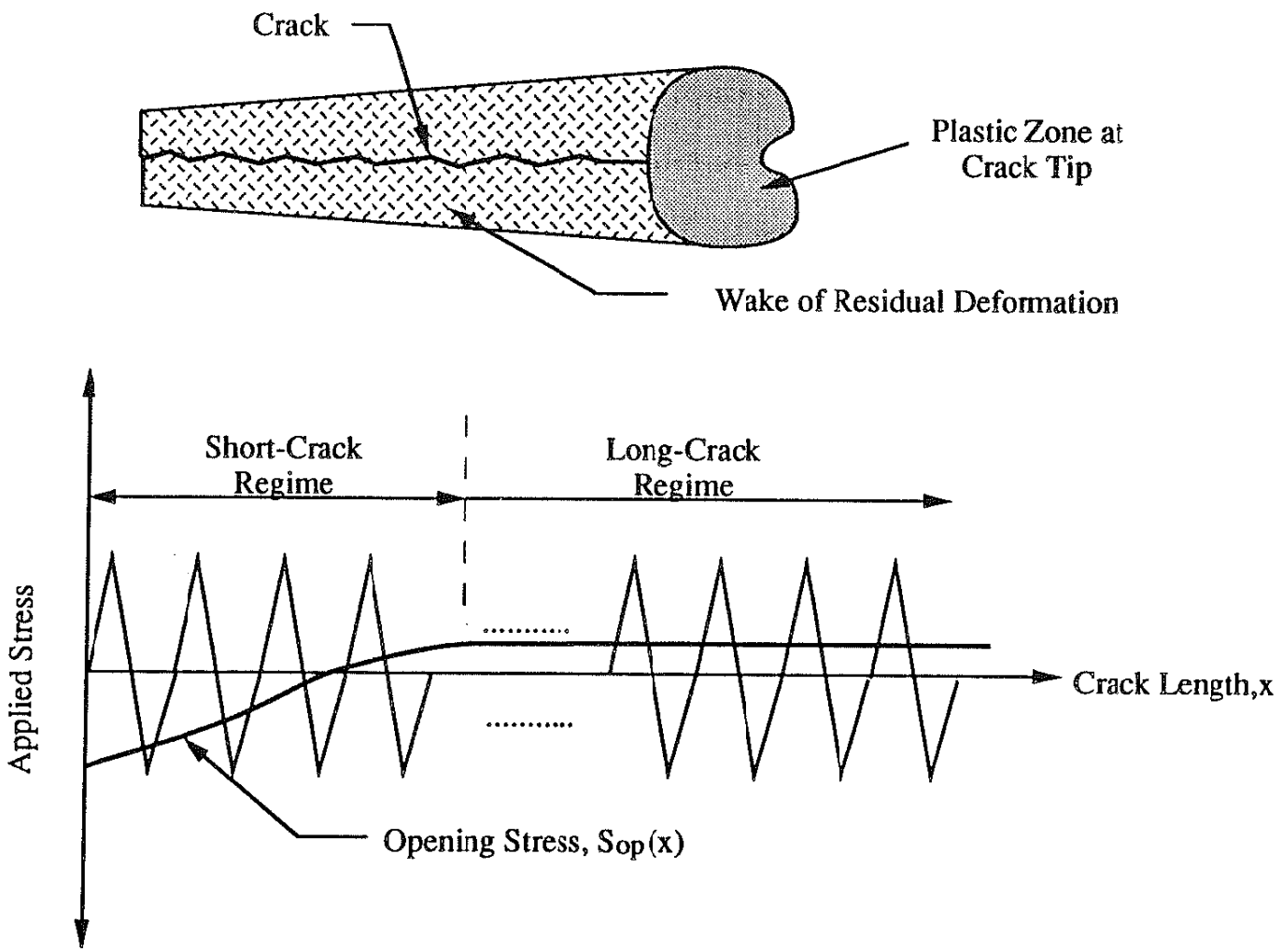


Figure 4 The variation of opening stress with crack length (A schematic diagram).

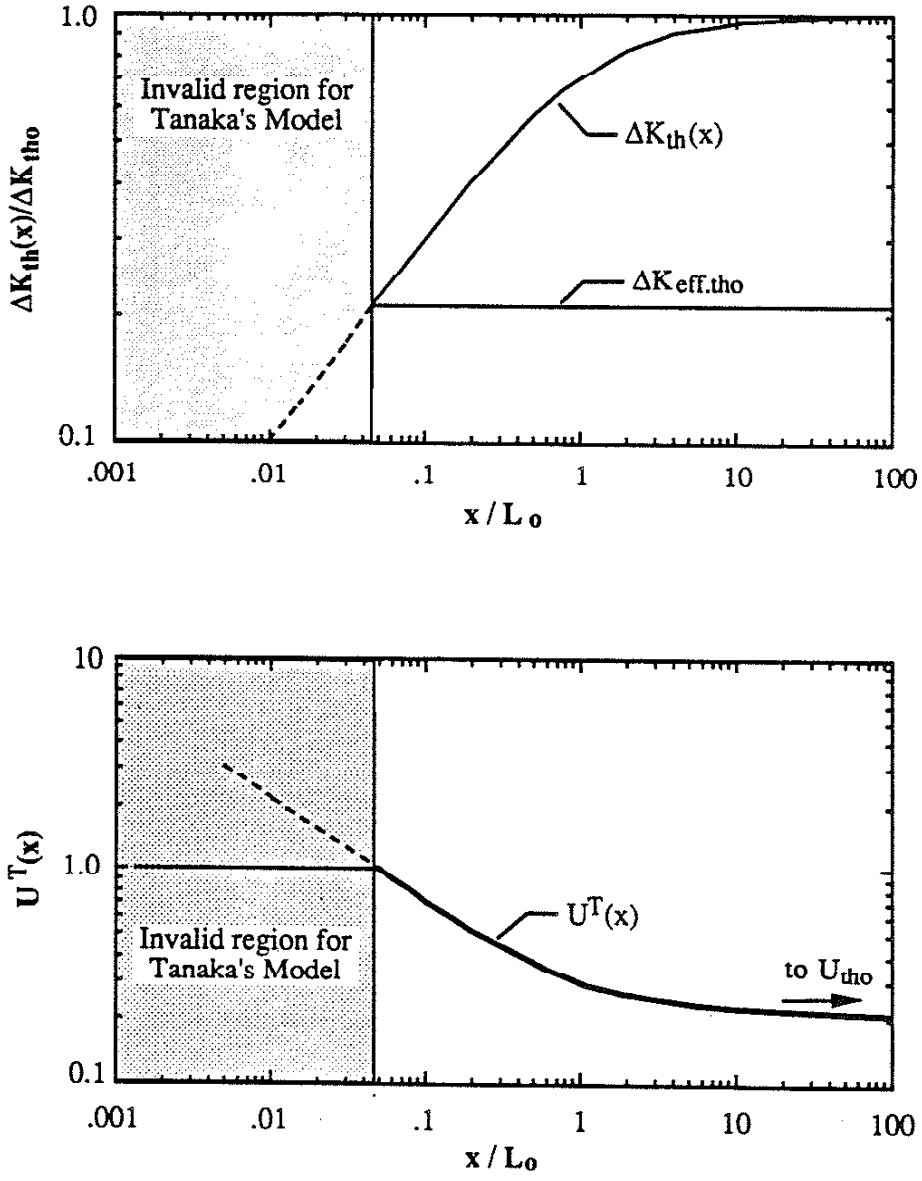


Figure 5 The functions of $\Delta K_{th}(x)$ and $U^T(x)$ from Tanaka's model [35]. In the very short crack region, Tanaka's model must be invalid since $U^T(x)$ becomes larger than 1. (A schematic diagram).

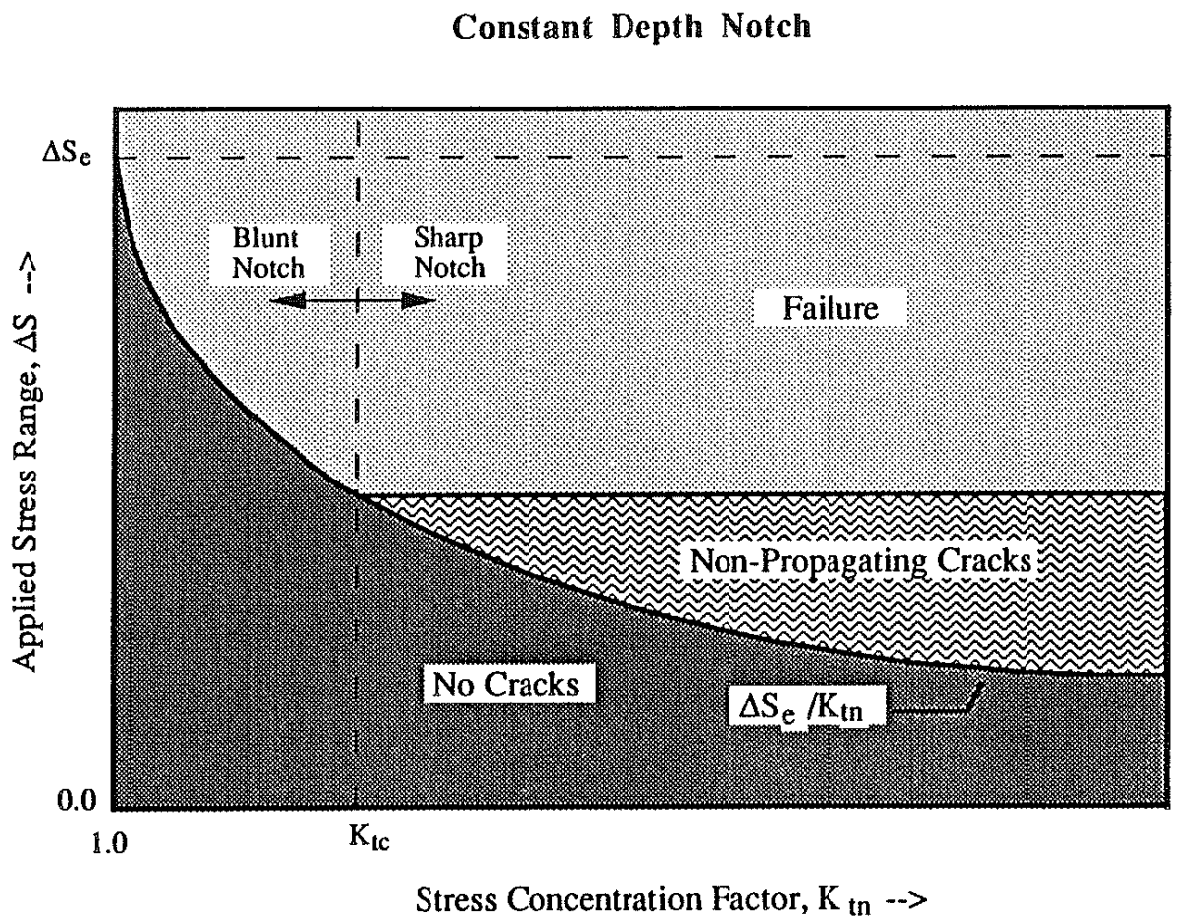


Figure 6 The fatigue behavior of a notched component as a function of stress concentration factor (net section) [37].

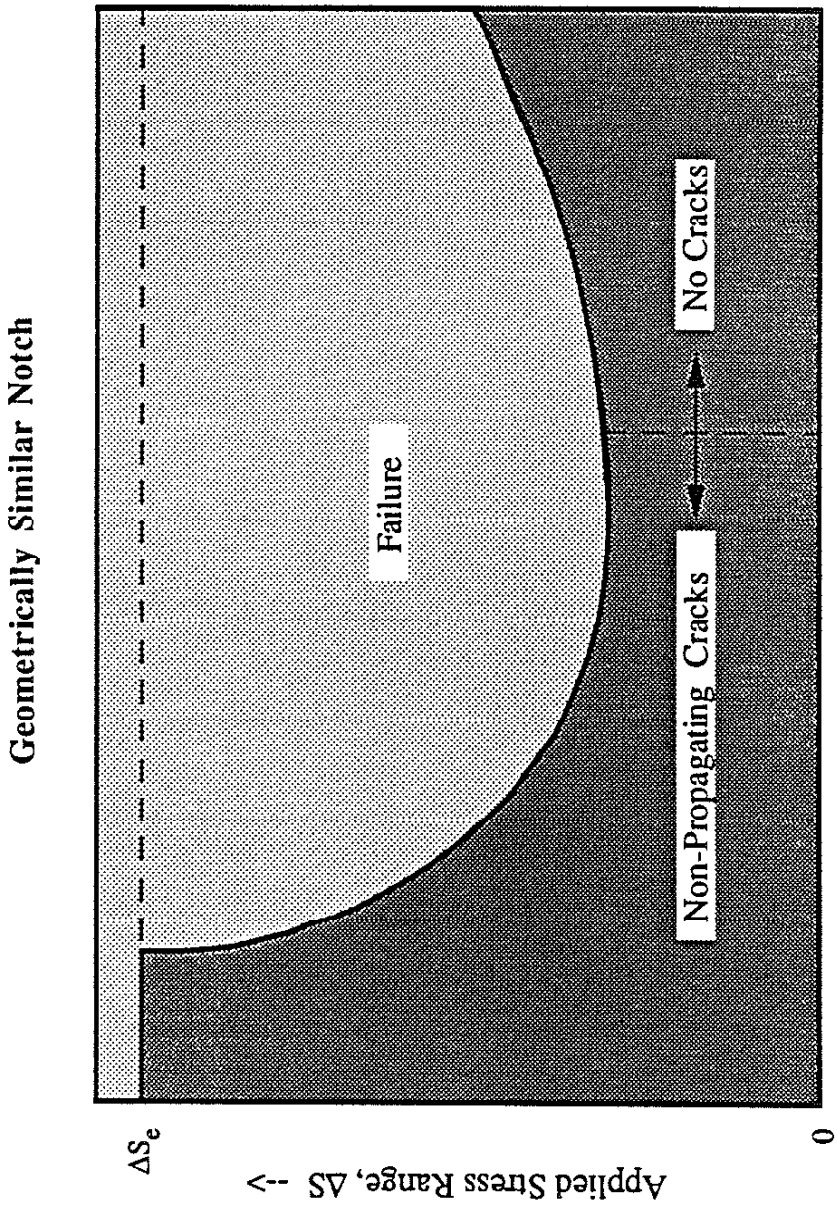


Figure 7 The fatigue behavior of a notched component as a function of notch depth for notches with constant $K_t$ values [39].

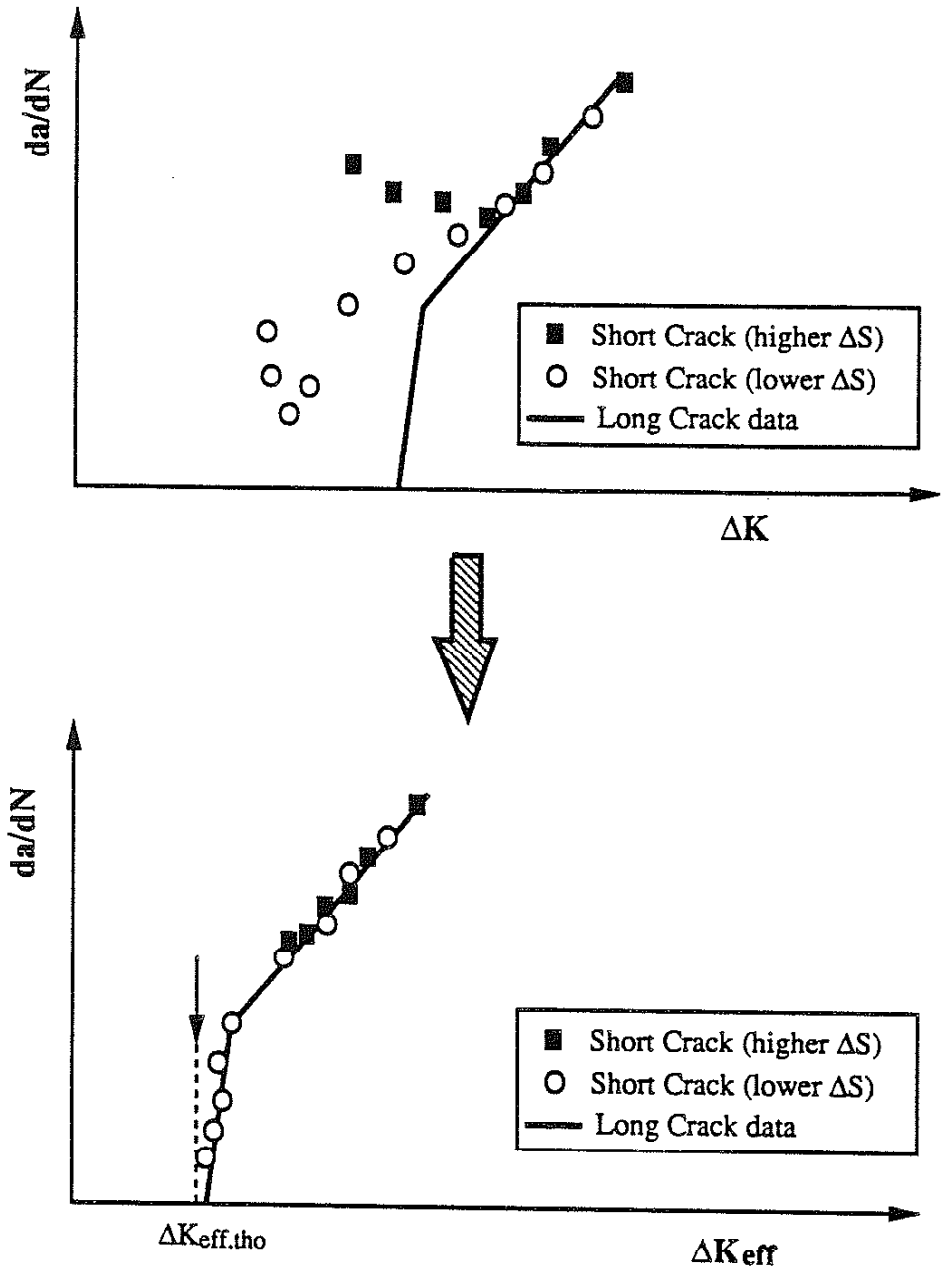


Figure 8 The relationship between da/dN and $\Delta K_{eff}$ is a unique material property with which the anomalous crack growth behavior of short cracks emanating from a notch can be rationalized. (A schematic diagram).

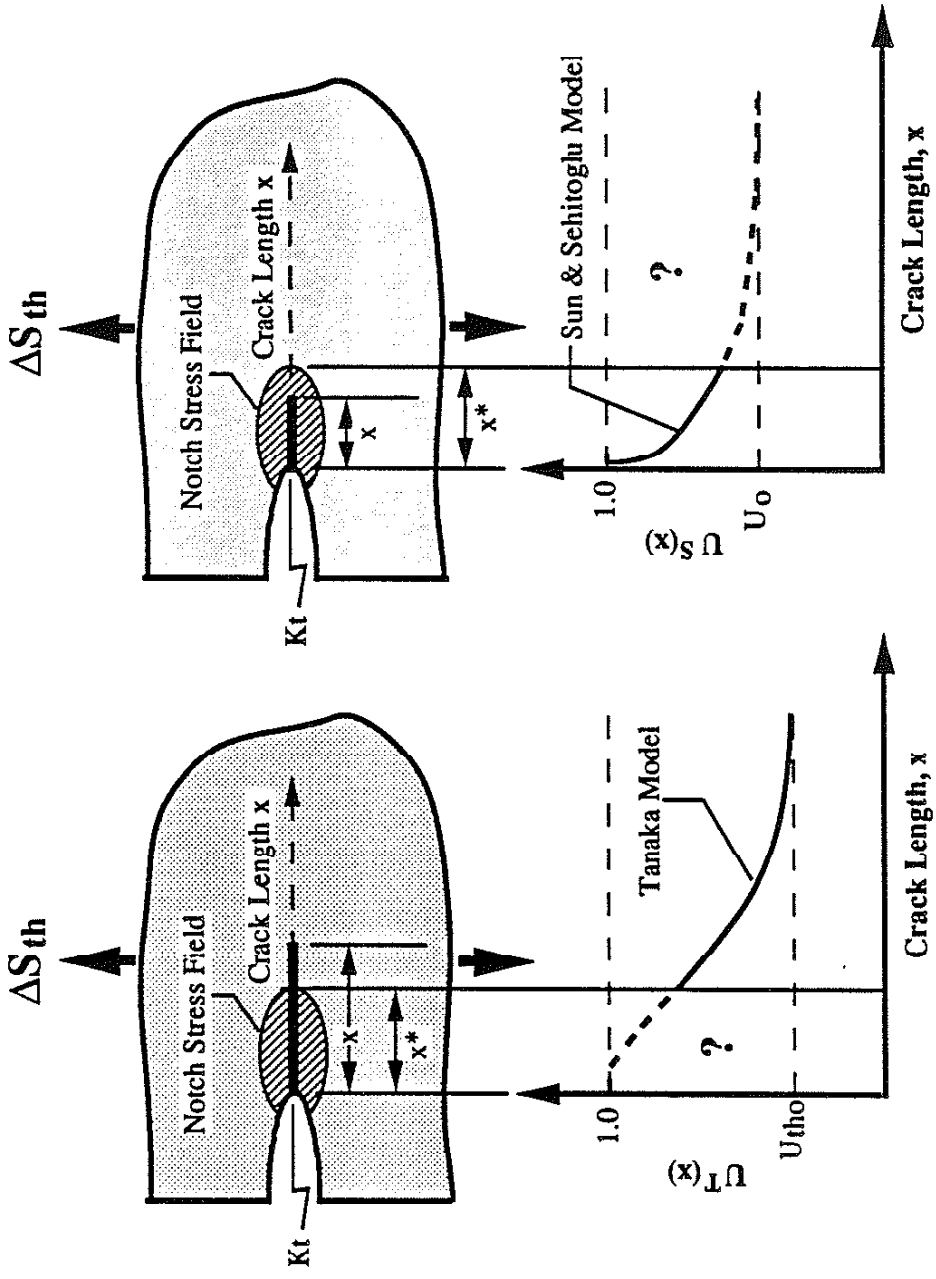


Figure 9 Comparison of Tanaka's and Sun and Sehitoglu's models. Tanaka's model (Left) is applicable when the crack is beyond the notch stress field. Sun and Sehitoglu's model (Right) is applicable when the crack is within the notch stress field.

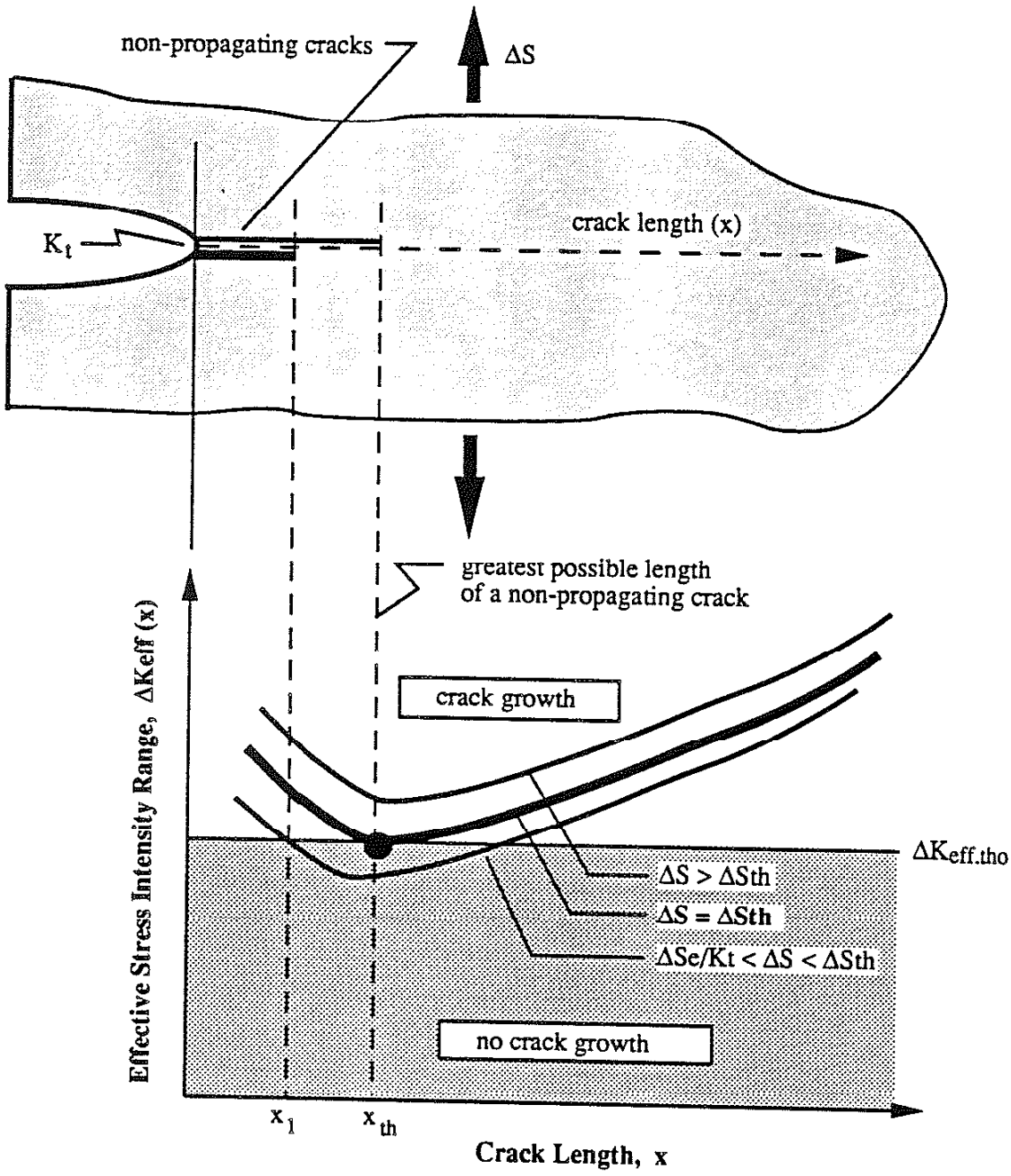


Figure 10 The variation of $\Delta K_{eff}(x)$ with crack length (x) as a function of applied stress range ($\Delta S$). Threshold stress range was determined when the minimum value of $\Delta K_{eff}(x)$ equals $\Delta K_{eff.tho}$.

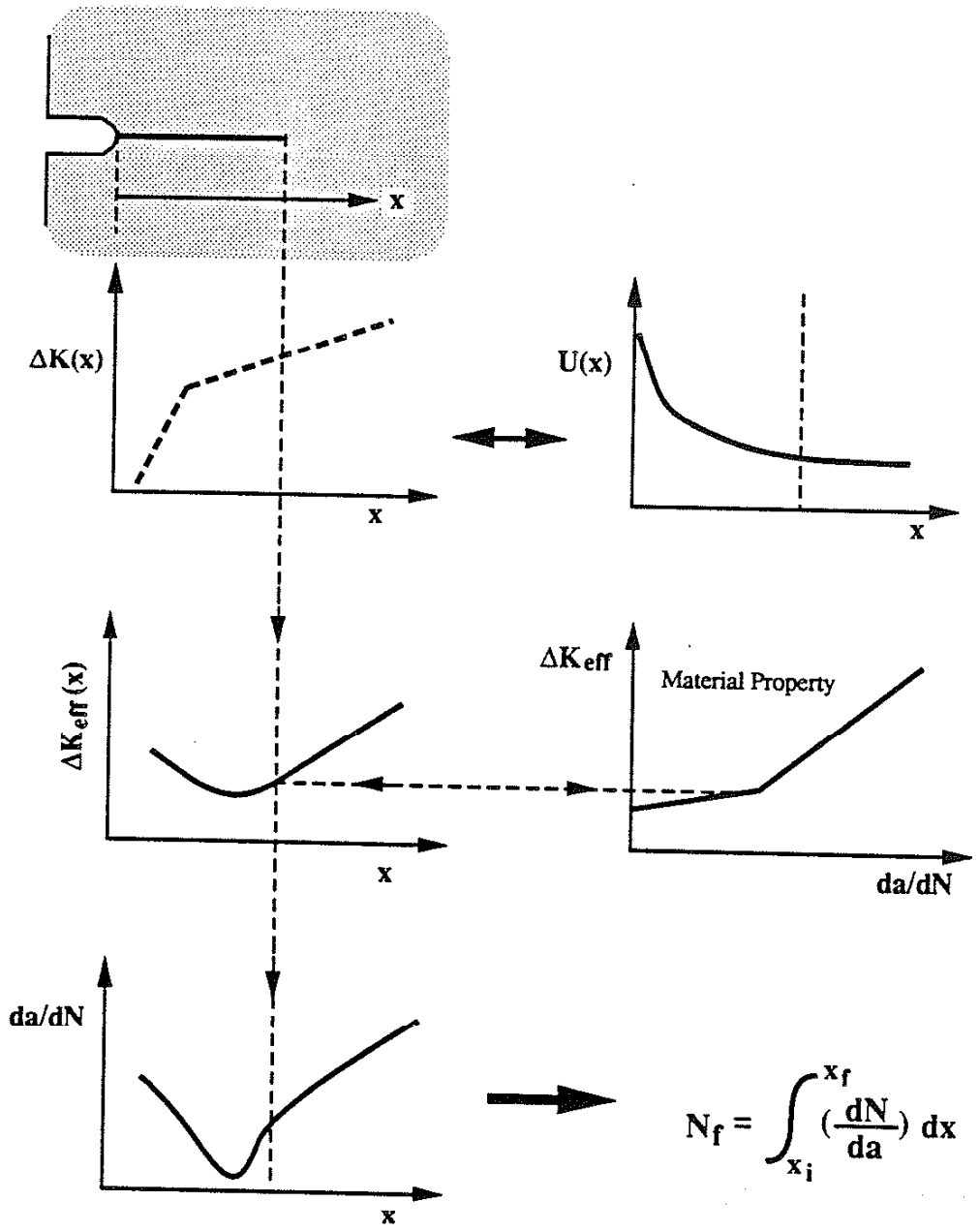


Figure 11 The general concept for estimating fatigue life ($N_f$) for a notched component using the CCN model.

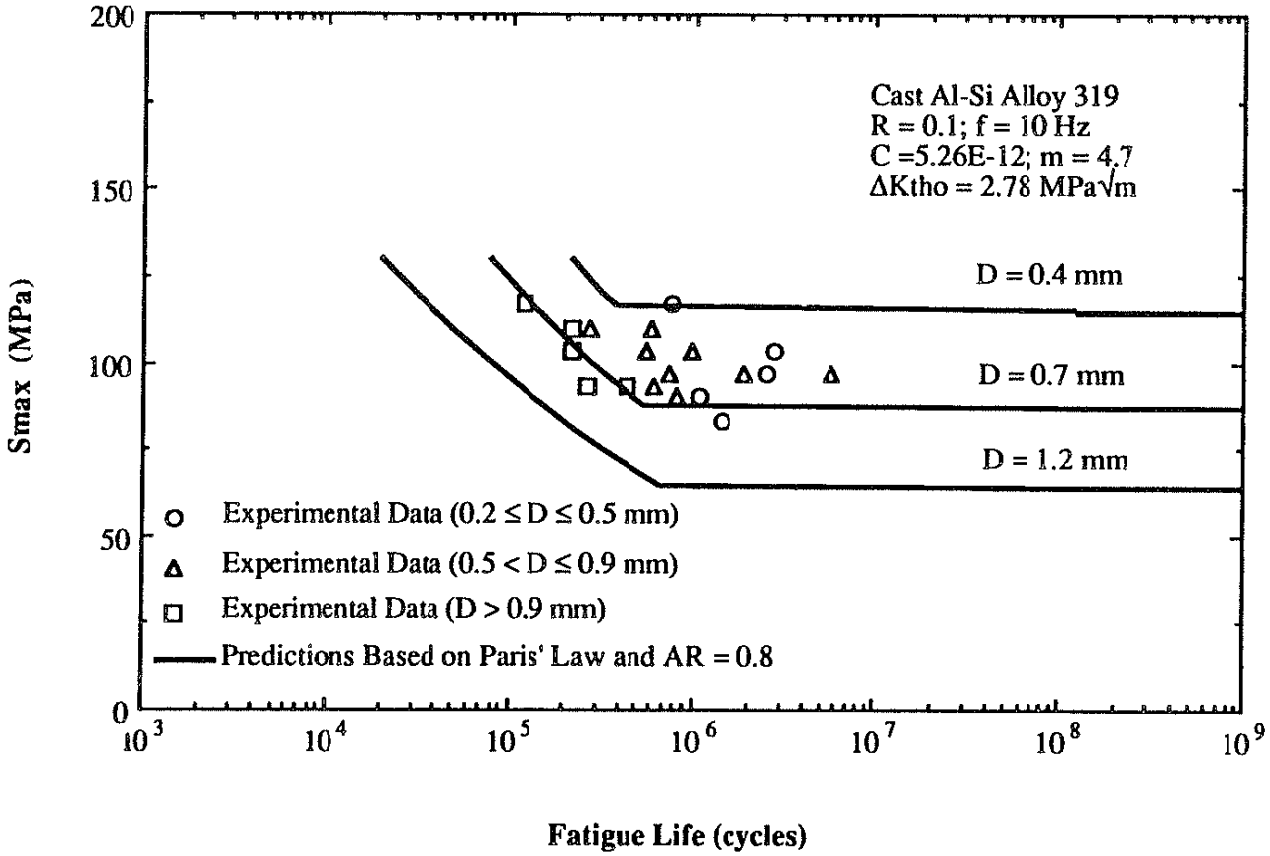


Figure 12 S-N test results (R = 0.1) from Siljander [47] are compared with the predictions based on simple LEFM model. Experimental data (points) are shown by three groups of defect depth (D), and predictions from three values of defect depth are shown by solid lines.

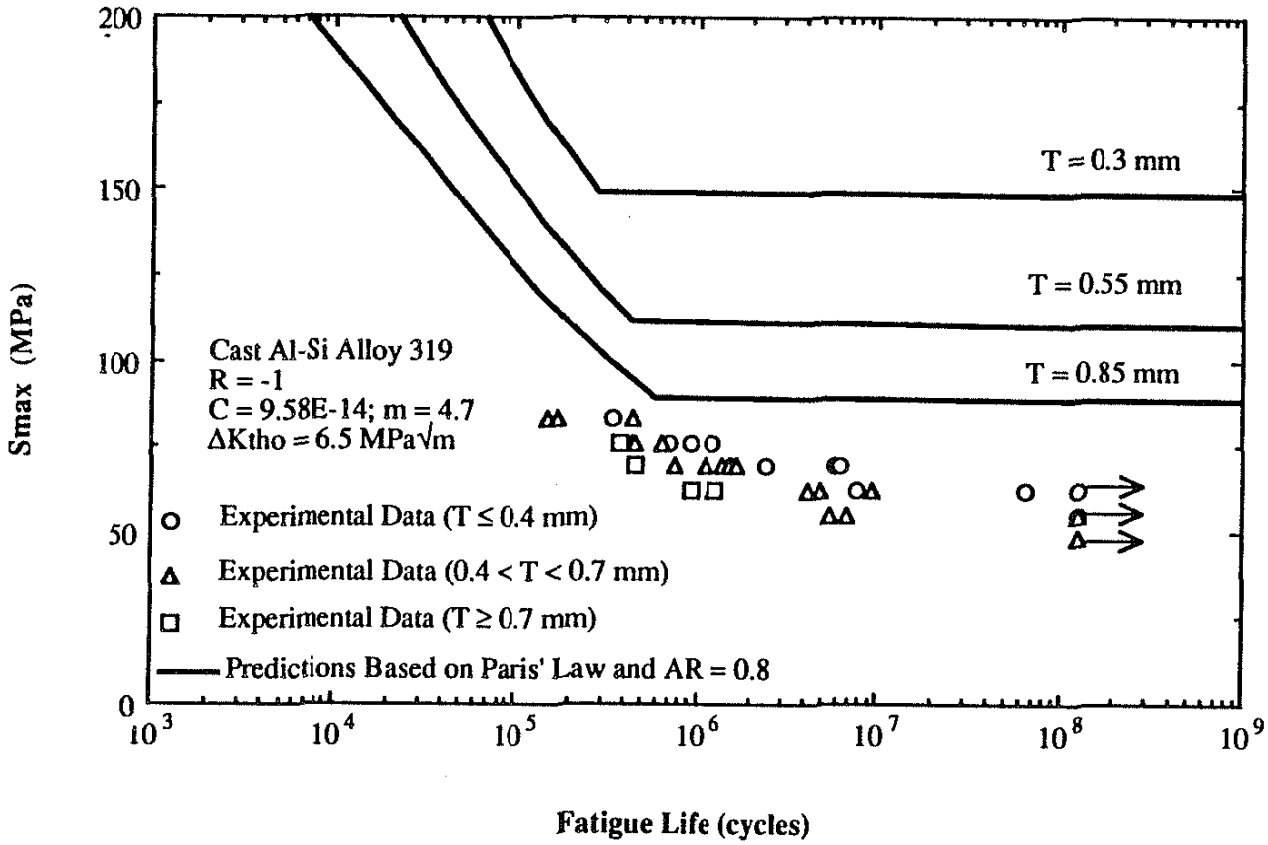


Figure 13 S-N test results (R = -1) from this study are compared with the predictions based on simple LEFM model. Experimental data (points) are shown by three groups of defect size (T), and predictions from three values of defect size are shown by solid lines.

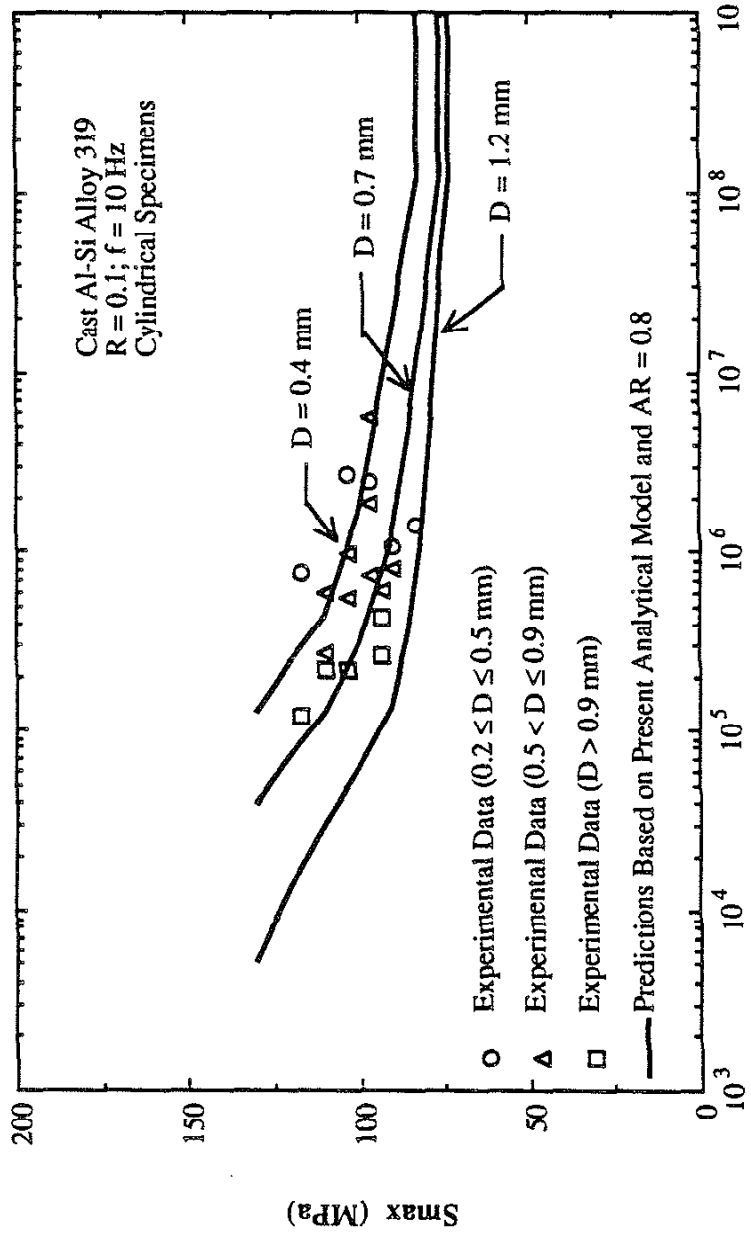


Figure 14 S-N test results (R = 0.1) from Siljander [47] are compared with the predictions based on the CCN model. Experimental data (points) are shown by three groups of defect depth (D), and predictions from three values of defect depth are shown by solid lines.

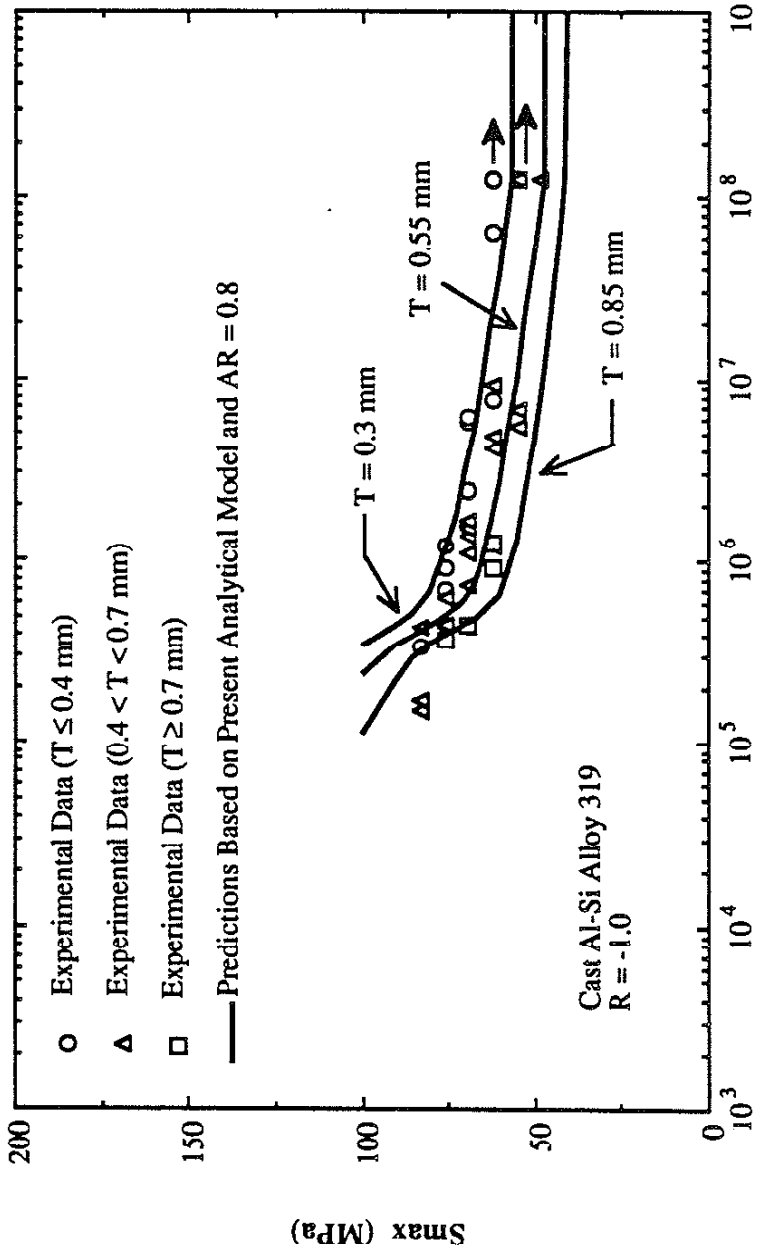


Figure 15 S-N test results (R = -1) from this study are compared with the predictions based on the CCN model. Experimental data (points) are shown by three groups of defect size (T), and predictions from three values of defect size are shown by solid lines.

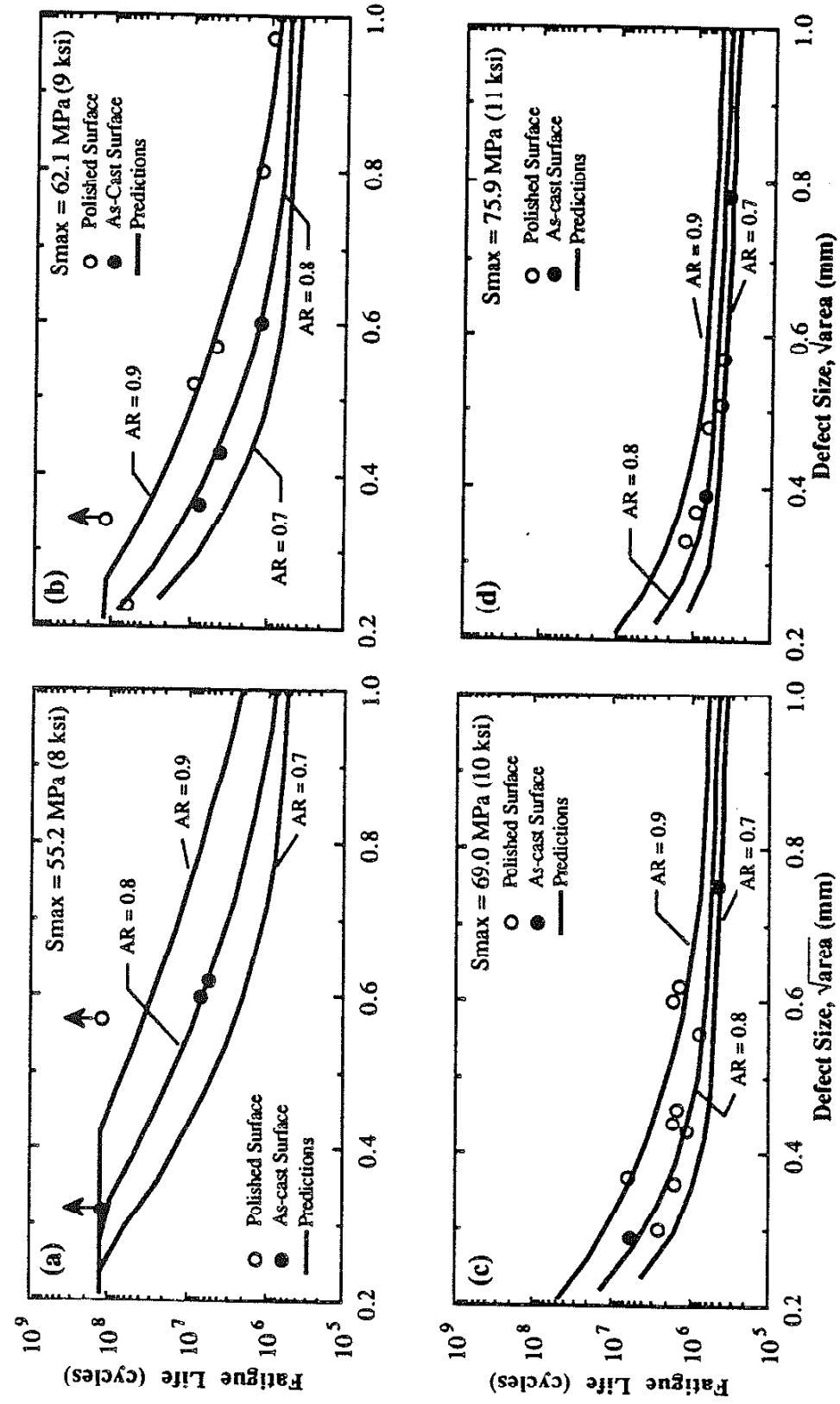


Figure 16 Comparison of experimental data with predictions from the CCN model at a given applied stress. Cast aluminum alloy 319 cylindrical specimens were tested at R = -1. (a) Smax = 55.2 MPa, (b) Smax = 62.1 MPa, (c) Smax = 69.0 MPa, and (d) Smax = 75.9 MPa.

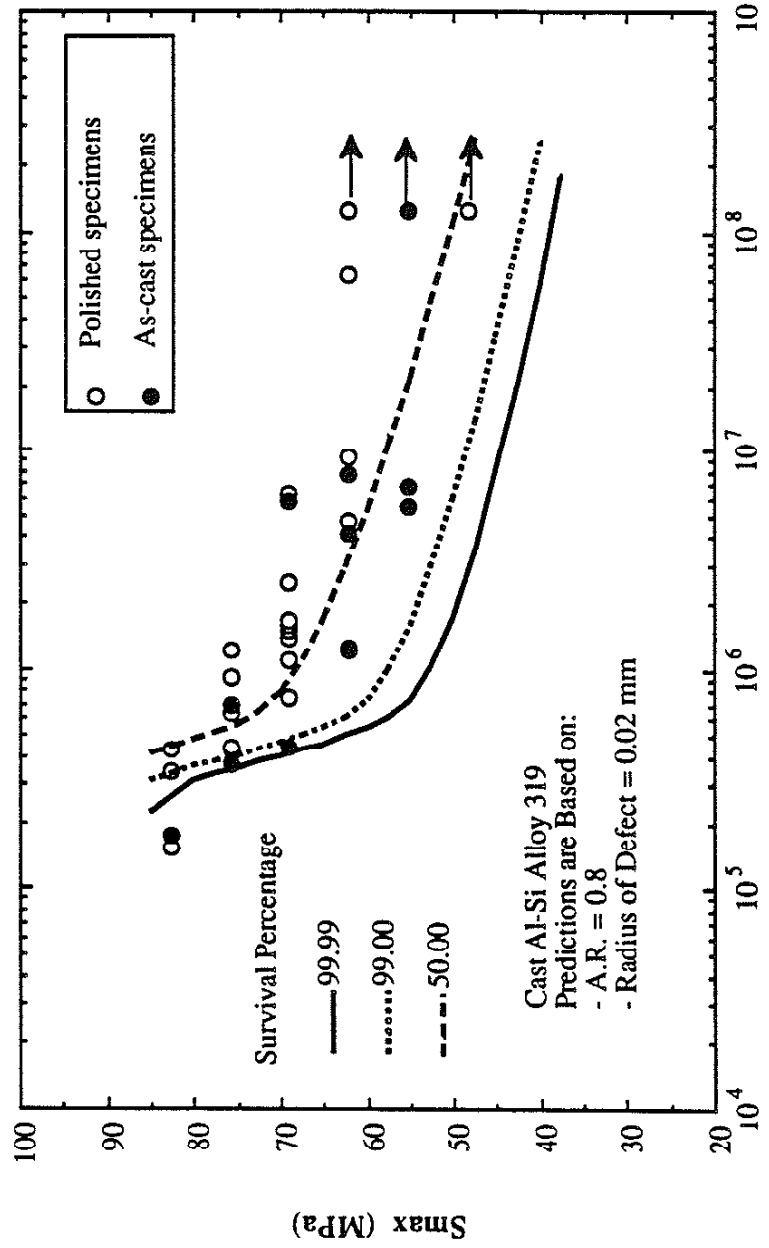


Figure 17 Comparison of the experimental data with three survival levels of predictions based on the CCN model. The test data were obtained in this study.

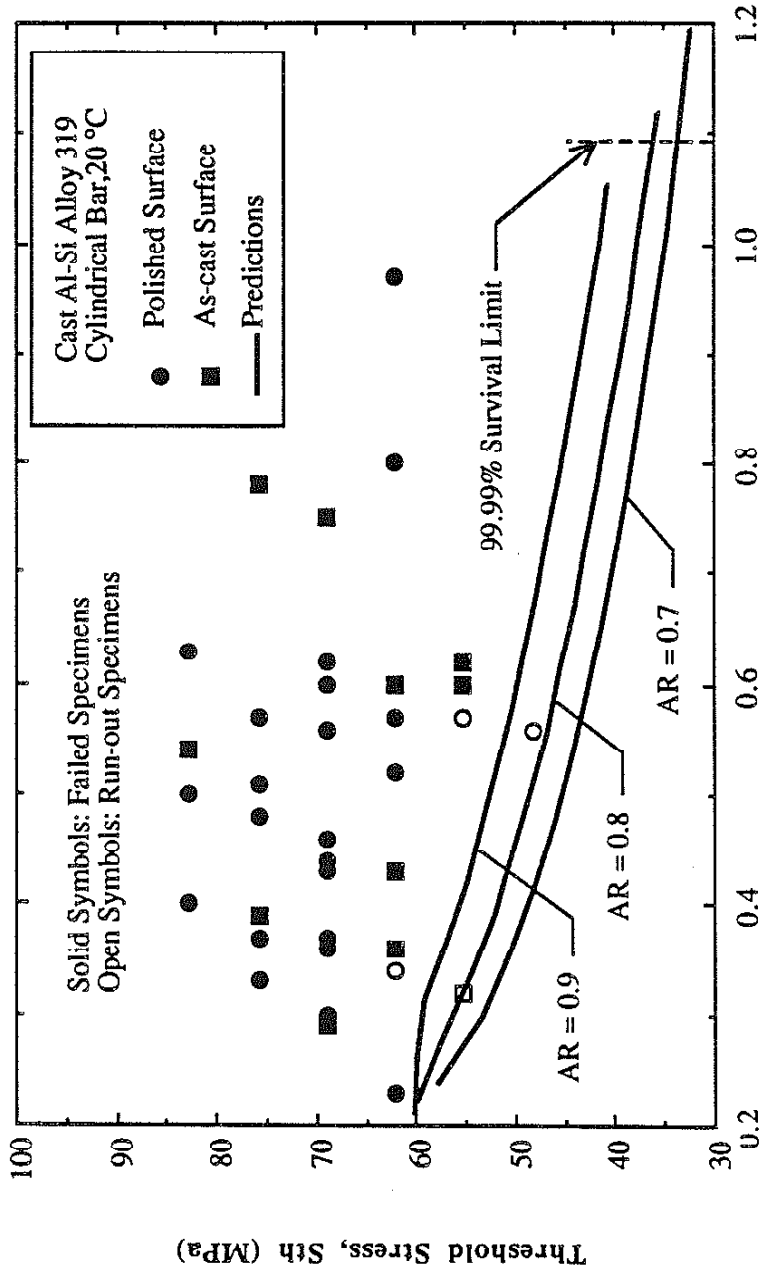


Figure 18 Comparison of experimental data with predictions of threshold stresses from CCN model. Solid symbol are broken specimens and open symbols are run-out test data ($1.25 \times 10^8$). Predictions are based on three values of aspect ratios (AR). The 99.99% survival limit is defined by defect size = 1.09 mm.

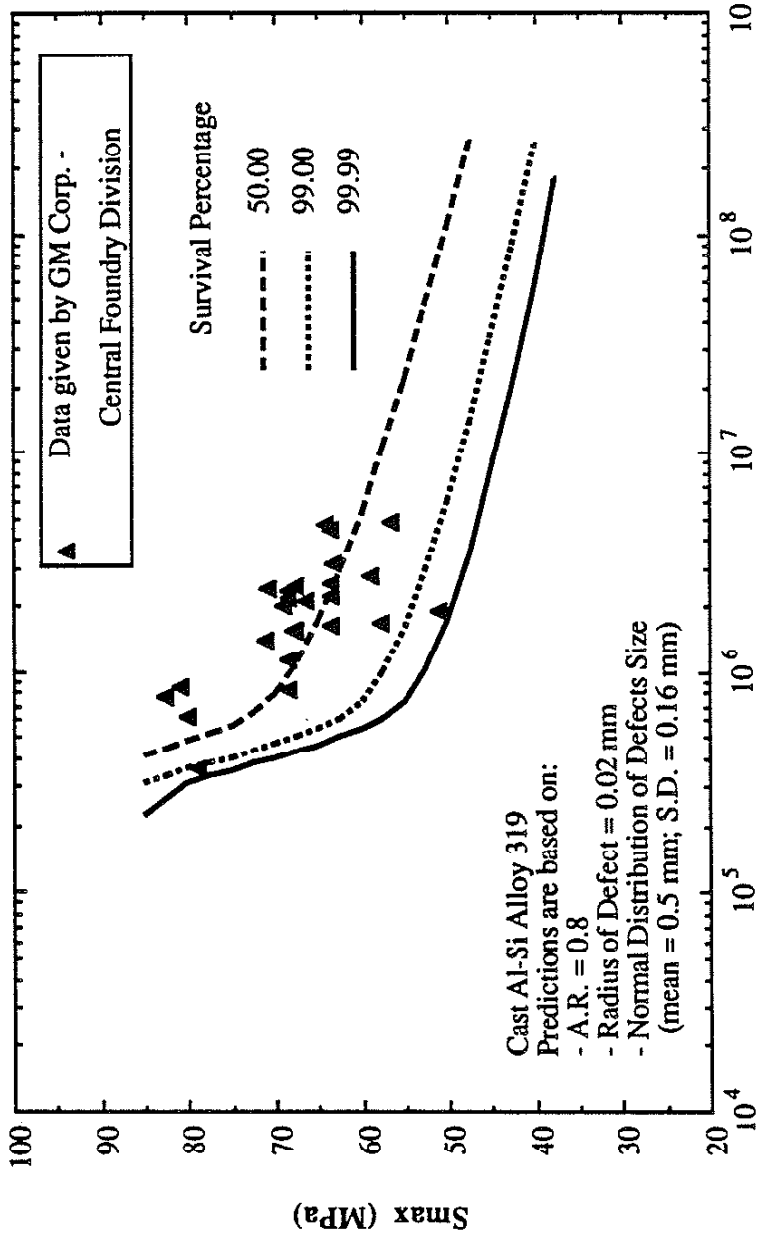


Figure 19 Comparison of test data with the predicted three survival levels. The test data were supplied by the General Motors Corporation [74].

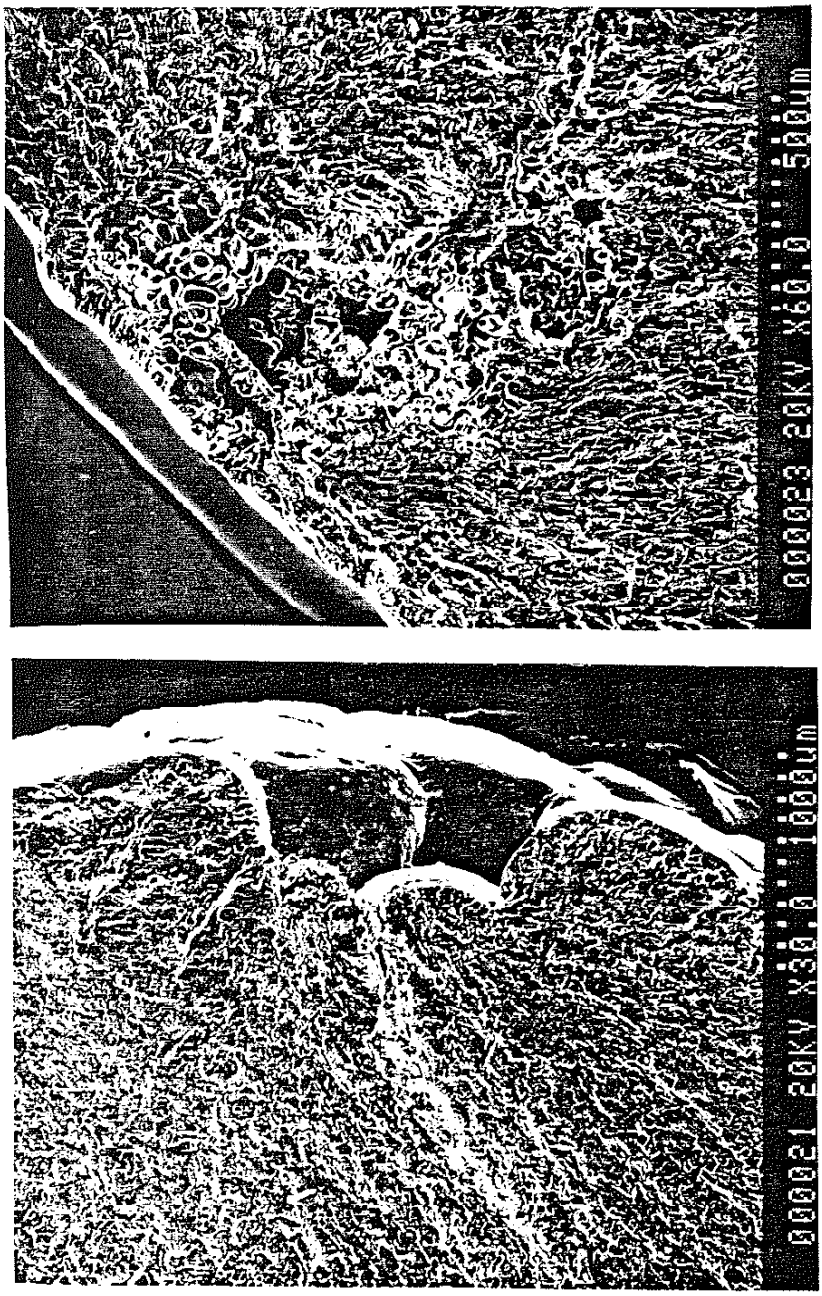


Figure 20 Fractographs of initiation site for as-cast specimens tested by the General Motors Corporation [74] (see Table 5). (a) specimen GM-32 (60x), (b) specimen GM-31 (30x).

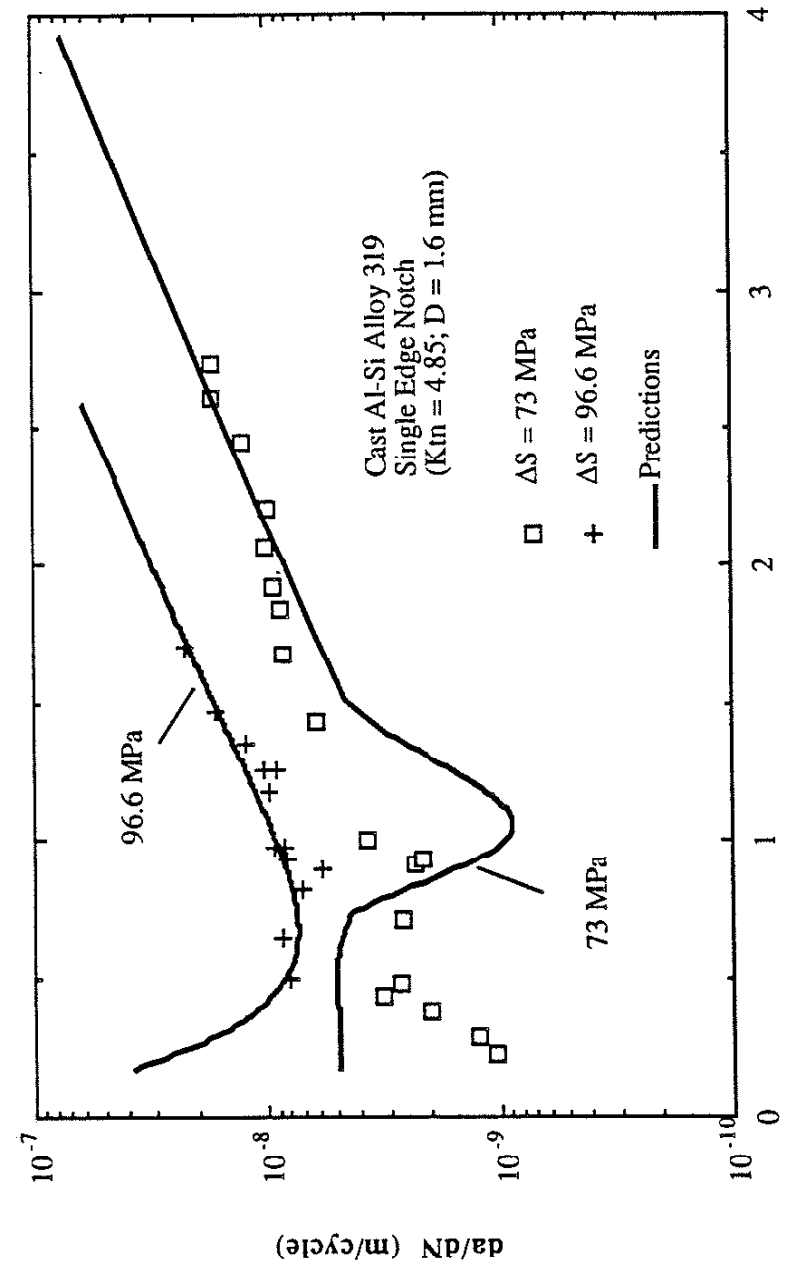


Figure 21a Comparison of experimental crack growth rates with the CCN model predictions for notches with $K_{tn} = 4.85$.

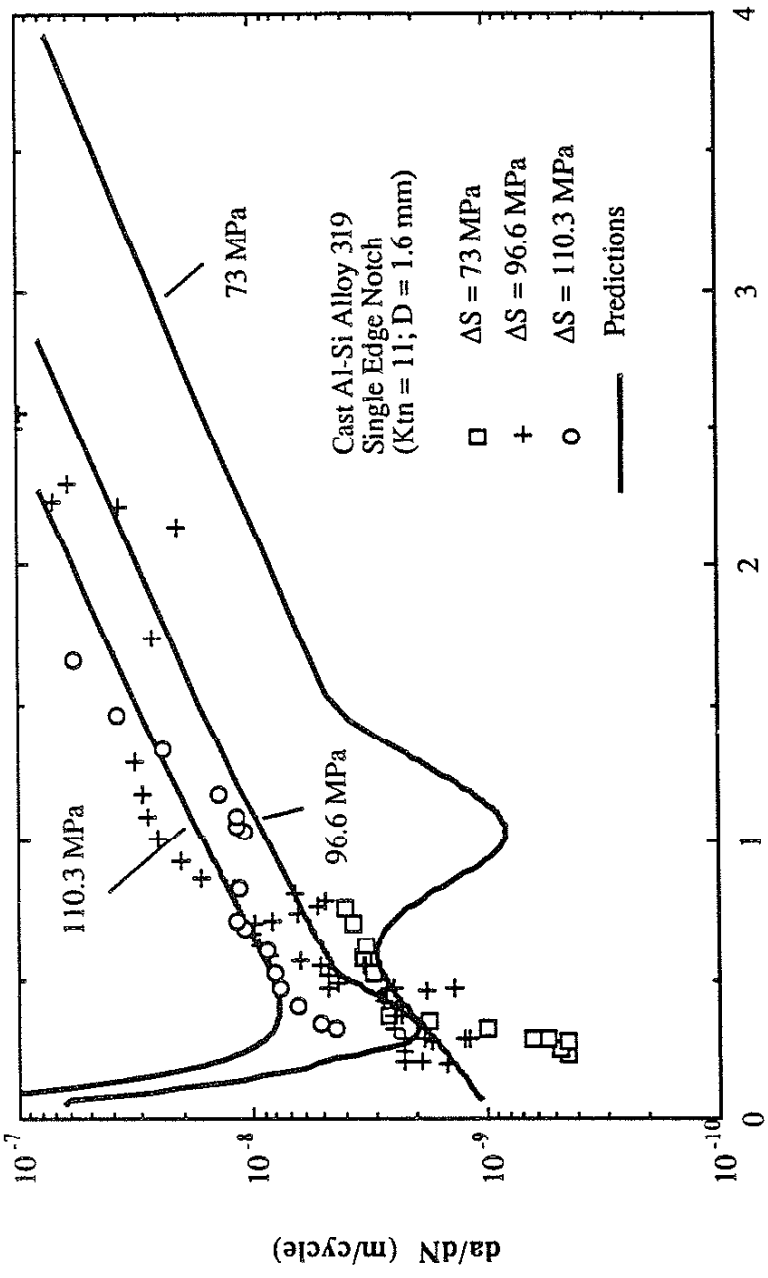


Figure 21b Comparison of experimental crack growth rates with the CCN model predictions for notches with $K_m = 11$.

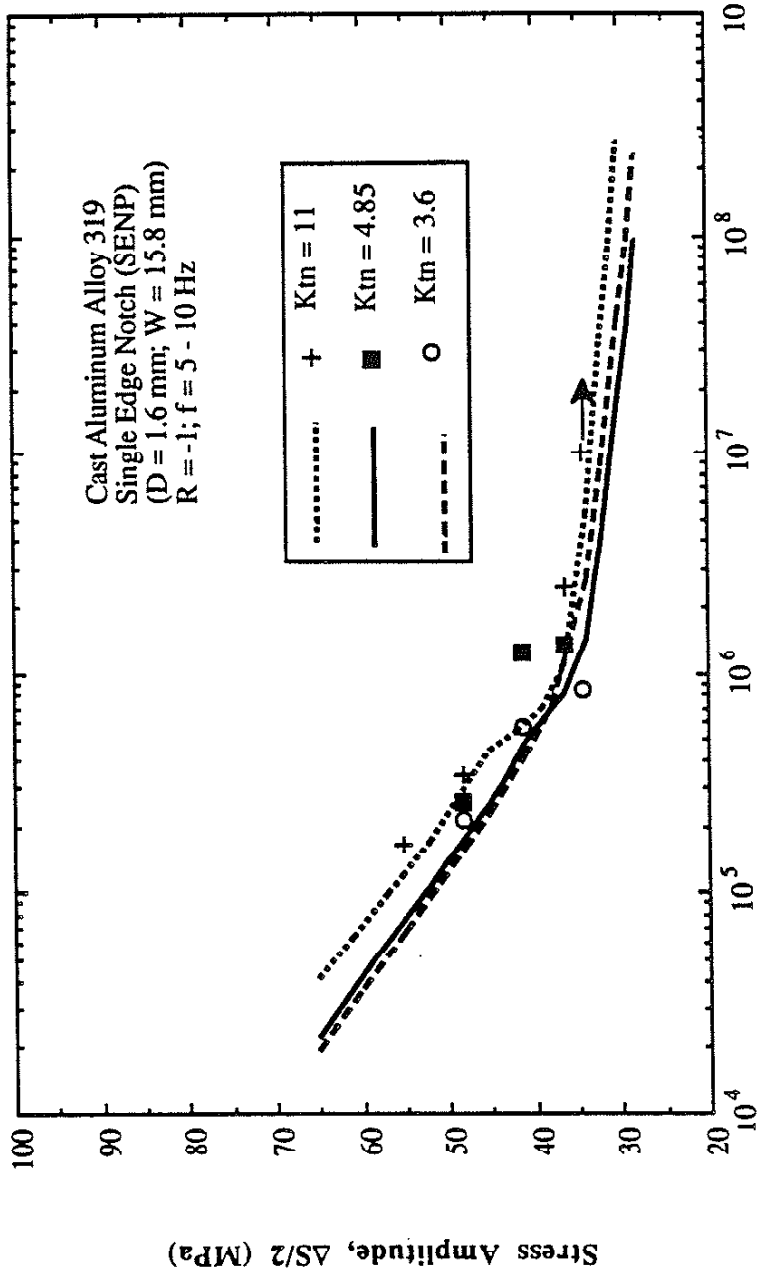


Figure 22 Comparison of experimental data from SENP specimens with predictions from the CCN model.

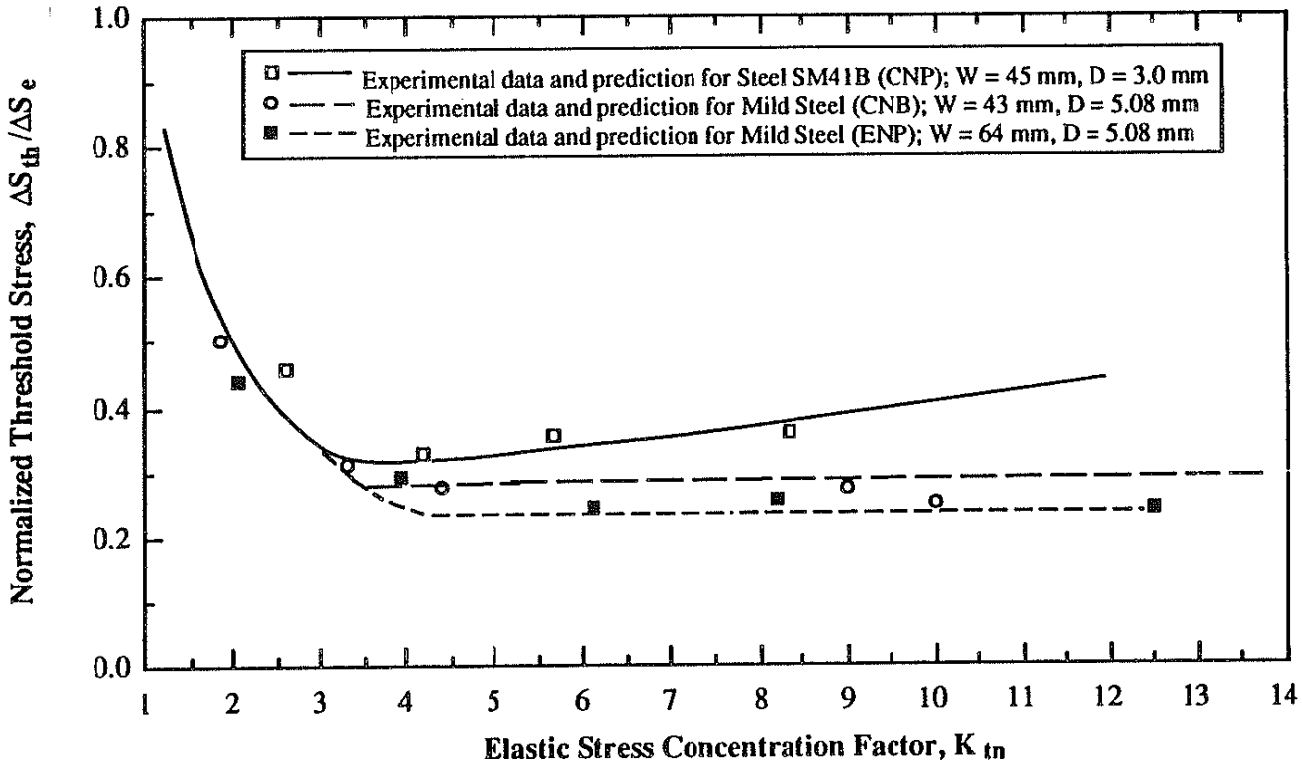


Figure 23 Comparison of experimental data with predicted results of the CCN model. Each set of data has a constant notch depth (D) but varying notch root radii (ρ).

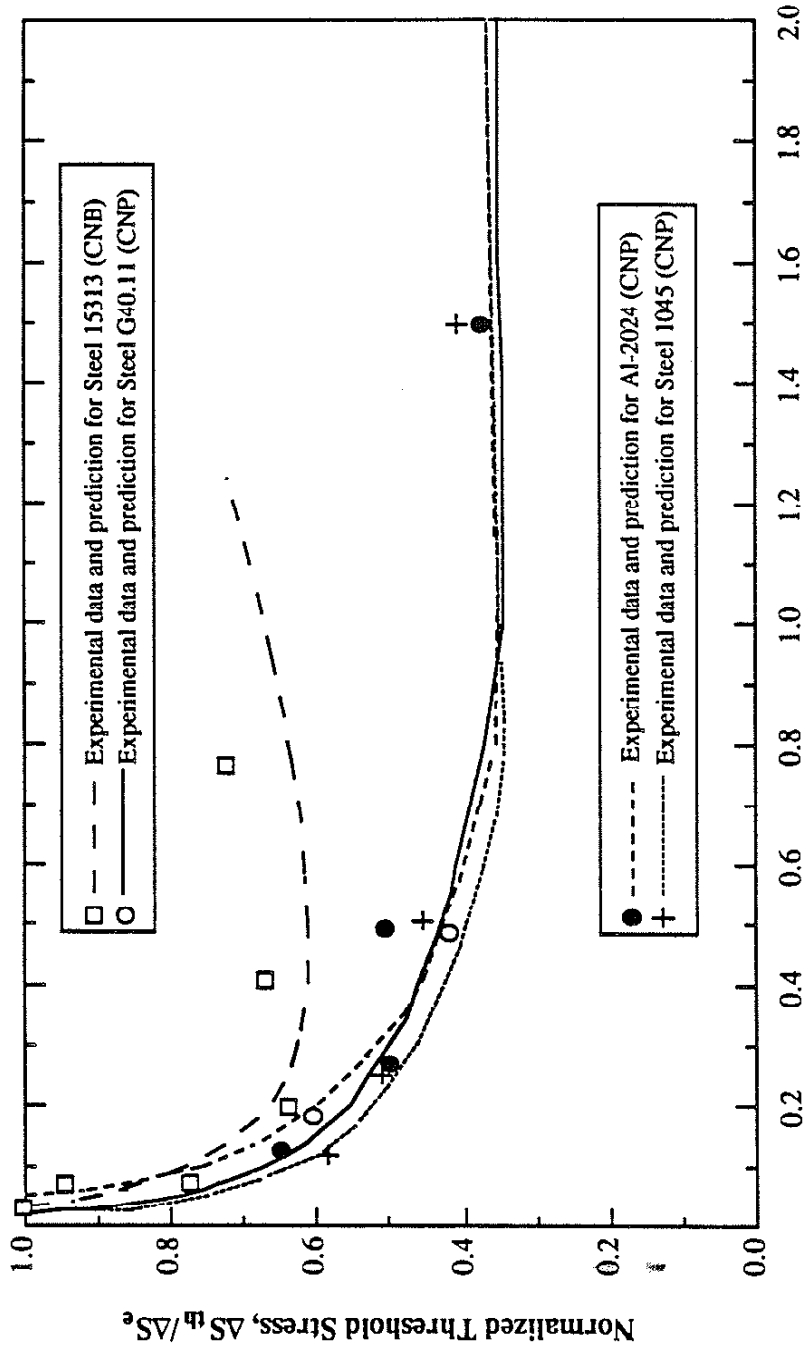


Figure 24 Comparison of experimental data with predicted results of the CCN model. The notch depth (D) is equal to notch root radius (ρ) for each case.

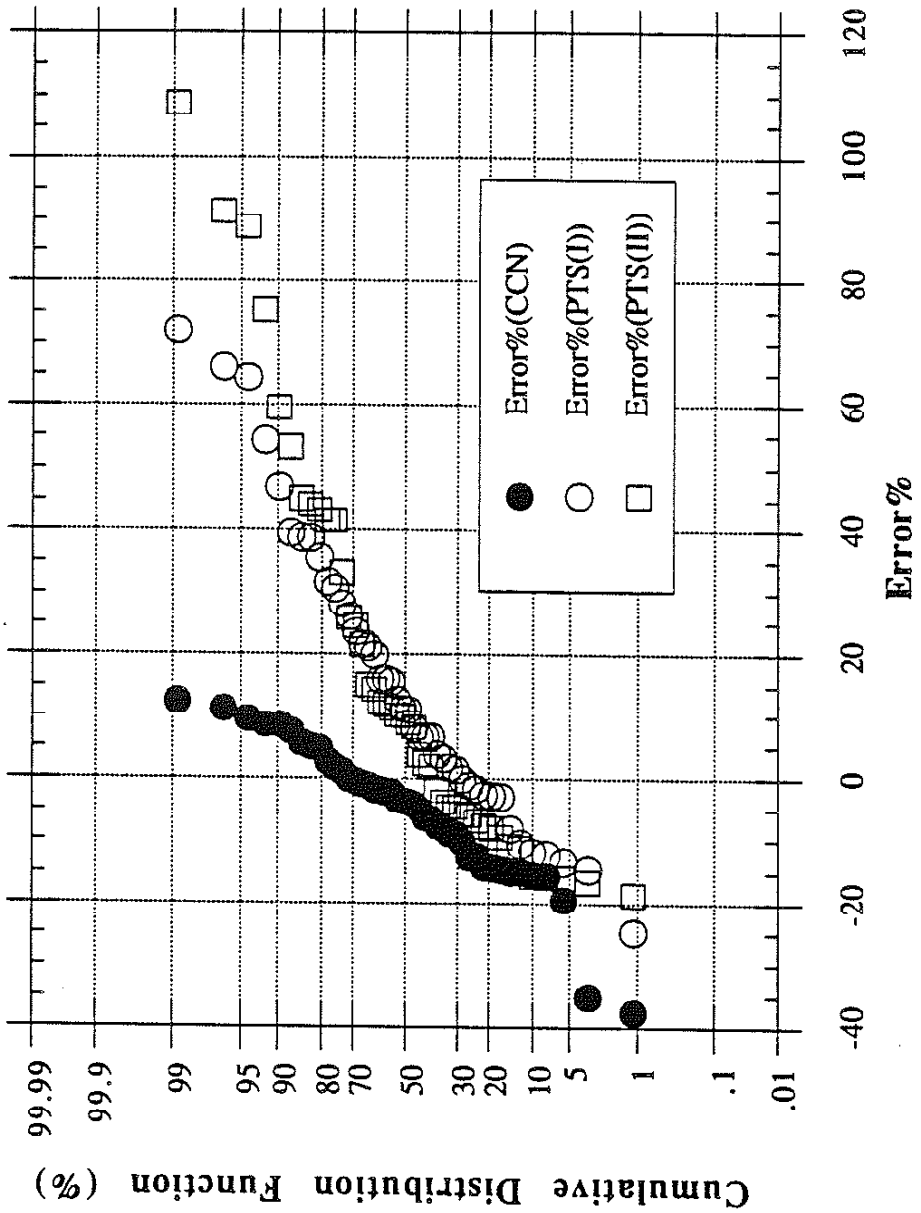


Figure 25 The cumulative distribution functions of "Error%" of threshold stress for the results predicted based on the CCN model and two types of Peterson's equations (using normal distribution plot).

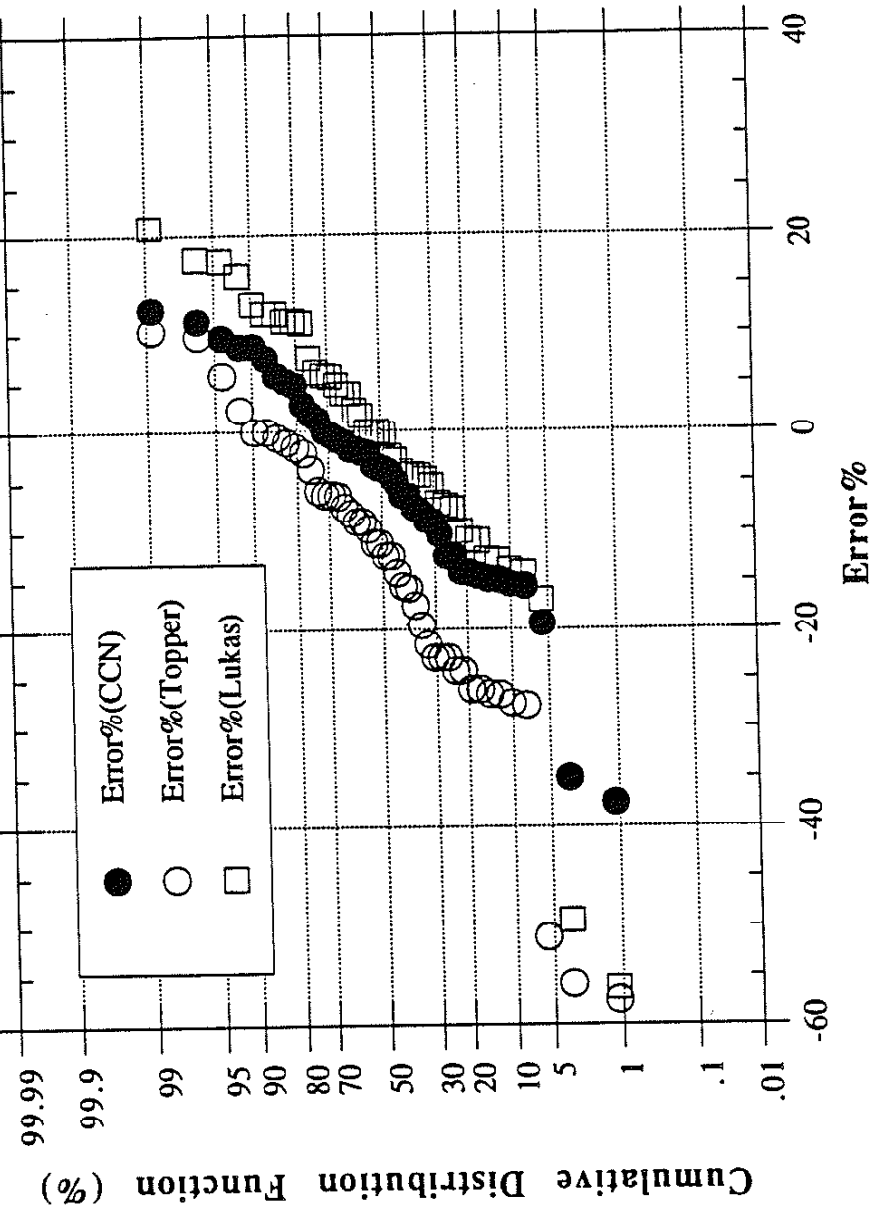


Figure 26 The cumulative distribution functions of "Error%" of threshold stresses for the results predicted based on the CCN model, Lukas model and Topper model (using normal distribuiion plot).

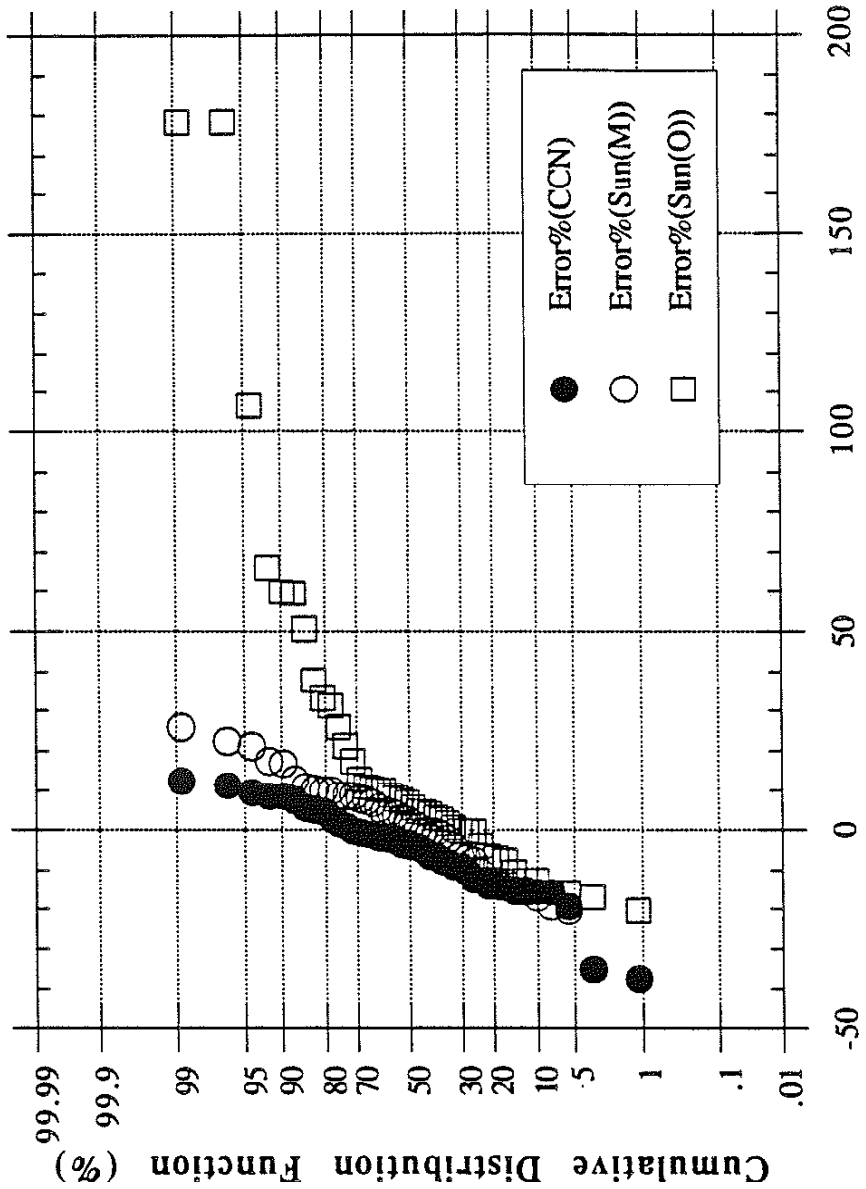


Figure 27 The cumulative distribution functions of "Error%" of threshold stresses for the results predicted based on the CCN model, Modified Sun and Sehitoglu (Sun(M)) model and Original Sun and Sehitoglu (Sun(O)) model (using normal distribution plot).

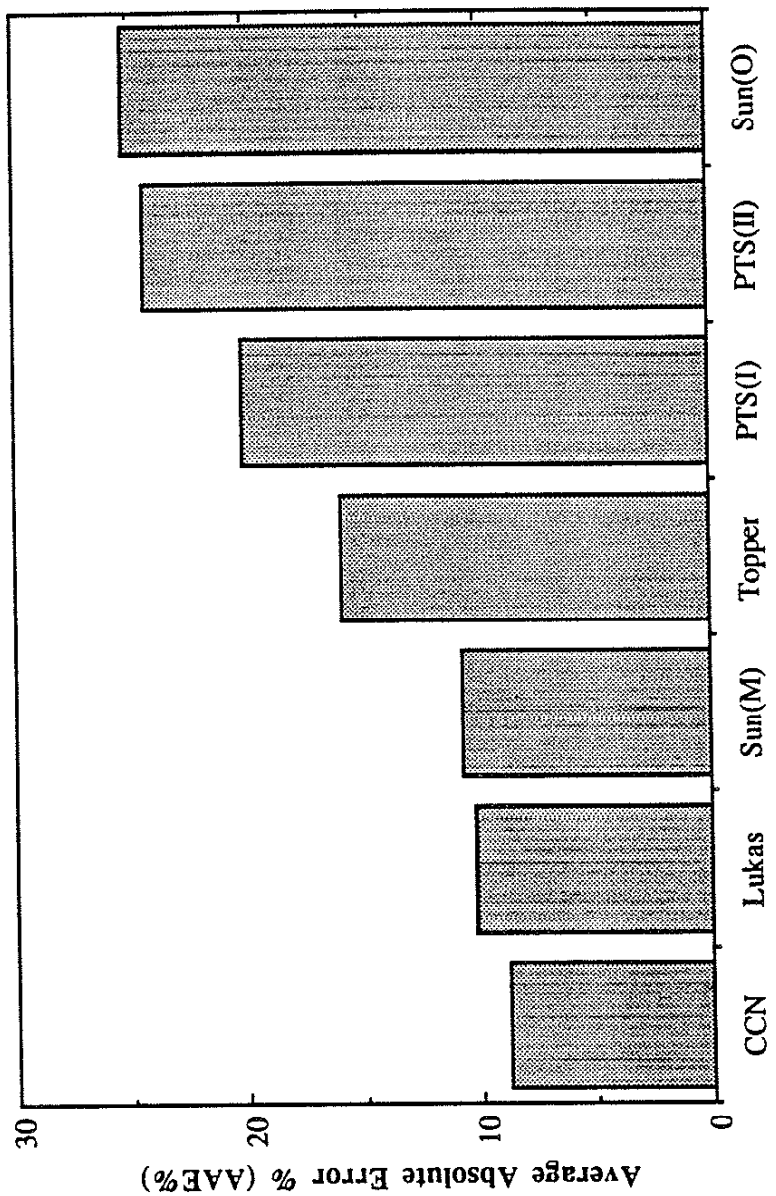


Figure 28 Comparison of the average absolute "Error%" (AAE%) for the threshold stress predicted based on seven different models.

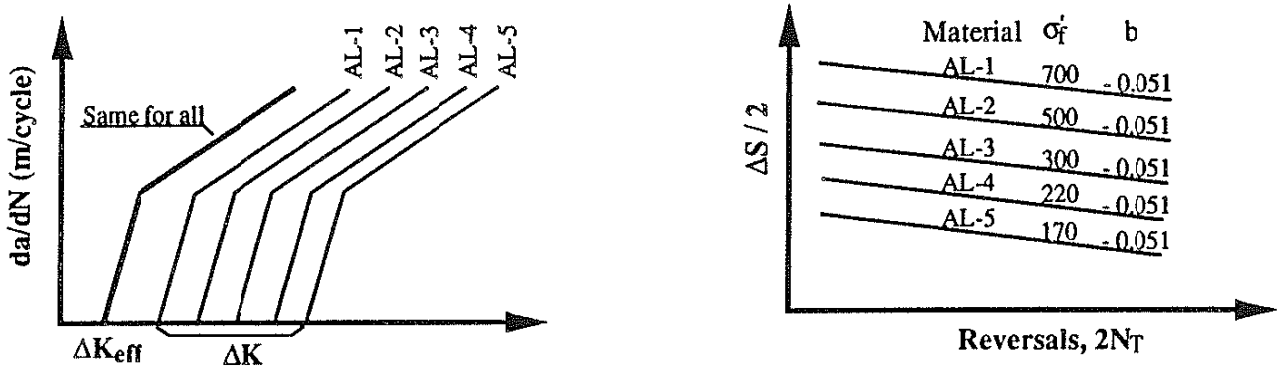


Basic Mechanical and Fatigue Properties for Simulations

| Materials designation | $\sigma_f'$ (MPa) | b | $\Delta S_e$ (MPa) | $S_y$ (MPa) | $\Delta K_{tho}$ (MPa$\sqrt{m}$) | $\Delta K_{eff.tho}$ (MPa$\sqrt{m}$) | $K_{IC}$ (MPa$\sqrt{m}$) | $U_{tho}$ | Lo (mm) |
|---|---|---|---|---|---|---|---|---|---|
| ST-1 or AL-1 | 700 | - 0.051 | 495 | 784 | 2.0 | 1.4 | 25.0 | 0.70 | 0.0052 |
| ST-2 or AL-2 | 500 | - 0.051 | 354 | 560 | 3.5 | 1.4 | 25.0 | 0.40 | 0.0312 |
| ST-3 or AL-3 | 300 | - 0.051 | 212 | 336 | 5.0 | 1.4 | 25.0 | 0.28 | 0.177 |
| ST-4 or AL-4 | 220 | - 0.051 | 156 | 260 | 5.7 | 1.4 | 25.0 | 0.25 | 0.427 |
| ST-5 or AL-5* | 170 | - 0.051 | 120 | 190 | 6.5 | 1.4 | 25.0 | 0.215 | 0.934 |

* Material AL-5 is the cast aluminum alloy 319 tested in this study except the value of $K_{IC}$

Figure 29 The basic material properties and fatigue properties used for simulations by the CCN model.

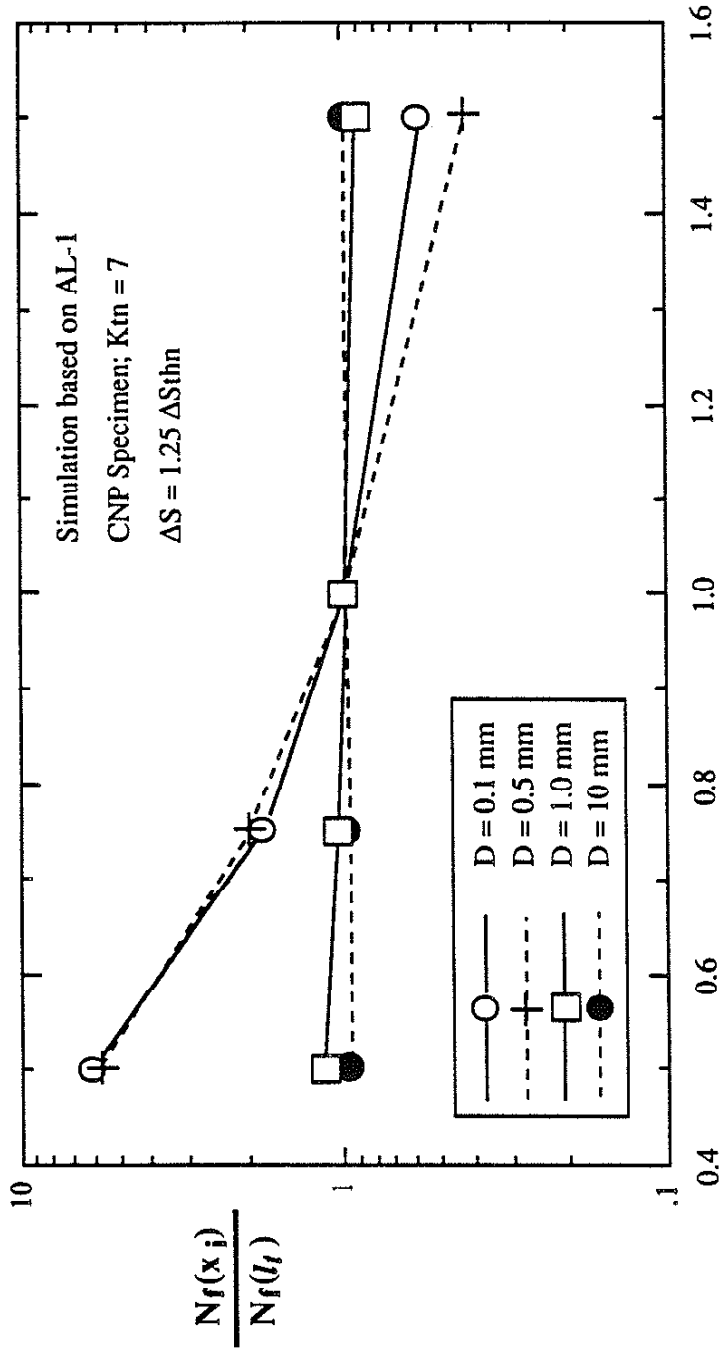


Figure 30 The influence of the selected initial crack length on the predicted fatigue life.

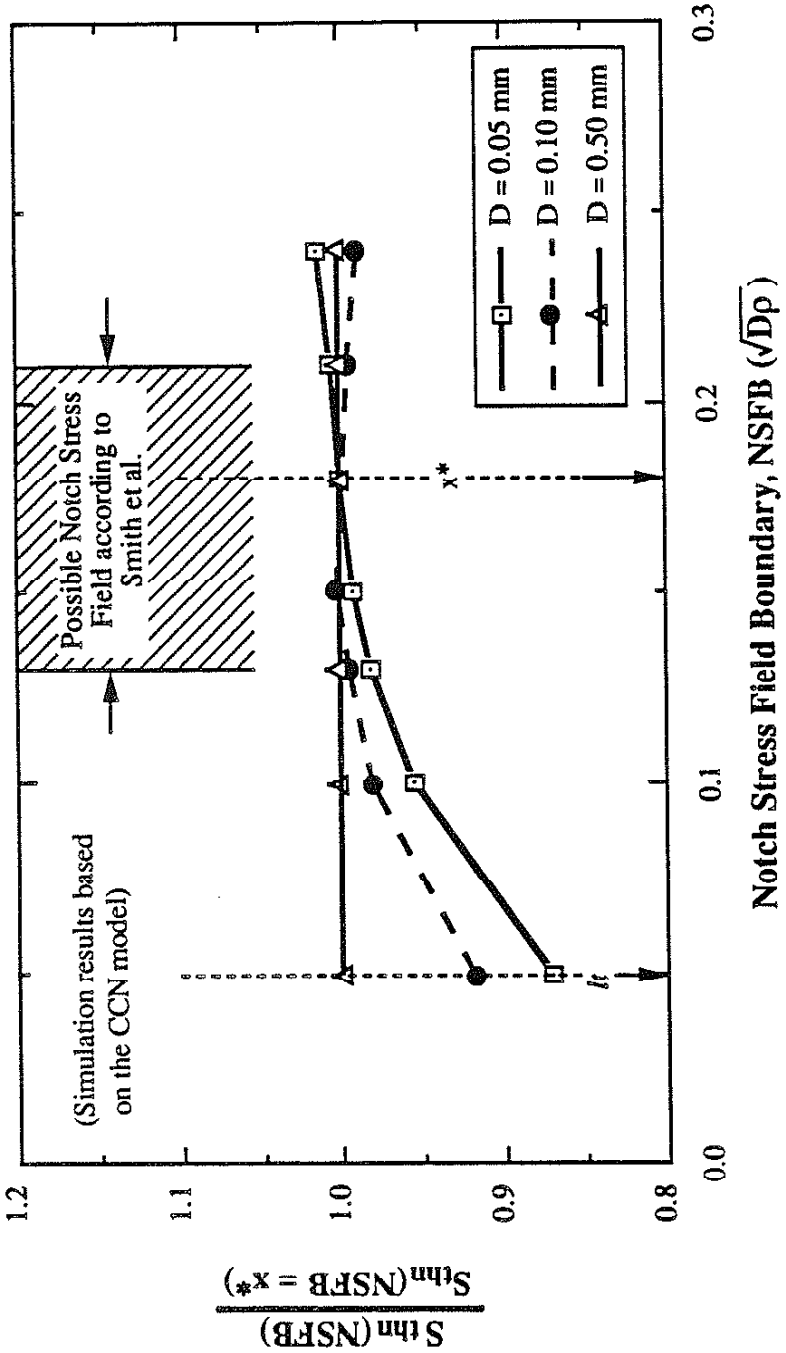


Figure 31 The influence of the selected notch stress field boundary on the predicted threshold stress.

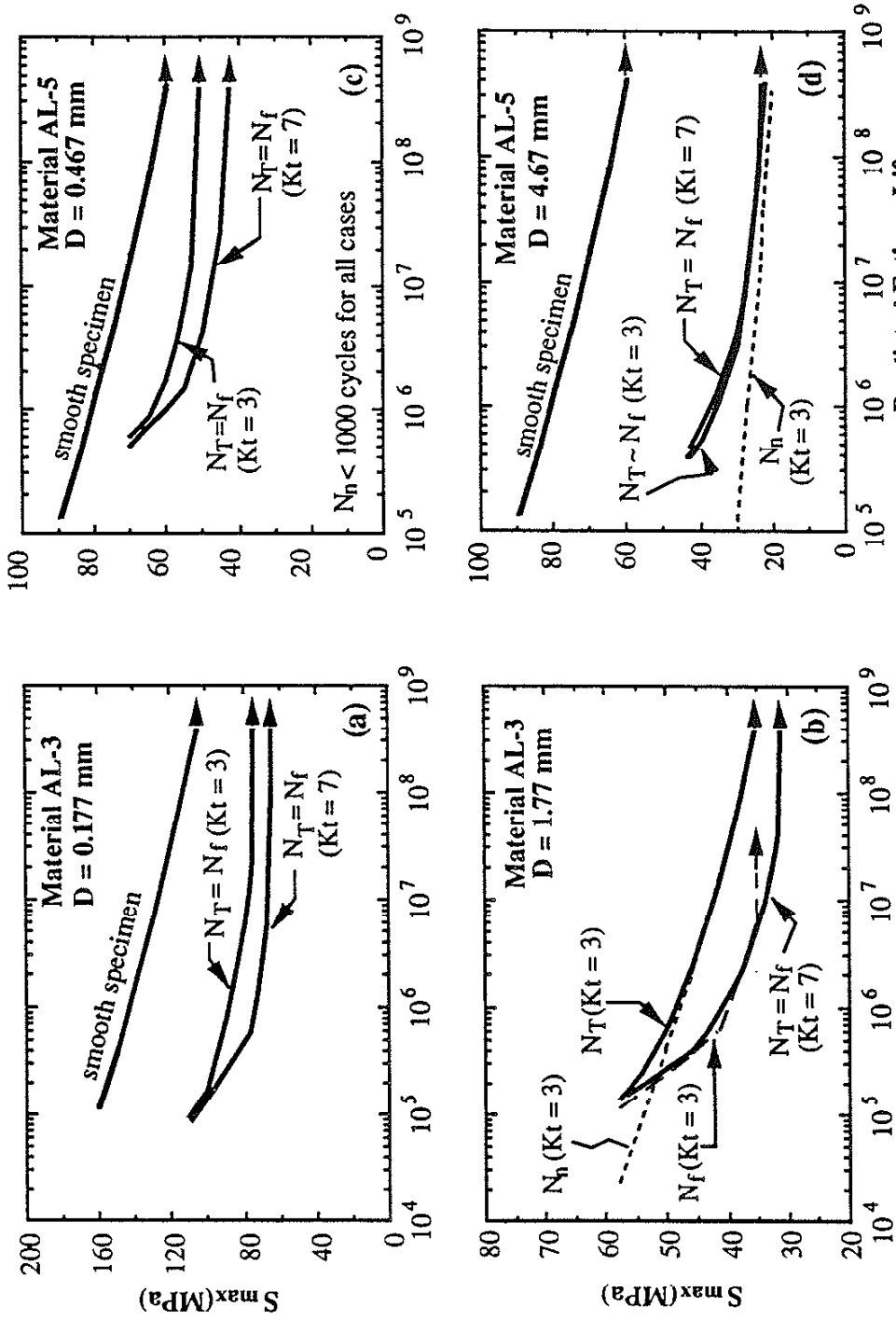


Figure 32 The effect of notch depth and notch acuity on the S-N behavior of AL-3 and AL-5.

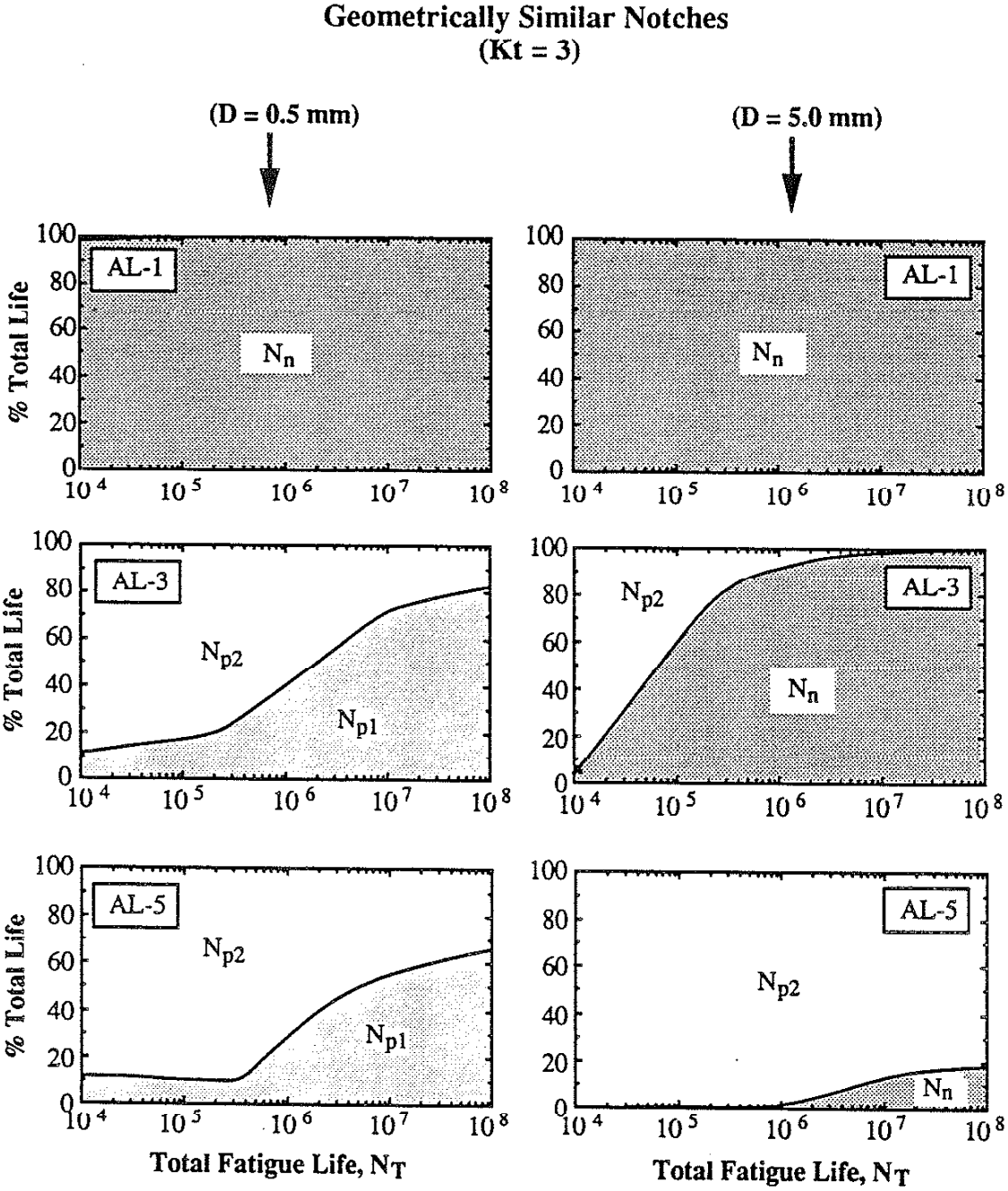


Figure 33a The effect of material properties and notch depth on the importance of each fatigue-life portion for geometrically similar notches with $K_t = 3$. ($N_n$ = crack nucleation life, $N_{p1}$ = early propagation life for crack growing to an engineering crack size (0.25 mm), and $N_{p2}$ = propagation life for crack growing from 0.25 mm to failure).

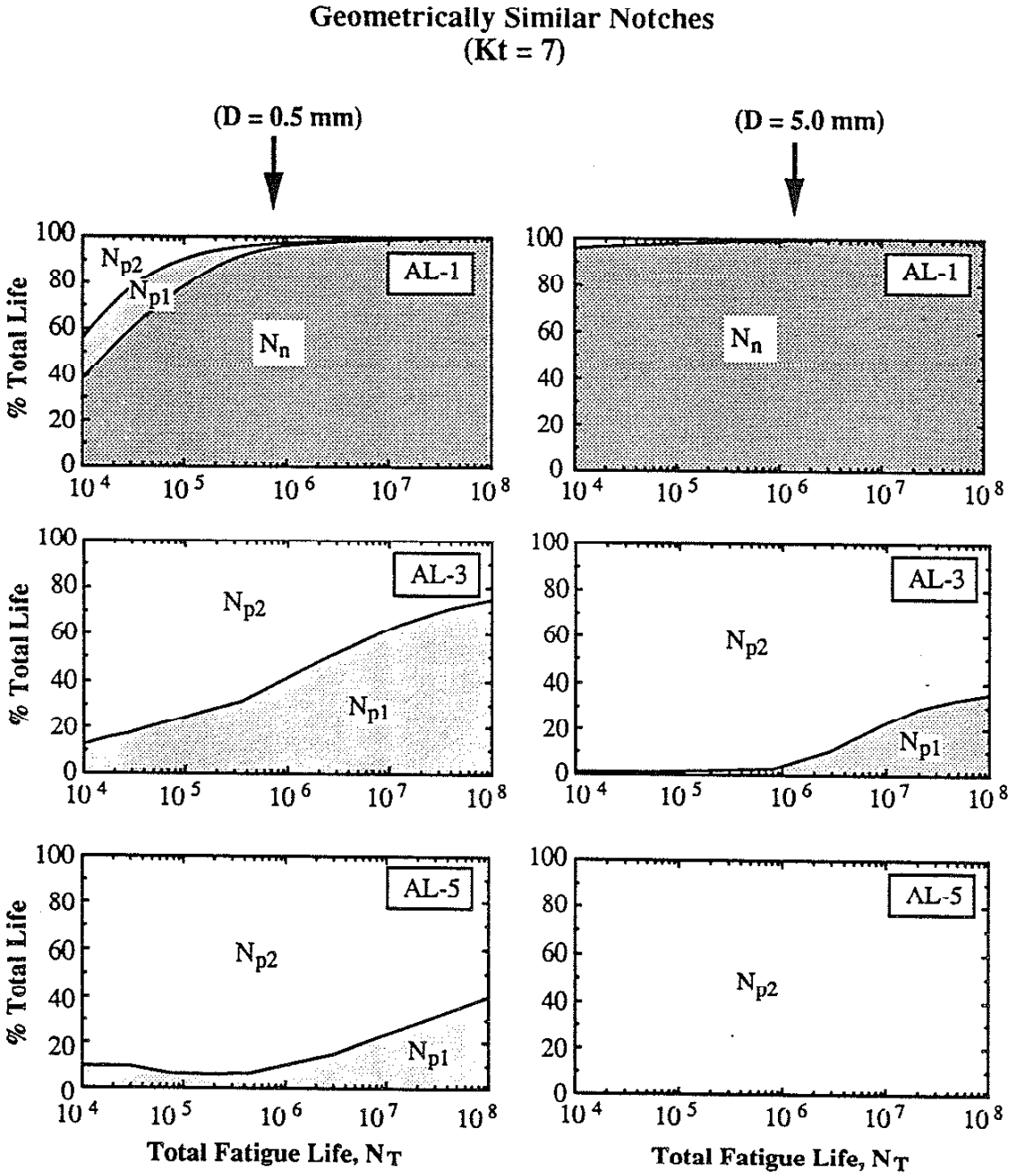


Figure 33b The effect of material properties and notch depth on the importance of each fatigue-life portion for geometrically similar notches with $K_t = 7$. ($N_n$ = crack nucleation life, $N_{p1}$ = early propagation life for crack growing to an engineering crack size (0.25 mm), and $N_{p2}$ = propagation life for crack growing from 0.25 mm to failure).

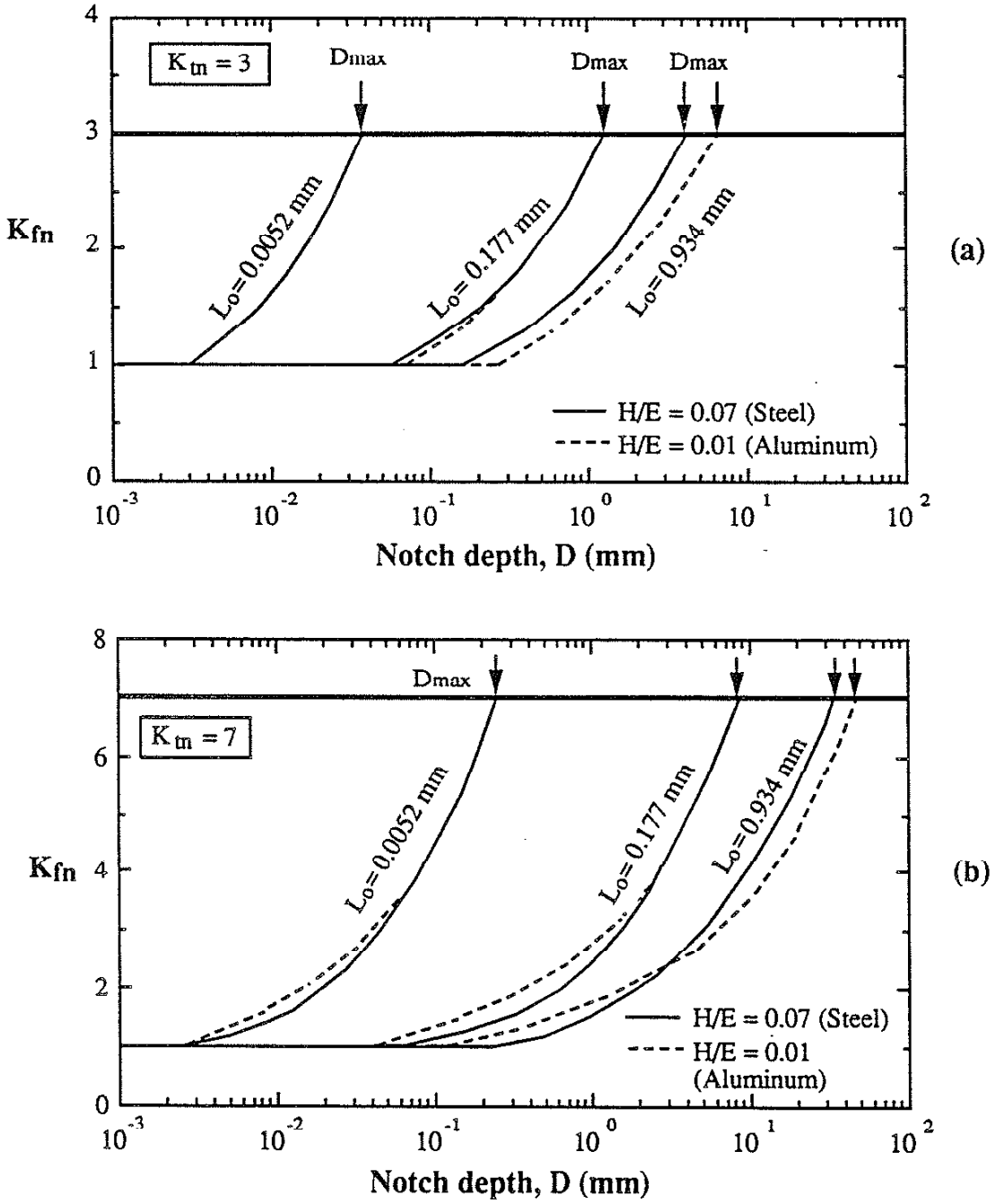


Figure 34 The relation between Kfn and notch depth as a function of material properties (Lo and value of H/E). (a) for blunt notch (Ktn = 3), (b) for sharp notch (Ktn = 7). The value of Dmax for a certain material and notch acuity is pointed by the arrow.
(Simulation results based on the CCN model).

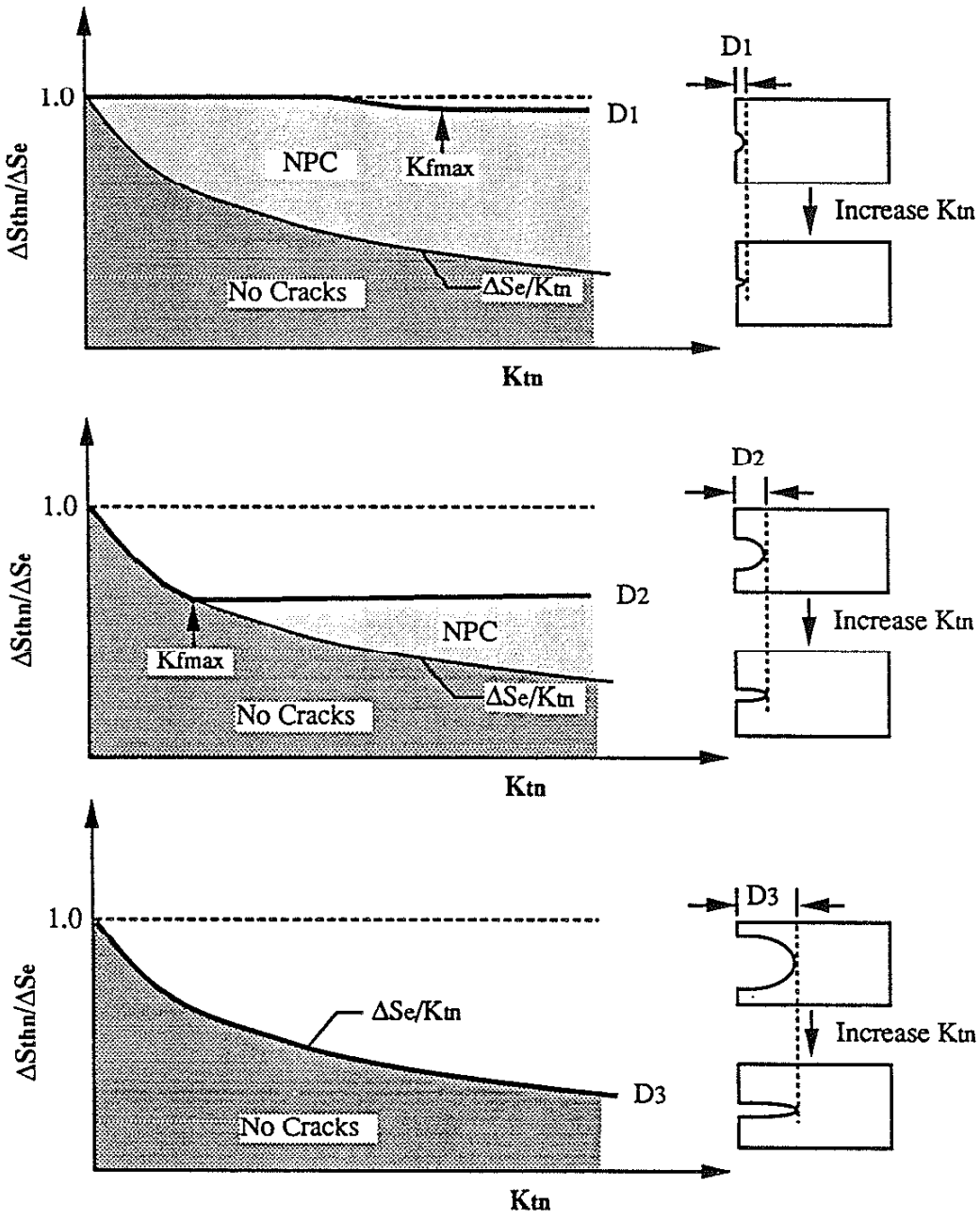


Figure 35 a The effect of notch depth on the threshold stresses for constant depth notches represented by the Frost relation.

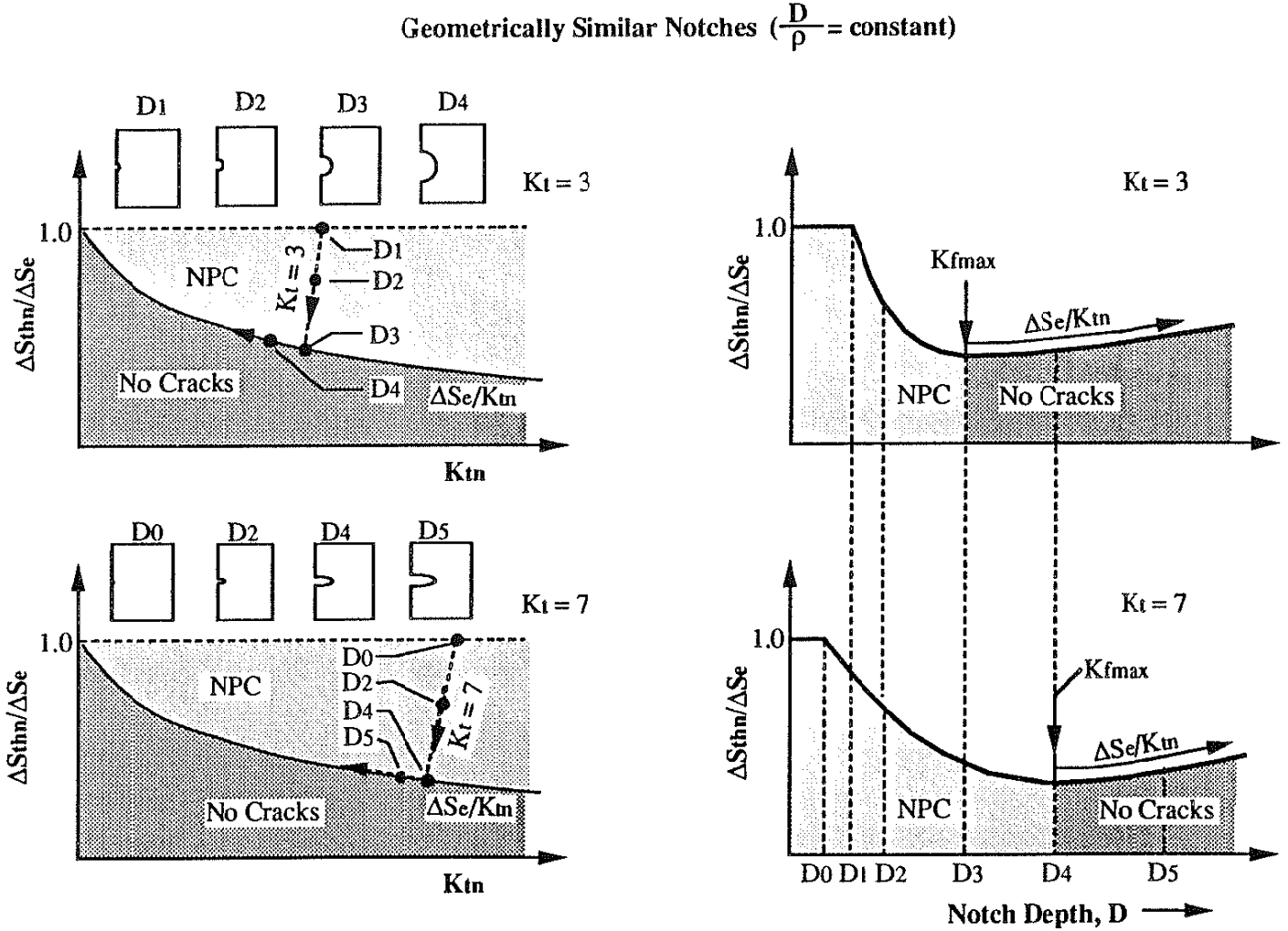


Figure 35b The effect of notch depth and notch acuity on the threshold stresses for geometrically similar notches represented by the Frost relation (left) and the Lukas relation (right).

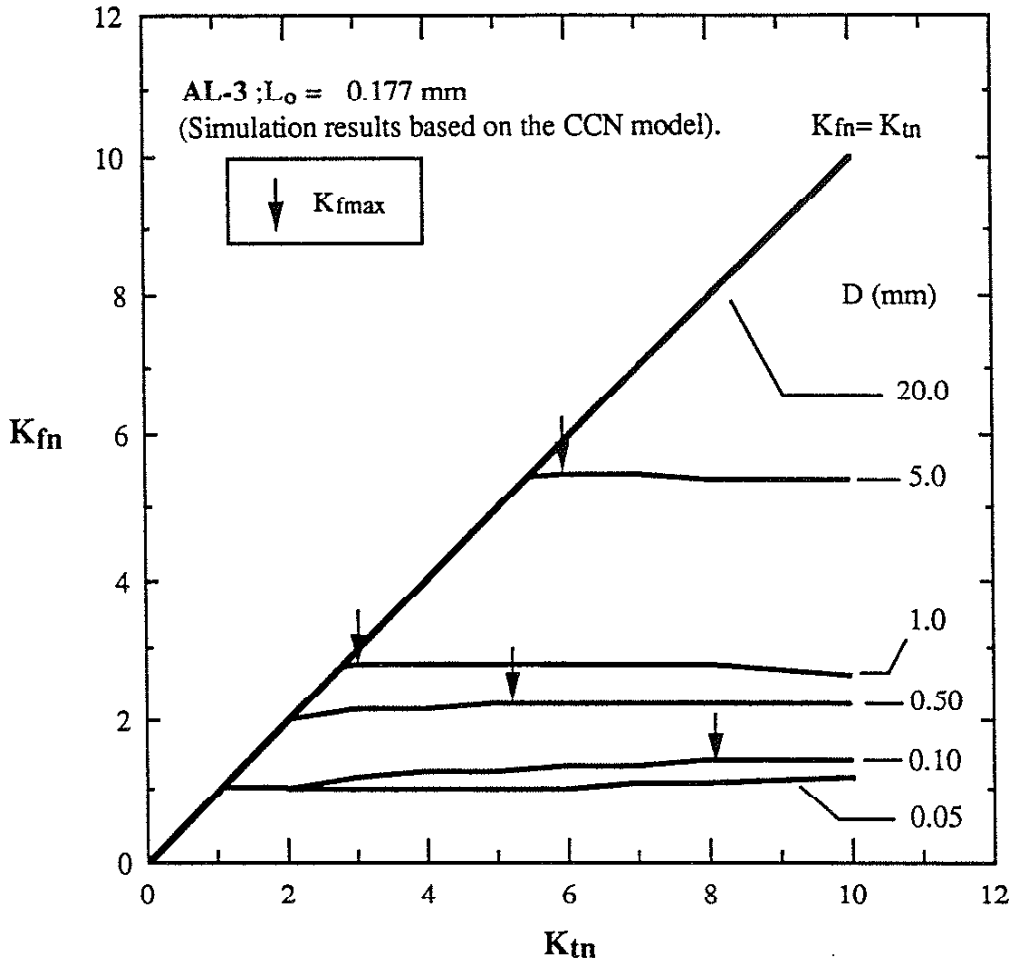


Figure 36a The effect of notch depth and acuity on the fatigue notch factor (Kfn) for constant depth notches. Note that there is a maximum Kfn value (Kfmax) for a given notch depth.

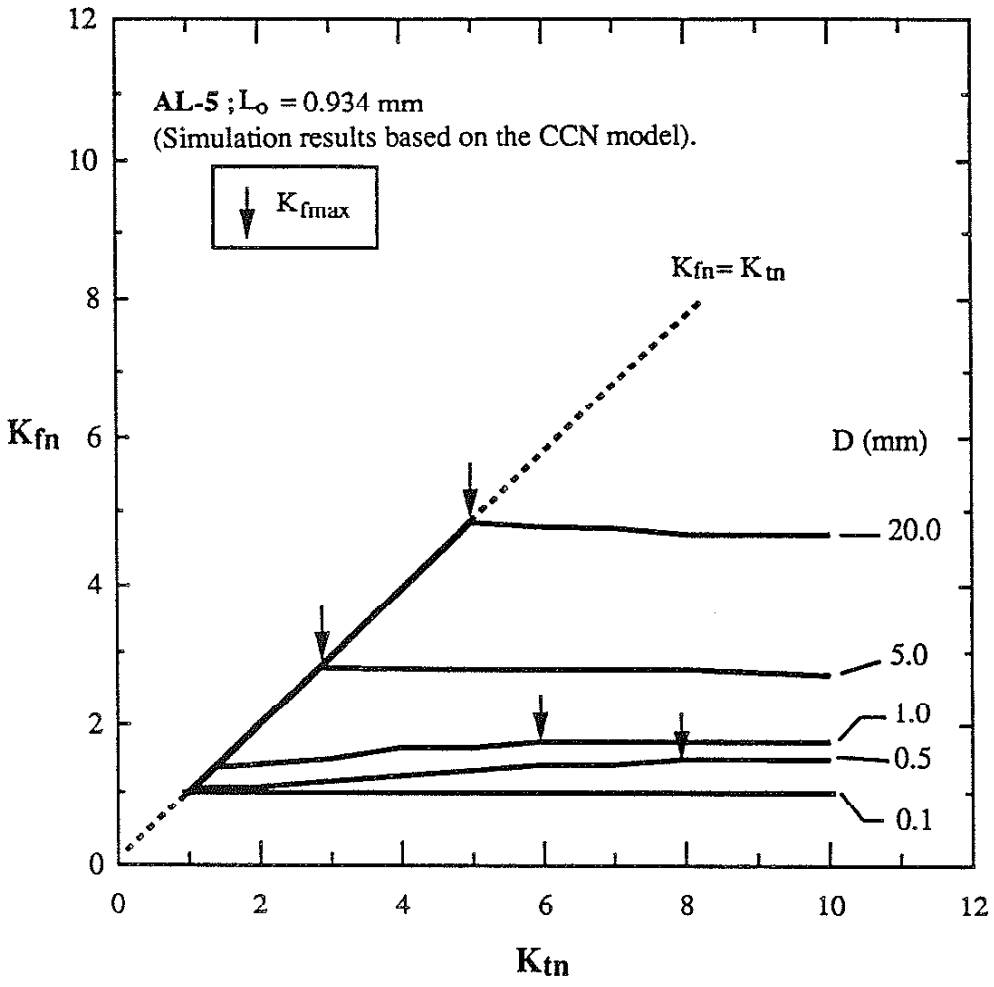


Figure 36b The effect of notch depth and acuity on the fatigue notch factor ($K_{fn}$) for constant depth notches. Note that there is a maximum $K_{fn}$ value ($K_{fmax}$) for a given notch depth.

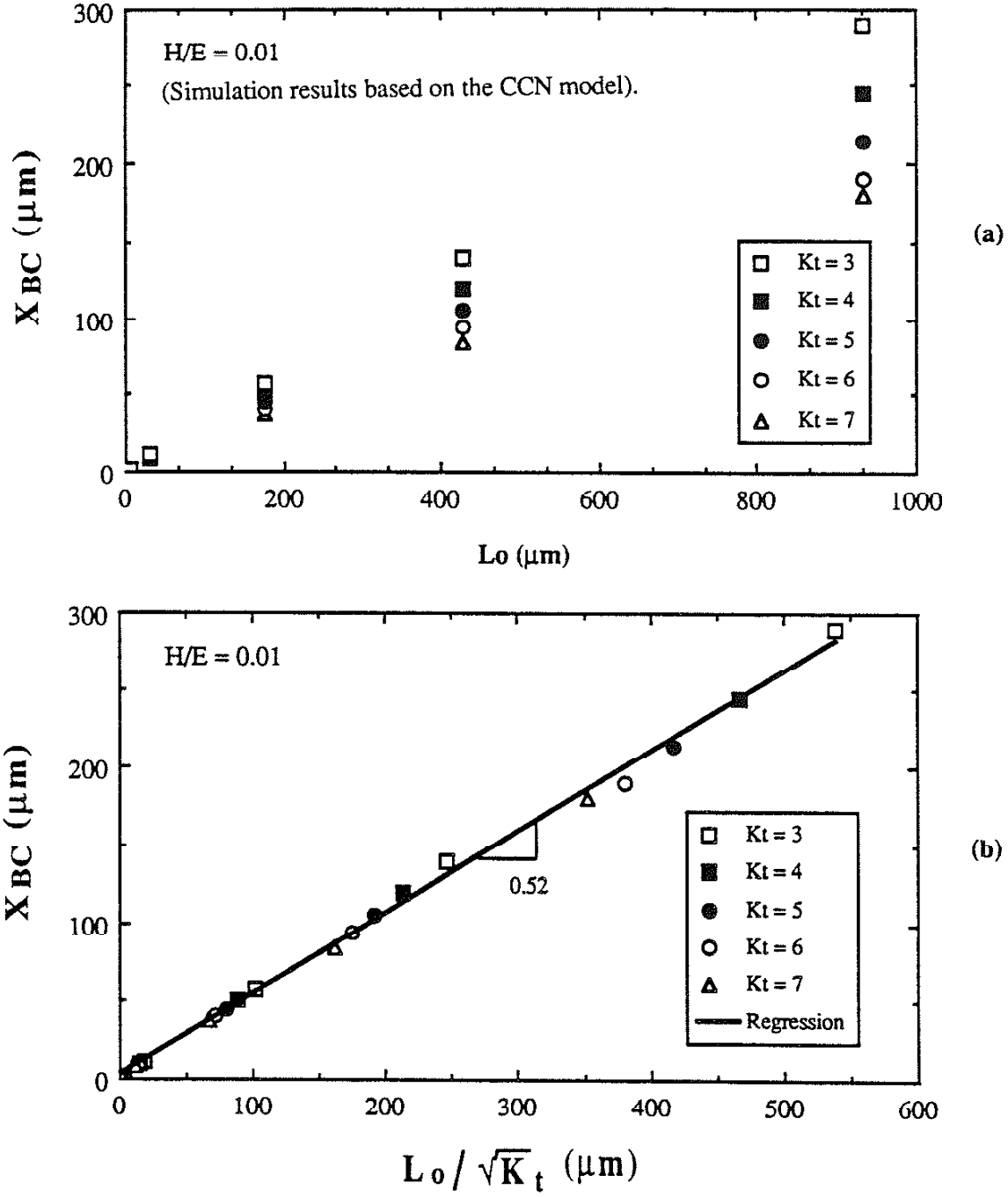


Figure 37 The influence of material property ($L_o$) and notch acuity ($K_t$) on the maximum non-damaging notch size ($X_{BC}$) for aluminum alloys. (a) the variation of $X_{BC}$ with $L_o$ showing the effect of $K_t$, (b) the linear relationship between $X_{BC}$ and $L_o/\sqrt{K_t}$.

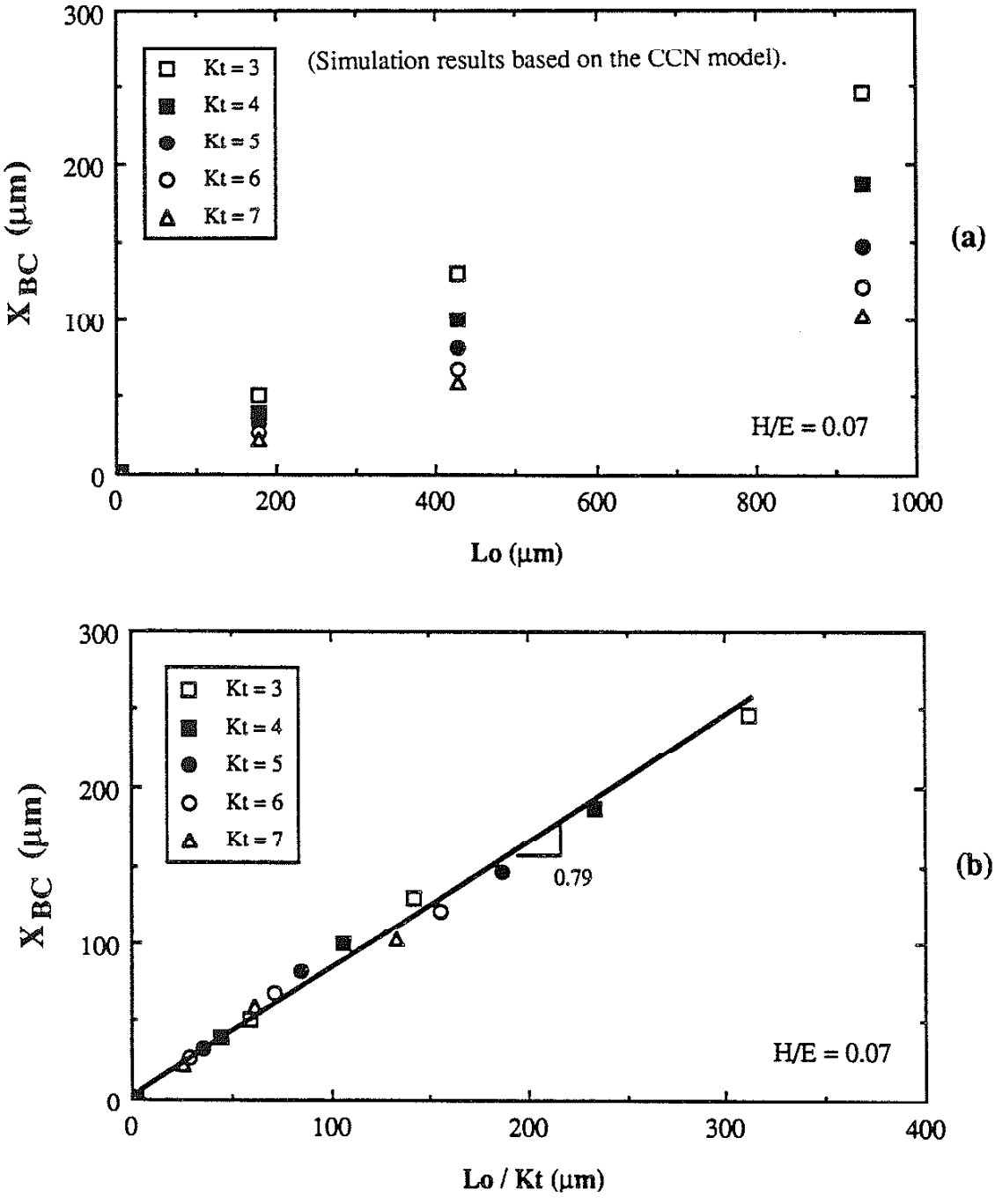


Figure 38 The influence of material property ($L_o$) and notch acuity ($K_t$) on the maximum non-damaging notch depth ($X_{BC}$) for steel. (a) the variation of $X_{BC}$ with $L_o$ showing the effect of $K_t$, (b) the linear relationship between $X_{BC}$ and $L_o/K_t$.

# APPENDIX A
# STRESS INTENSITY FACTOR SOLUTIONS

## A.1 Surface Cracks in Cylindrical Bar under Tension

The stress intensity factor in a cylindrical bar specimen containing an elliptical surface crack is given by Raju and Newman [54] in the form:

$$K_A = S F_A \sqrt{\frac{\pi a}{Q}} \qquad (A.1)$$

where:
- $K_A$ = The stress intensity factor at the maximum depth point A; see Fig. A.1
- $S$ = The remote tensile stress
- $F_A$ = The boundary correction factor at the maximum depth point A; see Fig. A.1
- $a$ = Crack depth along the direction from surface to circular center; see Fig. A.1
- $Q$ = The shape factor for an ellipse = $1.0 + 1.464\ (a/c)^{1.65}$
- $c$ = The half length of the crack on the surface; see Fig. A.1
- $a/c$ = Aspect ratio of the elliptical crack

Raju and Newman define $F_A$ in a tabular form. The following expression, used to facilitate calculations, was based on a polynomial curve fit to the $F_A$ data.

$$F_A = 1.078 + 2.973\ (a/W) + 4.564\ (a/W)2 - 4.3214\ (a/W)\ (a/c) \qquad (A.2)$$
$$(\text{for } a/c \leq 1.0)$$

where:
- $W$ = Specimen diameter

To date, there is no expression for $F_A$ when $a/c > 1.0$. When the fatigue crack emanated from a near-surface casting defect, the fatigue initiating defect size (T) was defined as $\sqrt{Area}$. Assuming that the fatigue initiating defect can be idealized as an elliptical shape on the surface of a cylindrical bar, the fatigue initiating defect can be defined by the depth, D and the surface length, 2c. The initial aspect ratio (AR) can be represented by D/c. The relationship between the depth and the measured area of the fatigue initiating defect can be approximately given by:

$$\sqrt{Area} = \sqrt{Dc} = \frac{D}{\sqrt{AR}} \qquad (A.3)$$

where:
- $D$ = Depth of the fatigue initiating defect

AR = The aspect ratio of the fatigue initiating defect
Area = Defect area

Thus,

$$D = \sqrt{AR}\,\sqrt{Area} \tag{A.4}$$

In cast materials, fatigue cracks nucleate at near-surface defects; casting pores, surface textures, or both. Consider a cast cylindrical bar. When a fatigue crack grows to a length x, the value of "a" used in Eqs. A.1 and A.2 would be equal to D + x. The aspect ratio is a function of the crack length in the radial direction, and the crack length on the surface. The aspect ratio changes when the fatigue crack propagates. Tokaji et al. [51] found that the aspect ratio for a surface crack ranges from 0.7 to 0.9 when the surface crack length is greater than 0.6 mm. Cox et al. [52] applied Monte Carlo simulations to predict the variation of aspect ratios of small cracks with the crack size (denoted by $\sqrt{ac}$). These predictions gave aspect ratios asymptotically approaching 0.8 for crack sizes greater than 0.3 mm. The aspect ratio is considered to range from 0.7 to 0.9.

A.2 Surface Cracks in a Plate under Tension

Consider an elliptical surface crack growing through the thickness of a plate. The plate is assumed to be of infinite width and finite thickness. The stress intensity factor for this elliptical surface crack can be given as follows [55]:

$$K_A = M_A S \sqrt{\frac{\pi a}{Q}} \tag{A.5}$$

where:
$K_A$ = The stress intensity factor at the maximum depth point A; see Fig. A.2
S = The remote uniform-tension stress
$F_A$ = The boundary correction factor at the maximum depth point A; see Fig. A.2
a = Crack depth along the direction from surface to circular center; see Fig. A.2
c = The half length of the crack on the surface; see Fig. A.2
a/c = Aspect ratio (AR) of the elliptical crack
Q = The shape factor for an ellipse = $1.0 + 1.464\,(a/c)^{1.65}$
$M_A = M_1 + M_2(\frac{a}{H})^2 + M_3\,(\frac{a}{H})^4$
H = Thickness of plate; see Fig. A.2

$$M_1 = 1.13 - 0.09(a/c)$$

$$M_2 = -0.54 + \frac{0.89}{0.2 + (a/c)}$$

$$M_3 = 0.5 - \frac{1.0}{0.65 + (a/c)} + 14(1.0 - \frac{a}{c})^{24}$$

Equation A.5 can be used to calculate the stress intensity factor for surface defects which propagate through the wall of an engine block.

A.3 Edge Notched Plate under Tension

The stress intensity factor for edged notch (or double notches) in a plate is given by [56]:

$$K = Y(a)\, S \sqrt{\pi a} \qquad (A.6)$$

where: a = Crack length from the edge of the plate

where Y(a) is the geometrical factor for stress intensity factor. For single edged notch and double edged notches, the calculations of Y(a) are different:

*Y(a) for Single Edge Notch in a Plate (SENP)*

$$Y(a) = 1.12 - 0.231(\frac{a}{W}) + 10.55\,(\frac{a}{W})^2 - 21.72\,(\frac{a}{W})^3 + 30.39\,(\frac{a}{W})^4 \qquad (A.7)$$

where: W = Width of the plate

*Y(a) for Double Edge Notches in a Plate (DENP)*

$$Y(a) = \frac{1.12 - 0.561(\frac{a}{B}) - 0.205\,(\frac{a}{B})^2 + 0.471\,(\frac{a}{B})^3 - 0.19\,(\frac{a}{B})^4}{\sqrt{1 - \frac{a}{B}}} \qquad (A.8)$$

where: B = Half width of the plate

A.4 Center Notch in a Plate (CNP) under Tension

The stress intensity factor solution has the same form as Eq. A.6, but the geometrical factor Y(a) is different and given by [56]:

$$Y(a) = \frac{1 - 0.025\left(\frac{a}{B}\right)^2 + 0.06\left(\frac{a}{B}\right)^4}{\sqrt{\cos\left(\frac{\pi a}{W}\right)}} \qquad (A.9)$$

where:
B = Half width of the plate
W = Width of the plate
a = Crack length from the center of the plate

A.5 Circumferential Notch in a Cylindrical Bar (CNB) under Tension

The stress intensity factor solution has the same form as Eq. A.6, but the geometrical factor Y(a) is different and given by [56]:

$$Y(a) = \frac{1.12 - 1.302\left(\frac{a}{B}\right) + 0.988\left(\frac{a}{B}\right)^2 - 0.308\left(\frac{a}{B}\right)^3}{\left(1 - \frac{a}{B}\right)^{1.5}} \qquad (A.10)$$

where:
B = Half width of the plate
a = Crack length from the center of the plate

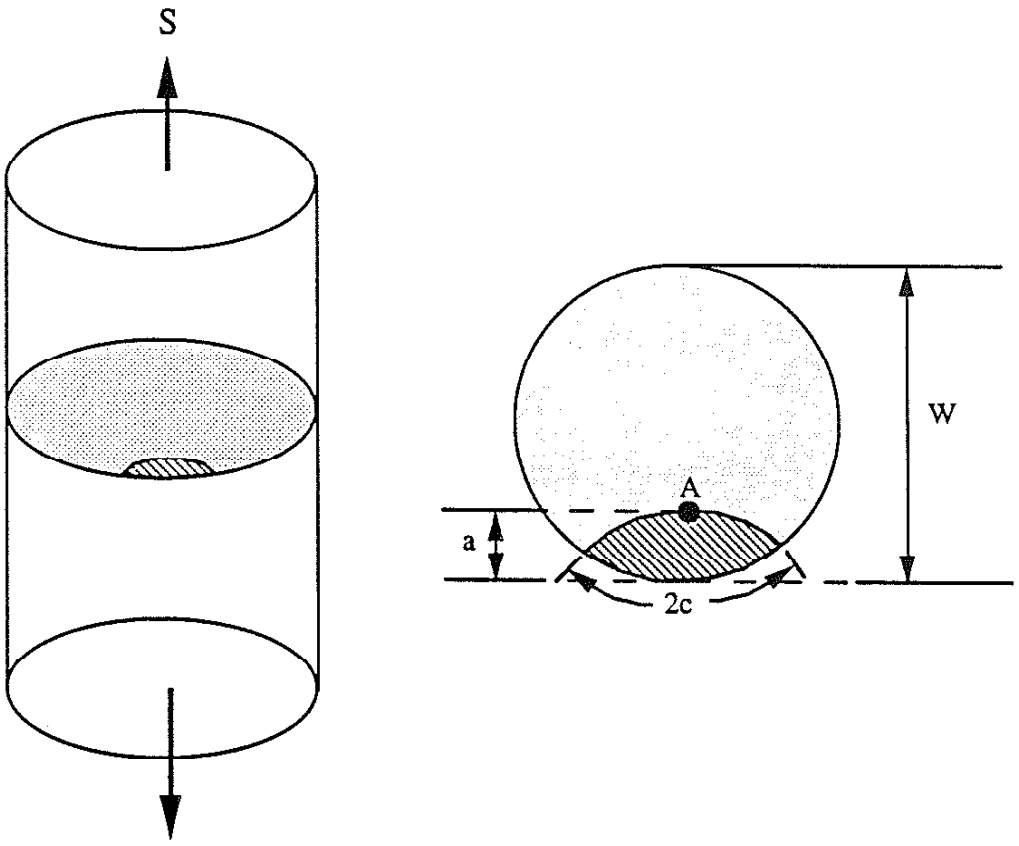


Figure A.1 The nomenclature and geometry of elliptical surface flaw in a cylindrical specimen. The planar geometry of a fatigue initiating defect is modelled by assuming aspect ratio, a/c (or AR) ranged between 0.7 and 0.9.

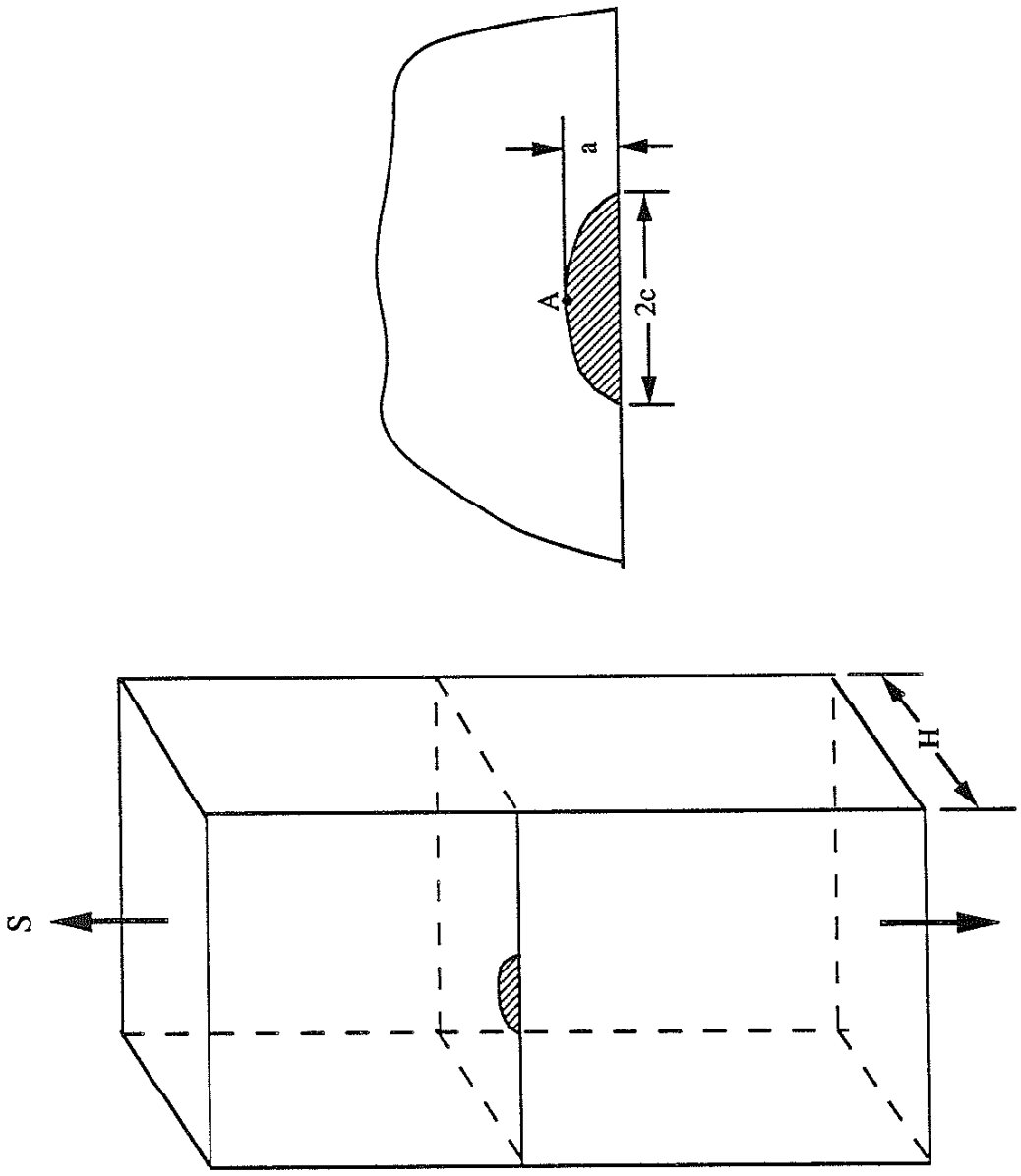


Figure A.2 The nomenclature and geometry of elliptical surface flaw in a plate. The crack propagates on the plane normal to the applied loading direction.

## APPENDIX B
## THE NOTCH-STRESS-FIELD BOUNDARY (NSFB)

Two major roles of the notch-stress-field boundary (NSFB) are involved in the CCN model. First, when the crack length (x) is shorter than the NSFB, the crack closure mechanism is assumed to be fully plasticity-induced crack closure (PICC). Second, the formulation of stress intensity for a crack length shorter than the NSFB is different from that for a crack length longer than the NSFB.

The value of NSFB remains poorly defined. Dowling [4] suggested an $l_t$ concept in which $l_t$ is the crack length at which the short-crack stress intensity factor equals that of the long crack. The short-crack stress intensity range at a notch ($\Delta K_S$) according to Dowling is :

$$\Delta K_S = 1.122 K_t \Delta S \sqrt{\pi x} \tag{B.1}$$

where:
$K_t$ = Stress concentration factor (gross section)
$\Delta S$ = Applied stress range (gross section)
$x$ = Crack length

When the crack length is greater than $l_t$, Dowling assumed that the influence of the notch on the stress intensity range is small; and thus, the stress intensity range is given by:

$$\Delta K = Y(a)\, \Delta S \sqrt{\pi a} \tag{B.2}$$

where:
$a$ = $D + x$; and $x \geq x^*$
$D$ = Notch depth
$Y(a)$ = Geometrical factor for stress intensity factor; see Appendix A
$\Delta S$ = Applied stress range (gross section)

From Eq. B.1 and B.2, the value of $l_t$ is:

$$l_t = \frac{D}{\left(\frac{1.12\, K_t}{Y(D+l_t)}\right)^2 - 1} \tag{B.3}$$

Based on Dowling's concept, the notch-stress-field boundary (NSFB) would be the value of $l_t$, which generally falls within the range of ρ/20 to ρ/4, where ρ is the radius of notch root; however, Smith and Miller [57] suggested $0.13\sqrt{D\rho}$ as the value of NSFB. Cameron and Smith [43] found that a better approximation of NSFB for notches with ρ/D $\leq 9$ is about $0.21\sqrt{D\rho}$. The values of NSFB found by Smith et al. are greater than those proposed by Dowling as shown in Fig. B.1. It seems that Dowling's $\Delta K_S$ formulation (Eq. B.2) over-predicts the stress intensity factor for the crack at a notch. Another $\Delta K_S$ formulation proposed by Lukas et al. (Eq. 2.21) provides better results than Dowling's, since Eq. 2.21 agrees well with the finite element results computed by Newman [58].

The value of NSFB for the CCN model is determined by equating Eq. 2.21 with Eq. B.2:

$$\frac{1.122K_t\sqrt{\pi x^*}}{\sqrt{1 + 4.5(x^*/\rho)}} = Y(a^*)\sqrt{\pi a^*} \qquad \text{(B.4)}$$

where:

$K_t$ = Stress concentration factor
ρ = Notch root radius
$x^*$ = Notch-stress-field boundary (NSFB)
$a^*$ = $D + x^*$
D = Notch depth

The value of $x^*$ calculated based on Eq. B.4 is $(0.15 \sim 0.2)\sqrt{D\rho}$ for a center notch in a plate (CNP) specimen and is $(0.2 \sim 0.25)\sqrt{D\rho}$ for a single edge notch in a plate (SENP) specimen. For both cases, the predicted $x^*$'s are close to those found by Cameron and Smith [43] and Tanaka et al.[27]. Thus, in this study, $x^*$ was used to represent the value of NSFB.

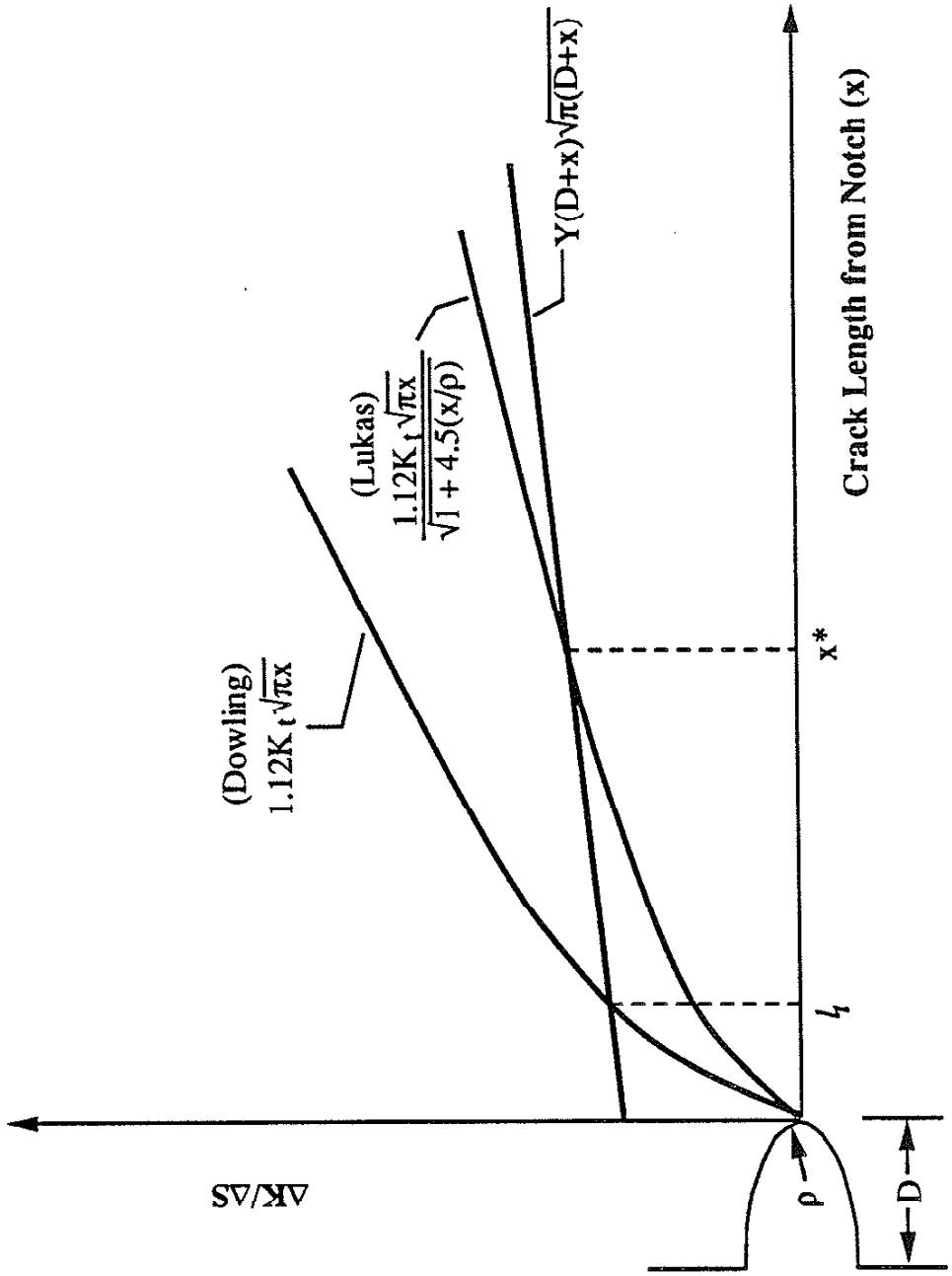


Figure B.1 Schematic diagram showing the concept for determination of initial crack length ($l_i$) and notch stress field boundary (x*). Note that $x^* > l_i$.

# APPENDIX C
# CCN MODEL FOR PREDICTING THE THRESHOLD STRESS

## C.1 Calculation of the Effective Threshold Stress Intensity Ratio at x* ($U^*_{th}$)

There are two possible outcomes for a notched component when the applied stress range ($\Delta S$) is equal to the threshold stress range ($\Delta S_{th}$). Both lead to an infinite fatigue life for the component. The two possible outcomes are:

1. No cracks initiate at the notch root.
2. Cracks initiate at the notch, but become non-propagating cracks (NPC) of length $x_{th}$.

The development of the CCN model starts with the case of the non-propagating crack.

Figure C.1 schematically shows the variation of da/dN with $\Delta K$ for short cracks emanating from a notch. Short cracks can propagate when their $\Delta K$ values are less than the long-crack threshold stress intensity range ($\Delta K_{tho}$). At the threshold condition, short crack starts growing at a rate which decreases with increasing crack length (or increasing $\Delta K$ values) and finally, becomes almost zero, resulting in a non-propagating crack.

Because the crack closure mechanisms at the threshold condition ($\Delta S = \Delta S_{th}$) are different from the mechanisms for the $\Delta S > \Delta S_{th}$ conditions, $U_{th}(x)$ is used to specify the threshold condition (for $\Delta S \le \Delta S_{th}$ ), and U(x) represents the general case for the following discussions. As schematically shown in Fig. C.2, the Tanaka model ($U^T(x)$) can be used to describe $U_{th}(x)$ for $x \ge x^*$ condition; see definition of x* in Appendix B. Under this condition, the crack tip "sees" a stress intensity range which is nearly identical to that of a smooth component at the threshold condition. On the other hand, when the crack is within the notch stress field boundary ($x \le x^*$), it is reasonable to use the Sun and Sehitoglu model ($U^S(x)$) to describe $U_{th}(x)$, since the notch's stress concentration makes the PICC mechanism dominate crack closure as suggested by Tao et al. [26], Shin et al. [29] and Sehitoglu et al. [32-34].

The valid ranges in applying $U^S(x)$ are $0.4 \le S_{max}/S_y \le 0.8$ and $3 \le K_t \le 7$, where $S_{max}$ is the maximum applied stress in a cyclic stress range. Extrapolation in the derivation of $U^S(x)$ is assumed to be valid when $S_{max}$ and $K_t$ are out of those ranges, but a modification is made as discussed below.

The values of $S_{opo}/S_{max}$, which are functions of $S_{max}/S_y$, calculated by the Sun and Sehitoglu model (Eq. 2.15b) are shown by the line a-b-c in Fig. C.3a for H/E = 0.01 under plane stress and the R equals -1 condition. This a-b-c line was calculated based on the PICC mechanism. At and below the threshold condition, the values of $S_{opo}/S_{max}$ are

constant, which is shown by the b-d line in Fig. C. 3. The extrapolation of $S_{opo}/S_{max}$ must be limited by the threshold conditions, where the maximum $S_{opo}/S_{max}$ was limited by the value of $U_{tho}$ (see Fig. C.3b). Thus, using Eq. 2.15b to determine the stabilized opening stress ($S_{opo}$) for a long crack, the relation between $S_{opo}/S_{max}$ and $S_{max}/S_y$ must follow the curve a-b-d. The constant $S_{opo}/S_{max}$ at and below the threshold condition (in the low stress regime, i.e., the line b-d in Fig. C.3) is determined by :

$$\frac{S_{opo}}{S_{max}} = 1.0 - (1.0 - R)U_{tho} \qquad (C.1)$$

Figure C.3b shows that the relation between $U_o$ and $S_{max}/S_y$ can be derived from the relation between $S_{opo}/S_{max}$ and $S_{max}/S_y$. After this relationship (Fig. C.3b) is determined, the function of U(x) in the vicinity of notch root (i. e. $x \leq x^*$) can be modelled using Eqs. 2.14 - 2.16. When $\Delta S = \Delta S_{th}$, the value of effective threshold stress intensity ratio ($U^*_{th}$) at $x = x^*$ can be derived from $U^S(x)$ using the following steps:

(1) Specifying material properties such as $S_y$, $U_{tho}$, and H/E (0.07 for steel and 0.01 for aluminum alloys) and the notched conditions such as $K_t$ and D;
(2) Assuming an applied stress ($S_{max}$) to be the threshold stress ($S_{th}$) at a given R ratio, then calculating $S_{opo}$ using Eq. 2.15 and the concept shown in Fig. C.3;
(3) Deriving $S_{op}(x^*)/S_{max}$ from Eq. 2.14 ;
(4) Deriving the value of $U^*_{th}$ (i.e. $U^S(x^*)$) from Eq. 2.16.

## C.2 The Derivation of a Hypothetical "Effective Notch Depth ($D_{eff}$)"

Figure C.4 is a schematic diagram which shows the method used to combine these $U^T(x)$ and $U^S(x)$ models to form a hybrid crack-closure model, $U_{th}(x)$. For $x \leq x^*$, the function of $U_{th}(x)$ can be modelled by employing the (modified) Sun and Sehitoglu model ($U^S(x)$); for $x \geq x^*$, the function of $U_{th}(x)$ can be modelled by employing the Tanaka model ($U^T(x)$). The initial value of $U^T(x)$ for $x = x^*$ was taken as the value of $U^S(x)$ at $x = x^*$ (termed $U^*_{th}$). Thus, the transition from $U^S(x)$ to $U^T(x)$ was forced at the notch stress field boundary ($x^*$) in the manner described: see Fig. C.4.

$U^*_{th}$ was determined by using $U^S(x)$ model, which requires a value for the applied stress range. However, the applied threshold stress range ($\Delta S_{th}$) is unknown; thus, the value of $U^*_{th}$ was obtained from a "guessed" threshold stress as described above. To

simplify the calculation of $\Delta S_{th}$, a hypothetical "Equivalent Crack in an Un-Notched Specimen" (ECUNS) is defined which has the same value of $U^*_{th}$ at x* as the crack in the notched specimen. The length of the ECUNS (denoted as x') is found by substituting $U^*_{th}$ into Eq. 2.13:

$$x' = \frac{L_o}{\left(\frac{U^*_{th}}{U_{tho}}\right)^2 - 1} \tag{C.2}$$

When the actual crack length is longer than the notch stress field boundary ($x \geq x^*$), $U^T(x)$ can be used to describe the variation of crack closure with crack length. The initial condition for $U^T(x)$ at $x = x^*$ is the value of $U^*_{th}$. Therefore, at $x = x^*$, $U^*_{th}$ can also be expressed by :

$$U^*_{th} = U^T(x') = U_{tho}\sqrt{\frac{L_o + x'}{x'}} \tag{C.3}$$

Let

$$\Delta x = x' - x^* \tag{C.4}$$

The value of $\Delta x$ is the difference between the actual length of the notch stress field boundary in the notched specimen (x*) and the length of the ECUNS (x') when the applied stress range is $\Delta S_{th}$. Another important physical meaning of $\Delta x$ is that $\Delta x$ represents the difference between the crack lengths, at the same crack closure level, of a crack originating from a smooth specimen and a crack emanating from a notch. Actually, this difference results from the effect of the notch stress field. The $\Delta x$ value was determined using the Sun and Sehitoglu model and was used to modify the Tanaka model. If the value of $U^T(x)$ at $x = x^*$ is larger than that of $U^S(x)$ at $x = x^*$, $\Delta x$ is positive; on the other hand, if the value of $U^T(x)$ at $x = x^*$ is smaller than that of $U^S(x)$ at $x = x^*$, $\Delta x$ is negative.

The effective notch depth ($D_{eff}$) is defined by:

$$D_{eff} = D - \Delta x \tag{C.5}$$

C.3 Calculation of $\Delta S_{th}$ for the Relatively Small Notches

The effective stress intensity range as a function of crack length for a crack emanating from a notch is given by:

$$\Delta K_{eff}(x) = U(x)\Delta K \qquad \text{(for the general case)} \qquad \text{(C.6a)}$$

and

$$\Delta K_{eff.th}(x) = U_{th}(x)\Delta K \qquad (\text{for } \Delta S = \Delta S_{th} \text{ only}) \qquad \text{(C.6b)}$$

When the applied stress range equals the threshold stress range ($\Delta S_{th}$), the variation of the effective threshold stress intensity range with the crack length is expressed by $\Delta K_{eff.th}(x)$. $\Delta K_{eff.th}(x)$ is a special expression of the threshold condition which is termed as a special condition of the general expression for the effective stress intensity range ($\Delta K_{eff}(x)$). The function U(x) (at $\Delta S > \Delta S_{th}$) decreases with increasing crack length and asymptotically approaches a constant value $U_o$; whereas the function of $U_{th}(x)$ (at $\Delta S = \Delta S_{th}$) asymptotically approaches $U_{tho}$. The fact that U(x) decreases with crack length and $\Delta K$ increases with crack length results in the variations of $\Delta K_{eff}(x)$ with crack length in the manner shown in Fig. C.5.

As seen in Fig. C.5, there is a minimum value of $\Delta K_{eff.th}(x)$ for a crack growing from a notch. When a curve of $\Delta K_{eff.th}(x)$ has its minimum value equal to $\Delta K_{eff.tho}$, the corresponding applied stress range is the threshold stress range of the notched component. Figure C.5 shows three different effective stress intensity curves ($\Delta K_{eff}(x)$) for a crack emanating from a notch. When the applied stress range is larger than $\Delta S_{th}$, $\Delta K_{eff}(x)$ is always higher than $\Delta K_{eff.tho}$, and thus the crack will keep propagating until final fracture. When the applied stress range is smaller than $\Delta S_{th}$, the $\Delta K_{eff}(x)$ fall below $\Delta K_{eff.tho}$ before reaching its minimum value; thus, the specimen will never fail, and the non-propagating crack length equals $x_1$. If the applied stress range equals $\Delta S_{th}$, the effective stress intensity range for a crack emanating from a notch is termed $\Delta K_{eff.th}(x)$, which has a minimum value of $\Delta K_{eff.tho}$. The greatest possible length of a non-propagating crack is located at $x = x_{th}$.

Tanaka et al. [27] found that the non-propagating crack length increased with increasing applied stress range ($\Delta S$) in the range $\Delta S \leq \Delta S_{th}$. The greatest possible NPC lengths were reached at $\Delta S = \Delta S_{th}$, and their values were always greater than the notch stress field boundary (NFSB). The same results were also found by Yates and Brown [42], who collected several test results from other sources.

The fact that the maximum NPC length was observed when the applied stress range ($\Delta S$) equals $\Delta S_{th}$ and its length was always greater than x* implies that the minimum value of $\Delta K_{eff.th}(x)$ is located beyond the NSFB. Thus, to predict the threshold stress for a notched component, it is only necessary to study the variation of $\Delta K_{eff.th}(x)$ for $x \geq x^*$.

When the crack length (x) is longer than the notch stress field boundary x*, the variation of $U_{th}(x)$ is obtained from Eq. C.3:

$$U_{th}(x) = U_{tho} \sqrt{\frac{L_o + x + \Delta x}{x + \Delta x}} \tag{C.7}$$

The variation of the effective threshold stress intensity range (with $\Delta S = \Delta S_{th}$) for a crack beyond the notch stress field boundary ($x \geq x^*$) is:

$$\Delta K_{eff.th}(x) = U_{th}(x)\, \Delta K = U_{th}(x)\, Y(x)\, \Delta S_{th} \sqrt{\pi(x+D)} \tag{C.8}$$

An expression for $\Delta K_{eff.th}(x)$ can be further derived by combining Eq. C.7 and Eq. C.8:

$$\Delta K_{eff.th}(x) = Y(x)\, \Delta S_{th}\, U_{tho} \sqrt{\frac{\pi\,(x+D)\,(L_o+x+\Delta x)}{x+\Delta x}} \tag{C.9}$$

The minimum value of $\Delta K_{eff.th}(x)$ occurs at $x = x_{th}$, where $x_{th}$ can be found by setting the derivative of $\Delta K_{eff.th}(x)$ equal to zero:

$$\frac{d}{dx}\left[\Delta K_{eff.th}(x)\right] = 0 \qquad (\text{at } x = x_{th}) \tag{C.10}$$

Thus, the maximum non-propagating crack length ($x_{th}$) is:

$$x_{th} = \sqrt{DL_o - \Delta x L_o} - \Delta x = \sqrt{D_{eff}\, L_o} - \Delta x \tag{C.11}$$

The value of $\Delta K_{eff.th}(x_{th})$ equals $\Delta K_{eff.tho}$. Thus, $\Delta S_{th}$ can be found by substituting $x_{th}$ (Eq. C.11) into Eq. C.9 and using the definition $\Delta K_{eff.tho} = U_{tho}\Delta K_{tho}$:

$$\Delta S_{th} = \frac{\Delta S_e}{Y(x_{th})} \sqrt{\frac{L_o\,(x_{th} + \Delta x)}{(x_{th} + D)(L_o + x_{th} + \Delta x)}} \tag{C.12}$$

Generally, Eq. C.12 is used to calculate the value of $\Delta S_{th}$ for a relatively small notch. As seen in Eq. 2.19, the fatigue notch factor ($K_f$) is defined as the fatigue limit of a smooth specimen divided by the fatigue threshold stress ($\Delta S_{th}$; gross-section basis); thus, Eq. C.12 can be represented by:

$$K_f = Y(x_{th}) \sqrt{\frac{(x_{th} + D)\,(L_o + x_{th} + \Delta x)}{L_o\,(x_{th} + \Delta x)}} \tag{C.13}$$

According to Eq. C.11,

$$x_{th} + \Delta x = \sqrt{D_{eff}\,L_o} \tag{C.14}$$

substituting Eq. C.14 into Eq. C.13,

$$K_f = Y(x_{th}) \sqrt{\frac{(D_{eff} + \sqrt{D_{eff}L_o})\,(L_o + \sqrt{D_{eff}L_o})}{L_o\,\sqrt{D_{eff}L_o}}} \tag{C.15}$$

and

$$K_f = Y(x_{th}) \sqrt{\frac{2D_{eff}L_o + (D_{eff} + L_o)\sqrt{D_{eff}L_o}}{L_o\,\sqrt{D_{eff}L_o}}} \tag{C.16}$$

$$K_f = Y(x_{th}) \sqrt{\frac{2\sqrt{D_{eff}L_o} + D_{eff} + L_o}{L_o}} \tag{C.17}$$

Equation C.17 can be further represented by:

$$K_f = Y(x_{th})\,(1 + \sqrt{\frac{D_{eff}}{L_o}}) \tag{C.18}$$

For a center notch in an infinite plate (CNP) specimen, $K_{fn}$ (net-section basis) can be assumed equal to $K_f$ (gross-section basis), thus,

$$K_{fn} = 1 + \sqrt{\frac{D_{eff}}{L_o}} \tag{C.19}$$

For a center notch in an infinite plate (CNP) specimen, $K_{fn}$ (net-section basis) can be assumed equal to $K_f$ (gross-section basis), thus,

$$K_{fn} = 1 + \sqrt{\frac{D_{eff}}{L_o}} \tag{C.19}$$

Equation C.19 is similar to the Topper model (see Eq. 2.30) and Lawrence's $K_{fmax}$ model (Eq. 2.20). As discussed in section 2.4.4, the Topper model was derived based on the Tanaka model, which did not consider the effect of the notch stress concentration on the crack closure level. In the CCN model, the effect of the notch stress concentration on crack closure was considered based on the Sun and Sehitoglu model. The difference in $U_{th}(x)$ between the CCN model (based on the cooperation of $U^T(x)$ and $U^S(x)$ models) and the Topper model (based on $U^T(x)$ model only) leads to different $K_{fn}$ values. In the Topper model, the ratio of actual notch depth (D) to $L_o$ ($D/L_o$) was used to predict $K_{fn}$; while in the CCN model, the ratio of effective notch depth ($D_{eff}$) to $L_o$ ($D_{eff}/L_o$) was used to predict $K_{fn}$.

Note that the values of $\Delta x$ and $x_{th}$ were both obtained from the previously assumed value of $\Delta S_{th}$, which was used to calculate the value of $U^*_{th}$. Thus, an iteration must be carried out to obtain the exact values of $\Delta S_{th}$ and $\Delta S_{thn}$ (calculated from the $\Delta S_{th}$ and area of gross and net-section).

## C.4 Calculation of $\Delta S_{th}$ for the Relatively Large Notches

When the value of $x_{th}$ calculated based on Eq. C.11 is smaller than x* (i.e., $x_{th} < x^*$), the minimum value of $\Delta K_{eff.th}(x)$ for a crack emanating from a notch falls within the notch stress field boundary. This condition may occur in the large notches, and for these large notches, the minimum values of $\Delta K_{eff.th}(x)$ are forced at $x = x^*$:

$$\Delta K_{eff.th}\,(x = x^*) = U^*_{th}\, Y(x^*)\, \Delta S_{th} \sqrt{\pi\,(D + x^*)} = \Delta K_{eff.tho} \tag{C.20}$$

and thus,

$$\Delta S_{th} = \frac{\Delta S_e\, U_{tho}}{U^*_{th}\, Y(x^*)} \sqrt{\frac{L_o}{(D + x^*)}} \tag{C.21}$$

For a center notch in an infinite plate (CNP) specimen, $K_{fn}$ (net-section basis) can be assumed equal to $K_f$ (gross-section basis), thus,

$$K_{fn} = \frac{U_{th}^*}{U_{tho}} \sqrt{\frac{(D+x^*)}{L_o}} \tag{C.23}$$

Assuming that $x^* = 0.18\sqrt{D\rho}$ and $\rho = 4D/(K_{tn} - 1)^2$, then

$$K_{fn} = \frac{U_{th}^*}{U_{tho}} \sqrt{\frac{D + \frac{0.36\ D}{(K_{tn} - 1)}}{L_o}} \tag{C.24}$$

Thus,

$$K_{fn} = \left(\frac{U_{th}^*}{U_{tho}}\right) \sqrt{\frac{(K_{tn} - 0.64)}{(K_{tn} - 1)}} \sqrt{\frac{D}{L_o}} = (UK)_{eff} \sqrt{\frac{D}{L_o}} \tag{C.25}$$

For a very large notch, the value of $(UK)_{eff}$ approaches unity, thus, $K_{fn}$ can be estimated by $\sqrt{D/L_o}$. This leads to the same expression proposed by Smith et al. (see Eq. 2.18).

The value of $U_{th}^*$ is an applied stress dependent variable. Thus, an iteration must be carried out to obtain the exact values of $\Delta S_{thn}$ and $U_{th}^*$. When the calculated value of $\Delta S_{thn}$ is smaller $\Delta S_e/K_{tn}$, no fatigue crack should form at the notch root and Eqs. C.18 and C.22 are invalid; therefore, under this condition, the largest applied stress range for infinite life ($\Delta S_{thn}$) would be limited by $\Delta S_e/K_{tn}$. In this case, the threshold stress is controlled by the crack nucleation process.

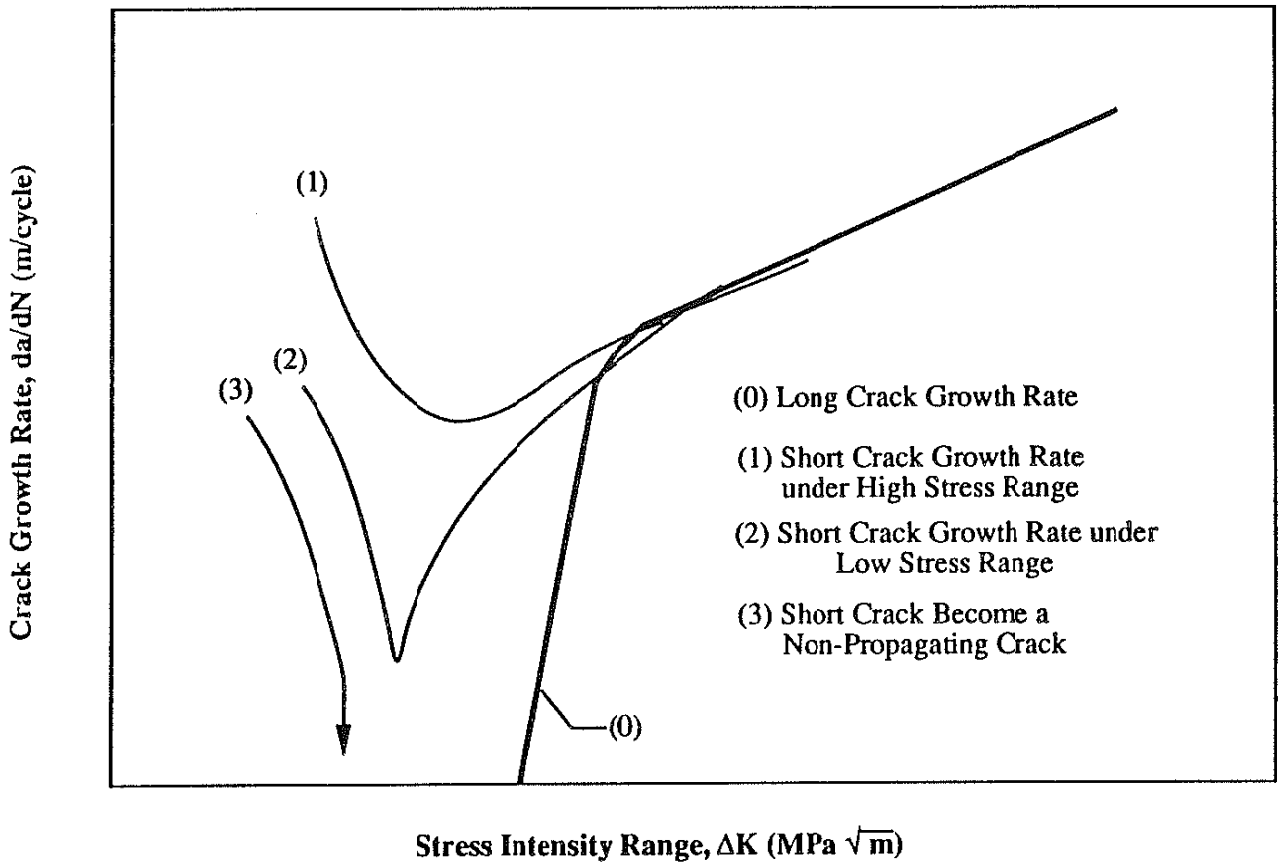


Figure C.1 The anomalous crack growth behavior of short cracks.

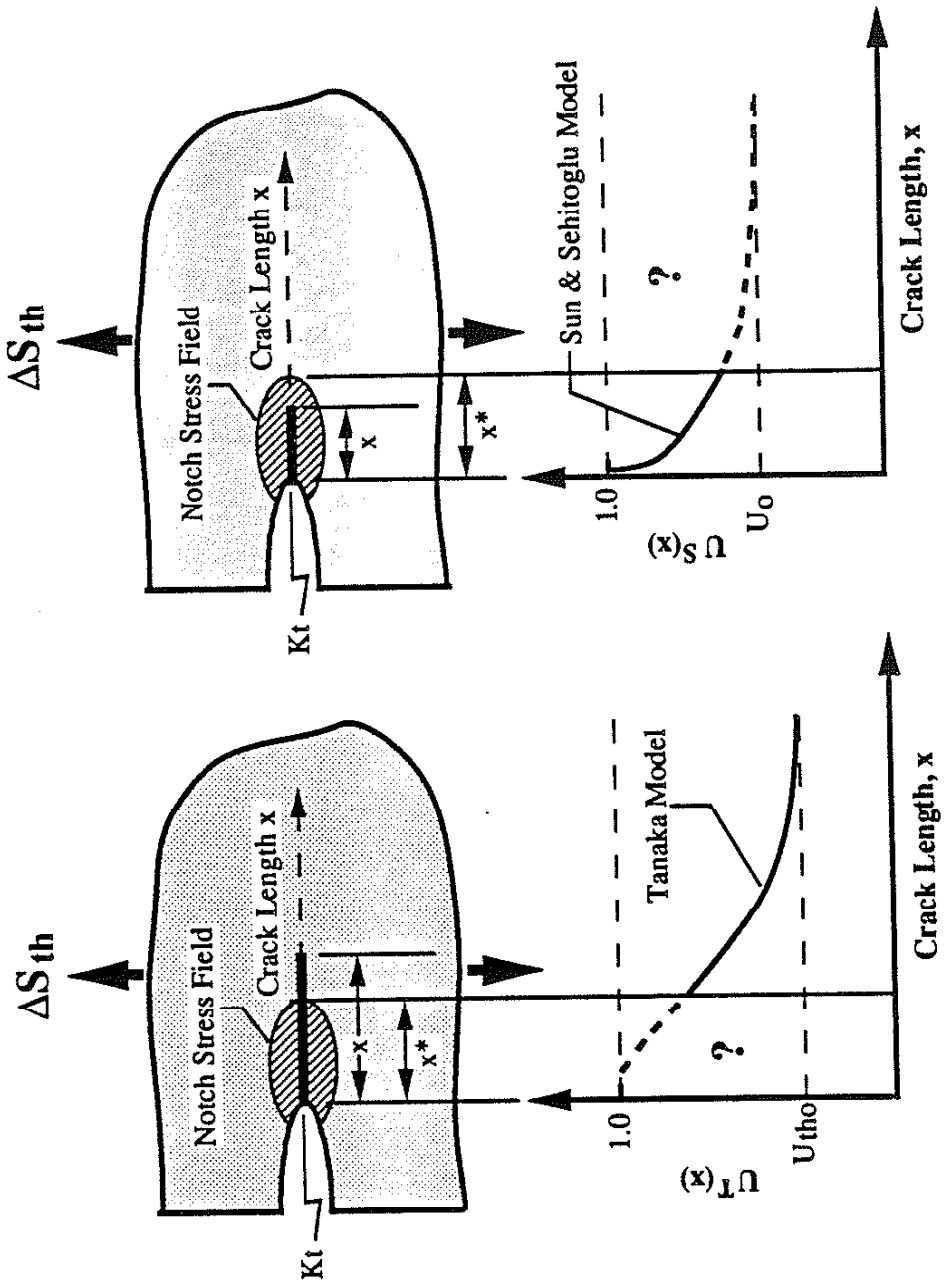


Figure C.2 Comparison of Tanaka's and Sun and Sehitoglu's models. Tanaka's model (Left) is applicable when the crack is beyond the notch stress field. Sun and Sehitoglu's model (Right) is applicable when the crack is within the notch stress field.

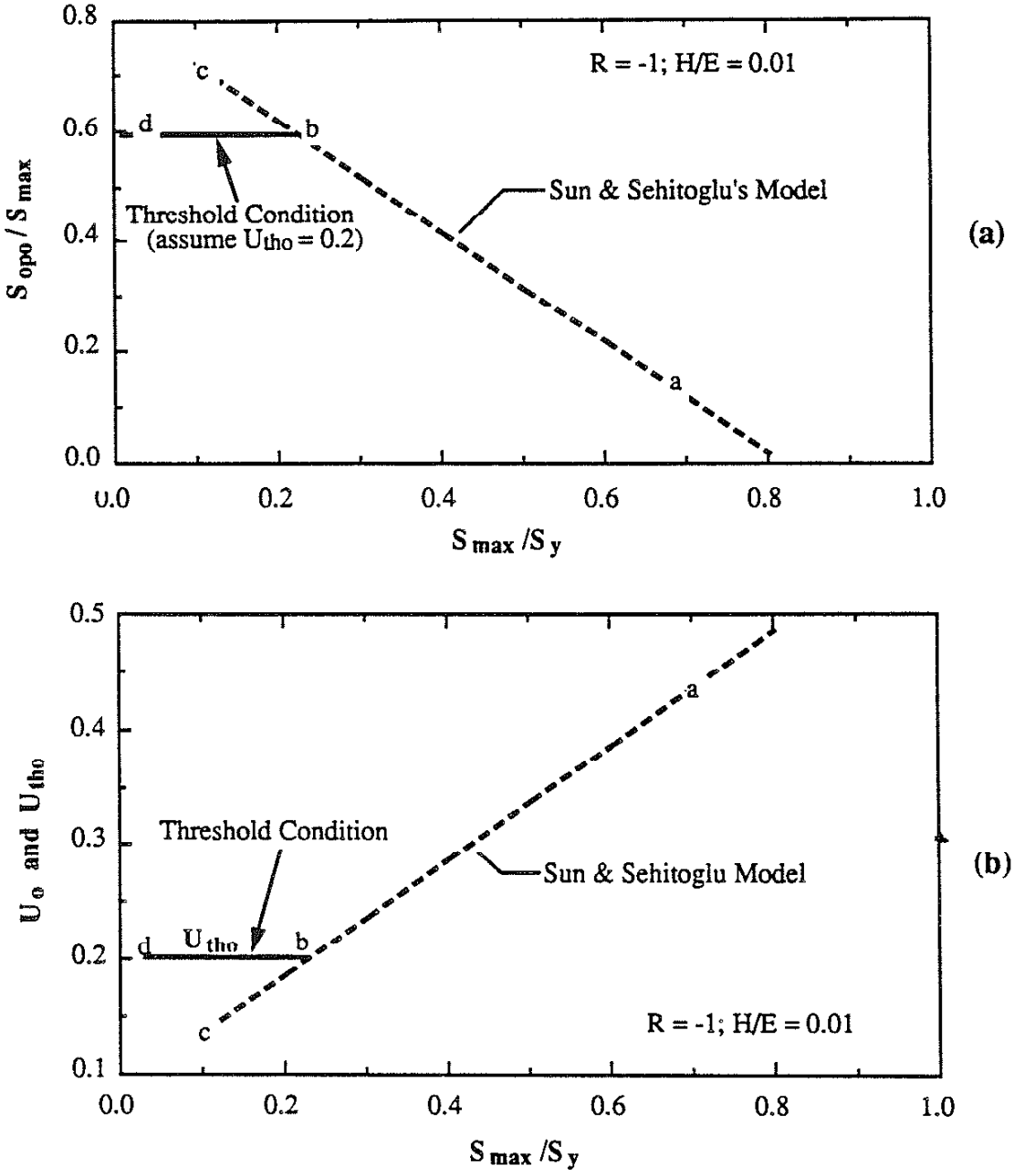


Figure C.3 The values of $S_{max}/S_y$ and $U_o$ calculated from Sun and Sehitoglu model are limited by the threshold condition. (a) the relation between $S_{max}/S_y$ and $S_{max}/S_y$ follows line a-b-d, (b) the relation between $U_o$ (or $U_{tho}$) and Smax/Sy must follow line a-b-d.

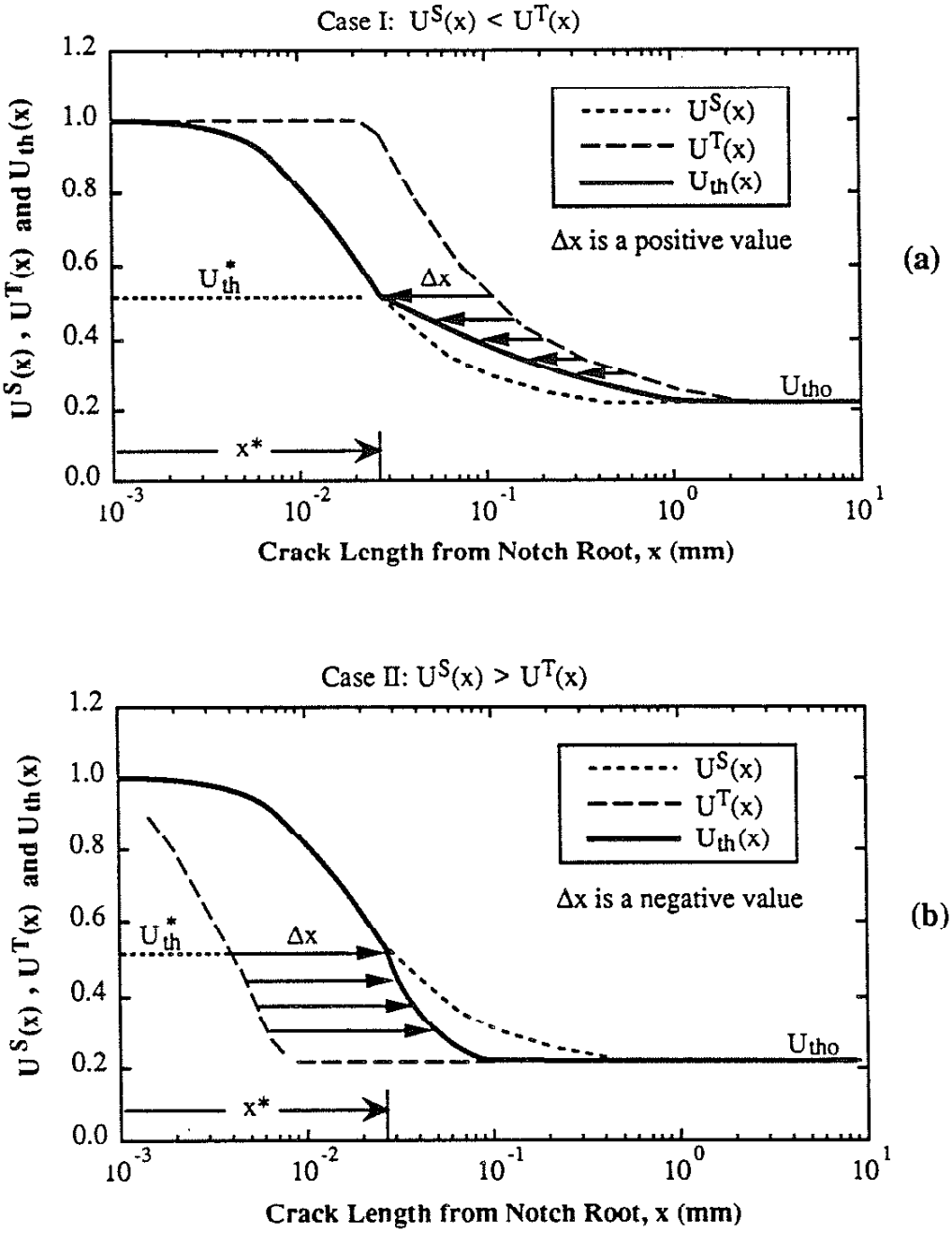


Figure C.4 Schematic diagram showing two possible cases for deriving the $U_{th}$ (x) functions. Both cases are derived from the combinations of the Tanaka model and the Sun and Sehitoglu model.

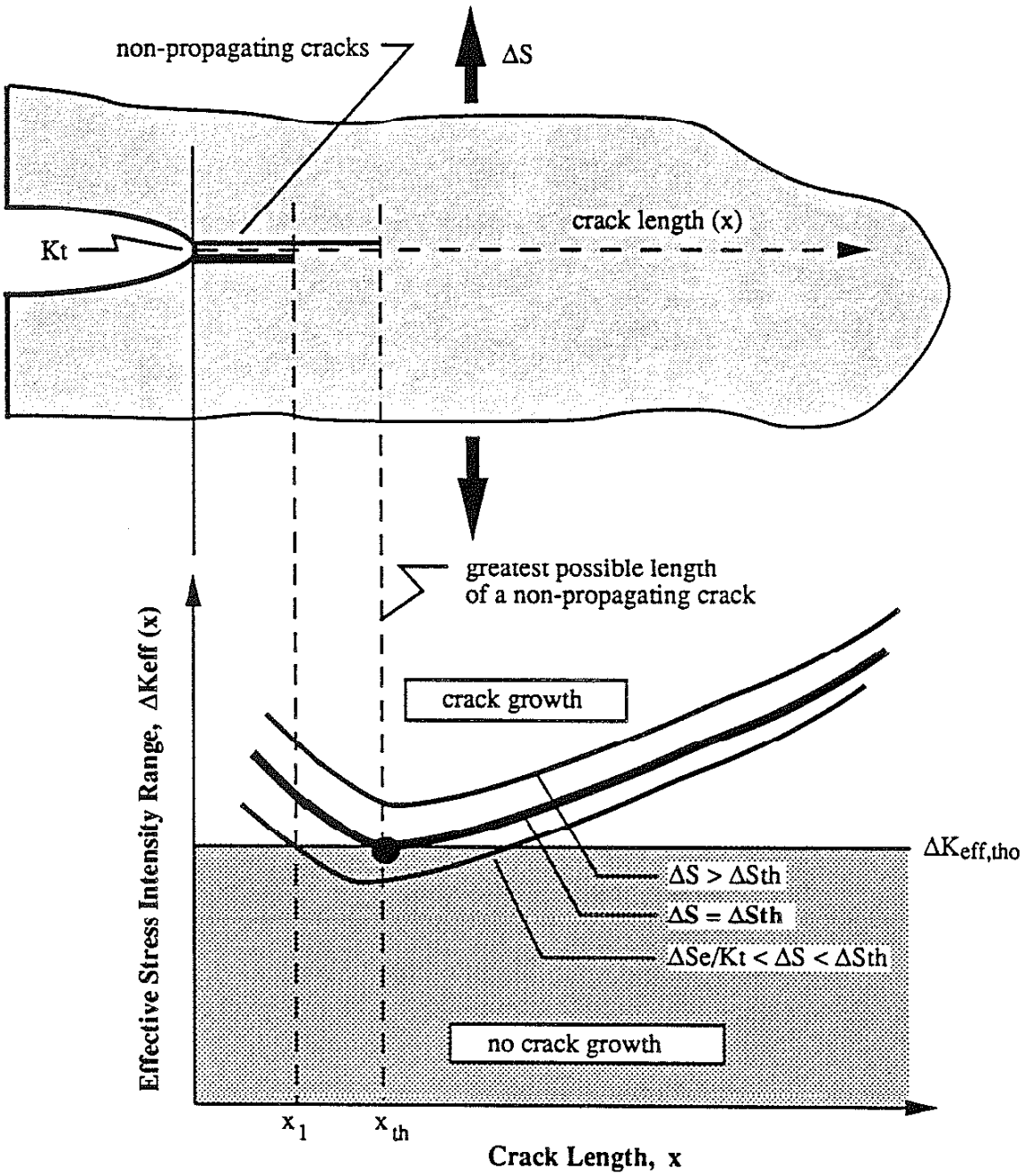


Figure C.5 The variation of $\Delta K_{eff}(x)$ with crack length (x) as a function of applied stress range ($\Delta S$). Threshold stress range was determined when the minimum value of $\Delta K_{eff}(x)$ equals $\Delta K_{eff,tho}$.

# APPENDIX D

## MODEL FOR FATIGUE LIFE BASED ON SHORT AND LONG CRACK PROPAGATION

### D.1 Crack Closure at Greater-Than-Threshold Conditions

When the crack is beyond the notch stress field boundary at $\Delta S > \Delta S_{th}$, the crack "sees" only the remote stress. The significance of each crack closure mechanism is dependent on the level of the applied stress intensity range. When the applied remote stress is low, such that the crack driving force is in near threshold conditions, the RICC and/or OICC mechanisms play more important roles than the PICC mechanism. Thus, $U^T(x)$ reasonably describes the variation of crack closure with crack length in the low stress regime. However, according to the concept proposed by Suresh et al.[9] and Allison [10], when the applied stress (or $K_{max}$) is much larger than threshold stress, the PICC mechanism may play a more important role than the other mechanisms. The transition of the crack closure mechanism from RICC/OICC dominant to PICC dominant must be quantitatively described and is believed to be a function of $S_{max}$ or $K_{max}$.

To determine the value of $\Delta K$ (termed $\Delta K_x$) above which crack closure behavior can be assumed to be entirely PICC dominant, a hypothesis based on the relation between da/dN and $\Delta K$ of long crack is proposed. The da/dN versus $\Delta K$ relationship of the long crack can be formulated as a bi-linear curve and categorized as two regions (see the inserted plot in Fig. D.1): the near-threshold region (stage I) and the mid-growth rate region (stage II). There is a point of intersection ($\Delta K_x$) which represents the boundary between these two regimes. The point of intersection ($\Delta K_x$) is assumed to be the transition point at which the crack closure mechanism changes from a fully PICC controlled mechanism in the mid-growth rate regime to an only partially PICC controlled mechanisms in the near-threshold regime, and finally to a fully RICC and/or OICC controlled mechanism when $\Delta K$ falls below $\Delta K_{tho}$.

When a crack grows beyond the notch stress field boundary ($x \geq x^*$), the crack closure mechanisms under the $\Delta S = \Delta S_{th}$ condition will be different from the $\Delta S > \Delta S_{th}$ condition. For the case of a notched component loaded in a high applied stress range (where $\Delta S >> \Delta S_{th}$), the variation of U(x) can be considered to be fully dominated by the PICC mechanism, in which the value of $U_o$ is determined by the Sun and Sehitoglu model (Section 2.3.2) and is dependent upon the value of $S_{max}$. At the threshold condition ($\Delta S = \Delta S_{th}$), the crack closure mechanism can be considered to be dominated by the OICC and/or RICC mechanisms, and the Tanaka model is used to describe the function of U(x) (this

$U(x)$ was denoted as $U_{th}(x)$ in Appendix C). When the applied stress is a little higher than the threshold stress, the applied stress intensity range of the crack may fall in the near-threshold regime of the da/dN versus $\Delta K$ curve. Under this condition, the function $U(x)$ may be determined partly by the Sun and Sehitoglu model (the PICC dominated mechanism) and partly by the Tanaka model (the OICC/RICC dominated mechanism).

When a short crack emanates from a notch, the $U(x)$ is modelled by:

$$U(x) = U^S(x) \qquad \text{for } x \le x^* \qquad \text{(D.1)}$$

and

$$U(x) = F_p\, U^S(x) + (1 - F_p)\, U^{O/R}(x) \qquad \text{for } x > x^* \qquad \text{(D.2)}$$

where: $x^*$ = The notch stress field boundary (see Appendix B)

$F_p$ = The fraction of the crack closure mechanism that is PICC

$U^S(x)$ = The function of $U(x)$ calculated entirely based on the PICC mechanism

$U^{O/R}(x)$ = The function of $U(x)$ calculated entirely based on the RICC/OICC mechanism

The procedures used to derive the function of $U^{O/R}(x)$ are the same as those derived for the function $U_{th}(x)$ as discussed in Appendix C, except that the applied stress range ($\Delta S$) is a known value and is greater than the threshold stress range ($\Delta S_{th}$).

The fraction of the crack closure mechanism that is PICC ($F_p$) is assumed to be 100% when the $\Delta K$ value is greater than $\Delta K_x$ and 0% when the $\Delta K$ value is smaller than $\Delta K_{tho}$. When the applied $\Delta K$ is between $\Delta K_x$ and $\Delta K_{tho}$, the fraction of the crack closure mechanism that is PICC ($F_p$) is assumed to be an exponential function which is dependent on the two slopes of the long-crack da/dN versus $\Delta K$ bi-linear curve. The proposed exponential function shown in Fig. D.1 is given by:

$$F_p = 1 - \exp\left(-m_1\left(\frac{\Delta K - \Delta K_{tho}}{\Delta K_x - \Delta K_{tho}}\right)^{m_2}\right) \qquad \text{(D.3)}$$

where: $m_1$ = Slope of the bi-linear curve of da/dN vs. $\Delta K$ in the near-threshold regime (Stage I)

$m_2$ = Slope of the bi-linear curve of da/dN vs. $\Delta K$ in the mid-growth rate regime (Stage II)

It is noted that the value of $F_p$ is also a function of crack length because $\Delta K$ is a function of crack length. Figure D.2 shows two possible cases of U(x) when $\Delta S > \Delta S_{th}$. When $U^T(x^*) > U^S(x^*)$, the $U^{O/R}(x)$ is larger than the $U^S(x)$ for $x \geq x^*$ (see case I in Fig. D.2). When $U^T(x^*) < U^S(x^*)$, the $U^{O/R}(x)$ is smaller than the $U^S(x)$ for $x \geq x^*$ (see Case II in Fig. D.2). For both cases, the function U(x) lies in the region bounded by the functions $U^S(x)$ and $U^{O/R}(x)$.

Once the U(x) function is derived, the value of $\Delta K_{eff}(x)$ for a short crack emanating from a notch can be derived from the relation $\Delta K_{eff}(x) = U(x)\ \Delta K$. Using the unique material property of the da/dN versus $\Delta K_{eff}$ relationship, the variation of crack growth rate with crack length can be modelled. Consequently, the total propagation life for a notched component can be estimated.

## D.2 Fatigue Life Prediction for Constant Amplitude Loading Condition

Two formulations of the stress intensity range for a crack within and beyond the notch stress field boundary are used:

when $x < x^*$,

$$\Delta K_S = \frac{1.122 K_t \Delta S \sqrt{\pi x}}{\sqrt{1 + 4.5(x/\rho)}} \qquad \text{(D.4)}$$

where:

$K_t$ = Stress concentration factor (gross section)
$\Delta S$ = Applied stress range (gross section)
$\rho$ = Notch root radius
$x$ = Crack length from notch root

and when $x \geq x^*$,

$$\Delta K = Y(a)\ \Delta S \sqrt{\pi a} \qquad \text{(D.5)}$$

where:

$a$ = $D + x$; and $x \geq x^*$
$D$ = Notch depth

Y(a) = Geometrical factor for stress intensity factor; see Appendix A

The formulations of $\Delta K$ (or $\Delta K_S$) depend upon the notch size, the notch shape and the specimen geometry. The function $\Delta K_{eff}(x)$ equals $U(x)\Delta K$; the function of U(x) is derived using Eqs. D.1 - D.3. The value of $U_o$ used for $U^S(x)$ and $U^{O/R}(x)$ is determined using Eq. 2.15 and the concept of the $U_{tho}$ constraint as described in Appendix C (i.e., Fig. C.3).

The CCN model considers in detail the behavior of short cracks and early crack growth by modeling U(x) for short cracks emanating from a notch. The total propagation life is estimated by integrating the relation between da/dN and $\Delta K_{eff}$. The limits of integration start at a defined initial crack length ($l_t$ concept of Dowling [35], see Eq. B.3) and end at final fracture. The transition from the $\Delta K_S$ formulation (Eq. D.4) to the $\Delta K$ (Eq. D.5) occurs when the crack length equals the notch stress field boundary (x*). The behavior of the crack growth rate is represented by a bi-linear model in which the relations between da/dN and $\Delta K_{eff}$ are represented by two sets of C' and m values. The steps in deriving these two sets of C' and m values are discussed in Appendix E. The total propagation life ($N_f$) for a notch is given by:

$$N_f = \int_{x_i}^{x_f} \frac{dx}{C'_i \left(U(x)\,\Delta K\right)^{m_i}} \qquad \text{(D.6)}$$

Where:
- x = Crack length from notch
- $C'_i$, $m_i$ = Constants, see Appendix E
- U(x) = The variation of stress intensity ratio with crack length; see Eq. D.1 - D.3.
- $x_i$ = Initial crack length for integration = $l_t$
- $l_t$ = Transition crack length from Dowling; see Eq. B.3
- $x_f$ = Final crack length at failure
- $\Delta K$ = Stress intensity range; see Eqs. D.4 and D.5.

The final crack length at failure ($x_f$) is derived by:

$$K_{IC} = S_{max}\, Y(D+x_f) \sqrt{\pi(D+x_f)} \qquad \text{(D.7)}$$

where: $S_{max}$ = Maximum stress (gross section)

$Y(D+x_f)$ = Geometrical factor; see details in Appendix A

$K_{IC}$ = Fracture toughness (may use the $K_{IQ}$ value)

Because the CCN model discussed above considers early growth life in the short crack regime, the crack nucleation life ($N_n$) may be derived based on the Basquin-Morrow equation (Eq. 2.2), in which $K_{fn}$ (or $K_f$) is replaced by $K_{tn}$ (or $K_t$):

$$N_n = \frac{1}{2}\left(\frac{S_a K_t}{\sigma'_f \left[1 - \frac{\sigma_m}{\sigma'_f}\right]}\right)^{1/b} \qquad (D.8)$$

where:

$S_a$ = Remote applied stress amplitude (gross section)

$K_t$ = Theoretical stress concentration factor (gross section)

$\sigma'_f$ = Fatigue strength coefficient for smooth specimen

$b$ = Fatigue strength exponent for smooth specimen

$\sigma_m$ = Local mean stress

For notches sizes comparable to the microstructure of the material (e.g. grain size), the anomalous growth behavior of short crack can not be simply explained by crack closure; thus, the CCN model is not applicable. The limit of the CCN model applicability is discussed in Appendix F.

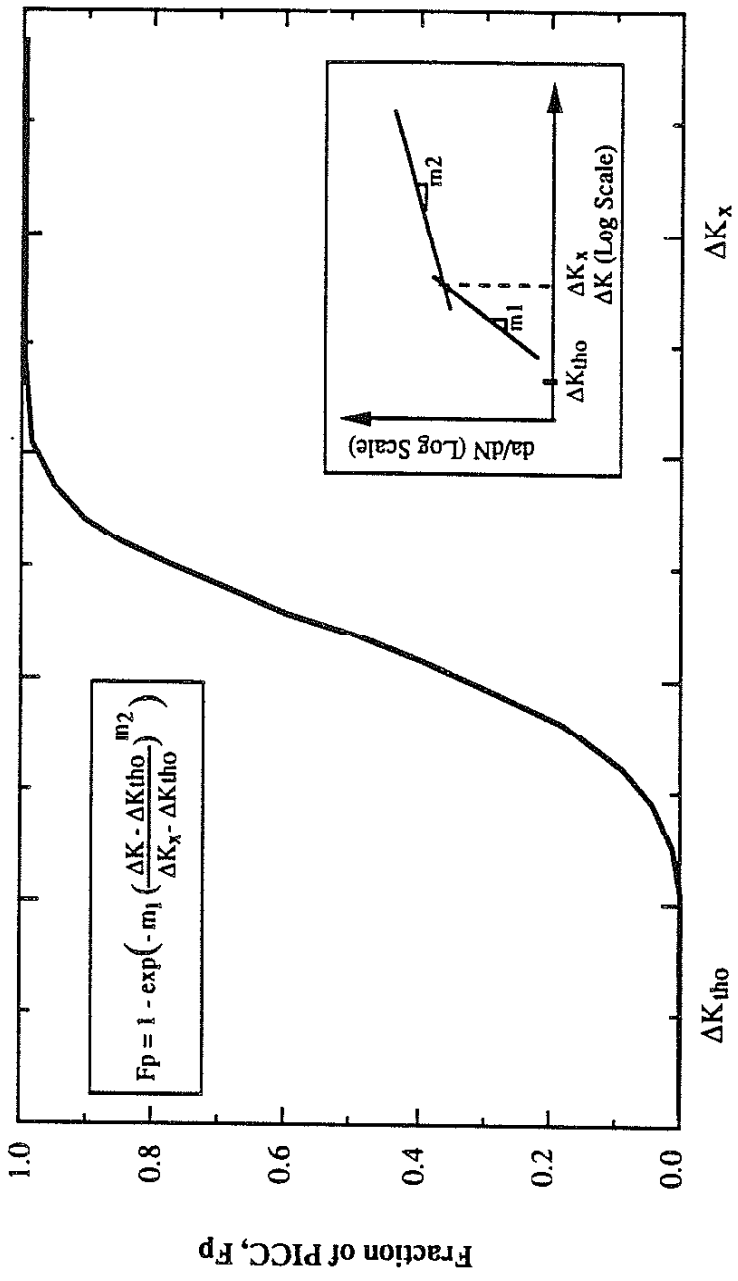


Figure D.1 The exponential function of $F_p$ is a function of ΔK when the crack is beyond the notch stress field. This function is used to determine the U(x) when crack is beyond the notch stress field. (A schematic diagram).

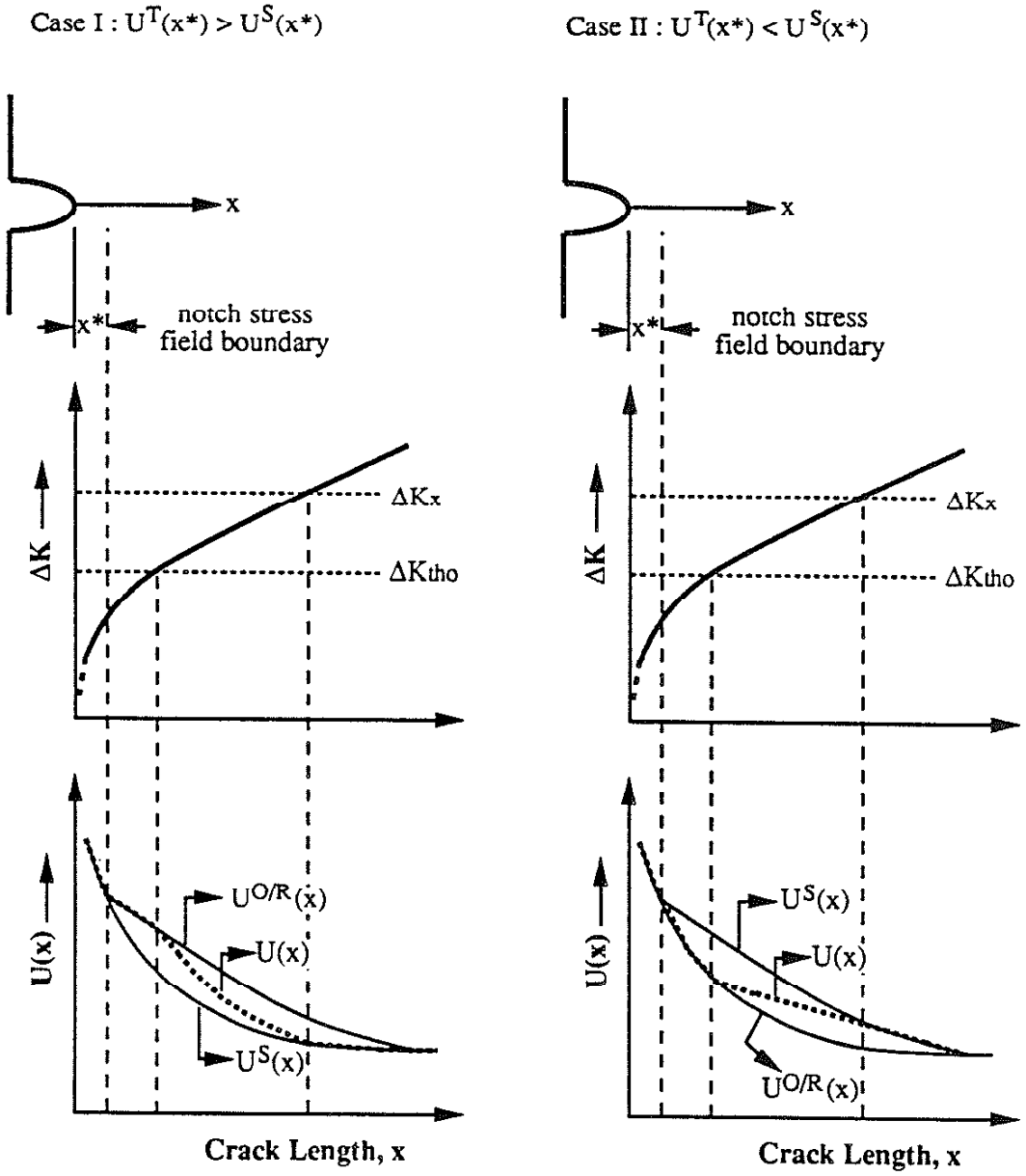


Figure D.2 The possible two cases of U(x) which lie in the region limited by the functions of $U^S(x)$ and $U^{O/R}(x)$.

# APPENDIX E
## THE RELATIONSHIP BETWEEN da/dN AND $\Delta K_{eff}$

The relationship between da/dN and $\Delta K_{eff}$ is assumed to be a unique material property for crack growth behavior, but the relationship between da/dN and $\Delta K$ is dependent upon the maximum applied stress ($S_{max}$), crack length (x), and the load ratio (R). Different $S_{max}$ or different R conditions result in different stabilized effective stress intensity ratios ($U_o$). Using the same concept of Fig. C.3, figure E.1 shows the relations between $U_o$ (or $U_{tho}$) and $S_{max}/S_y$ for materials with H/E = 0.01 and H/E = 0.07 and for three R ratios (R = -1, 0, 0.4). The value of $U_{tho}$ for each R ratio depends upon material properties such as grain size (d) and yield strength ($S_y$). The values of $U_o$ for the materials with H/E = 0.07 (steel) are always larger than those with H/E = 0.01 (aluminum alloys) at the same R ratio and $S_{max}/S_y$.

Figure E.2 assumes that the values of $U_{tho}$ (at R = -1) for both materials are 0.2. The value of $U_o$ is constant (= $U_{tho}$) in the low stress range for the H/E = 0.01 material, but the values of $U_o$ are different in all the stress ranges for the H/E = 0.07 material. If $U_{tho}$ for an H/E = 0.07 material equals 0.3, there will be a constant $U_o$ in the low $S_{max}/S_y$ range. The fact that the value of $S_{max}$ affects the da/dN versus $\Delta K$ relationship has been observed in 1070 and 1026 steel for the R equals -1 condition [72], in which a higher maximum stress results in a higher crack growth rate at the same $\Delta K$. Nisitani et al. [59] examined the crack growth behavior of 1045 steel and found that the relation of da/dN versus $\Delta K$ did not vary with the applied stress in the low stress region, but did vary in the high stress region. However, most of the tests that were performed using the Compact-Tension (CT) specimens did not see this $S_{max}$ dependence on the da/dN versus $\Delta K$ relationship. This discrepancy may be explained by the fact that the tests were generally performed at a constant $U_o$ range (low $S_{max}/S_y$). For the $R \geq 0$ conditions, $U_{tho}$ is generally greater than 0.5; thus, $U_o$ is almost a constant (= $U_{tho}$) in most of the stress regions. Additionally, most of the crack growth rate tests were carried out under the positive R ratio conditions. The above discussion may explain why the effect of $S_{max}$ on the da/dN versus $\Delta K$ relation was not found in the majority of the reports.

One method of deriving the da/dN versus $\Delta K_{eff}$ relationship from the da/dN versus $\Delta K$ relationship is to use sharply notched specimens and test in the very low $S_{max}$ range. However, the occurrence of a non-propagating crack may cause difficulties in the measurement of crack growth rate. A load-shedding method which may solve this problem is discussed below.

Sharply notched specimens ($K_{tn} \geq 7$) were selected and tested in an R equals -1 condition. The initial maximum applied stress ($S_{max}$) is selected as low as possible and tested until a through-thickness fatigue crack is observed which is longer than the notch-stress-field boundary x* (estimated by $0.21\sqrt{D\rho}$). The applied stress ranges (at the same R ratio) are then gradually decreased according to the instruction of ASTM E647 until the crack length becomes long enough to be considered a long crack. After the crack growth rate reaches the near-threshold regime (about $10^{-10}$ m/cycle), the stress is kept constant until the specimen breaks. Based on this load-shedding procedure, the relation of da/dN versus $\Delta K$ in both the near-threshold and the mid-growth rate regimes can be obtained. Additionally, the effective stress intensity range ($\Delta K_{eff}$) can be derived by the relation, $\Delta K_{eff} = U_{tho}\Delta K$. For the H/E = 0.07 materials, $U_o$ and $U_{tho}$ may need to be treated separately (depending upon the value of $U_{tho}$).

The value of $U_{tho}$ can be estimated by Eq. 2.10:

$$U_{tho} = \frac{\Delta K_{eff.tho}}{\Delta K_{tho}} = \frac{\eta E}{\Delta K_{tho}} \qquad \text{(E.1)}$$

where $\eta = 1.5 \times 10^{-5}$ for steel

$\eta = 2.0 \times 10^{-5}$ for aluminum alloys

$E$ = Young's modulus (MPa)

$\Delta K_{eff.tho}$ = Effective long-crack threshold stress intensity range ($MPa\sqrt{m}$)

A bi-linear model is applied to correlate the measured data of long crack growth rate (da/dN) with $\Delta K$, which is given by:

$$\frac{da}{dN} = C_i (\Delta K)^{m_i} \qquad (i = 1,2) \qquad \text{(E.2)}$$

Where $C_1$ = Crack growth coefficient in the near-threshold regime

$m_1$ = Crack growth exponent in the near-threshold regime

$C_2$ = Crack growth coefficient in the mid-growth rate regime

$m_2$ = Crack growth exponent in the mid-growth rate regime

Note that the long-crack growth data represented by Eq. E.2 is obtained from a very low applied stress. The effective stress intensity ratio in the entire range of $\Delta K$ can be

assumed to be a constant value which is the long-crack effective threshold stress intensity ratio ($U_{tho}$). The crack growth rate (da/dN) as a function of $\Delta K_{eff}$ is given by:

$$\frac{da}{dN} = C'_i (\Delta K_{eff})^{m_i} \qquad (i = 1,2) \qquad \text{(E.3)}$$

Where: $C'_1 = C_1 / (U_{tho})^{m_1}$ (in the near-threshold regime, Stage I)

$C'_2 = C_2 / (U_{tho})^{m_2}$ (for H/E = 0.01 material in Stage II)

$C'_2 = C_2 / (U_o)^{m_2}$ (for H/E = 0.07 material in Stage II)

For a crack emanating from a notch, equation E.3 can be used to rationalize the anomalous crack growth rate of a (mechanically) short crack, because the da/dN versus $\Delta K_{eff}$ relationship is a "real" material property and is independent of the load ratio and the applied stress level.

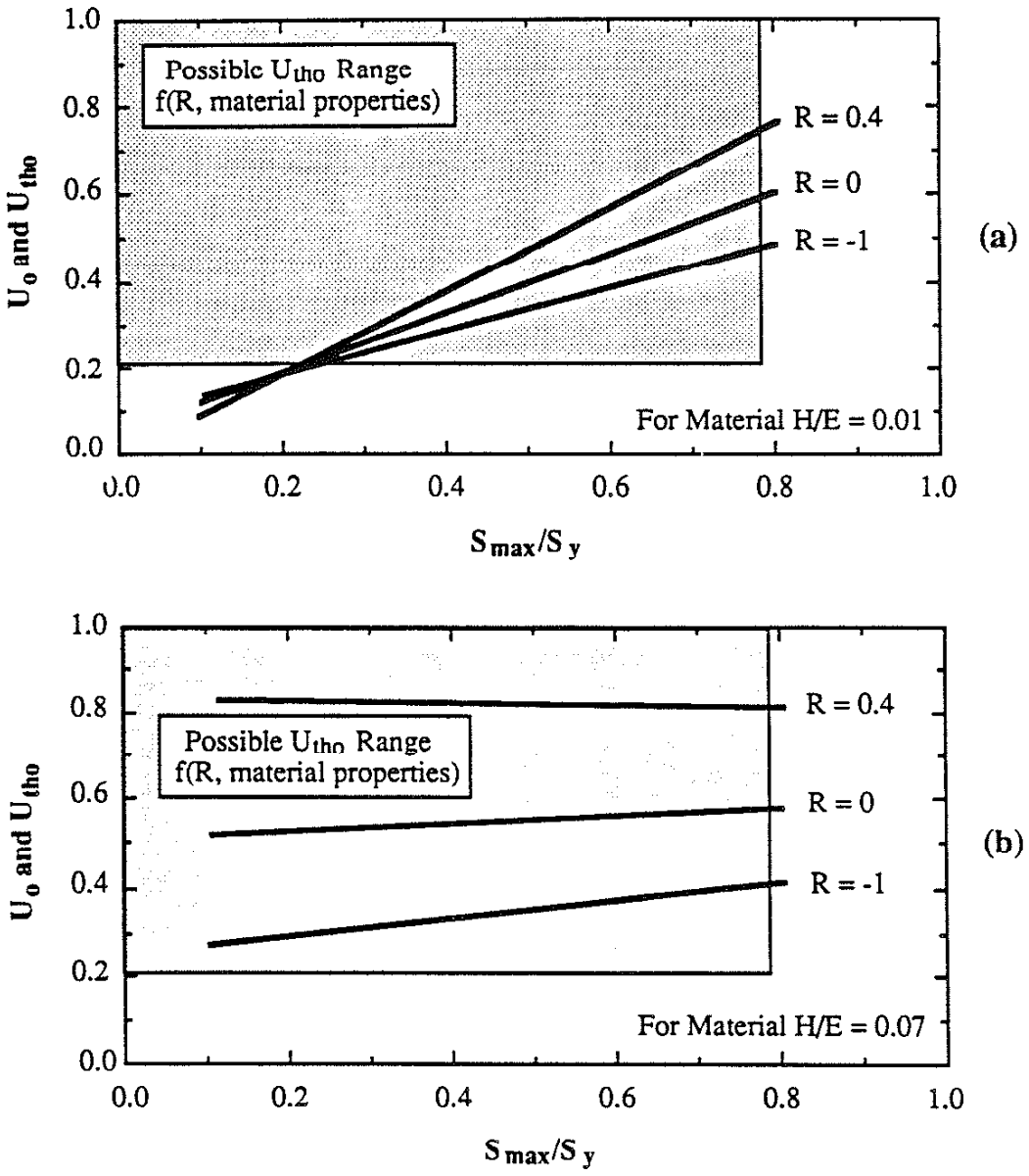


Figure E.1 The variation of $U_o$ with $S_{max}/S_y$ for various R ratios. Shaded area shows the possible value of $U_{tho}$ which is load ratio and material properties dependent variable. (a) for H/E = 0.01 material (aluminum alloy), and (b) H/E = 0.07 material (steel). (A schematic diagram).

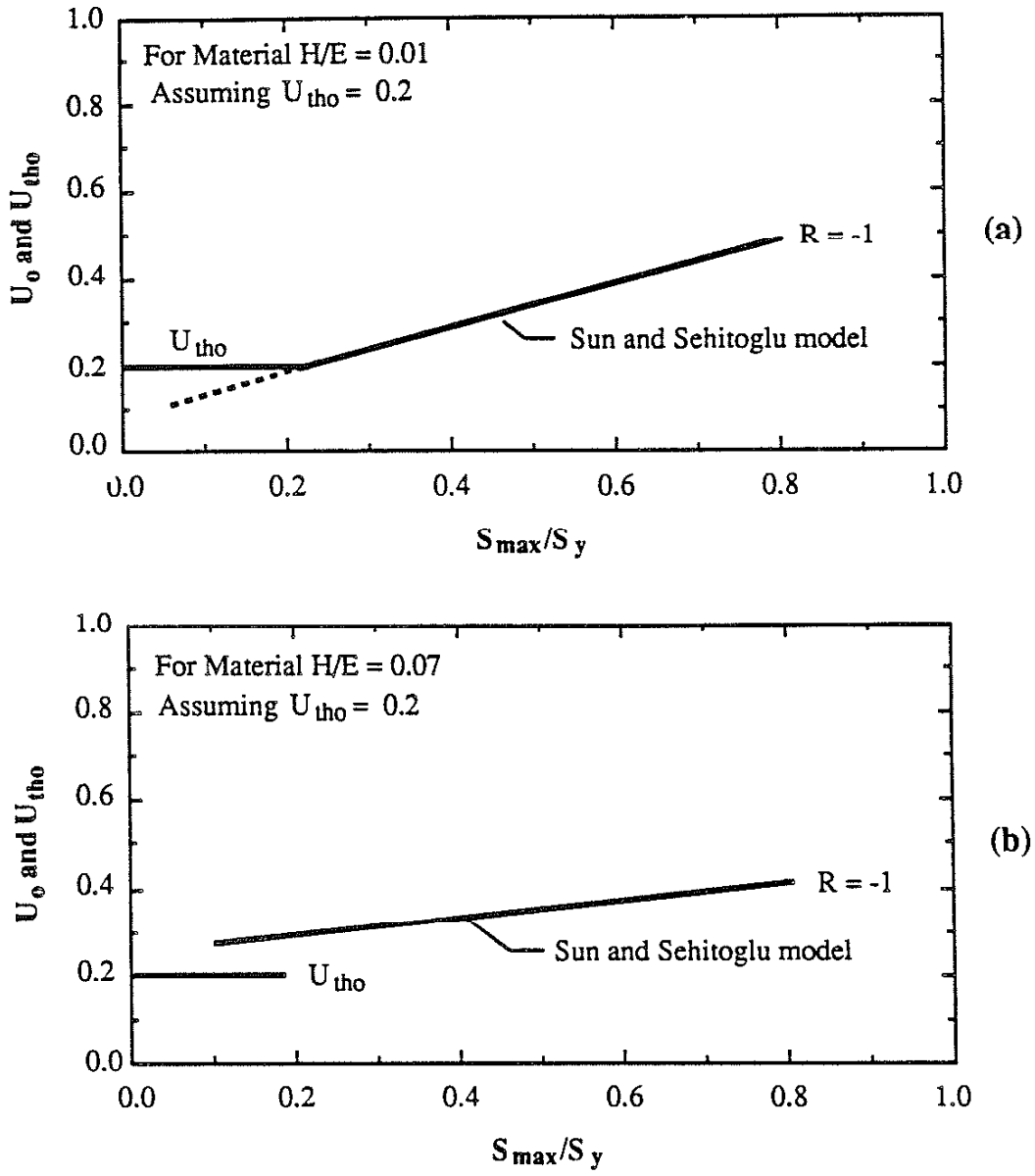


Figure E.2 The difference of $U_o$ vs. $S_{max}/S_y$ between two different H/E materials for R = -1. Assuming $U_o$ = 0.2 for both materials, (a) there will be a region where $U_o = U_{tho}$ for H/E = 0.01 material (aluminum alloy), and (b) no region where $U_o = U_{tho}$.

# APPENDIX F
# THE LIMIT OF THE CCN MODEL APPLICABILITY

From a metallurgical point of view, there is no truly "notch-free" material. The grain boundaries, the inclusions, the second phases and the inevitable surface roughness are all intrinsic defects in a material. However, it seems that those small defects do not behave like notches. For very small defects (e.g. D < grain size), the role of microstructural interactions on crack growth rate becomes significant, and thus, the CCN model may not be applicable. This fact raises to several questions:

1. What is the defect size for which the CCN model is not applicable ?
2. Is this size material dependent ?
3. Is this size dependent on the acuity of the defect ?

Quantitative determination of the boundary between the region where the CCN model is applicable and the region where the CCN model is not applicable is important because the main contribution of the CCN model is its capability in dealing with the small notch problem.

A short crack emanating from a notch can be categorized as a mechanically short crack. In most cases, crack closure for a mechanically short crack can be modelled, and the CCN model is applicable. However, when the defect size is comparable to the microstructural size, the use of the CCN model is invalid. A short crack originating from a "very small" defect would be categorized as a microstructurally small crack because the crack growth rate is still strongly affected by the microstructural barriers. The following discussion proposes a concept (or methodology) to quantitatively determine the Limit of the CCN Model Applicability (LCMA) based on the characteristics of microstructurally and mechanically short cracks.

Tokaji [51] proposed a diagram which qualitatively separates the regions between microstructurally and mechanically small cracks. Figure F.1, adapted from the Tokaji concept, shows four regions of small cracks categorized by crack length (also compared with the grain size (d)). The CCN model is applicable only when the crack length (or the total length of notch depth and the short crack length) is larger than the boundary between the microstructurally dominated region and the mechanically small (short) crack region. Figure F.1 also shows that the LCMA increases with increasing grain size. As will be discussed below, Fig. F.1 is not a complete representation of the process used to determine the LCMA. The applied stress is also an important parameter affecting the LCMA.

F.1 The Maximum Allowable Stress Range for ΔK Formulation

The cyclic plastic zone of a crack tip ($r_p$) is related to the applied stress intensity range and is given by Taylor [53]:

$$r_p = 0.04 \left(\frac{\Delta K}{S_y}\right)^2 \tag{F.1}$$

Taylor stated that the condition for valid use of ΔK is given by:

$$r_p/a \leq 0.1 \tag{F.2}$$

where: a = Crack length

The ΔK for notch with initial depth (D) can be estimated by:

$$\Delta K = Y \Delta S \sqrt{\pi D} \tag{F.3}$$

where: Y = Geometrical factor; Y ~ 0.76 for thumbnail cracks (notches) in a cylindrical bar and Y ~1.12 for through thickness cracks (notches).

Combining Eqs. F.1-F.3 and assuming D = a, the maximum allowable applied stress range (ΔS) is:

$$\Delta S \leq \frac{0.892}{Y} S_y \tag{F.4}$$

F.2 Applicable Regions for the CCN Model

McEvily et al. [19] suggested that when the ΔK value of a crack falls to the left of the $\Delta K_{eff}$ curve on the da/dN vs.ΔK graph, the crack growth rate is dominated by stress and microstructure (this region is denoted as Microstructure Dominated Region, MDR). In this case, the crack-closure based LEFM model (e.g., like the CCN model) is not applicable for life prediction. Conversely, when the ΔK value of a crack falls to the right of the $\Delta K_{eff}$ curve on the da/dN vs. ΔK graph, the crack-closure based LEFM model is applicable. This concept is schematically shown in Fig. F.2 in which the LCMA is the da/dN versus $\Delta K_{eff}$ curve in the da/dN versus ΔK diagram.

Figure F.2 can be mapped with a diagram showing the relationship between stress and notch depth (S - D). This concept is shown schematically in Fig. F.3. The three regions shown in Fig. F.3 are the smooth specimen region, the no failure region and the CCN model applicable region. When defect depth (or crack length) is smaller than the LCMA and the applied stress is higher than the fatigue limit of a smooth specimen ($S_e$), the crack growth rate is dominated by stress and microstructure, and the fatigue properties can be considered to be the same as those of the smooth specimen (i.e. $K_{fn} = 1$). For this case, the long-life-regime fatigue properties are reflected by the Basquin-Morrow equation. When the applied stress is lower than $S_e$ and the notch size is so small that the crack emanating from a notch would have a crack growth rate of approximately zero, the notched specimen will have an infinite life (no failure region).

The LCMA for an applied stress less than $\Delta S_e$ ($\Delta S \leq \Delta S_e$) represents the variation of the threshold stress range with notch depth. The determination of this threshold stress relationship has been proposed in Appendix C. As will be discussed below, the LCMA for $\Delta S \geq \Delta S_e$ is determined using the hypothesis that, at the same applied stress, the minimum crack growth rate of a crack emanating from a notch equals the average crack growth rate of a small crack originating from a smooth specimen ($R_S$).

The "average" crack growth rate of a microstructurally small crack in the MDR can be assumed to be dependent only upon stress range. The total fatigue life in this "smooth" specimen is assumed to consist mainly of the life spent from zero crack length to the intrinsic crack length $L_o$ (Eq. 2.12). Thus, the average crack growth rate of the microstructurally short crack ($R_S$) can be derived by:

$$N_T = \int_0^{L_o} \frac{1}{R_S} dx = \frac{L_o}{R_S} \tag{F.5}$$

where: $R_S$ = Average crack growth rate of the microstructurally small crack
$N_T$ = Total fatigue life of a smooth specimen

Combining Eq. F.5 with the Basquin-Morrow equation ( Eq. 2.2 with $K_{fn} = 1$), $R_S$ as a function of applied stress range is given by:

$$R_S = \frac{2L_o}{\left(\frac{\Delta S}{2\sigma'_f}\right)^{1/b}} \tag{F.6}$$

where: $\Delta S$ = Applied stress range
$\sigma'_f$ = Fatigue strength coefficient
b = Fatigue strength exponent

Using Eq. F.6 to determine $R_s$ for a naturally flawed material such as casting alloy is difficult because "real" smooth specimens are not obtainable and thus $\sigma'_f$ and b must be derived by an alternative method. Figures F.4 and F.5 show the procedures to solve this problem for the cast aluminum alloy 319 used in this study. The fatigue life versus casting defect depth (D) for various applied stresses is shown in Fig. F.4. The fatigue life of defect-free conditions for a certain applied stress ($S_{max}$) can be obtained by extrapolating the regression lines to zero casting defect depth. Once these fatigue lives for defects of zero depth are obtained at a certain applied stress, the values of $\sigma'_f$ and b can be derived by the (Basquin-Morrow) relation between stress amplitude and reversals ($2N_T$) as shown in Fig. F.5. The values of $\sigma'_f$ and b for the pore-free cast aluminum alloy 319 tested in this study are 169.6 MPa and -0.051, respectively.

F.3 Algorithm to Determine the Limit of the CCN Model Applicability (LCMA)

The algorithm to determine the limit of the CCN model applicability (LCMA) is:

1. Known conditions:
   ---> A given notch depth D and acuity $K_t$,
   ---> A given applied stress range $\Delta S$ and load ratio R, and
   ---> Material properties ($\sigma'_f$, b, $\Delta S_e$, $\Delta K_{tho}$, $S_y$, E, da/dN vs. $\Delta K_{eff}$ data)

2. Procedures:
   ---> Start checking when $x \geq l_t$,
   ---> Calculate U(x) and $\Delta K_{eff}(x)$ using the CCN model,
   ---> Determine $da/dN_{(m)}$ (the minimum crack growth rate for a crack emanating from a notch) based on the da/dN vs. $\Delta K_{eff}$ curve,
   ---> Determine $R_s$ based on Eq. F.6 (the average crack growth rate for a crack originating from a smooth specimen),
   ---> If $da/dN_{(m)} \leq R_s$, then the combination of the notch depth and the stress conditions is in the MDR region, otherwise it is in the CCN applicable region,

---> The LCMA (at the given applied stress) is the notch depth at which $da/dN_{(m)} = R_S$.

Figures F.6 and F.7 illustrate the above concept. Figure F.6 compares two different notch depths under the same applied stress. The minimum crack growth rate of a crack emanating from a shallow notch (the left case in Fig. F.6) is lower than the average crack growth rate of a crack originating from a smooth specimen ($R_S$); thus, this notch must be considered a "non-effective" notch. On the other hand, when a crack emanates from an "effective" notch ($K_{fn} > 1$), the growth rates for the crack emanating from this "effective" notch must always be faster than the $R_S$ (the right case in Fig. F.6). Figure F.7 shows a constant notch depth loaded by three different applied stresses. Both the $R_S$ and the da/dN of the crack emanating from the notch increase with increasing applied stress. For a very low stress (i.e., $\Delta S_1$ in Fig. F.7), this notch will have infinite life. When the applied stress increases to $\Delta S_2$, the CCN model may be applied to predict the fatigue life. However, when the applied stress increases to $\Delta S_3$, the minimum value of da/dN falls below $R_S$; thus, under this condition, the CCN model is not applicable. The fatigue life may be estimated by the strain-life approach (with $K_{fn} = 1$).

When a crack emanates from a notch with a minimum crack growth rate equal to the $R_S$, the notch depth is the LCMA. From an engineering point of view, the LCMA is the maximum tolerable defect depth of a material. When a defect depth is less than this maximum tolerable defect depth, this defect will not affect the fatigue strength. This non-effective defect specimen is considered to be smooth specimen. The long-life regime fatigue life for this non-effective notch may be estimated using the Basquin-Morrow equation with $K_{fn} = 1$. However, when the defect depth is larger than this maximum tolerable defect depth, the fatigue properties are not those of a smooth specimen. The CCN model must be employed under this condition. The value of the LCMA at the fatigue limit is denoted as $X_{BC}$ (see Fig. F.3) which is the maximum non-damaging notch depth. For a notch with a depth smaller than $X_{BC}$, the threshold stress of the notched component equals the fatigue limit of a smooth specimen.

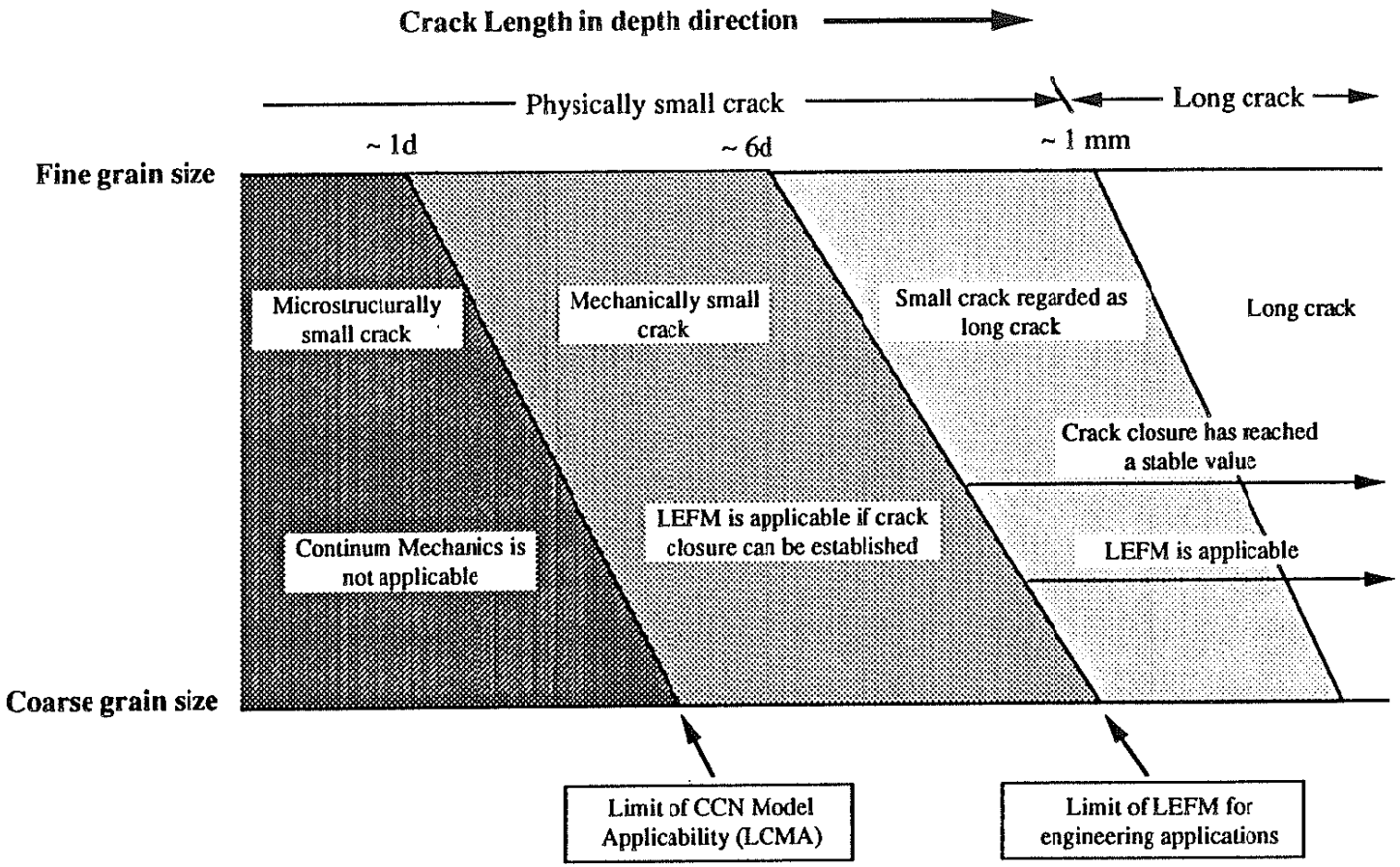


Figure F.1 Classification of small fatigue cracks showing the regime where the CCN model can be used (modified after Ref. 51).

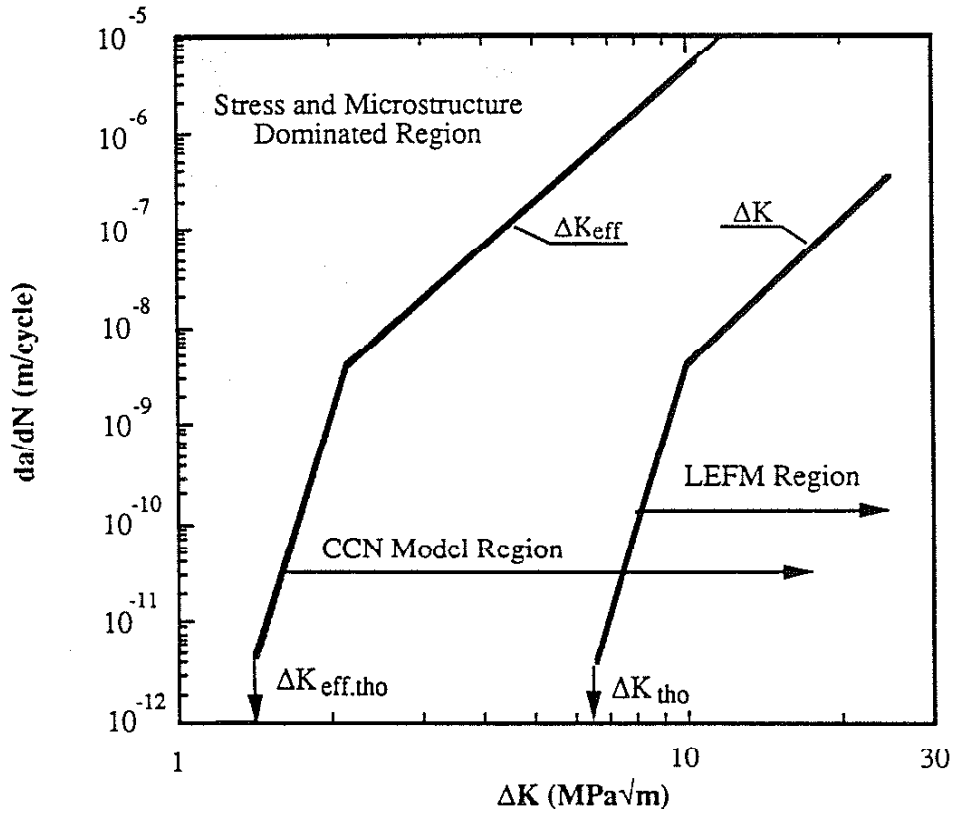


Figure F.2 Regions of applicability of the CCN model and LEFM model (modified after Ref. 19). When ΔK values of a small crack emanating from a notch fall in the stress and microstructure dominated region, the CCN model is not applicable.

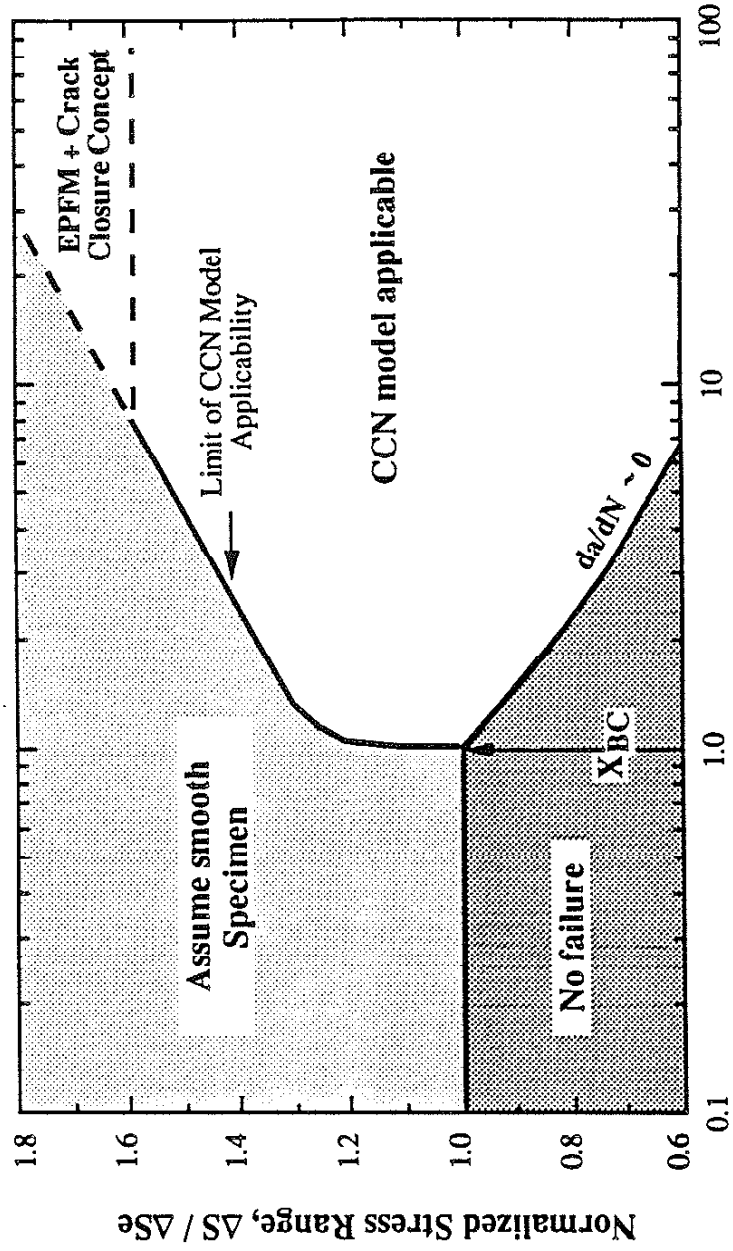


Figure F.3 Schematic S-D diagram showing the limit of the CCN model applicability and the $X_{BC}$. When defect size is smaller than $X_{BC}$, the long-life regime fatigue properties may be estimated using Basquin-Morrow's equation with $K_{fn} = 1$.

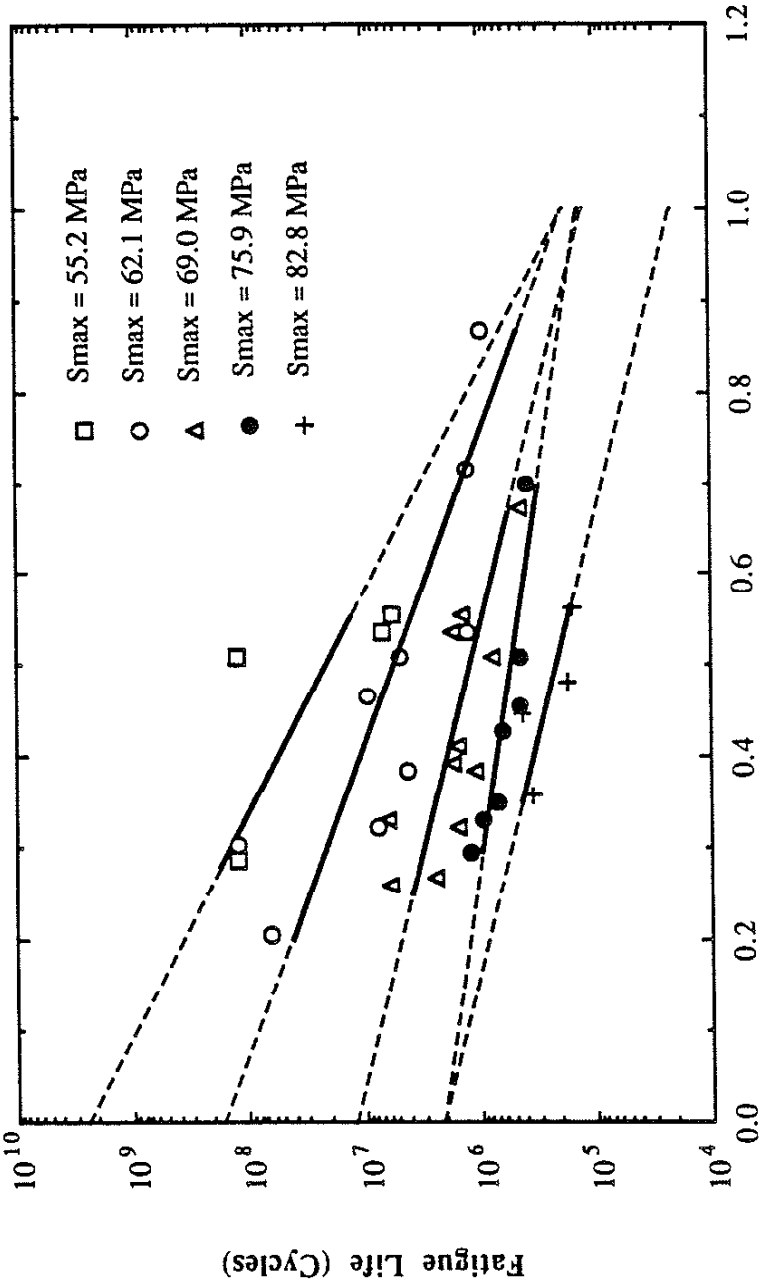


Figure F.4 The relationship between fatigue life and the depth (assuming AR = 0.8) of fatigue initiating defects of cast aluminum alloy 319 under different ranges of applied stresses for R = -1.

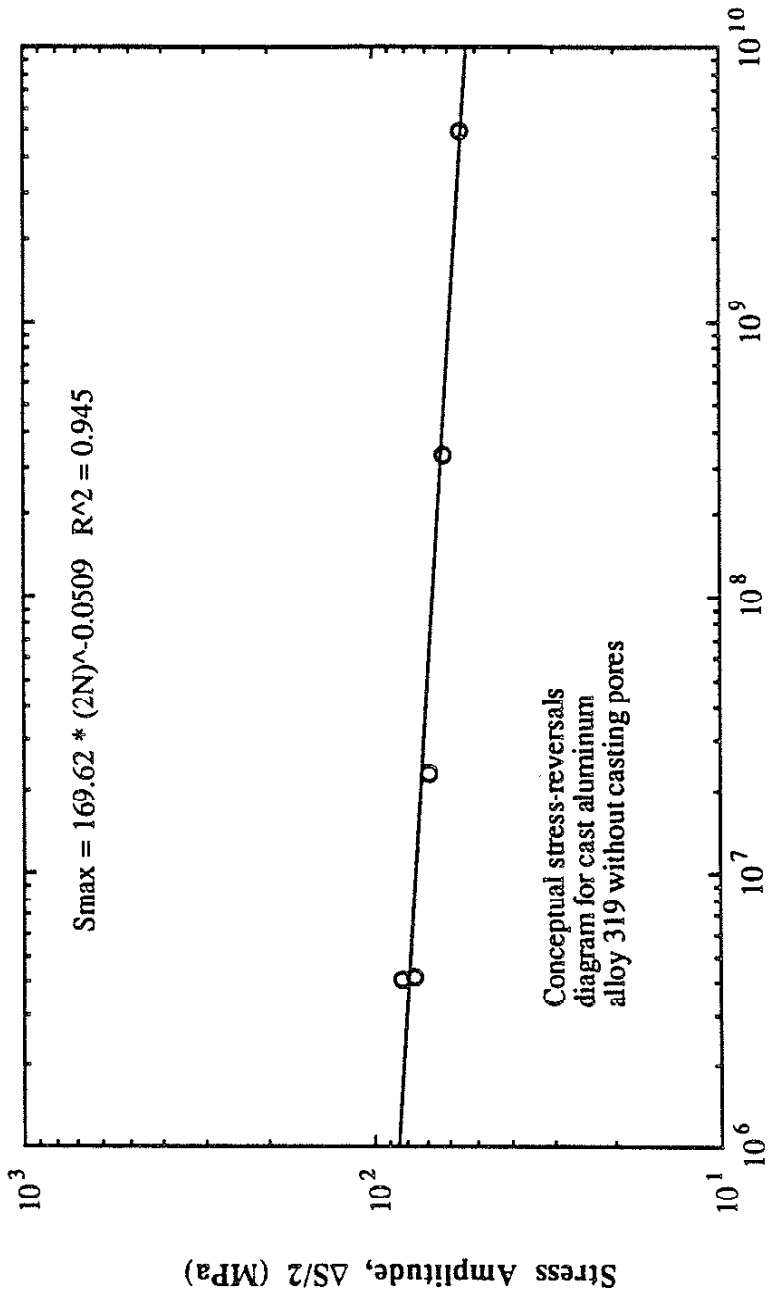


Figure F.5 The hypothetical Stress-Reversals diagram for cast aluminum alloy 319 without casting defects.

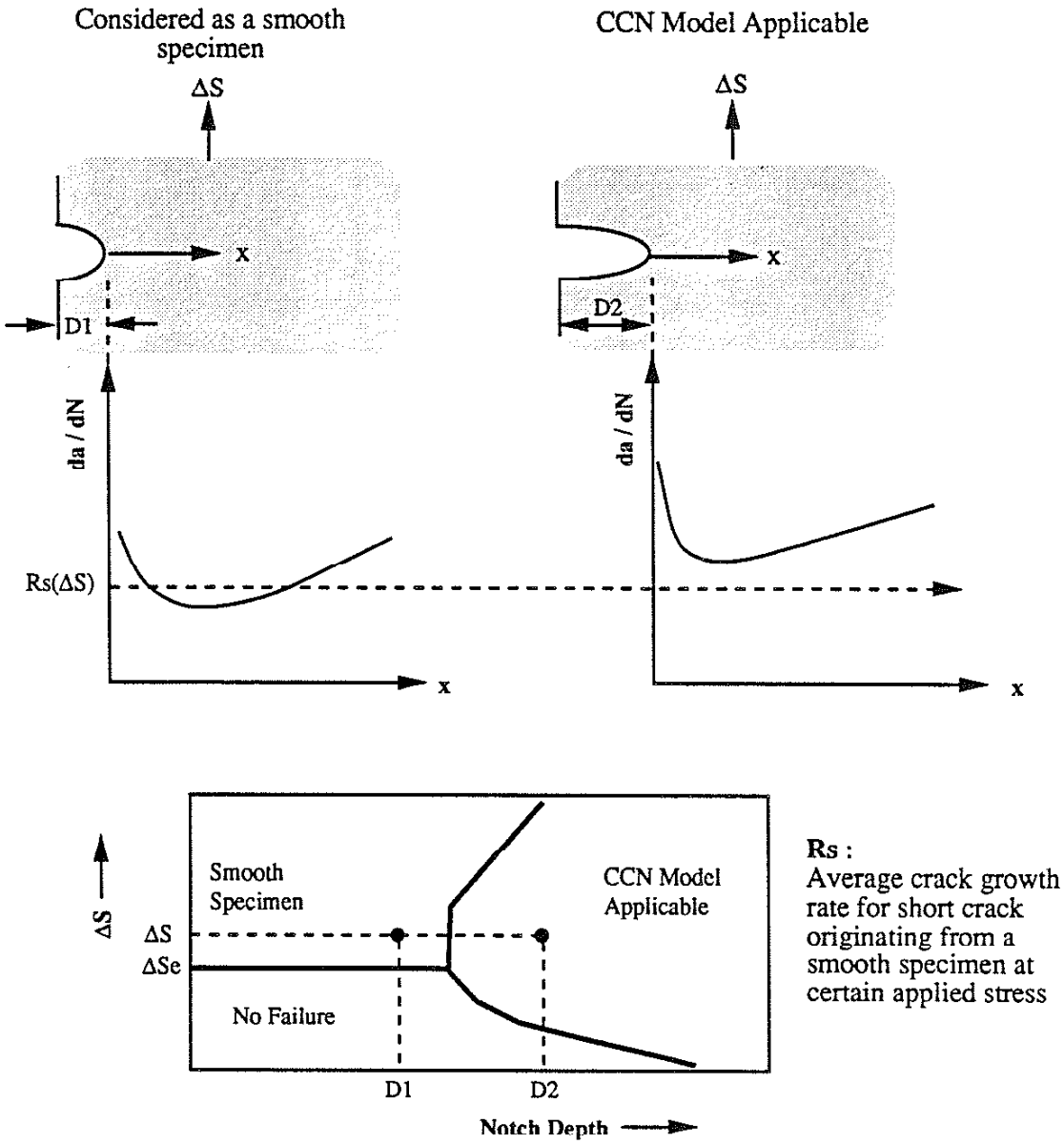


Fig. F.6 Schematic diagram showing the concept to derive the limit of the CCN model applicability. The crack growth rates of cracks emanating from two notches (different depths) with the same applied stress were compared.

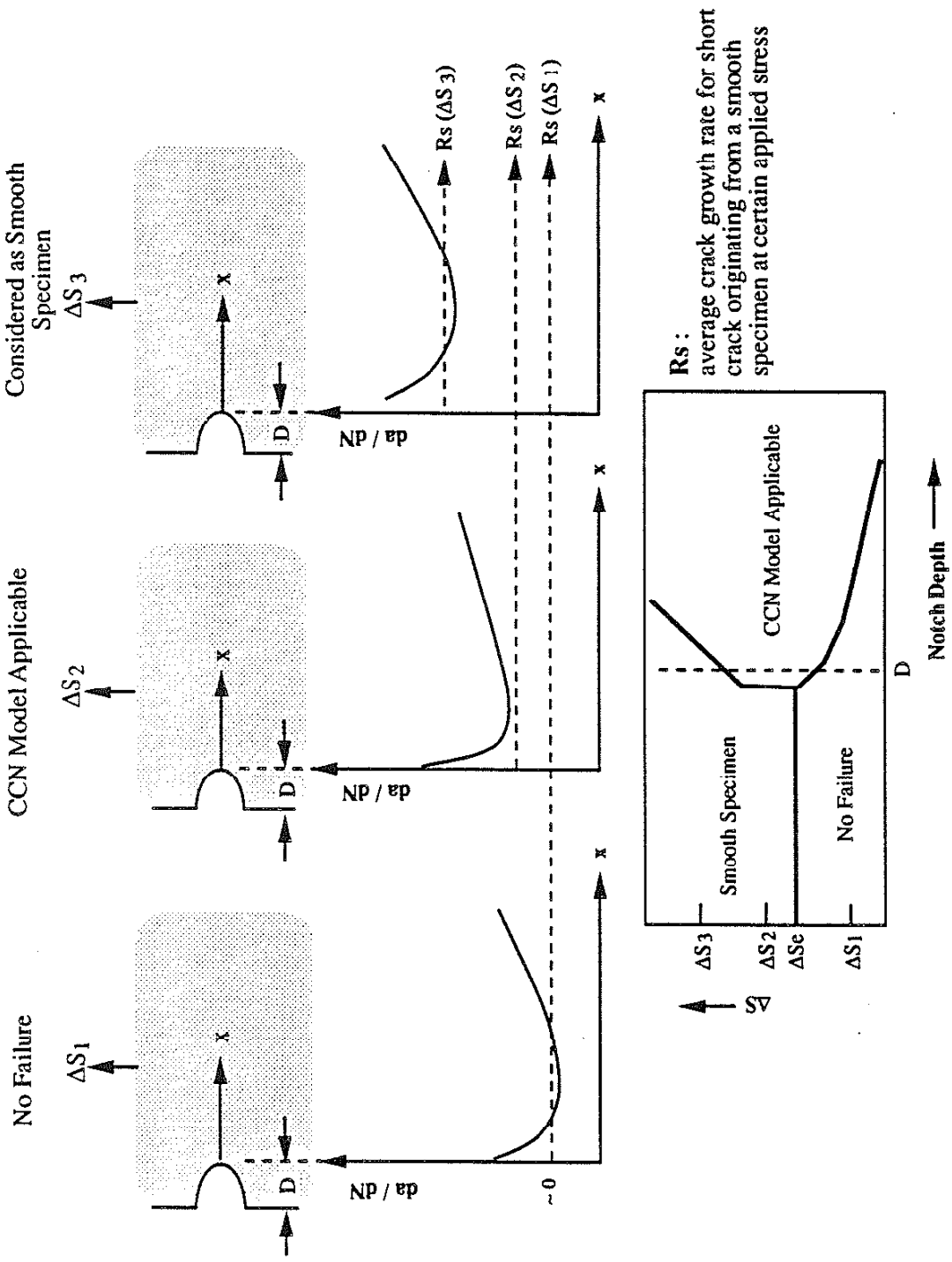


Figure F.7 Schematic diagram showing the derivation of the limit of CCN model applicability. A constant notch depth with three different applied stresses are compared.

# APPENDIX G

# EXPERIMENTAL PROCEDURES AND RESULTS FOR A CAST ALUMINUM ALLOY 319

## G.1 Material and Basic Mechanical Properties

The cast aluminum alloy 319 used in this study was cast and heat-treated by the General Motors Corporation. The chemical composition of this alloy and heat treatment process are given in References 60 and 73. The mechanical properties of this material are given in Table 1.

The microstructure shown in Fig. G.1 is an aluminum-based dendritic structure. Each arm of the dendrite is enveloped in eutectic. The micro-hardness of the aluminum-based dendrites is about HV 50 (standard deviation = HV 9 from 15 measurements) and that of the eutectic is about HV 280 (standard deviation = HV 60 from 15 tests). Dendrite cell size (DCS) and dendrite arm spacing (DAS) were measured by using a line intercept method in which lines were drawn on a magnified micrograph and the number of cells (or secondary dendrite arms) on each line were counted. In this way, the dendrite cell size can be determined. The dendrite cell size had a mean value of 0.07 mm and a standard deviation of 0.009 mm from 20 (10 micrographs) measurements. The dendrite arm spacing had a mean value of 30 μm.

There were a lot of casting pores in this cast alloy. The casting defects in the cast alloy are three-dimensional in nature but can only be observed as two dimensional features by optical or scanning electron microscopy (SEM). From the fracture mechanics point of view, it is necessary to represent the defect size by a simple one-dimensional scalar quantity. However, the irregular shape of these defects makes it impossible to characterize the defects by measuring a single, characteristic dimension. Thus, the defect size (T) defined below was used throughout this study as a measure of casting-defect severity:

$$T = \sqrt{Area} \tag{G.1}$$

Where: Area = The area occupied by projecting pore (or defect) onto a plane normal to the observation direction: see Fig. G.9b.
T = Defect (or pore) size

Samples for measuring the casting pore size distribution were prepared from the fatigue-tested cylindrical specimens by sectioning each of them in several locations. Each section was then mounted and polished, and photographed at a 50x magnification. Several

randomly selected locations on each plane of polish were photographed. Images of a total of 584 pores were collected and analyzed to determine the statistical distribution of pore size.

The casting pore size exhibits an exponential distribution:

$$f(T) = \lambda \exp(-\lambda T) \tag{G.2}$$

Where: $f(T)$ = Probability density function of pore size (T)
$\lambda$ = Parameter of exponential density function; to be determined
$T$ = Square root of defect area, a measure of casting pore size

Equation G.2 can be rearranged using the concept of cumulative distribution function, F(T), and F(T) is given by:

$$F(T) = 1 - \exp(-\lambda T) \tag{G.3}$$

Where: $F(T)$ = Cumulative distribution function of pore size $= \frac{n(T)}{N+1}$
$n(T)$ = Number of pores which have pore size $\leq T$
$N$ = Total sampling number (in this case, N = 584)

Equation G.3 can be further rearranged as:

$$\ln (1 - F(T)) = - \lambda T \tag{G.4}$$

Figure G.2 shows the data based on Eq. G.4 in which it can be seen that ln (1 - F(T)) is linearly related to the pore size (T) and that the slope ($\lambda$) is 19.6. Figure G.3 shows the comparison between the histogram of experimental data and calculated f(T) using Eq. G.2 with $\lambda = 19.6$. Thus, the casting pores size can be represented by an exponential function which has parameter $\lambda$ of 19.6, that is:

$$f(T) = 19.6 \exp(-19.6T) \tag{G.5}$$

## G.2 Fatigue Tests

### G.2.1 Test Specimens

Two surface conditions of cylindrical specimens were used: polished-surface and as-cast surface conditions. The polished-surface specimens were cast to 12.8 mm diameter

cylindrical bars and machined to have 8.38 mm diameter x 25.4 mm gage sections. The surfaces of the machined specimens on the gage section were then polished using the 30 μm abrasive polish-ribbons. The as-cast surface specimens had 8.38 mm diameter x 38.1 mm gage sections.

In addition to the cylindrical specimens, single edge notched plate (SENP) specimens were also used. The SENP specimens were machined out of cylindrical bars of 19.2 mm diameter. The typical shape and dimensions of an SENP specimen are shown in Fig. G.4 in which the prismatic gage section has a width of 15.8 mm and a thickness of 5 mm. The single edge notch has a 1.6 mm depth; the notch root radii were 0.06, 0.4, and 0.8 mm which produced net-section elastic stress concentration factors ($K_{tn}$) of 11.0, 4.85, and 3.6, respectively [61]. Each specimen was electro-chemically polished to remove residual stress which may have been induced by the machining.

G.2.2 Stress-Life Tests (S-N Curves)

The uniaxial fatigue tests were performed at a load ratio R = -1 and frequency of 10 to 25 Hz. Cylindrical specimens with both as-cast surface and polished surface conditions were tested. Failure was defined as complete separation of the specimen, and run-out was defined as $1.25 \times 10^8$ cycles. The run-out test specimens were retested using progressively higher applied stress ranges until the specimens failed.

G.2.3 Fatigue Crack Growth Rate Tests (da/dN versus ΔK curves)

Two kinds of measurements for crack growth rate were carried out using the SENP specimens: constant-load (constant stress amplitude) tests in which the applied load was kept constant throughout the entire life and load-shedding tests in which the applied load was gradually decreased during the test.

The constant-load fatigue tests were used to determine the relation of fatigue cycles with crack length and the stress-life relation (S-N curve). These tests were performed at a load ratio R = -1 and frequency of 5 to 10 Hz. Failure was defined as complete separation of the specimen, and run-out was defined as the absence of crack growth for $10^7$ cycles. The applied (constant) stress ranges (ΔS) for measuring the crack growth rate were between 69 MPa and110 MPa (based on gross section).

A microscope and camera were installed to periodically measure the crack length. Measurements began whenever a crack length became greater than 0.2 mm. A seven-point incremental polynomial method specified by ASTM standard E647 was used to analyze the relations between da/dN and ΔK.

In addition to the constant-load tests, load-shedding tests described in ASTM E647 was also used to measure the long crack growth rate in the same SENP specimens at R = -

1. A travelling microscope was used for crack-length measurement. The rate of load shedding was larger than the value specified in the standard. According to the standard, the criteria of normalized K-gradient ($C_n$) is given by:

$$C_n = (\frac{1}{K})(\frac{dK}{da}) > -0.08 \text{ mm}^{-1} \quad \text{(G.6)}$$

Because of the dimensional limitations of the SENP specimen, the width in the gage section was too narrow to follow the criterion ($C_n > -0.08$ mm$^{-1}$); thus, the values of $C_n$ in this test were limited to $C_n > -0.2$ mm$^{-1}$. The observed relationship between da/dN and $\Delta K$ was considered to be that of a long crack when the crack emanating from a notch was longer than 2.5 mm.

## G.3 Experimental Results

### G.3.1 The Stress-Life (S-N) Relations for the Cylindrical Specimens

The fatigue test results for all tests are shown in Fig. G.5. The test results for each surface condition are given by different symbols. The scatter in the fatigue life data increases with decreasing applied maximum stress ($S_{max}$) (or stress amplitude since R = -1 for all tests). Using the test statistics discussed in Appendix H to check the independence of these two S-N data sets, it seems that there are no significant differences between the two surface conditions. Thus, for the cast aluminum alloy 319 tested in this study, the fatigue strength was not significantly affected by the surface conditions.

### G.3.2 The Stress-Life (S-N) Relations for the SENP Specimens

The Stress-Life (S-N) curves for the single edge notch in a plate (SENP) specimens tested under constant stress amplitude are shown in Fig. G.6. The stress amplitude is based on the gross section. A run-out (defined as $10^7$ cycles) was found for the specimen with a $K_{tn}$ value of 11 at $S_{max}$ = 34.5 MPa. The specimens with $K_{tn}$ = 11 have a longer fatigue life than those with $K_{tn}$ = 3.6 or 4.85 when compared at the same stress amplitude: when the applied stress amplitude equals 34.5 MPa, the fatigue life was found at $8.6 \times 10^5$ for $K_{tn}$ = 3.6 specimens; whereas, the run-out condition was found for $K_{tn}$ = 11 specimens. The results imply that fatigue life may be affected by the notch root radius; also, the trend indicates that the sharpest notch is not the worst-case notch.

G.3.3 The Fatigue Crack Initiating Sites and the Size of Fatigue Initiating Defects

The fact that the fatigue cracks initiated from the sub-surface casting pores near the outer surface was observed in the study described in Appendix I. The observations in Appendix I lead to the conclusion that the fatigue cracks initiate from the near-surface casting pores and that the eutectic microstructure had little effect on the fatigue initiation and early propagation.

The fatigue initiation sites were also observed for the broken cylindrical specimens. The appearance of the fatigue fracture surfaces of a cylindrical specimen exhibited smooth and flat asperities (Fig. G.7). The fracture surfaces of each cylindrical specimen were examined using a scanning electron microscope (SEM) to observe the fatigue initiation sites. There are two categories of defects which caused fatigue crack initiation: near surface casting pores which were most frequently observed in the polished surface specimens; and cast-surface texture which were only present in the as-cast specimens. Figure G.8 shows that the fatigue crack initiated from a near-surface casting pore for a polished specimen and that the crack initiated and propagated on the plane normal to the direction of applied stress. Figure G.9a shows a fractograph of an as-cast specimen in which the surface texture caused fatigue crack initiation. Figure G.9b shows the trace of the area of fatigue initiation defects from Fig. G.9a.

The fatigue initiating defect size ($T = \sqrt{Area}$) has been defined by Eq. G.1. The data used for the statistical analysis of fatigue initiating defect size were obtained from 23 polished specimens and 11 as-cast specimens. For the polished surface condition, most of the fatigue initiation sites were near-surface casting pores. For the as-cast surface condition, most of the fatigue initiation sites were the surface texture discontinuities. The defect size (T) and the corresponding S - N test results are listed in Table 3 (for polished specimens) and Table 4 (for as-cast specimens).

The cumulative distribution functions of fatigue initiating defects size for both polished and as-cast surface conditions are shown in Fig. G.10. The open circles represent the data for the polished surface condition and the solid symbols represent the as-cast surface condition. The dashed lines are the regression lines for both conditions. It is obvious that the fatigue initiating defect sizes for both conditions follow normal distributions, and there is no significant difference between these two conditions. When these data are treated as one group, the mean value of the fatigue initiating defect size is 0.50 mm and the standard deviation is 0.16 mm.

The normal probability distribution function is given by:

$$f(T) = \frac{1}{\sigma\sqrt{2\pi}} \exp\left[-\frac{1}{2}\left(\frac{T-\mu}{\sigma}\right)^2\right] \qquad (G.7)$$

where:
- $T$ = Fatigue initiating defect size
- $\mu$ = Mean value (= 0.5 mm in this analysis)
- $\sigma$ = Standard deviation (= 0.16 mm in this analysis)

The comparison between the histogram of fatigue initiating defect size and Eq. G.7 is shown in Fig. G.11. The average size of the fatigue initiating defects is bigger than the average size of the casting pores as shown in Fig. G.12. It would seem that the statistics of extreme can be used to correlate these two distribution functions. Unfortunately, the fatigue initiating defects are not simply a single casting pore or single as-cast surface texture. On the contrary, in many cases, the fatigue initiating defects were composed of more than one casting pore or were composed of a combination of casting pores and surface textures (in the as cast specimens). Thus, an analysis based on the extreme-value statistics is not possible at the present time. The average fatigue initiating defect size is characteristic of the tail of the casting pore size distribution.

### G.3.4 The Influence of Fatigue Initiating Defect Size on the Fatigue Life

The influence of the size of fatigue initiating defects on the fatigue life at a given applied stress is shown in Figs. G.13(a-d) for four applied stress ranges. It is clear that the size of fatigue initiating defects affects the fatigue life; the larger the size, the lower the fatigue life. The main reason that the S-N data are same for both the polished and as-cast surface conditions is attributed to the same size distribution of fatigue initiating defects for both surface conditions. Figure G.13 also shows a trend that the lower the applied stress, the stronger the effect of defect size. The dependence of the fatigue life of this cast alloy on the initiating defect size and the sensitivity of this defect size effect on stress level lead the application of the ASTM E739 to the test data to be meaningless, because the basic assumption in ASTM E739 is that the deviation of fatigue life is independent of the applied stress. A better approach for determining the confidence bands using the CCN model is discussed in Chapter 4.

## G.4 Measurement of Fatigue Crack Propagation Rate

Single edge notch in a plate (SENP) specimens were used for determining the crack growth rates of short cracks and of long cracks for the R = -1 condition. The short crack

growth rates were determined by the constant-load tests. The long-crack growth rates were determined by the load-shedding tests using the sharply notched specimens with $K_{tn} = 11$.

The variations of the fatigue crack length with fatigue cycles for the constant load test are shown in Fig. G.14. The seven-point incremental polynomial method suggested by ASTM E647 was used to convert the experimental data from Fig. G.14 into the relation of da/dN versus $\Delta K$. The function used for calculating stress intensity range ($\Delta K$) is discussed in Appendix A.

For the load-shedding test, da/dN was determined by the change of crack length divided by the fatigue cycles at each load step. $\Delta K$ is the mean value of the starting $\Delta K$ and the ending $\Delta K$ at each load step. The starting applied stress range for initiating a crack is $S_{max}/S_y = 0.25$. Figure G.15 shows the relation between da/dN and $\Delta K$ for long cracks ($x \geq 2.5$ mm) obtained by the load-shedding tests. The threshold stress intensity range ($\Delta K_{tho}$) for R = -1 is approximately 6.5 MPa$\sqrt{m}$.

A bi-linear model was used to correlate the long crack growth rate (da/dN) with the stress intensity range ($\Delta K$):

$$\frac{da}{dN} = C_i (\Delta K)^{m_i} \qquad (i = 1,2) \qquad \text{(G.8)}$$

where:

| | | | |
|---|---|---|---|
| $C_1$ | = | 1.18E-25 | (in the near-threshold regime, Stage I) |
| $m_1$ | = | 16.7 | (in the near-threshold regime, Stage I) |
| $C_2$ | = | 9.58E-14 | (in the mid-growth rate regime, Stage II) |
| $m_2$ | = | 4.7 | (in the mid-growth rate regime, Stage II) |

Figure G.16 combines the experimental results for both load-shedding and constant load tests. The solid lines in this figure illustrate the relationships obtained for the long cracks ($x \geq 2.5$ mm) from the load-shedding tests (i.e. Eq. G.8 and Fig. G.15). The data points in Fig G.16 include the results for short cracks ($x > 0.2$ mm in most cases) which exhibit faster growth rates than the long cracks when compared on the basis of $\Delta K$.

Since the long-crack da/dN versus $\Delta K$ relation was obtained by the load-shedding method and consequently by a $\Delta K$-increasing procedures, the applied stress range in this condition was so low that the value of $U_o$ in the mid-growth rate regime can be assumed to be the same as $U_{tho}$ in the threshold regime (see Appendix E). The results obtained by the load-shedding method were all long-crack data ($x \geq 2.5$ mm), and the crack closure level can be assumed to be a stable value - the long crack effective threshold stress intensity ratio

($U_{tho}$). The value of effective stress intensity range ($\Delta K_{eff}$) for the long crack in both near-threshold and mid-growth rate regimes is obtained from:

$\Delta K_{eff} = U_{tho}\,\Delta K$ (for long crack obtained from the load-shedding method) (G.9)

The value of $\Delta K_{eff.tho}$ can be estimated to be 1.4 MPa$\sqrt{m}$ (see Appendix E); thus, $U_{tho}$ at R = -1 for the cast aluminum alloy 319 of this study can be assumed to be 0.215. The bi-linear curve of da/dN versus $\Delta K_{eff}$ for long cracks as described in Appendix E is:

$$\frac{da}{dN} = C'_i\,(\Delta K_{eff})^{m_i} \qquad (i = 1,2) \qquad (G.10)$$

where:

| | | | |
|---|---|---|---|
| $C'_1$ | = | 1.747E-14 | (in the near-threshold $\Delta K_{eff}$ regime, Stage I) |
| $m_1$ | = | 16.7 | (in the near-threshold $\Delta K_{eff}$ regime, Stage I) |
| $C'_2$ | = | 1.32E-10 | (in the mid-growth rate $\Delta K_{eff}$ regime, Stage II) |
| $m_2$ | = | 4.7 | (in the mid-growth $\Delta K_{eff}$ regime, Stage II) |

The faster growth rates of the data points shown in Fig. G.16 are the results of the "short crack problem" which causes short cracks to have higher effective stress intensity ratios (U(x)) than the stabilized long crack effective threshold stress intensity ratio ($U_{tho}$). The calculation of U(x) for short cracks under constant applied stress range is discussed in Appendix D. Taking an example for the notch with $K_{tn}$ = 4.85 under constant applied stress conditions, the variations of U(x) with the crack lengths x were predicted based on the concept discussed in Appendix D (see Eqs. D.1 - D.3). As shown in Fig. G.17, two stress ranges were calculated: $\Delta S$ = 73 MPa and 96.6 MPa at R = -1, respectively. The lower stress range has lower values of U(x) when the crack is within the notch-stress-field boundary ($x < x^*$), but has higher values of U(x) when the crack is beyond the notch-stress-field boundary ($x \geq x^*$).

The relations of da/dN versus $\Delta K_{eff}$ of the cast aluminum alloy 319 for both short cracks and long cracks are shown in Fig. G.18. The solid line is the bi-linear model of da/dN versus $\Delta K_{eff}$ derived from the long crack data (load-shedding tests) and Eq. G.10; whereas, the data points were derived based on the relation that $\Delta K_{eff}(x) = U(x)\Delta K$. The fact that the short crack data merge with the long crack data in the relation of da/dN versus $\Delta K_{eff}$ shown in Fig. G.18 indicates that the use of this da/dN versus $\Delta K_{eff}$ relation can rationalize the crack growth rates for both short cracks and long cracks.

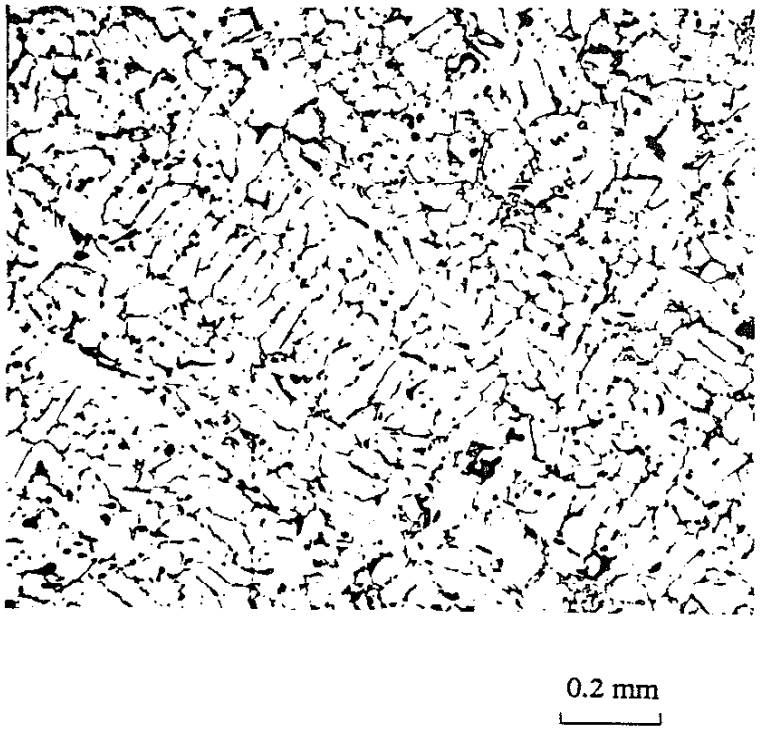


Figure G.1 Photomicrograph of cast aluminum alloy 319 (72X). Keller's etch.

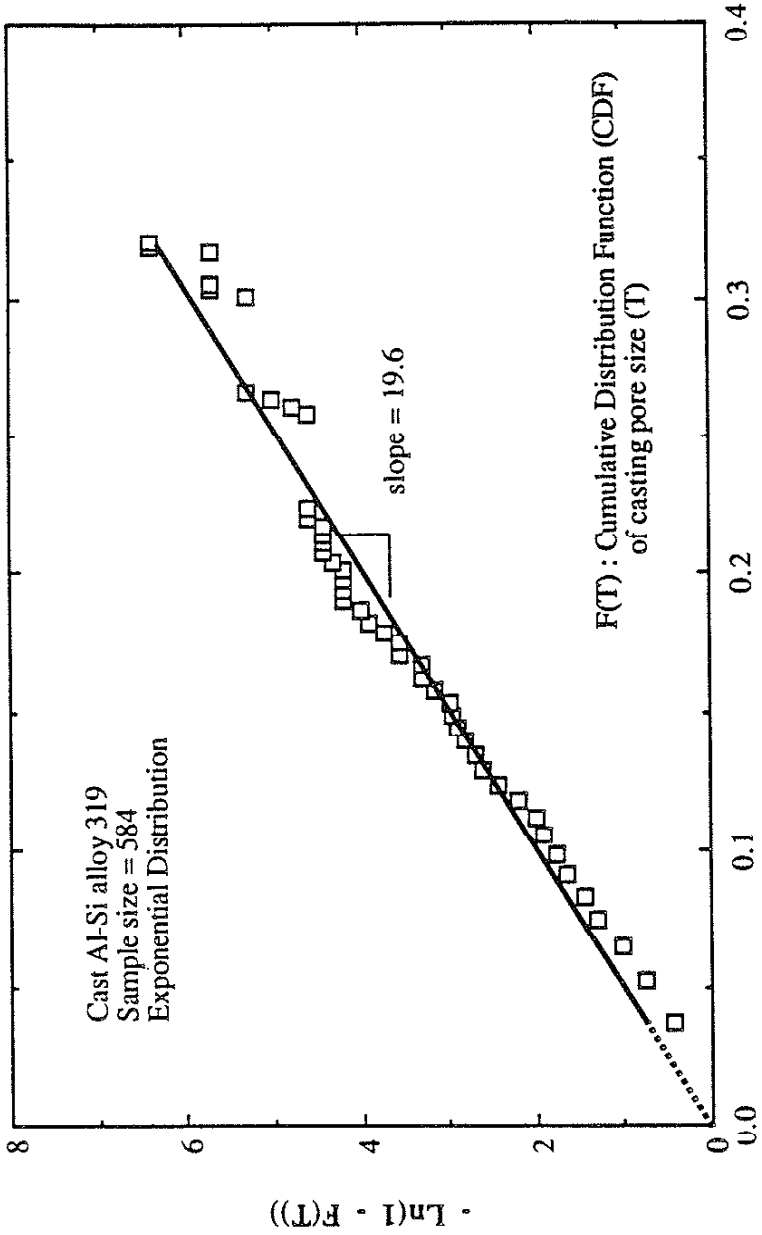


Figure G.2 The exponential distribution of pore size. The linear relationship between ln (1 - F(T)) and pore size indicates that the casting pore size is exponential distribution with parameter $\lambda = 19.6$.

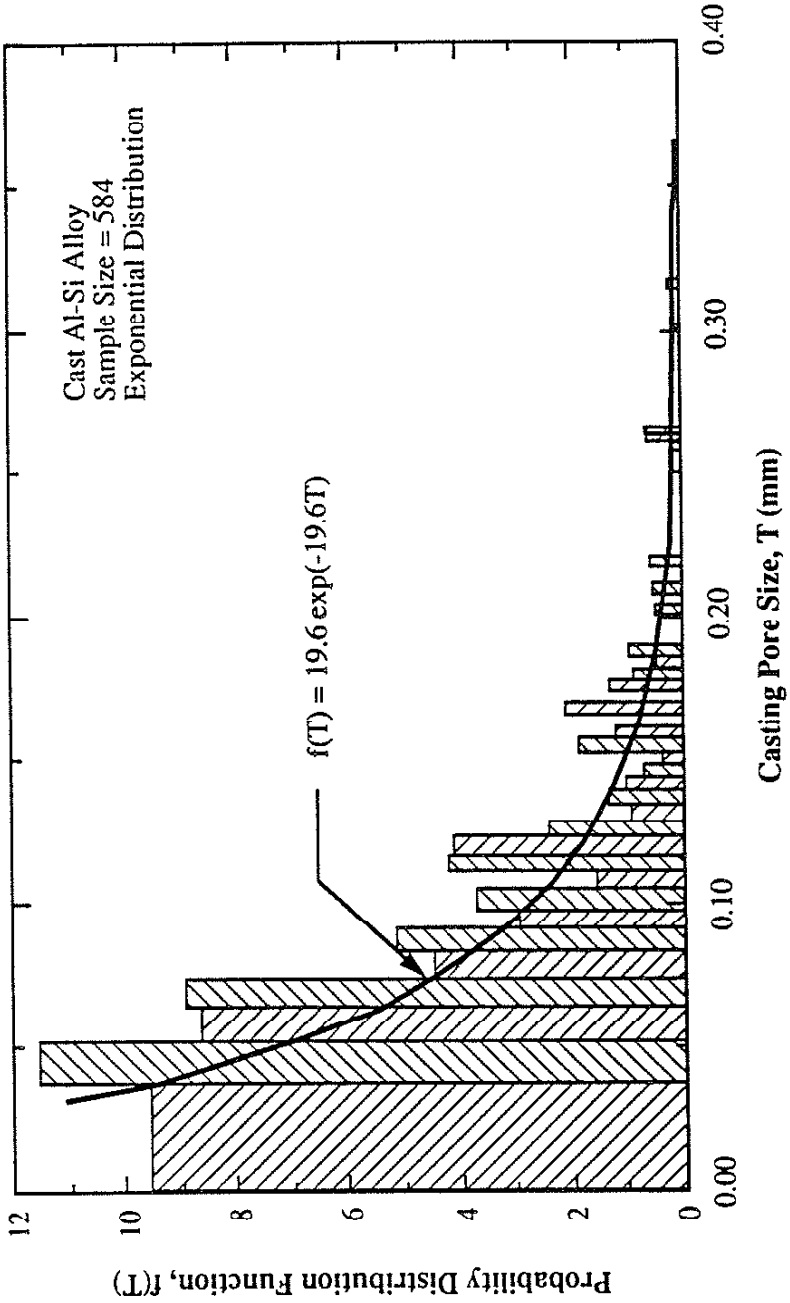


Figure G.3 Comparison of histogram of casting pore size and predicted exponential function.

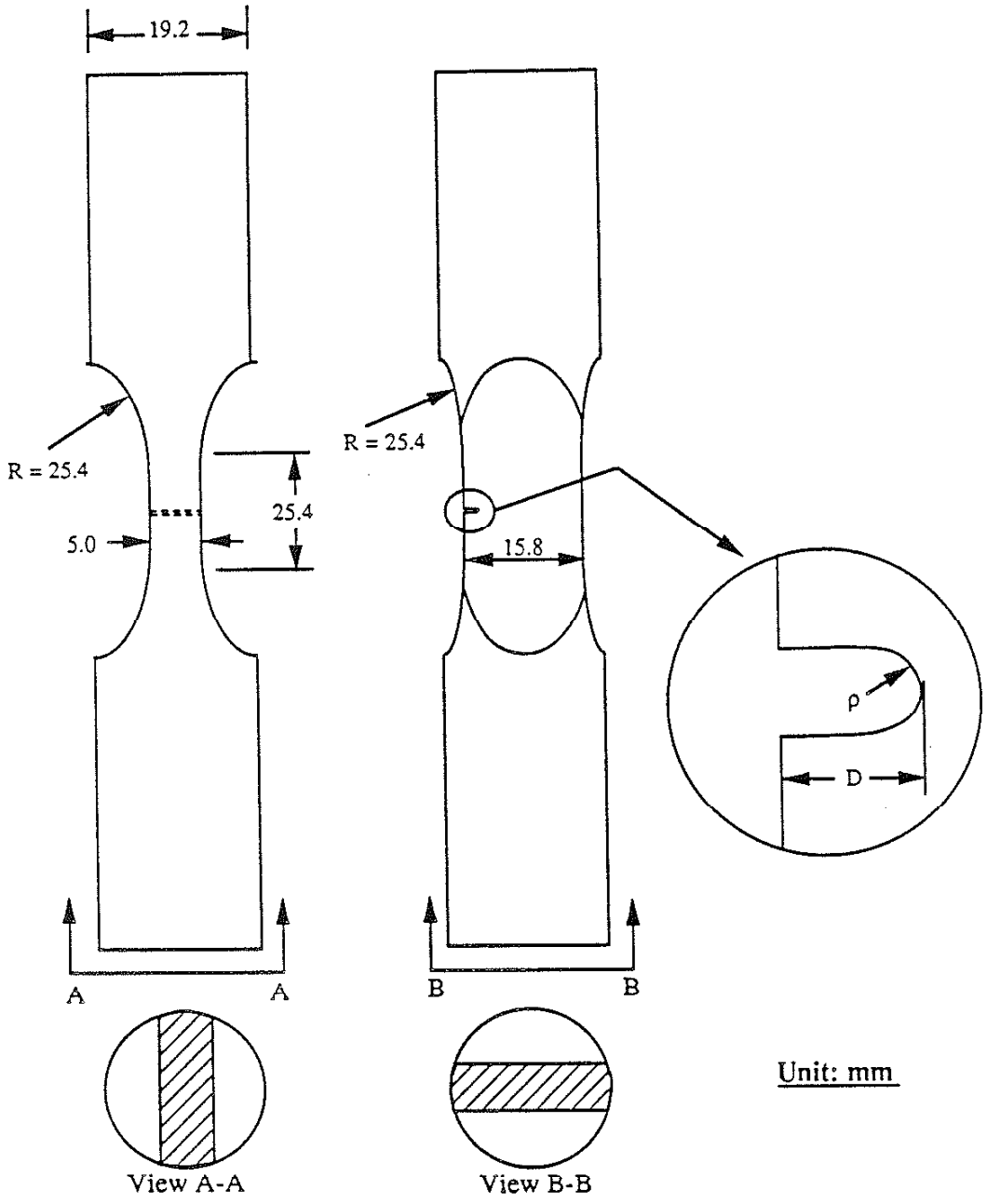


Figure G.4 Specimen geometry of single edge notched plate (SENP) specimen.

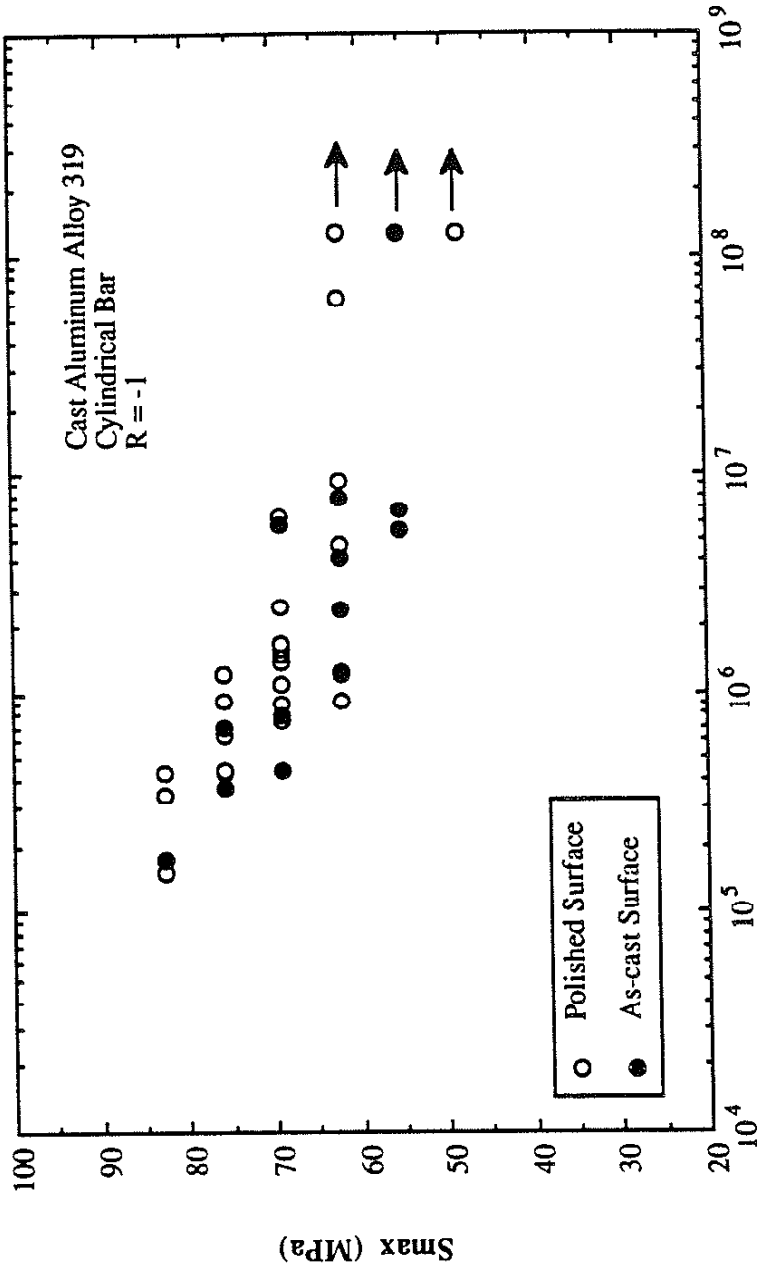


Figure G.5 S-N diagram of cast aluminum alloy 319 for cylindrical bar specimens with two different surface conditions .

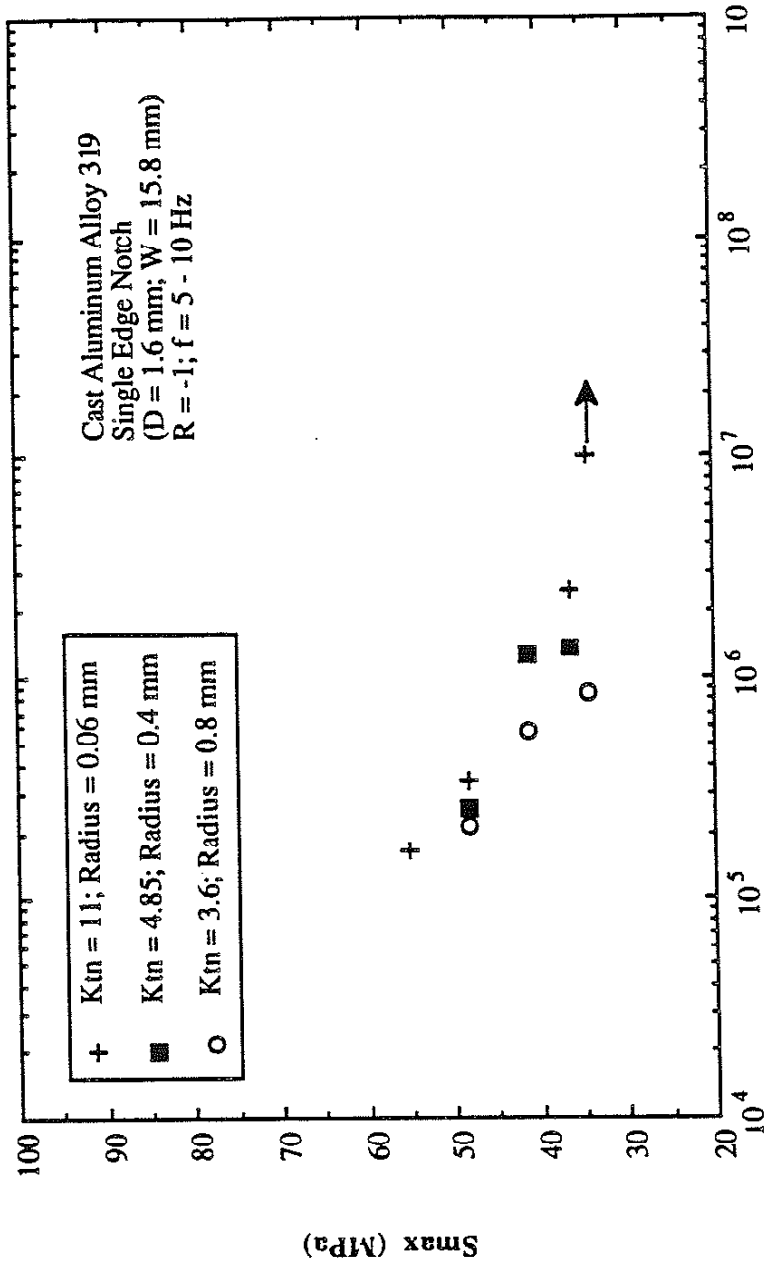


Figure G.6 S-N diagram of cast aluminum alloy 319 for SENP specimens with three different notched conditions.

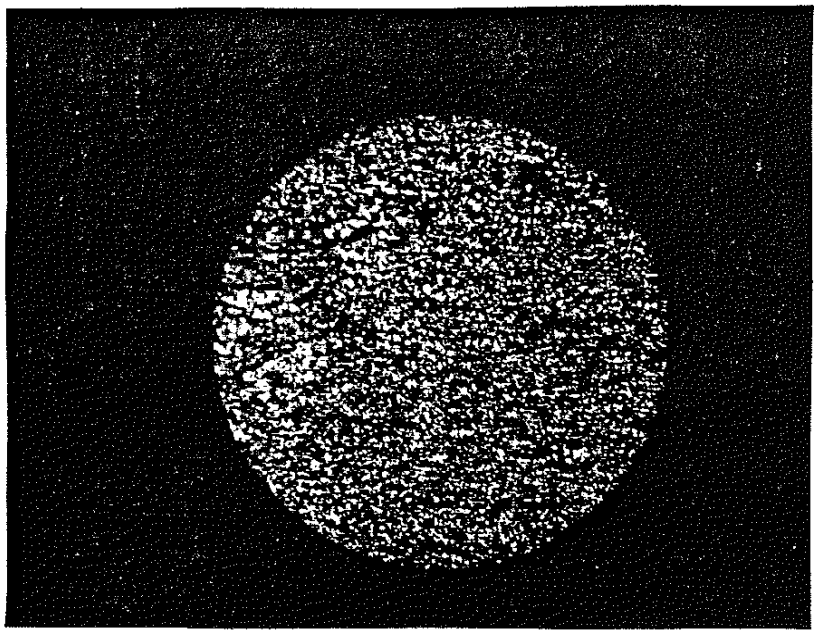

Figure G.7 Fatigue fracture surface of a cast aluminum alloy 319.

(a)

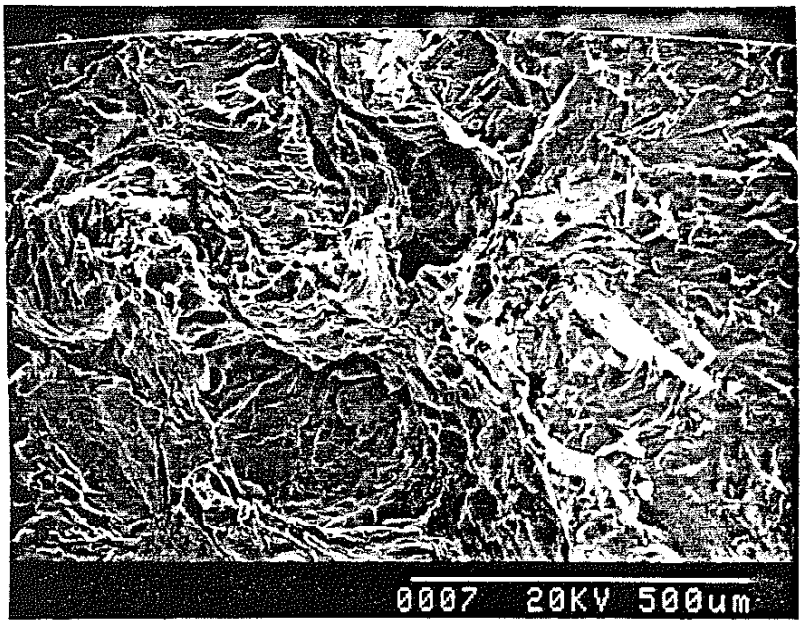


Specimen: B92
Smax = 62 MPa
T = 0.52 mm
N = 9.38 x $10^6$cycles

(b)

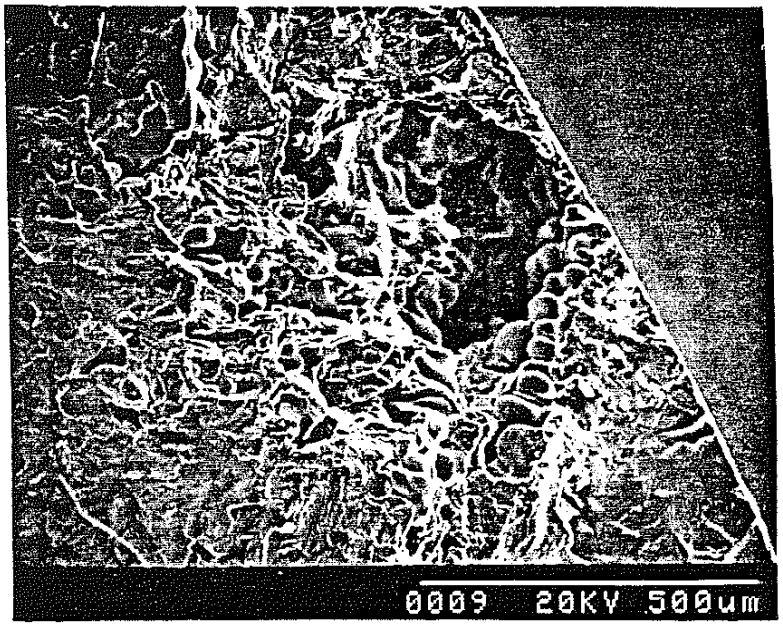


Specimen: B15
Smax = 62 MPa
T = 0.57 mm
N = 4.78 x $10^6$cycles

Figure G.8 Fractographs of initiation site for a polished specimens (a) specimen B92 (97x), and (b) specimen B15 (97x).

(a)


Specimen: AC12
Smax = 55.2 MPa
T = 0.62 mm
N = 5.56 x $10^6$cycles

(b)

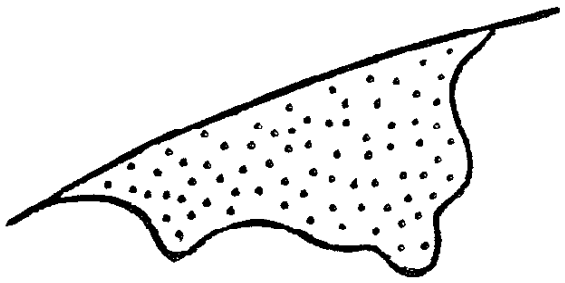

Figure G.9 (a) Fractograph of initiation site for as-cast specimen AC12 (50x). The black spots are ink stains. (b) The trace for estimating the area of fatigue initiation site in (a).

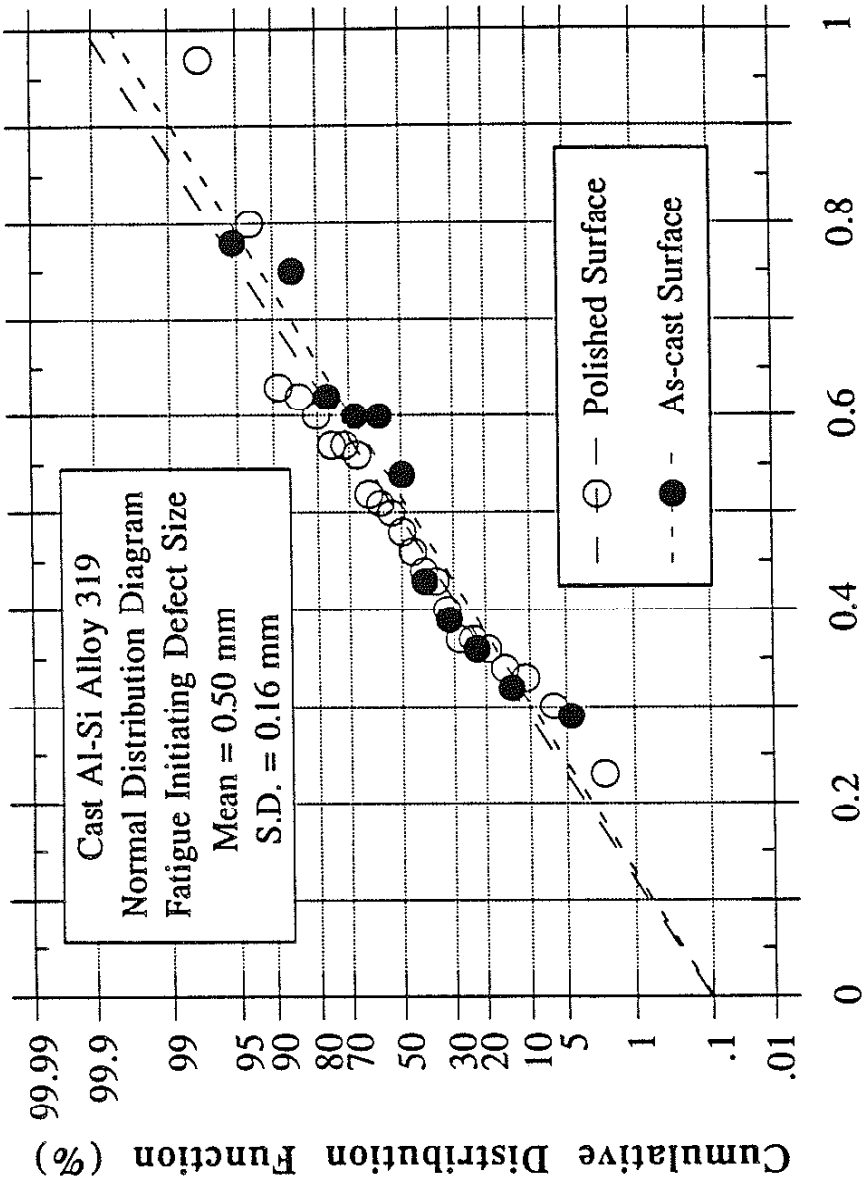


Figure G.10 The size of fatigue initiating defects for specimens with two different surface conditions (plotted on the normal distribution probability paper).

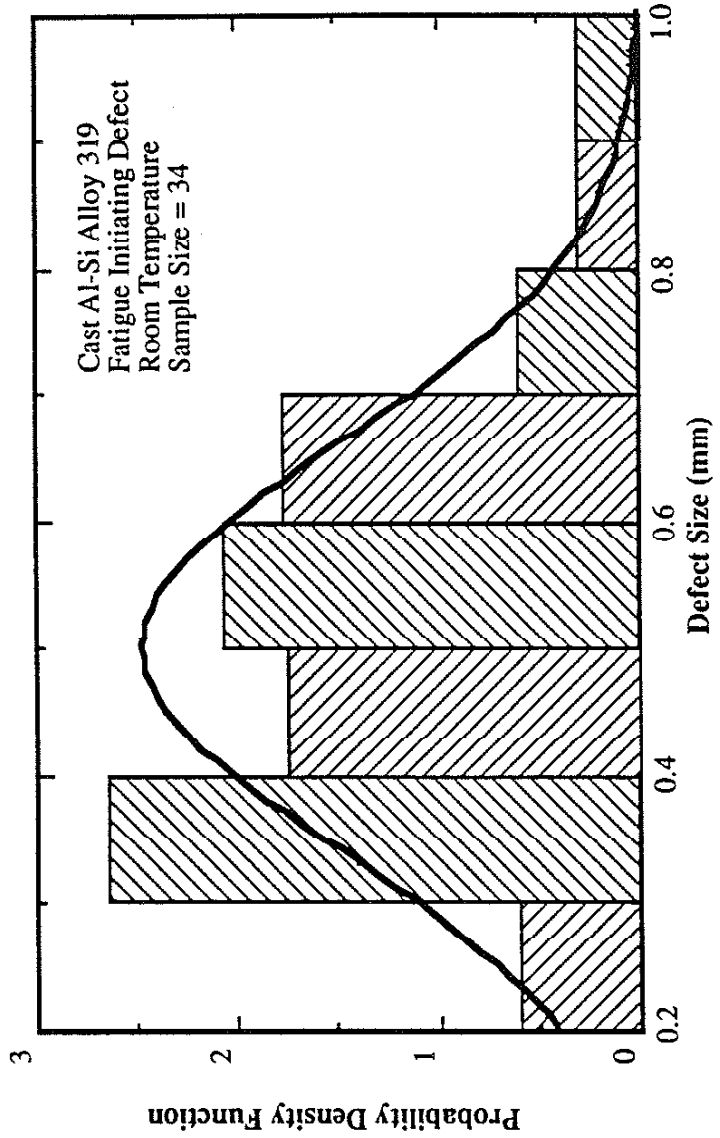


Figure G.11 Comparison of histogram of fatigue initiating defects size and predicted normal distribution function.

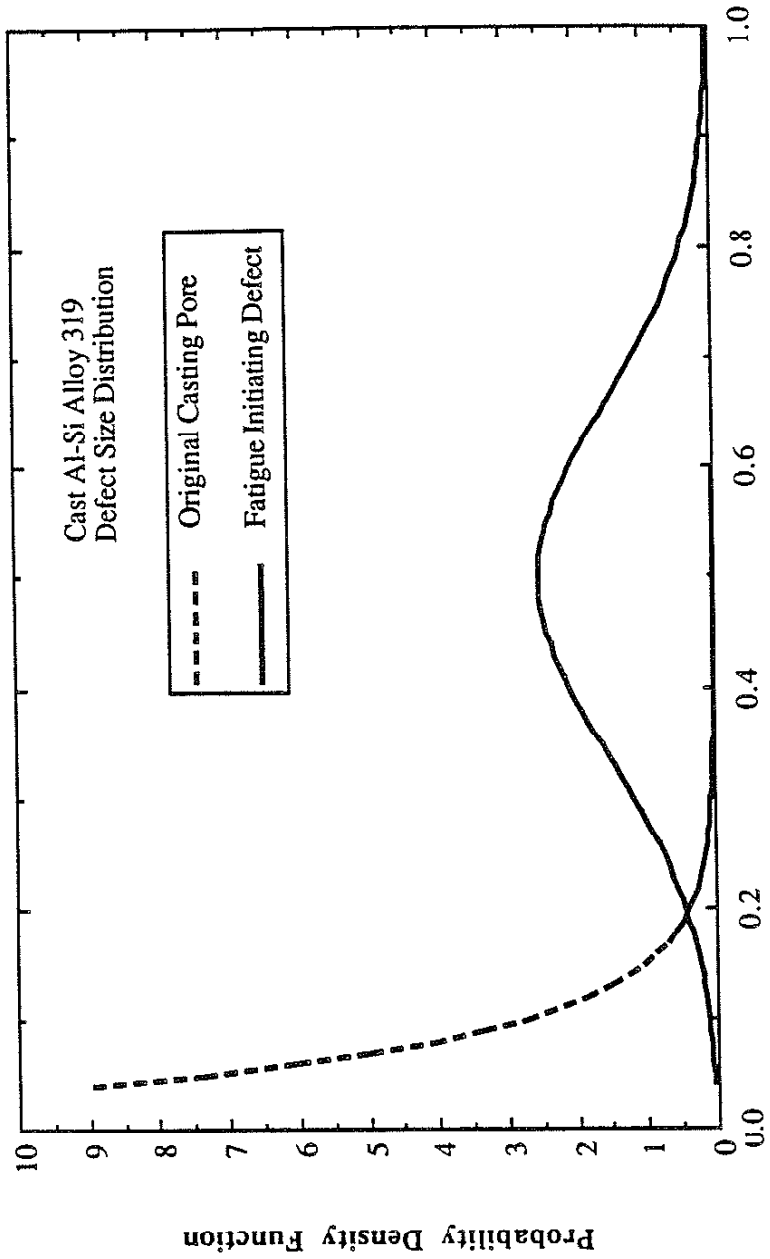


Figure G.12 Comparison of the statistical distribution of casting pore size and fatigue initiating defect size.

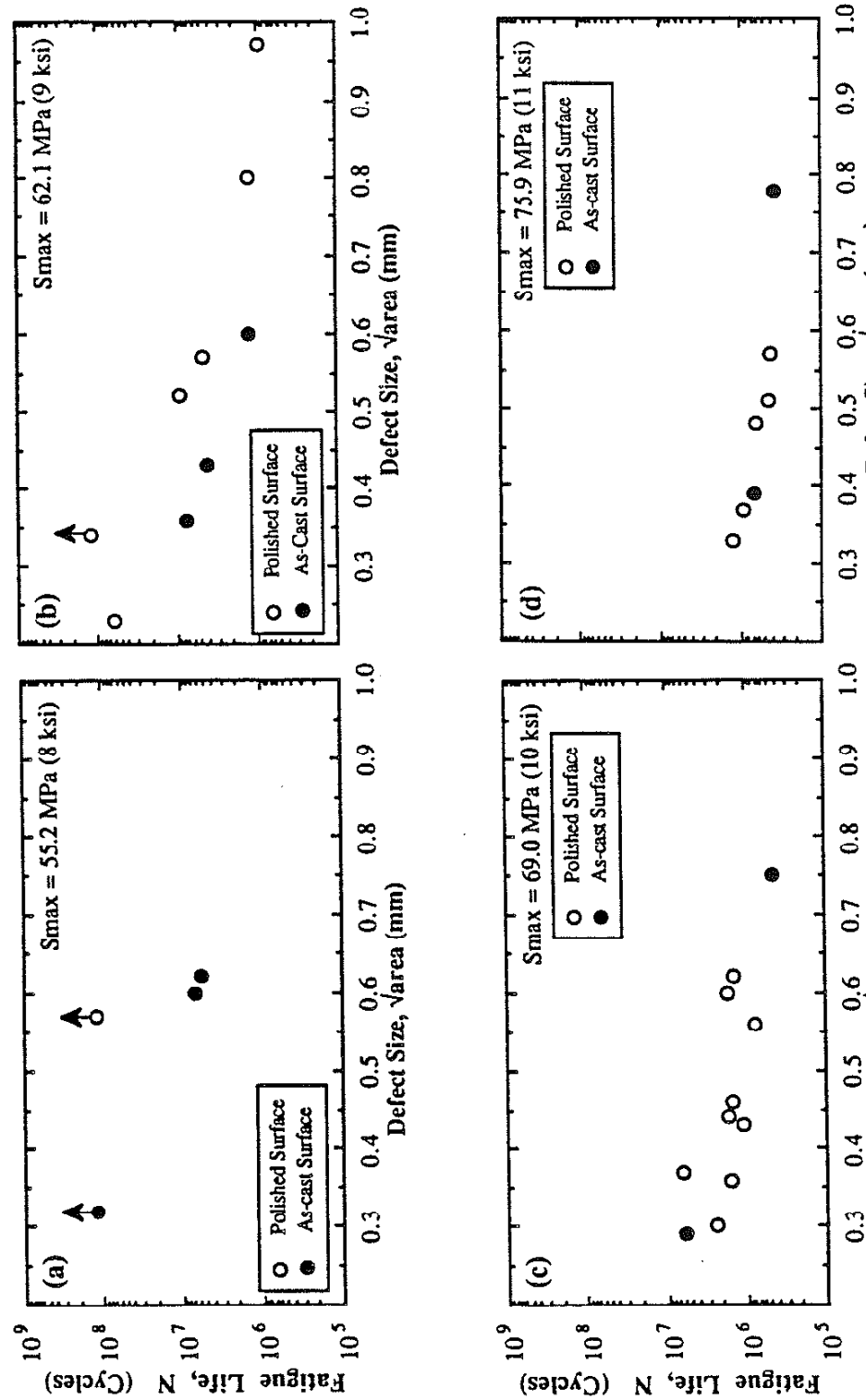


Figure G.13 The influence of fatigue initiating size on the fatigue life at a given applied stress. (a) Smax = 55.2 MPa, (b) Smax = 62.1 MPa, (c) Smax = 69.0 MPa, and (d) Smax = 75.9 MPa. All data points are for cylindrical specimens of cast aluminum alloy 319 tesied under R = -1 and 20 °C.

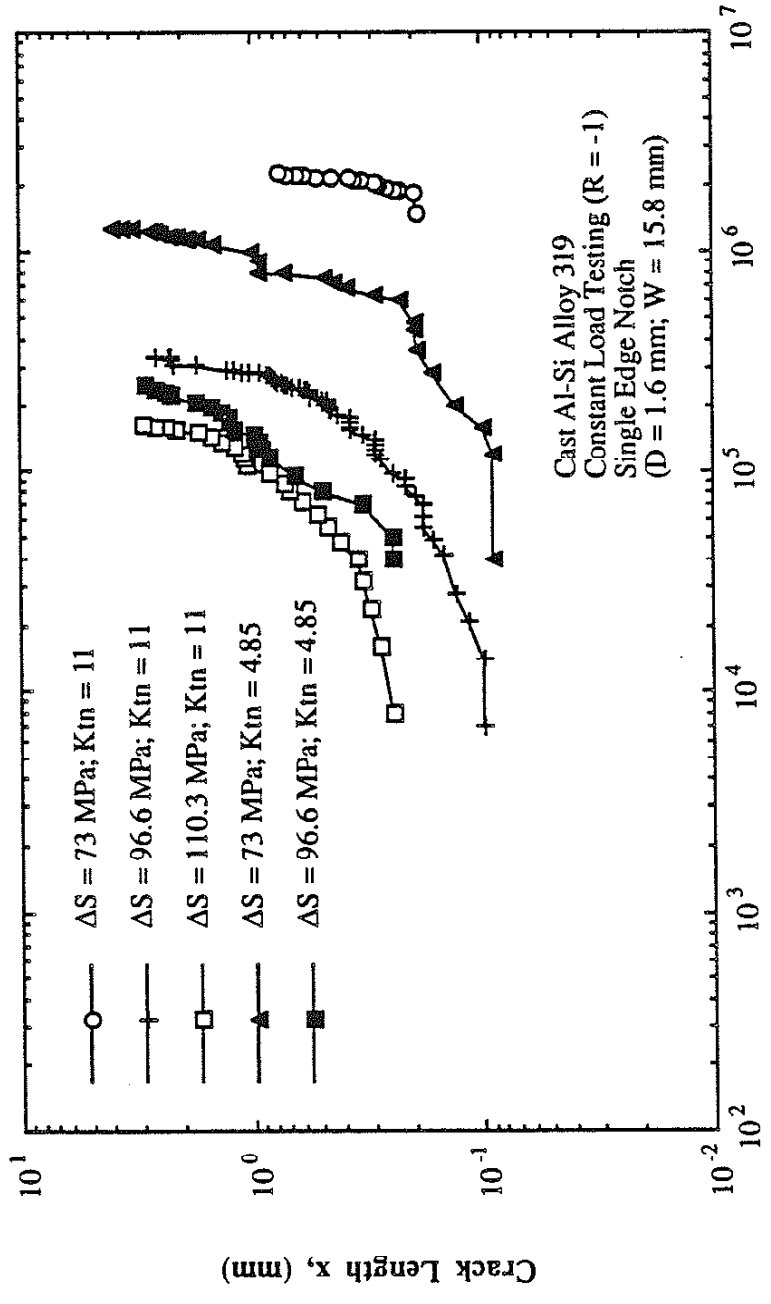


Figure G.14 The variation of fatigue crack length with fatigue cycles under constant loading condition for $R = -1$. SENP specimens were used.

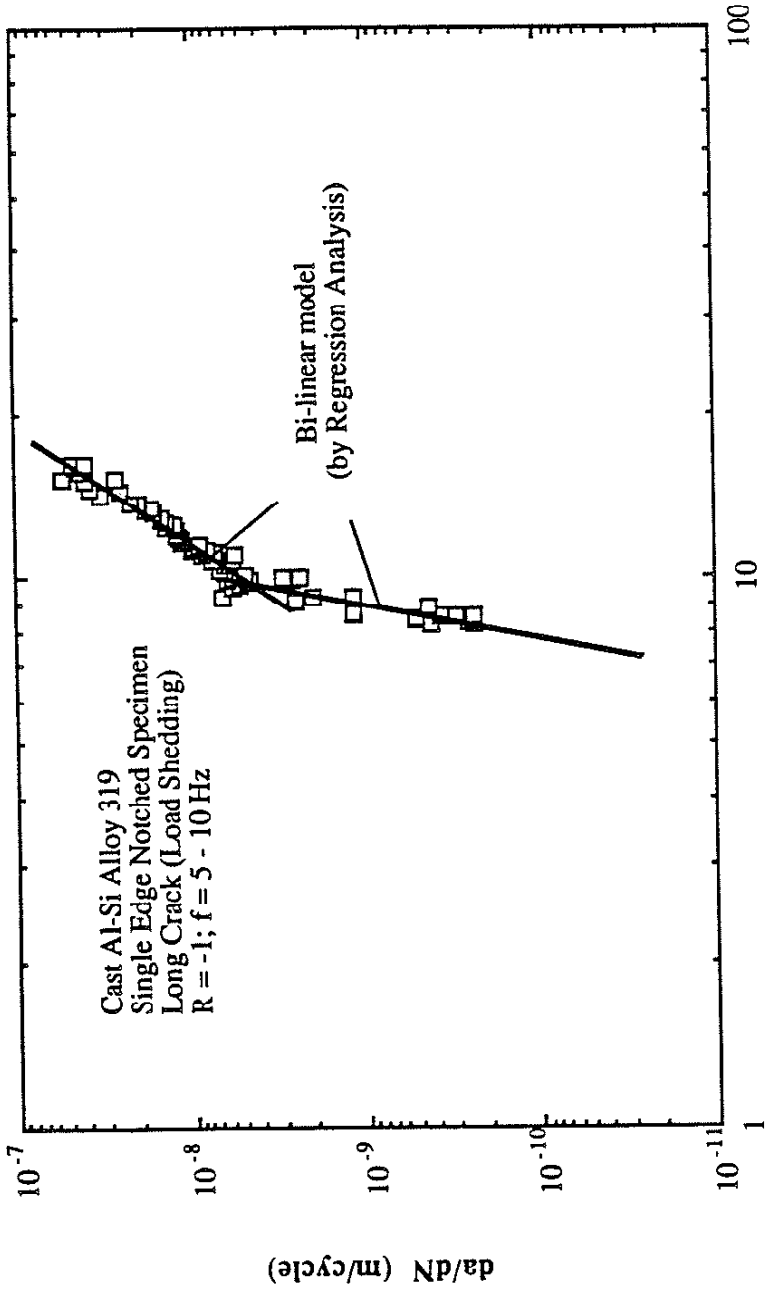


Figure G.15 The long-crack da/dN vs. ΔK data obtained by load-shedding tests under R = -1. Tests was performed by using SENP specimens. Data points are the experimental results and solid lines are the bi-linear regression line for the test data which separates the test data into Stage I (low ΔK regime) and Stage II (mid-growth rate regime).

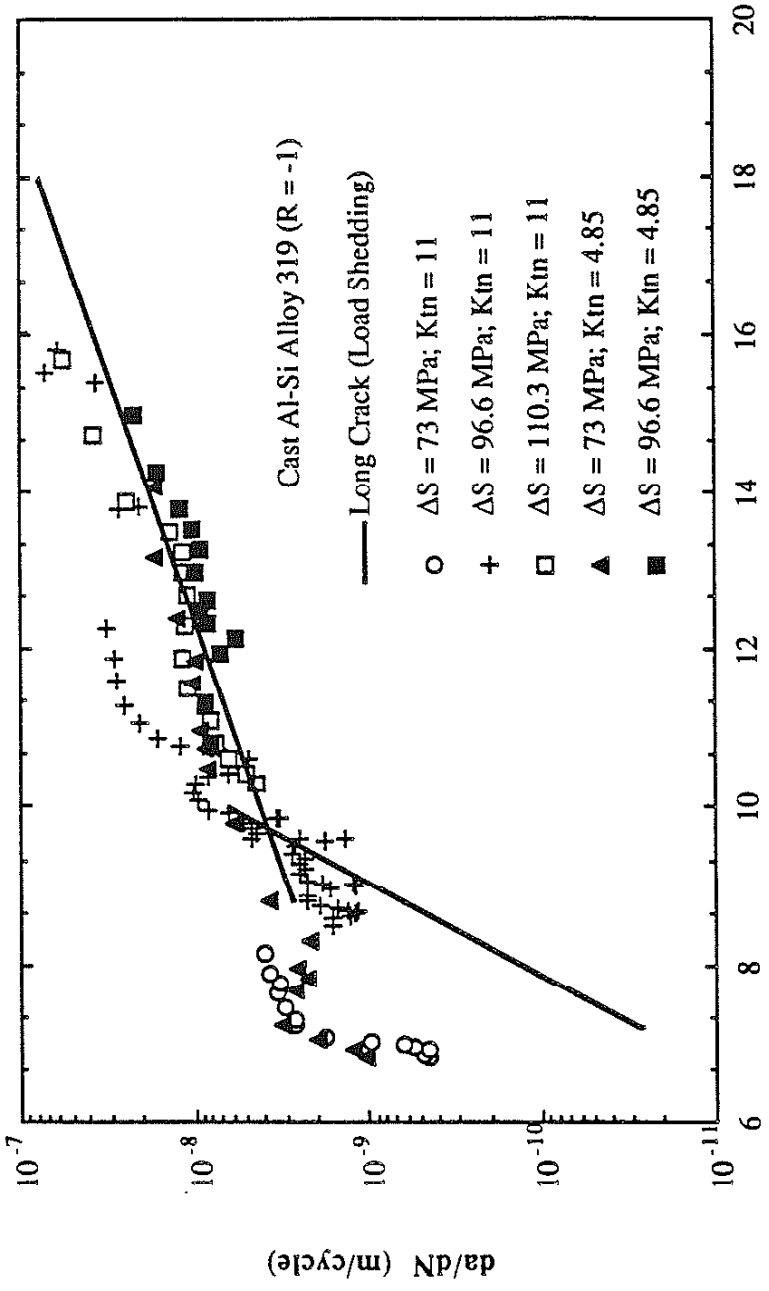


Figure G.16 Comparison of crack growth rate between load-shedding test results (solid lines) and constant load test results (data points) based on da/dN vs. ΔK diagram for R = -1. In the low ΔK regime, the fact that the crack growth rate shown by data points are higher than solid line indicates the anomalous crack growth rate of short-crack behavior.

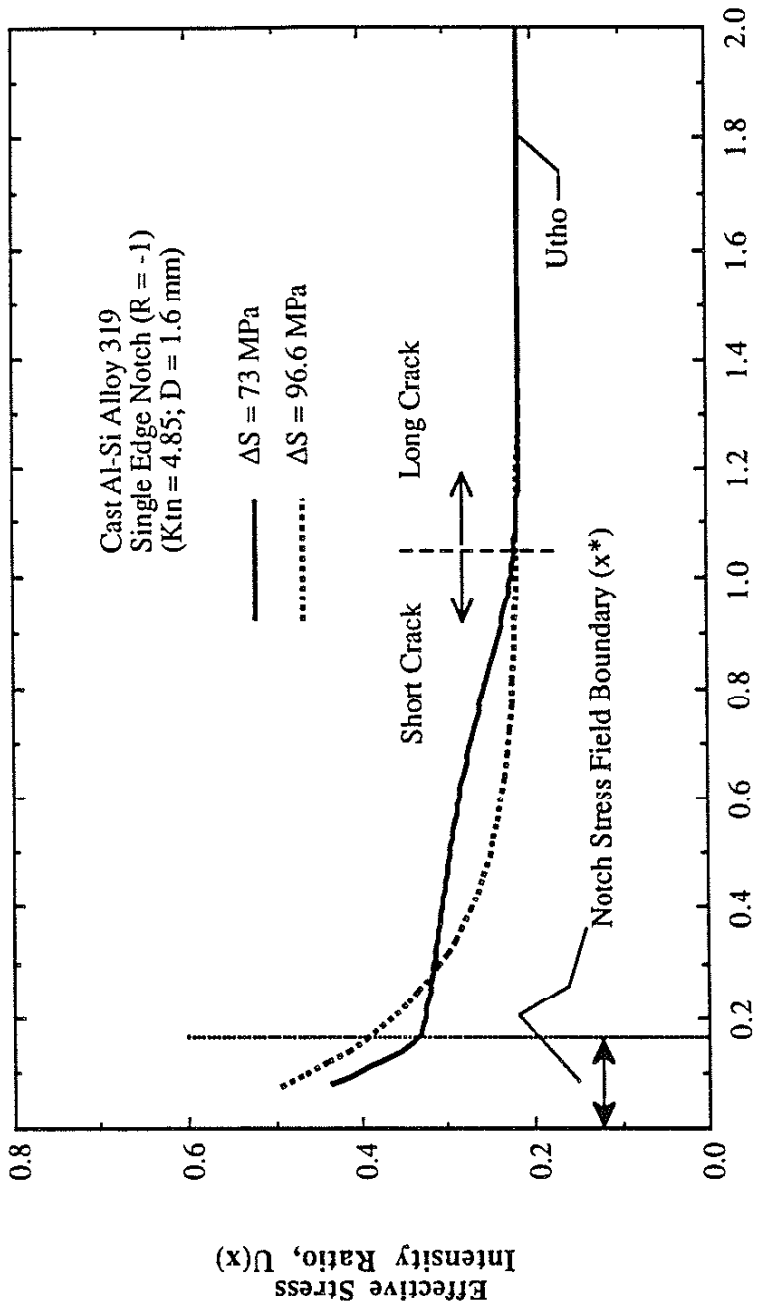


Figure G.17 The predicted U(x) with crack length for two stress ranges.

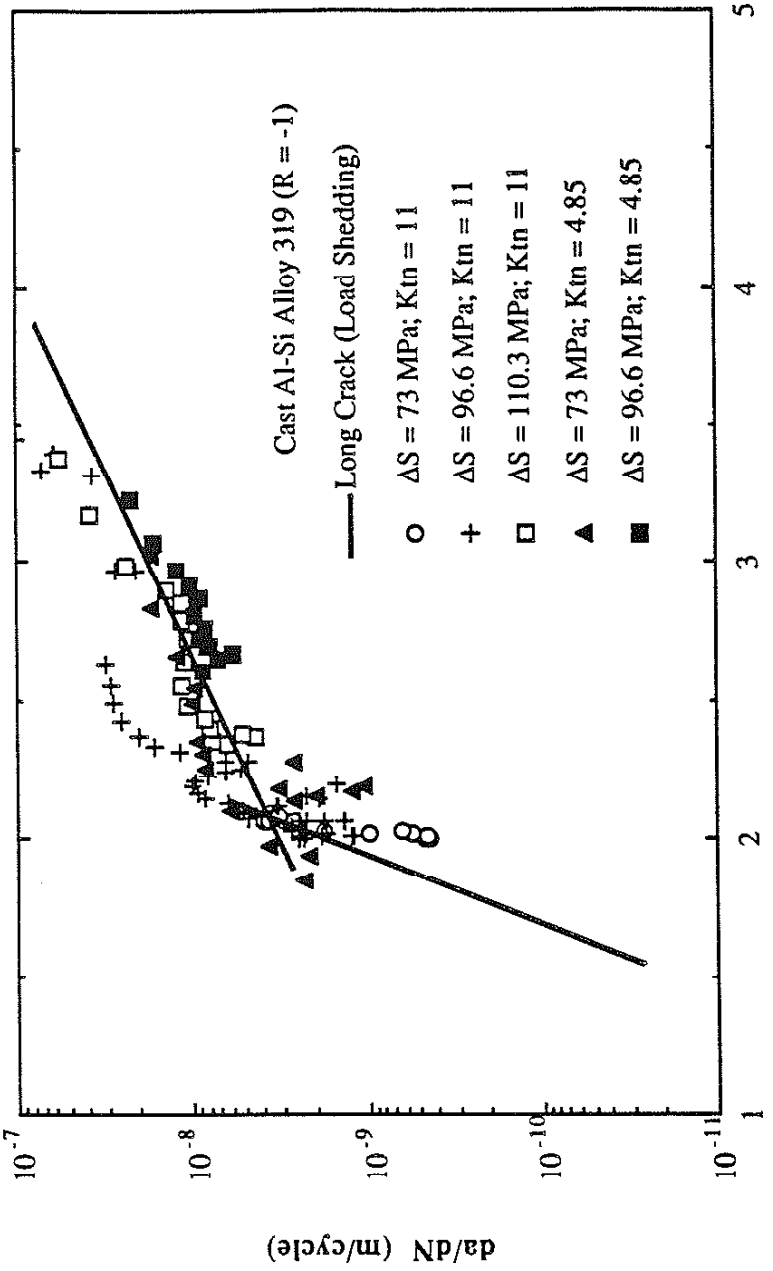


Figure G.18 Comparison of crack growth rate between load-shedding test results (solid lines) and constant load test results (data points) based on da/dN vs. $\Delta K_{eff}$ diagram for R = -1. That the data points converged with solid lines indicated the short-crack growth rate can be rationalized by using effective stress intensity range ($\Delta K_{eff}$).

# APPENDIX H

## S-N DATA TEST STATISTICS

### H.1 Introduction

The experimental portions of this study involved stress-controlled (R = -1) fatigue tests on cylindrical specimens of the cast aluminum alloy 319 under two surface conditions:

(1) PL - Specimens with a polished surface condition, and
(2) AC - Specimens with an as-cast surface condition.

The test statistic is used to compare whether two S-N curves are identical. The method that determines the confidence bands of an S-N curve was followed by ASTM standard E739. The test statistic was used to check whether there were significant differences between the two test conditions. Before making the comparison for the experimental S-N data, the fundamentals [62] of the test statistic are summarized below.

### H.2 The Fundamentals of Test Statistic for Two or More S-N Curves

The experimental data from two surface conditions are considered. The procedures developed are used to test the equality of two regression lines which are obtained by treating these two groups of data separately. The model which provides regression line for each S-N data is:

$$Y_{ij} = A_j + B_j X_{ij} + \varepsilon_{ij} \qquad \text{(II.1)}$$

where:

| | | |
|---|---|---|
| $Y_{ij}$ | = | Logarithm of fatigue life (N), i.e. log $(N)_{ij}$ |
| $X_{ij}$ | = | Stress amplitude ($S_{ij}$) |
| $A_j$ | = | Intercept of the Y coordinate |
| $B_j$ | = | Slope of the regression line |
| $\varepsilon_{ij}$ | = | Residual error |
| i | = | $1,2,....k_j$ |
| j | = | The specific group of data sets which is considered; for testing whether two S-N curves are identical, the j is either 1 or 2. |
| $k_j$ | = | Number of S-N data |

For both conditions of S-N data, the coefficients $A_1$, $B_1$, $A_2$, and $B_2$ can be obtained. Also, the error sum of square ($SSE_j$) is:

$$SSE_j = \sum_{i=1}^{k_j} (Y_{ij} - \hat{Y}_{ij})^2 \qquad (H.2)$$

where: $\hat{Y}_{ij}$ = Predicted values based on the regression line

The $SSE_j$ have $(k_j - 2)$ degrees of freedom (DOF). The error sum of squares for the regression for the first test conditions of S-N data is denoted as $SSE_1$ and that for second condition is denoted as $SSE_2$. The sum of $SSE_1$ and $SSE_2$ is represented as SSE(F), i.e., $SSE(F) = SSE_1 + SSE_2$. The number of degrees of freedom associated with SSE(F) are $(k_1 - 2) + (k_2 - 2) = k_1 + k_2 - 4$

When the two sets of S-N data are considered as one, the fitted regression line is:

$$Y_i = A_o + B_o X_i + \varepsilon_i \qquad (H.3)$$

where:
- $Y_i$ = Logarithm of fatigue life, i.e. $\log (N_f)_i$
- $X_i$ = Stress amplitude $(S_i)$;
- $A_o$ = Intercept of Y coordinate
- $B_o$ = Slope of the regression line
- $\varepsilon_i$ = Residual error
- $i$ = $1,2,....(k_1 + k_2)$; see definition of $k_1$ and $k_2$ in Eq. H.1.

The error sum of square calculated from Eqs. H.2 and H.3 is denoted SSE(R), and the number of degrees of freedom associated with SSE(R) are $(k_1 + k_2 - 2)$.

The test statistic for the analysis of variance approach is denoted F*:

$$F^* = \frac{\dfrac{SSE(R) - SSE(F)}{(k_1 + k_2 - 2) - (k_1 + k_2 - 4)}}{\dfrac{SSE(F)}{(k_1 + k_2 - 4)}} = \frac{\dfrac{SSE(R) - SSE(F)}{2}}{\dfrac{SSE(F)}{(k_1 + k_2 - 4)}} \qquad (H.4)$$

Usually, the significance levels ($\alpha$) of 0.01 or 0.05 are selected. If $F^* \geq F(1 - \alpha; 2, k_1 + k_2 - 4)$, then it can be concluded that the linear regression functions for the two conditions of S-N data are $(1 - \alpha)\%$ confidence indicating a difference. Otherwise, there is no significant difference between these two regression lines.

This procedure can be extended to test the equality of three or more error sums of squares for each of the separate regression lines, and the degree of freedom (DOF) would need to modified accordingly.

H.3 Test Statistic of the Experimental S-N Data

In deriving the regression line of S-N data, the run-out data should be excluded. The parameters computed from the regression analysis for each of the conditions and the lumped conditions are listed in Table H-1. A new parameter $\hat{\sigma}^2$, the estimation of variance of the normal distribution for $(\log N)_j$, is given by:

$$\hat{\sigma}^2 = \frac{SSE}{k - 2} \tag{H.5}$$

The confidence band for the entire median S-N curve can be computed using the following equation:

$$A + BX \pm \sqrt{2F_p\hat{\sigma}}\left[\frac{1}{k} + \frac{(X - \bar{X})^2}{\sum_{i=1}^{k}(X_i - \bar{X})^2}\right]^{0.5} \tag{H.6}$$

where: $F_p = F(1 - \alpha; 2, k-2)$
$X$ = Stress amplitude
$\bar{X}$ = Average of X

H.3.1 Whether PL and AC are Identical

Figure H.1 shows the 99% confidence band of median S-N curve for the polished surface condition (PL). Figures H.2 show the 99% confidence band of median S-N curve for the as-cast surface condition (AC). The test statistic for testing the equality of PL and AC conditions of the cast aluminum alloy 319 are computed as follows:

SSE (F) = 3.08543 + 1.08792 = 4.17335
SSE (R) = 4.37518

$$F^* = \frac{\dfrac{0.020183}{2}}{\dfrac{4.17335}{(24 + 12 - 4)}} = 0.7738$$

Select $\alpha = 0.05$, then $F(0.95; 2, 32) = 3.31$

Since $F^* = 0.7738 < F(0.99; 2, 32) = 3.31$, the linear regression functions for the two S-N conditions (PL and AC) are identical. The 99% confidence band of median S-N curve for the combined data of PL and AC is plotted in Fig. H.3. From the test statistic, one can conclude that there is no significant difference in fatigue strength between the polished and as-cast surface conditions of the cast aluminum alloy 319.

TABLE H-1

PARAMETERS COMPUTED FROM REGRESSION ANALYSES OF S-N CURVES FOR THE CAST ALUMINUM ALLOY 319

| Test Condition | k | A | B | SSE | $\hat{\sigma}$ |
|---|---|---|---|---|---|
| PL | 24 | 10.377 | -0.05997 | 3.08543 | 0.374495 |
| AC | 12 | 9.922 | -0.05568 | 1.08792 | 0.329836 |
| PL + AC | 36 | 9.997 | -0.05531 | 4.37518 | 0.358723 |

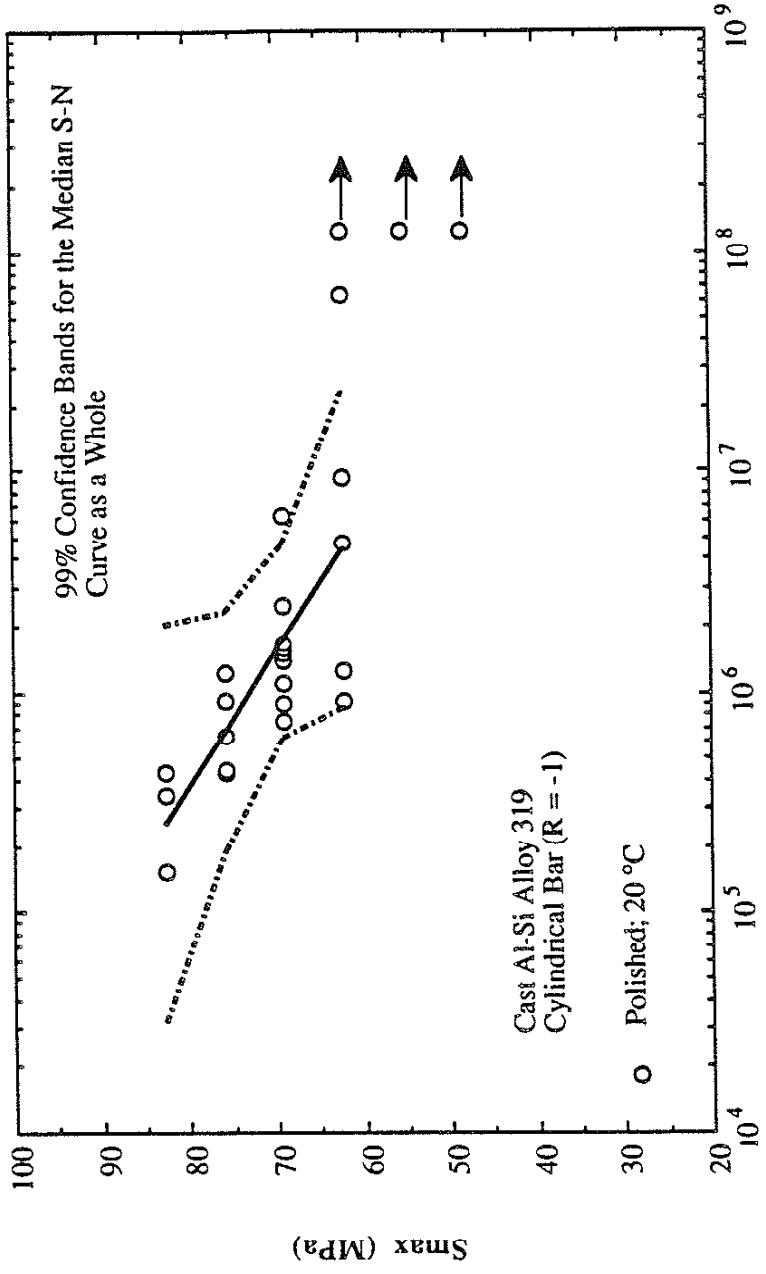


Figure H.1 The 99% confidence band of median S-N curve for polished specimens.

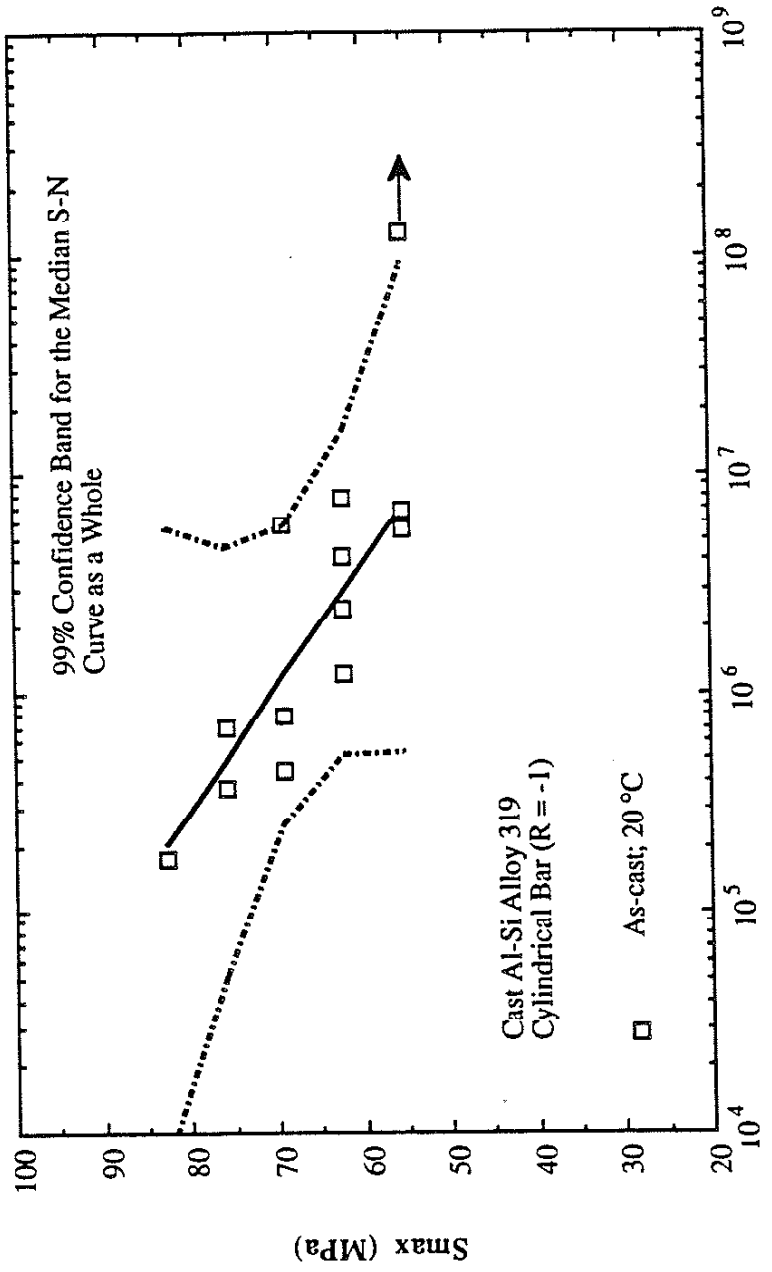


Figure II.2 The 99% confidence band of median S-N curve for as-cast specimens.

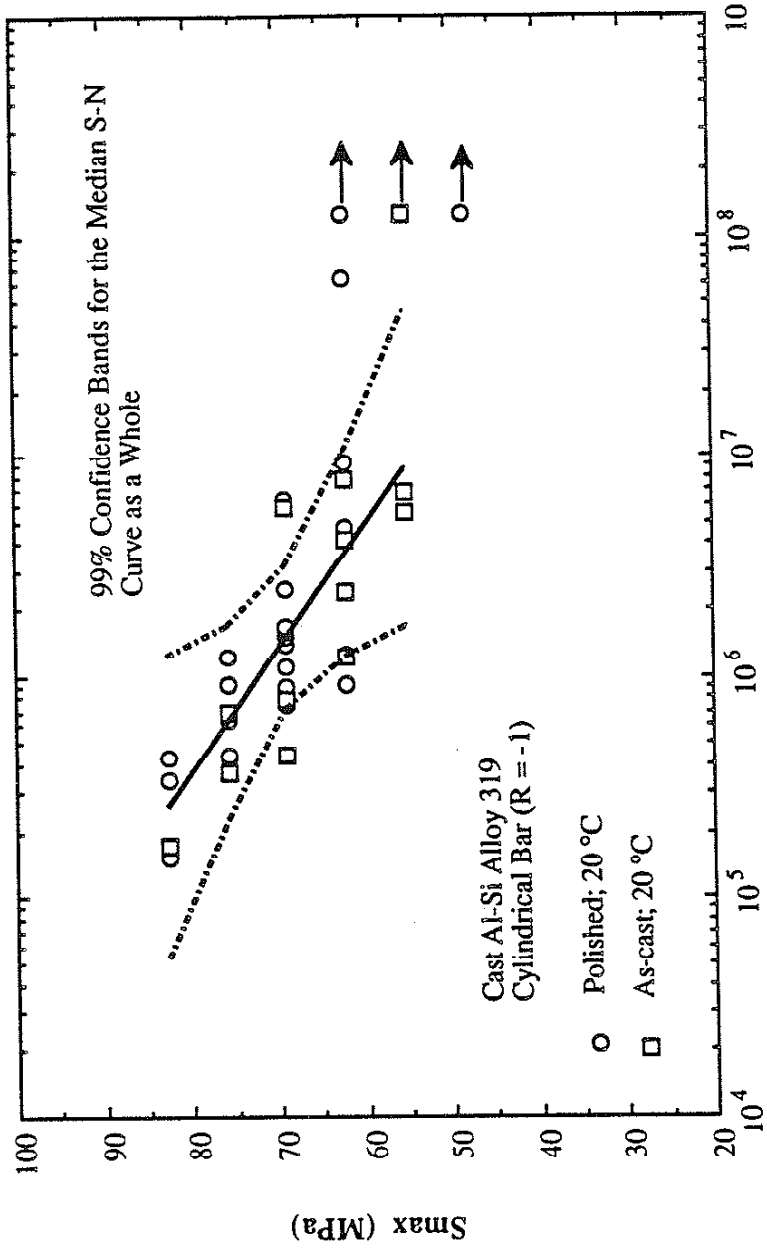


Figure H.3 The 99% confidence band of median S-N curve for both polished and as-cast specimens.

# APPENDIX I

## OBSERVATION OF CRACK NUCLEATION AND EARLY GROWTH

### I.1 Specimens and Testing Procedures

Prismatic specimens for three-point-bending tests were prepared to study the location of fatigue crack initiation sites. The specimens had a height of 16.5 mm, a width of 9.5 mm and a length of 73 mm. The geometry and fixture for testing the specimens is shown in Fig. I.1. The span between the support rollers on the bottom surface was 63 mm. Prior to testing, the bottom surface of the prismatic specimen was prepared for studying fatigue crack initiation by polishing it using a 0.5 μm alumina abrasive.

Bending fatigue tests were performed under a R ratio of 0.1 and frequency of 10 Hz. at room temperature condition. The maximum extreme fiber stress at mid-span was 124 MPa. Acetyl cellulose films were used to take replicas of the bottom surface periodically during fatigue testing. The replicas were gold coated to facilitate observation using reflected-light microscopy.

Fatigue testing was stopped when a growing (surface) crack larger than 1 mm in length was detected. The crack path into the specimen surface was examined by successively polishing and photographing the crack. The depth of polish ($\Delta h$) from the original surface was measured to an accuracy of $\pm$ 0.005 mm using a travelling microscope.

### I.2 Crack Nucleation and Early Growth

Several small surface cracks were found at various locations on the original surface during fatigue testing, but most of them arrested without growing further. For each of the specimens studied, a dominant crack which propagated with increasing fatigue cycles was found.

Figures I.2 show the crack development observed in one specimen which had no visible casting pore on the original polished surface. When the number of cycles was $2.5 \times 10^5$, a surface crack about 0.4 mm in length was found as shown in Fig. I.2a. The arrows (a,b,c and d) in Fig. I.2a indicate crack positions discussed below. The locations (arrows) "a" and "b" show that the crack passed through the eutectic; the location "c" shows that the crack propagates along the boundary between eutectic and aluminum-based matrix, and the location "d" shows a secondary crack which lies within the aluminum-based matrix.

Fatigue testing of this specimen was stopped at $1.5x10^6$ cycles when the dominant fatigue crack was longer than 1 mm as shown in Fig. I.2b. Note that the picture shown as Fig. I.2b was taken directly from the surface of post-test specimen; and thus, the image is the reverse of that in Fig. I.2a which was taken form a replica. However, the marks (a,b,c and d) on the two pictures still indicate the same locations.

The cracked specimen was further investigated by polishing inward from the outer surface. The crack and microstructure on the plane of polish at $\Delta h = 0.01$ mm is shown in Fig. I.2c in which several small casting pores are apparent indicating that the casting pores (or pore) existed beneath the original surface. The fact that the cracks link with these pores suggests these pores were the actual crack initiation sites. Additional observations at deeper planes of polish (larger $\Delta h$) gave additional support to this idea.

The features observed at planes of polish $\Delta h = 0.015$ , 0.02 and 0.04 mm are shown in Figs. I.2d, I.2e, and I.2f, respectively. The areas of the casting pores increase with increasing $\Delta h$. At a polish depth of $\Delta h = 0.04$ mm (Fig. I.2f), the small arrows mark the location where the crack links with the casting pore. At this depth ($\Delta h = 0.04$), the locations "c" and "d" on the crack are replaced by the casting pores.

Further polishing to a depth $\Delta h = 0.08$ mm, bigger casting pores are seen as shown in Fig. I.2g. At this depth, all the crack locations "a", "b", "c" and "d" were replaced by the pores. Comparing Figs. I.2a, I.2b and I.2h, it seems that the dominant fatigue crack initiated from the sub-surface casting pore (or a group of pores). The casting pore has an irregular three-dimensional shape; thus, it is hard to determine whether the observed casting pores (or pore) located under the original surface are a single pore or a cluster of independent smaller pores.

A similar experiment was carried out on a second specimen. This specimen had lots of sponge-type casting pores (a group or cluster with several small pores) on the original surface. Figure I.3a shows a dominant crack which propagated between two groups of casting pores at $2.5x10^6$ cycles. The locations marked by "b" and "c" are the first observed small cracks on the original surface as seen on the replica taken at $8x10^5$ cycles (see Fig. I.3b). In Fig. I.3b, two small surface cracks with length about 0.1 mm were observed at an early stage of fatigue life and are marked as "b" and "c". These small surface cracks grew slowly until $1.6x10^6$ cycles (see Fig. I.3c). From the $2.0x10^6$ cycles, a dominant crack started to propagate from the location "c" and propagated with a faster crack growth rate. The fatigue testing was stopped at $2.5x10^6$ cycles, and the microscopic features are shown in Fig. I.3d.

Fatigue testing of this specimen was stopped at $2.5x10^6$ cycles, and then the original surface was removed by successive polishing. The microscopic features shown in

Fig. I.3e were observed at $\Delta h = 0.015$ mm. The crack is connected to a small sub-surface pore (see the location "c"). In Fig. I.3f, the location "c" is within a small pore; the crack has almost disappeared at $\Delta h = 0.04$. At $\Delta h = 0.08$ mm in Fig. I.3g, the locations "a", "b" and "c" are all within the pores (or pore).

## I.3 Discussion

In both specimens studied, the dominant crack was linked with sub-surface pores: see Figs. I.2c and Fig. I.3e. Actually, these pores are probably not separated pores but the most acute locations on the outer perimeter of an unseen, single pore which is apparent at greater depths of polish: see Figs. I. 2g and I. 3g.

It appears that fatigue cracks initiate at near-surface (sub-surface) casting pores and quickly propagate to the outer surface through the thin ligament separating the pore from the outer surface. The state of stress in these ligaments must be much higher than the average stress; and thus, the crack was initiated from the inner to the outer surface.

The crack nucleation life (which must be shorter than the fatigue cycle at which the small cracks were first seen) is almost negligible when compared with the total fatigue life (which must be longer than the fatigue cycles at which surface-crack length was about 1 mm). The same results were also reported by Starkey [66].

## I.4 Conclusions

1. Fatigue cracks initiated from casting pores (or pores) just below the specimen surface.

2. The eutectic microstructure seems to have little effect on the fatigue crack initiation and early propagation.

3. The casting pores just below the specimen surface are more detrimental than pores located at the surface.

4. The cracks propagate through the ligament between the sub-surface pore and the outer surface. The crack nucleation life is short when compared with the total fatigue life.

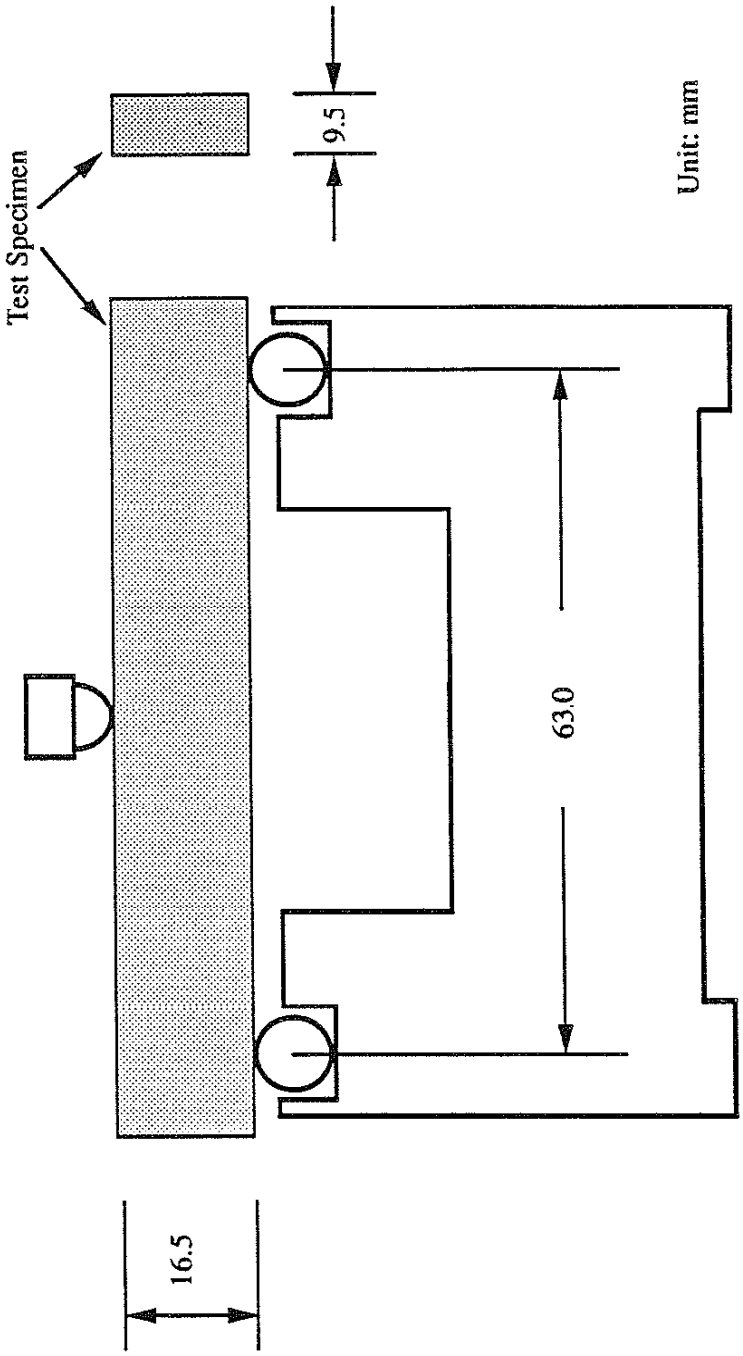


Figure I.1 Geometry and fixture of the specimen for the bending tests.

Figure I.2 Observation of crack development from a specimen without apparent casting pores on the original polished surface. The arrow marks "a", "b", "c" and "d" show the same locations for all photographs in this figure.

(a) $\Delta h = 0$, fatigue cycles = $2.5 \times 10^5$ (replica),

(b) $\Delta h = 0$, fatigue cycles = $1.5 \times 10^6$, stop fatigue testing at this fatigue cycles,

(c) $\Delta h = 0.01$ mm,

(d) $\Delta h = 0.015$ mm,

(e) $\Delta h = 0.02$ mm,

(f) $\Delta h = 0.04$ mm, arrayed small arrows point the crack,

(g) $\Delta h = 0.08$ mm , arrayed small arrows point the crack,

(h) $\Delta h = 0.08$ mm (half magnification of Fig. B.2g.).

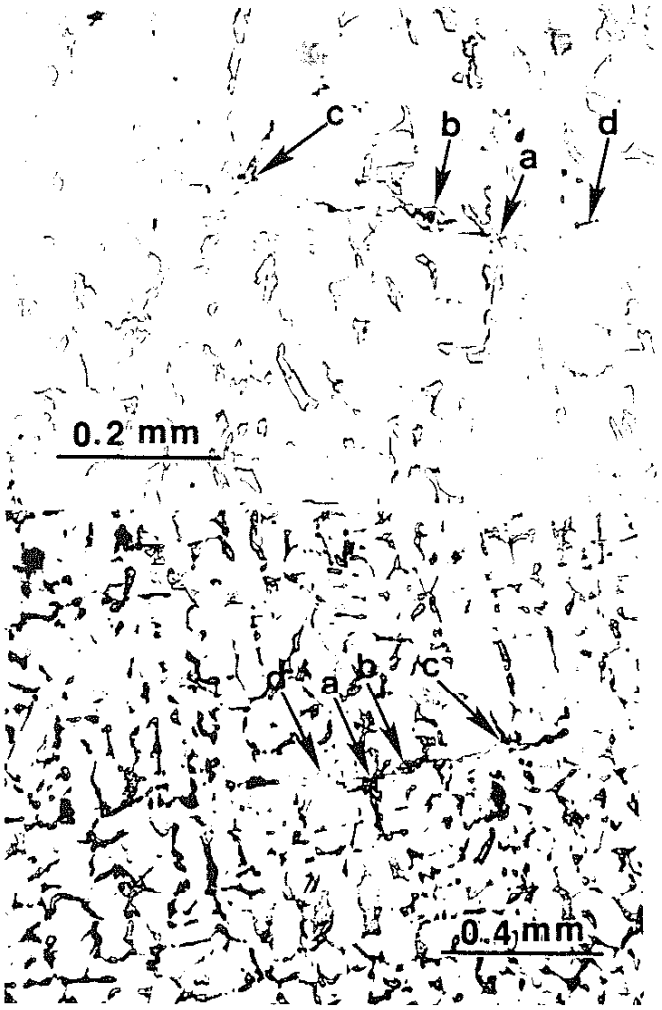


(I.2a)

$\Delta h = 0$
N = 2.5E5
(Replica)

(I.2b)

$\Delta h = 0$
N = 1.5E6

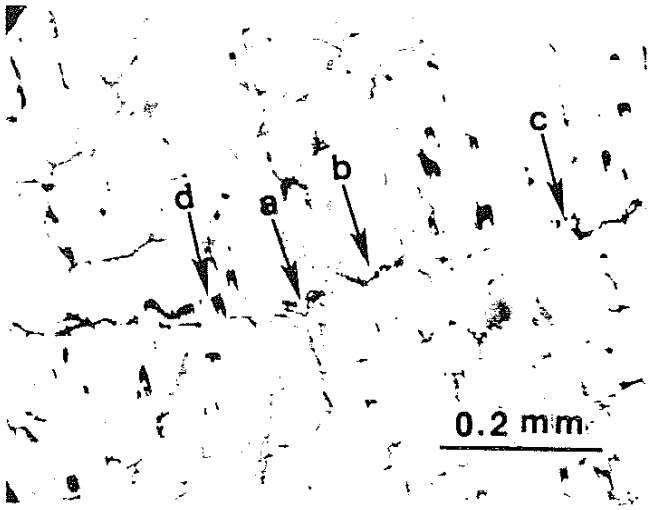


(I.2c)

$\Delta h = 0.01$ mm


(I.2d)

Δh = 0.015 mm


(I.2e)

Δh = 0.02 mm
N = 1.5E6


(I.2f)

Δh = 0.04 mm

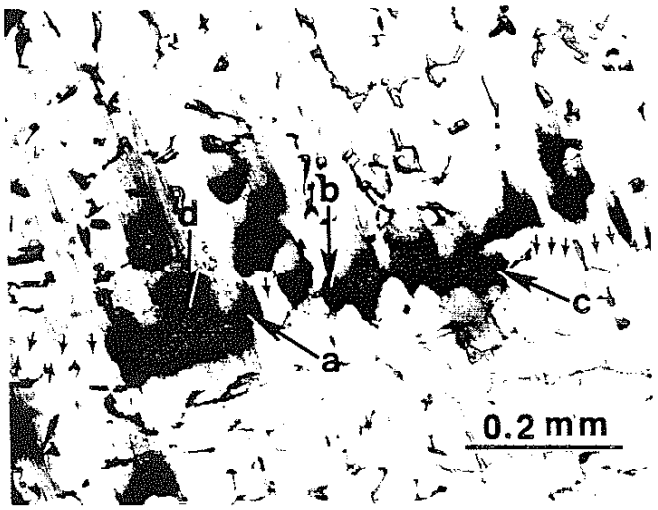


(I.2g)

Δh = 0.08 mm

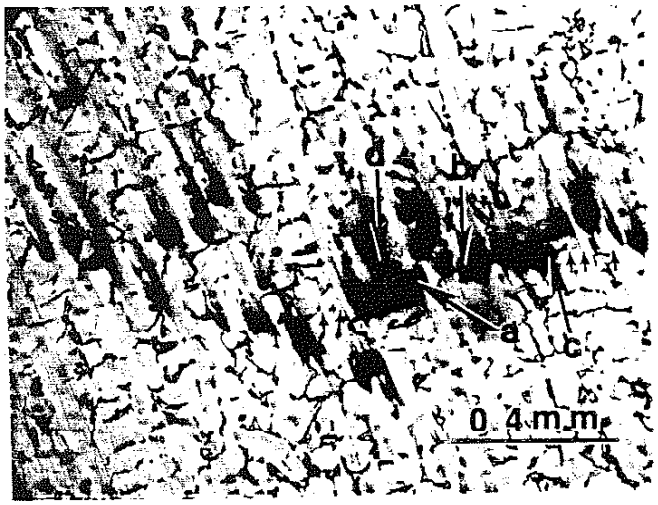


(I.2h)

Δh = 0.08 mm
(half magnification
of Fig. I.2g)

Figure I.3 Observation of crack development from a specimen with lots of apparent casting pores on the original polished surface. The arrow marks "a", "b", and "c" show the same locations for all photographs in this figure.

(a) $\Delta h = 0$, fatigue cycles = $2.5 \times 10^6$, stop fatigue testing at this fatigue cycles,

(b) $\Delta h = 0$, fatigue cycles = $8.0 \times 10^5$ (replica), initiated cracks start from "b" and "c",

(c) $\Delta h = 0$, fatigue cycle = $1.6 \times 10^6$ (replica)

(d) $\Delta h = 0$, fatigue cycles = $2.5 \times 10^6$, stop fatigue testing at this fatigue cycles (replica)

(e) $\Delta h = 0.015$ mm, arrayed small arrows point the crack,

(f) $\Delta h = 0.04$ mm, arrayed small arrows point the crack, "c" are located at positions where a pore below original surface,

(g) $\Delta h = 0.08$ mm, it is apparent that "a", "b" and "c" are located at positions where a pore below original surface.

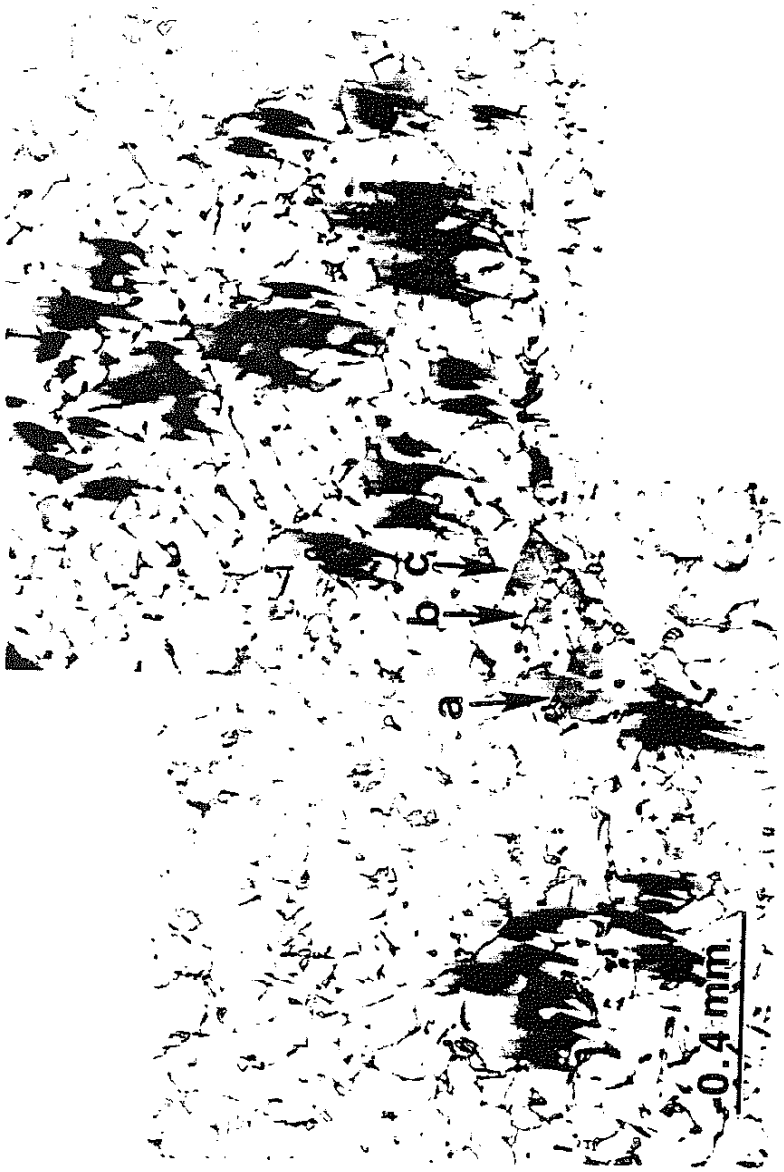


(I.3a)

$\Delta h = 0$
N = 2.5E6

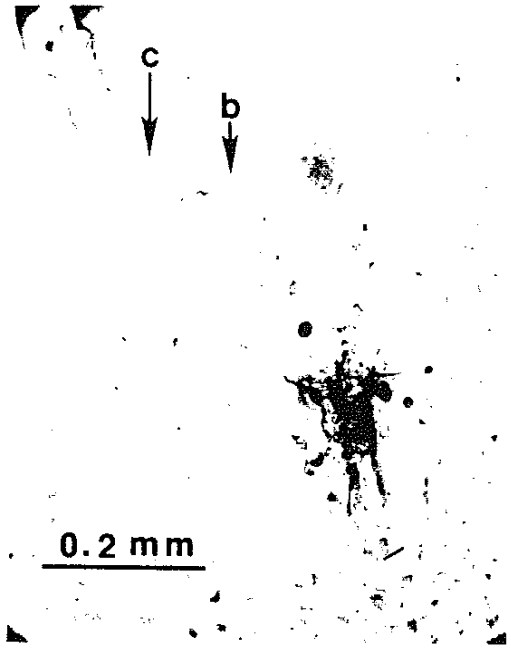


(I.3b) N = 8.0E5 Δh = 0

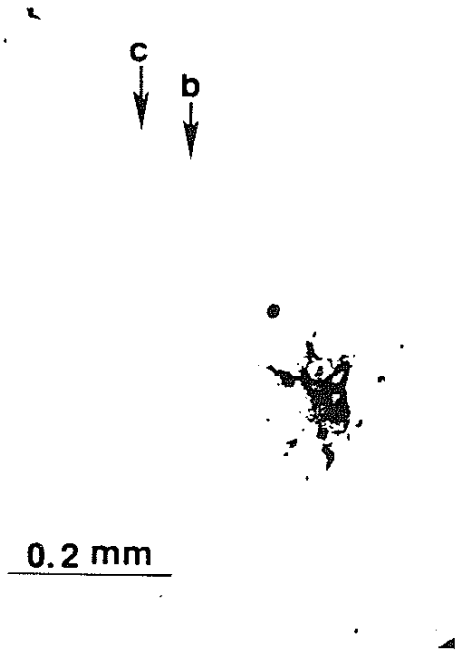


(I.3c) N = 1.6 E6 Δh = 0

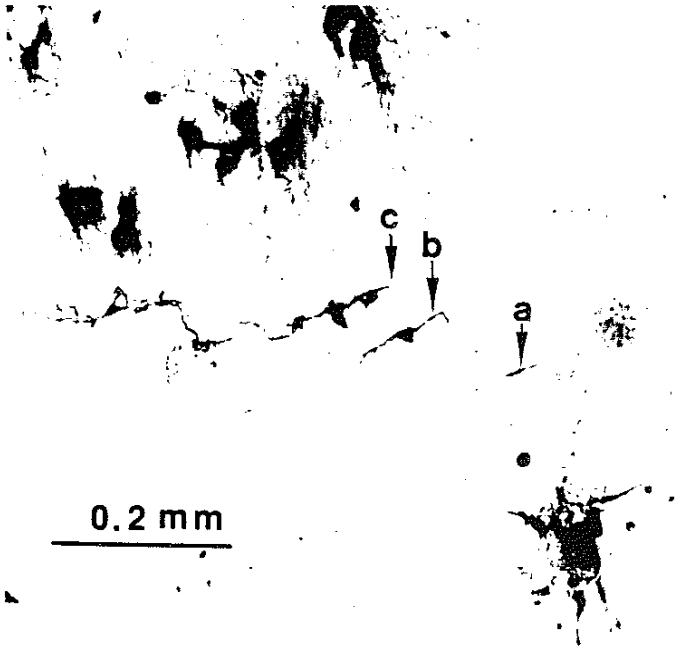


(I.3d)
Δh = 0
N = 2.5E6

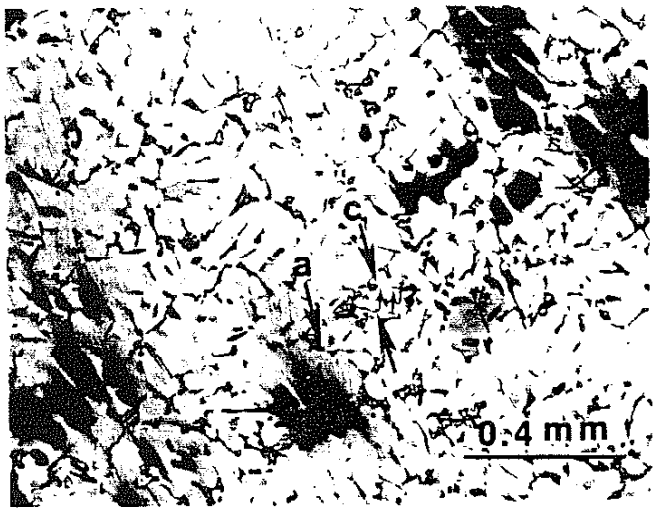


(I.3e)

Δh = 0.015 mm
N = 2.5E6

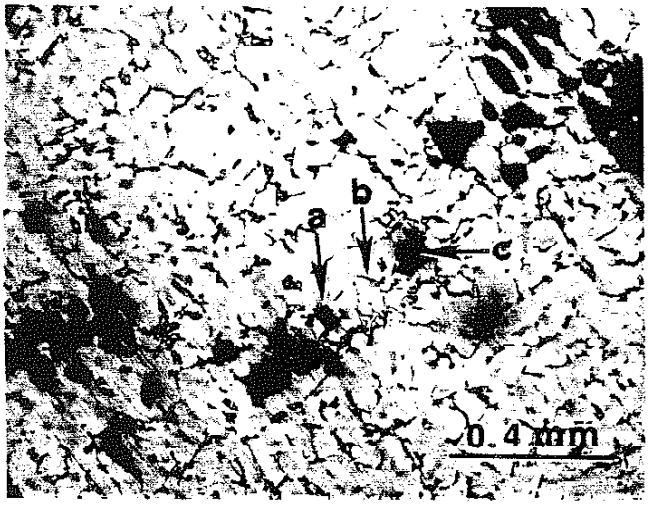


(I.3f)

Δh = 0.04 mm
N = 2.5E6

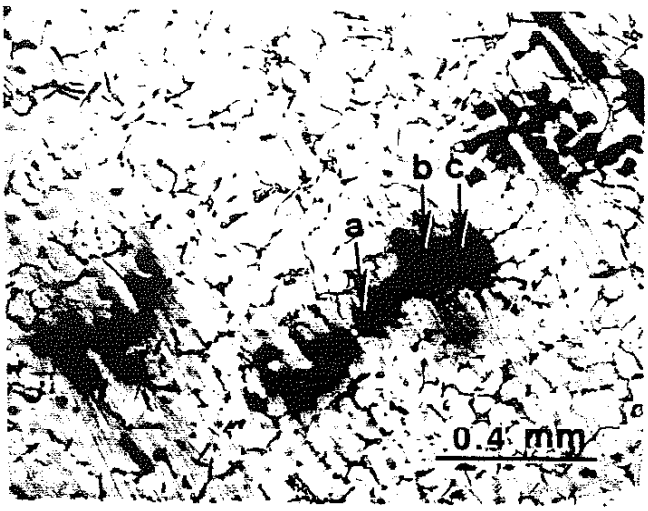


(I.3g)

Δh = 0.08 mm
N = 2.5E6

## REFERENCES


1. Chen W. C. and Lawrence F. V., Jr. (1979) A model for joining the fatigue crack initiation and propagation analysis. *FCP Report No. 32*, A report of the Fracture Control Program, University of Illinois at Urbana-Champaign.

2. McMahon J. C. (1986) Fatigue crack initiation and early growth in tensile-shear spot weldments. *Ph. D. Thesis*, University of Illinois at Urbana-Champaign.

3. Yung J. Y. (1985) Further development of the total life model for weldments and its application to fatigue design. *Ph. D. Thesis*, Department of Metallurgical Engineering, University of Illinois at Urbana-Champaign.

4. Dowling N. E. (1979) Fatigue at notches and the local strain and fracture mechanics approaches. *Fracture Mechanics ASTM STP 677*, (Edited by Smith C. W.), American Society for Testing and Materials, pp. 247-273.

5. Park S. K. and Lawrence F. V., Jr. (1988) A long-life regime probability-based fatigue design method for the weldments. *UILU-ENG 88-3603, Report No. 142*, the University of Illinois at Urbana-Champaign.

6. Socie D. F., Dowling N. E. and Kurath P. (1984) Fatigue life estimation of notched members. *Fracture Mechanics: Fifteenth Symposium. ASTM STP 833*, Edited by Sanfird R. J., American Society for Testing and Materials, pp. 284-299.

7. Mazumdar P. K., Chen W. C. and Lawrence F. V., Jr. (1981) An analytical study of the fatigue notch size effect. *Fatigue Thresholds: Fundamental and Engineering Applications*, Vol II, Edited by Backlund J., Blom A. F.,and Beevers C. J., pp. 845-865.

8. Paris P. C. and Erodgan F. (1963) A critical analysis of crack propagation laws. *Journal of Basic Engineering*, ASME Transactions, **85**, Series D, No. 4, pp. 528.

9. Suresh S. and Ritchie R. O. (1984) Propagation of short fatigue cracks. *International Metals Reviews*, **29**, pp. 445-475.

10. Allison J. E. (1988) The measurement of crack closure during fatigue crack growth. *Fracture Mechanics: Eighteenth Symposium, ASTM STP 945*, Edited by Read D. T. and Reed R. P., American Society for Testing and Materials, pp. 913-933.

11. Liaw P. K. (1988) Overview of crack closure at near-threshold fatigue crack growth levels. *Mechanics of Fatigue Crack Closure, ASTM STP 982* , Edited by Newman, J. C. and Elber W., American Society for Testing and Materials, pp. 62-92.

12. Liaw P. K. (1989) Long fatigue cracks - microstructural effects and crack closure. *MRS Bulletin* , **14**, pp. 25-35.

13. Richie R. O. and Suresh S. (1982) Some considerations on fatigue crack closure at near-threshold stress intensities due to fracture surface morphology, *Metallurgical Transactions A*, **13A**, pp. 937-940.

14. Elber W. (1971) The significance of fatigue crack closure. *Damage Tolerance in Aircraft Structures, ASTM STP 486*, American Society for Testing and Materials, pp. 230-242.

15. Schijve J.(1988) Fatigue crack closure: observations and technical significance. *Mechanics of Fatigue Crack Closure, ASTM STP 982*, Edited by Newman J. C. Jr. and Elber W., American Society for Testing and Materials, pp. 5-34.

16. Hudak S. J., Jr. and Davidson D. L. (1988) The dependence of crack closure on fatigue loading variables. *Mechanics of Fatigue Crack Closure, ASTM STP 982* Edited by Newman, J. C. Jr. and Elber W., American Society for Testing and Materials, pp. 121-138.

17. Ibrahim F. K., Thompson J. C. and Topper T. H. (1986) A study of the effect of mechanical variables on the fatigue crack closure and propagation. *Int. J. Fatigue*, **8**, pp. 135-142.

18. Richie R. O. (1979) Near-threshold fatigue-crack propagation in steels. *International Metals Reviews*, Nos. 5 and 6, pp. 205-230.

19. McEvily A. J., Minakawa K. and Nakamura H. (1984) Fracture mechanics, microstructure, and the growth of short and long fatigue cracks. *Fracture: Interactions of Microstructure, Mechanisms, and Mechanics*, Edited by Wells J. M. and Landes J. D. Proceedings of the symposium sponsored by the the AIME and ASM, held February 27-29,1984, at the 113th AIME Annual meeting in Los Angles,CA. pp. 215-233.

20. Suresh S., Zamiski G. F. and Richie R. O. (1981) Oxide-induced crack closure: an explanation for near-threshold corrosion fatigue crack growth behavior. *Metallurgical Transactions A*, **12A**, pp. 1435-1443.

21. Radhakrishnan V. M. and Mutoh Y. (1986) On fatigue crack growth in stage I. *The Behavior of Short Fatigue Cracks*, EGF Pub.1, Edited by K. J. Miller and E. R. de los Rios, Mechanical Engineering Publications, London, pp. 87-99.

22. Kendall J. M. and Knott J. F. (1988) Near-threshold fatigue crack growth in air and vacuum. *Basic Questions in Fatigue: Vol II, ASTM STP 924*, Edited by Wei R. P. and Gangloff R. P., pp. 103-114.

23. Beevers C. J. (1980) Micromechanisms of fatigue crack growth at low stress intensity. *Metal Science*, **August-September**, pp. 418-423.

24. Gray G. T. III, William J. C. and Thompson A. W. (1983) Roughness-induced crack closure, an explanation for microstructurally sensitive fatigue crack growth. *Metallurgical Transactions A*, **14A**, pp. 421-433.

25. Ritchie R. O. and Lankford J. (1986) Small fatigue cracks: a statement of the problem and potential solutions. *Material Science and Engineering*, **84**, pp. 11-16.

26. Tao Y., He J. and Hu N. (1990) Effect of notch stress field and crack closure on short fatigue crack growth. *Fatigue Fracture Engineering Material Structure*, **13**, 423-430.

27. Tanaka K. and Nakai Y. (1983) Propagation and non-propagation of short fatigue cracks at a sharp notch. *Fatigue of Engineering Material s and Structure*, **6**, 315-327.

28. Newman J. C. Jr. , Swain M. H. and Phillips E. P. (1986) An assessment of the small-crack effect for 2024-T3 aluminum alloy. *Small Fatigue Cracks*, Edited by Ritchie R. O. and Lankford J., Proceedings of the Second Engineering Foundation International Conference/Workshop, Santa Barbara, California, pp. 427-452.

29. Shin C. S. and Smith R. A. (1988) Fatigue crack growth at stress concentrations - the role of notch plasticity and crack closure. *Engineering Fracture Mechanism*, **29**, pp. 301-315.

30. Liaw P. K. and Logsdon W. A. (1985) Crack closure: an explanation for small fatigue crack growth behavior. *Engineering Fracture Mechanics*, **22**, pp. 115-121.

31. Ogura K., Miyoshi Y. and Nishikawa I. (1985) Fatigue crack growth and closure of small crack at the notch root. *Current Research of Fatigue Cracks, MRS*, **1**, Society of Material Science, Japan, pp. 67-91.

32. Lalor P., Sehitoglu H. (1987) Fatigue crack closure outside the small scale yielding regime. *Mechanics of Fatigue Crack Closure, ASTM STP 982*, Edited by Newman, J. C. Jr. and Elber W., American Society for Testing and Materials, pp.342-360.

33. Lalor P., Sehitoglu H. and McClung R. C. (1986) Mechanics aspects of small crack growth from notches - the role of crack closure. In *The Behavior of Short Fatigue Cracks,* EGF Publication No. 1, Edited by Miller K. J. and de los Rios E. R.), pp. 369-386. Mechanical Engineering Publications, London.

34. Sun W. (1991) Finite element simulations of fatigue crack growth and closure. *Ph. D. Thesis*, Department of Mechanical Engineering, University of Illinois at Urbana-Champaign.

35. Tanaka K., Nakai Y. and Yamashita M.(1981) Fatigue growth threshold of small cracks. *International Journal of Fracture*, **17**, pp. 519-533.

36. El Haddad M. H., Smith K. N. and Topper T. H. (1979) A strain based intensity factor solution for short fatigue cracks initiating from notches. In *Fracture Mechanics, ASTM STP 677*, Edited by Smith C. W., American Society for Testing and Materials, pp. 274-289.

37. Frost N. E. (1959) A relation between the critical alternating propagation stress and crack length for mild steel. *Proc. Instn. mech. Engrs.* **173**, pp. 811-834.

38. Tanaka K. and Akiniwa Y. (1987) Notch geometry effect on propagation threshold of short fatigue cracks in notched components. *Fatigue '87, Vol II* (Edited by Ritchie R. O. and Starke E. A. Jr.), Third International Conference on Fatigue and Fatigue Thresholds, Charlottesville,VA., pp. 739-748.

39. Lukas P., Kunz L.,Weiss B. and Stickler R. (1986) Non-damaging notches in fatigue. *Fatigue Fracture Engineering Material Structure*, **9**, pp. 195-204.

40. Topper T. H. and El Haddad M. H. (1981) Fatigue strength prediction of notches based on fracture mechanics, *Fatigue Thresholds: Fundamental and Engineering Applications*, Vol II, Edited by Backlund J., Blom A. F.,and Beevers C. J., pp. 777-798.

41. DuQuesnay D. L., Topper T. H., and Yu M. T. (1986) The effect of notch radius on the fatigue notch factor and the propagation of short cracks. In *The Behavior of Short Fatigue Cracks*, EGF Publication No. 1 , Edited by Miller K. J. and de los Rios E. R., Mechanical Engineering Publications, London, pp. 323-335.

42. Yates J. R. and Brown M. W.(1987) Prediction of the length of non-propagating fatigue cracks. *Fatigue Fracture Engineering Material Structure*, **10**, pp. 187-201.

43. Cameron A. D. and Smith R. A. (1981) Upper and lower bounds for the lengths of non-propagating cracks. *International Journal of Fatigue*, **9**, pp. 9-15.

44. Lukas P. and Klesnil M. (1978) Fatigue limit of notched bodies. *Materials Science and Engineering*, **34**, pp. 61 - 66.

45. Lukas P., Kunz L., Weiss B. and Stickler R. (1989) Notch size effect in fatigue. *Fatigue Fracture Engineering Materials and Structures*, **12**, pp. 175-186.

46. Shin C. S. and Smith R. A. (1985) Fatigue crack growth from sharp notches. *International Journal of Fatigue*, **7**, pp. 87-93.

47. Siljander A. and Lawrence F. V. (1988) The mechanical properties of Al-Si alloy 319, the role of casting porosity. *Report to General Motors Corporation. College of Engineering, University of Illinois at Urbana-Champaign*, Urbana, IL.

48. Suzuki H. and Kunio T. (1987) Influences of porous defect on scatter of fatigue strength of aluminum casting alloy, AC4B (JIS). *Proceeding of the role of Fracture in Modern Technology Conference*, Fukuoka, Japan, 1986. Elsevier Science Publishers B. V., Amsterdam, The Netherlands. pp. 225-232.

49. Couper M. J., Neeson A. E. and Griffiths J. R. (1990) Casting defects and the fatigue behavior of an aluminum casting alloy. *Fatigue Fracture Engineering Material Structure*, **13**, pp. 213-227.

50. Tyler G. B. (1986) Axial fatigue testing of lost-foam 319 and 390 alloys. *Reynolds Metals Company Project No. 4R-4C3-Z458S*. Product and Process Development Laboratory/Chemical, Mechanical and Casting Technology Department.

51. Tokaji K., Ogawa T., Harada Y. and Ando Z. (1986) Limitations of linear elastic fracture mechanics in respect of small fatigue cracks and microstructure. *Fatigue Fracture Engineering Material Structure*, **9**, pp. 1-14.

52. Cox B. N. and Morris W. L. (1988) Monte Carlo simulations of the growth of small fatigue cracks. *Engineering Fracture Mechanics*, **31**, pp. 591-610.

53. Taylor D. (1986) Fatigue of short cracks: the limitations of fracture mechanics. *The Behavior of Short Fatigue Cracks*, EGF Pub.1, Edited by K. J. Miller and E. R. de los Rios, Mechanical Engineering Publications, London, pp. 479-490.

54. Raju I. S. and Newman J. C. (1986) Stress-intensity factors for circumferential surface cracks in pipes and rods under tension and bending loads. *Fracture Mechanics: ASTM STP 905*, Edited by Underwood J. H. et al., American Society for Testing and Materials, pp. 789-805.

55. Raju I. S. and Newman J. C. (1981) An empirical stress-intensity factor equation for the surface crack. *Engineering Fracture Mechanics*, **15**, pp. 185-192.

56. Tada H., Paris P. C. and Irwin G. R. (1973) The Stress Analysis of Cracks Handbook, 2.2 Del Res. Corp., Hellertown, PA.

57. Smith R. A. and Miller K J. (1977) Fatigue cracks at notches. *Int. J. Mech. Sci.* **19**, pp. 11-22.

58. Newman J. C. (1971) An improved method of collocation for the stress analysis of cracked plates with various shaped boundaries. *NASA Technical Note*, D-6376.

59. Nisitani H. and Goto M. (1986) A small-crack growth law and its application to the evaluation of fatigue life. *The Behavior of Short Fatigue Cracks*, EGF Pub.1, Edited by K. J. Miller and E. R. de los Rios, Mechanical Engineering Publications, London, pp. 461-478.

60. Holloway K. S. (1990) Evaluation of the porosity distribution in cast Al-Si alloy 319 alloy through destructive and non-destructive method. *M.S. Thesis, Department of Material Science and Engineering, University of Illinois at Champaign-Urbana.*

61. Peterson R.E. (1974) *Stress Concentration Factors*, John Wiley & Sons, New York.

62. Neter J. and Wasserman W. (1974) Applied Linear Statistical Models, Volume I, Richard D. Irwin, Inc., Homewood, Illinois.

63. Yu M. T.,Topper T. H., and Au P. (1984) The effects of stress ratio, compressive load and underload on the threshold behavior of a 2024-T351 aluminum alloy, *Fatigue 84* , University of Birmingham, UK, Vol. 1, pp. 179-186.

64. El Haddad M. H. (1978) A study of the growth of short fatigue cracks based on fracture mechanics. *Ph. D. Thesis*, University of Waterloo, Waterloo, Ontario.

65. de Kazinczy F. (1970) Effect of small defects on the fatigue properties of medium strength cast steel. *J. Iron Steel Inst.*, **208**, pp. 851-855.

66. Starkey M. S. and Irving P. E. (1982) Prediction of fatigue life of smooth specimens of SG iron by using a fracture mechanics approach. *Low Cycle Fatigue and Life Prediction, ASTM STP 770*, Edited by Leis B. N. and Rabbe P., American Society for Testing and Materials, pp. 382-398.

67. Taylor D. and Knott J. F. (1982) Growth of fatigue cracks from casting defects in nickel-aluminum bronze. *Metal technology*, **9**, pp. 221-228.

68. Eylon D. and Strope B. (1979) Fatigue crack initiation in Ti-6 wt%Al-4 wt%V castings. *Journal of Material Science*, **14**, pp. 345-353.

69. Starkey M. S. and Irving P. E. (1982) A comparison of the fatigue strength of machined and as-cast surface of SG iron. *International Journal of Fatigue*, **4**, pp.129-136.

70. Härkegård G. (1981) An effective stress intensity factor and the determination of the notched fatigue limit. *Fatigue Thresholds: Fundamental and Engineering Applications*, Vol II, Edited by Backlund J., Blom A. F.,and Beevers C. J., pp. 867-879.

71. Frost N. E. (1957) Non-propagating cracks in Vee-notched specimens subject to fatigue loading. *The Aeronautical Quarterly*, **VIII**, pp. 1-20.

72. McClung R. C. (1987) Fatigue crack closure and crack growth outside the small scale yielding regime. *Ph. D. Thesis*, Department of Mechanical and Industrial Engineering, University of Illinois at Urbana-Champaign.

73. Ting J. and Lawrence F. V., Jr. (1991) The long-life regime fatigue analysis for cast aluminum alloy 319. *Final Report to the General Motors Corporation, University of Illinois at Urbana-Champaign.*

74. Crepeau P. N. (1990) Private communication, Metallurgy Department, General Motors Research Laboratories, the General Motors Corporation.